A Field and Laboratory Investigation of the Compliance of Fractured Rock

Rudi Lubbe



TM

Thesis submitted for the degree of Doctor of Philosophy
to the University of Oxford

Wolfson College and Department of Earth Sciences

Hilary Term, 2005

Short Abstract

Compressional and shear wave velocity and attenuation measurements were obtained in the laboratory from 50 mm diameter, cylindrical, limestone core samples over a confining pressure range of 5 – 60 MPa. Normal and tangential fracture compliance values, as a function of confining pressure, were calculated for a single fracture cut perpendicular to the long axis of the core. The ratio of the normal to tangential compliance was approximately 0.4 and was independent of the applied stress. Values of normal and tangential fracture compliance calculated were of the order 10^{-14} m/Pa, and decreased with an increase in confining pressure. Both Q_P^{-1} and Q_S^{-1} were shown to be small for these samples.

A borehole test site was constructed in a Carboniferous limestone quarry, at Tytherington, situated north of Bristol, UK. This quarry was chosen because the rock type was fairly homogeneous and the fractures could be mapped in the quarry walls as well as down three, 40 m vertical boreholes drilled in-line in the quarry floor. Wireline logs were obtained in all the holes and a seismic crosshole survey was carried out between the two outermost boreholes. An estimate of *in-situ* normal fracture compliance Z_N was obtained from the log and crosshole data, in 4 different ways, using effective medium theories as well as the displacement discontinuity theory. An additional estimate of Z_N was obtained from a separate borehole test site constructed in fractured Devonian meta-sediments at Reskajeage, Cornwall, UK. These fractures were much larger in size than those observed at Tytherington quarry. From the above field and laboratory measurements, fracture compliance was shown to increase approximately linearly with the size of the fractures. In addition, a study of crosshole seismic attenuation was performed at Tytherington quarry.

Q was found to be frequency dependent. This frequency dependence was interpreted as being due to scattering rather than intrinsic attenuation.

Long Abstract

The characterisation of fractures *in-situ* is crucially important in a wide variety of solid earth exploration problems, such as petroleum reservoir development, hazardous waste disposal, hydrology, underground mining, geothermal exploitation, and the geotechnical stability of engineering sites. The seismic visibility of fractures depends on the magnitude of their normal and tangential compliances and how these quantities vary with the scale of the fracture and depth of burial. The main objective of this research is to obtain experimental evidence of the validity and practical applicability of recent published theoretical work on wave propagation through complex fractured media, and to determine if there is any evidence of compliance scaling with fracture size. At present, theoretical understanding of this issue has outstripped experimental verification. If the theory is to be of any practical value, it is essential to compare theoretical predictions with data from experiments where there is good control on the fracture parameters.

The scaling effect of fracture compliance is not well understood, as the field evidence in the literature is extremely sparse. Laboratory measurements give some indication of scaling behaviour, but the question still remains as to how compliance would up-scale to mesoscale fractures encountered in the field where seismic wave propagation occurs over tens to thousands of metres. To obtain synthetic data with frequencies in the range 10 Hz - 200 Hz for realistic fracture reservoirs it is essential to have reliable estimates of fracture compliance for fractures with lengths of metres to tens of metres. Laboratory measurements, on the other hand, are performed on relatively small samples with sizes ranging from millimetres to a few centimetres.

In this thesis, laboratory and field estimates of fracture compliance are presented covering a range of fracture sizes. Order of magnitude estimates of fracture compliance were obtained and compliance is shown to increase approximately linearly with the size of the fractures. Assuming that the fracture weld radius is related to the fracture size, this scaling behaviour is consistent with theoretical predictions by Hudson et al. (1997) for shear compliance, and also, if the fracture is filled with a weak material, for normal compliance. By relating the weld radius, for a fixed value of the proportion of area in welded contact, to the fracture compliance, it is implicitly assumed that fractures have fractal properties as suggested by Mandelbrot (1982), Brown and Scholz (1985), Yielding et al. (1992) and Xie (1993).

To investigate the compliance of fractured rock at the laboratory scale, compressional and shear wave velocity and attenuation measurements were obtained in the laboratory from 50 mm diameter, cylindrical, limestone core samples over a confining pressure range of 5 – 60 MPa. Both Q_P^{-1} and Q_S^{-1} were shown to be small for these samples. Measurements were first performed on whole core samples after which single fractures were cut perpendicular to the long axis of the core samples. Normal Z_N and tangential Z_T fracture compliance values were then calculated, as a function of confining pressure, by relating the reflection coefficients of a compressional and shear wave at normal incidence on the fracture, to the linear slip theory of Schoenberg (1980). The normal to tangential compliance Z_N / Z_T ratio has recently emerged as having a potential benefit in terms of estimation of fluid flow, permeability anisotropy and pressure prediction in hydrocarbon reservoirs (Liu et al., 1996; Schoenberg, 1998; Liu and Li, 2000; Liu et al. 2000). This is an area of intense current interest because of its conceptual and practical importance. Values of normal and tangential fracture compliance calculated were of the order 10^{-14}

m/Pa, and decreased with an increase in confining pressure. The ratio of the normal to tangential compliance, in this study, was approximately 0.4 and was independent of the applied stress. These values were consistent with laboratory results of normal and shear stiffnesses calculated by Pyrak-Nolte et al. (1990a) for single natural fractures in three samples of quartz monzonite, for a range of axial stresses from 1.4 – 85 MPa.

In addition, to investigate the compliance of fractured rock at the field scale, a borehole test site was constructed in a Carboniferous limestone quarry, at Tytherington, situated north of Bristol, UK. This quarry was chosen because the rock type was fairly homogeneous and the fractures could be mapped in the quarry walls as well as down three, 40 m vertical boreholes drilled in-line in the quarry floor. In order to reliably assign some chosen seismic attributes to the fracture compliance rather than the cumulative effect of three or four factors (such as seismic intrinsic attenuation, scattering off irregular interfaces, lithology, fracture distribution, etc.), one needs a detailed knowledge of the rocks through which the seismic waves have passed. Every attempt was made to constrain knowledge of the test area. Near and far-field full waveform sonic, resistivity, natural gamma, caliper and optical televiewer wireline logs were obtained in all the holes. A formation density log was obtained in one of the holes. In addition, a seismic crosshole survey was also carried out between the two outermost boreholes. An estimate of *in-situ* normal fracture compliance was obtained from the compressional wave sonic log and crosshole data using effective medium theories as well as the displacement discontinuity theory. To decide on a suitable analytical model one needs to make a prior assumption of the Z_N / Z_T ratio. This ratio is sensitive to the microstructural properties of the fracture as well as the fracture infill. To allow for the uncertainty in Z_N / Z_T ratio the estimates of Z_N were obtained in 4 different ways. Firstly, Z_N was calculated from the group time delay

the pulse experienced as it propagated across a set of open fractures (Schoenberg, 1980; Pyrak-Nolte et al., 1987). Secondly, Z_N was calculated by modelling the transmission amplitudes with the Schoenberg (1980) displacement discontinuity theory (Pyrak-Nolte et al., 1990a; Myer et al., 1995). Thirdly, Z_N was calculated from the modelled open fracture related fracture density ε_f (Hudson, 1980, 1981; Crampin, 1984). Finally, Z_N was calculated using the theory developed by Schoenberg and Sayers (1995). These authors have shown that any number of fracture sets with arbitrary orientations is long wavelength equivalent to three mutually perpendicular, rotationally invariant scalar fracture sets at most.

An additional estimate of Z_N was obtained from a separate borehole test site constructed in fractured Devonian meta-sediments at Reskajeage, Cornwall, UK. These fractures were larger in size than those observed at Tytherington quarry. Two, unlined, near vertical boreholes have been drilled approximately 25 m apart, to depths up to 300 m into the Mylor Slate Formation. Compressional wave seismic and electrical crosshole experiments were carried out between the two boreholes. A band of low seismic velocity, high electrical conductivity, very high seismic anisotropy (most values in excess of 30%) and large electrical anisotropy was observed in the upper fractured region between the two boreholes and was associated with relatively high values of hydraulic transmissivity in both holes. To obtain an open fracture related fracture density ε_f, this region was modelled by assuming that seismic anisotropy was a superposition of the inherent anisotropy of the rock fabric, and the anisotropy calculated for a set of fractures at an arbitrary angle introduced into an anisotropic background medium. An estimate of *in-situ* normal fracture compliance was then obtained from this fracture density value using

effective medium theories. The displacement discontinuity theory was also used to calculate a normal fracture compliance from the group time delay.

A study of crosshole seismic attenuation was also performed at Tytherington quarry. *Q* was found to be frequency dependent. This frequency dependence was interpreted as being due to scattering rather than intrinsic attenuation. This study also highlights the problems that can occur when modelling and interpreting seismic attenuation data.

Acknowledgements

I would like to express my sincere gratitude to Professor Michael Worthington for this research opportunity and for his kind support and inspirational supervision throughout the course of this research.

The financial support from the Natural Environment Research Council, Ernst and Ethel Eriksen Trust and the Peter Haworth/Robert and Cicely Wahl scholarship is gratefully acknowledged. I would also like to thank Wolfson College for their timely grant in the concluding months of this project.

This research began at Imperial College London, but the majority of the work was completed at Oxford University, whilst the laboratory experiments were performed at Reading University. Many people were instrumental in this work at the three institutions. Many thanks are due to Dr. John Cosgrove (Imperial College London) who suggested the Tytherington field site and assisted us with the field mapping, Dr. John Harrison (Imperial College London) who helped us in analysing the fracture network, and ARC Southern Ltd. for access to their quarry at Tytherington and much practical support. Many thanks are also due to Professor Clive McCann, Dr. Tim Astin, and in particular Mr. Jeremy Sothcott, for their expertise and input in the acoustic laboratory experiments at Reading University.

I would like to thank my friends and colleagues for making academic life an even more rewarding experience; firstly, at Oxford University: Simon Payne, Igor Escobar, Felicia Shaw, Richard Phillips, as well as Drs. Joe Olliver, Harry Tsikos and Annette Kleppe.

Secondly, at Imperial College London: Caterina Chironi, Stuart Humber, Patrick Alberts, Mohammed Al-Mazroey and Ibrahim Al-Ismaili, and a special mention to Jörg Herwanger for his valuable scientific input and the source of many valuable ideas. Thirdly, at Reading University: Stephen Hennah and Dr. Solomon Assefa. Special thanks also must go to May Chung (Oxford University) for fixing and fine-tuning my computer, and keeping it in perfect running order.

I sincerely thank my wife Mary who contributed to the completion of this thesis in so many different ways. Without her constant support and encouragement this work would not have been possible in the first place. My family was always in my thoughts and gave me the perseverance to succeed.

Finally, I would like to dedicate this thesis to my father and mother who gave me a firm grounding in life. Julle beteken die wȩreld vir my en het altyd in my geglo. Baie, baie dankie vir alles.

Table of Contents

Chapter 1: Introduction and Literature Review 20

1.1 Discontinuities in rock 20

1.2 Effective medium theories 26

1.3 Seismic theory of a displacement discontinuity 38

1.4 Seismic attenuation 43

1.5 Summary of chapters 45

Chapter 2: Laboratory Acoustic Experiment 48

2.1 Introduction 48

2.2 Sample preparation 50

2.3 Pressure cell and rig 54

2.4 Transducers and transducer assembly 55

2.4.1 Single P and S-wave transducers 55

2.4.2 Dual P and S-wave transducers 56

2.5 Pulse generators 56

2.6 Data acquisition and storage 59

2.7 Core sample length measurements 60

2.8 Measuring the bulk volume 61

2.9 Measuring the bulk density 63

2.10 Determination of porosity using the Helium Porosimeter 63

2.11 Transmission losses 66

2.12 Diffraction correction 67

2.12.1 Diffraction correction for travel time 70

2.12.2 Diffraction correction for attenuation 73

2.13 Experimental data 74

2.14 Picking the travel time difference 77

2.15 Methodology: Procedure to calculate Z_N and Z_T 79

2.16 Whole samples 80

2.16.1 Results and discussion 80

2.17 Cut samples 86

2.17.1 Results and discussion 86

2.18 Grooved sample 90

2.18.1 Results and discussion 92

Chapter 3: Tytherington Quarry - Wireline Data 96

3.1 Introduction 96

3.2 Geographical location and geology of Tytherington quarry 98

3.2.1 Geographical location 98

3.2.2 Geology 98

3.3 Fracture analysis 104

3.3.1 Fracture orientation from mapping 104

3.3.2 Fracture orientation from optical televiewer log 104

3.3.3 Wireline logging 108

3.4 Correlation between the open fractures and the wireline data 109

3.5 Calculating a fracture compliance from the compressional wave sonic data 111

3.6 Discussion 113

Chapter 4: Tytherington Quarry – Crosshole Travel Time Data 122

4.1 Introduction 122

4.2 Acquisition parameters 122

4.3 Picking of the travel times 125

4.4 Evidence of anisotropy 128

4.5 Calculating the anisotropy 129

4.5.1 Modelling the velocity dispersion 130

4.6 Estimating the lithology induced anisotropy 131

4.7 Calculating the fracture density ε_f 135

4.8 Calculating the normal compliance 136

4.9 Conclusions 138

Chapter 5: Tytherington Quarry – Crosshole Amplitude Study 146

5.1 Introduction 146

5.2 Receiver calibration 146

5.3 Spectral processing 147

5.4 Q dependence on frequency 153

5.5 Discussion 156

Chapter 6: Reskajeage Quarry 159

6.1 Introduction 159

6.2 Reskajeage test site 160

6.3 Fractures in an anisotropic background medium 165

6.4 Calculating the compliance and modelling the transmission amplitudes 171

6.4.1 Compliance from travel times 171

6.4.2 Modelling the transmission amplitudes 172

Chapter 7: Conclusions and Suggestions for Further Research 177

7.1 Conclusions 177

7.2 Suggestions for Further Research 183

Appendix 186

A.1 Proof that: $T_{BR}T_{RB} = 1 - R_{BR}^2$ 186

A.2 Calculating Z_N or Z_T from the reflection coefficients 187

A.3 Helium Porosimetry 189

A.4 Calculating the reflection coefficients of the crack from the acoustic data 192

A.4.1 Correcting the reflection coefficient of the crack interface for Q 192

A.4.2 Correcting the first reflection off the crack interface for transmission and Q 194

A.4.3 Correcting the first multiple reflection off the crack interface for transmission and Q 194

A.5 Benson and Kiyohara (1974) diffraction table 196

Bibliography 198

List of Figures

1.1 Interrelationships among fracture properties 23

1.2 A single set of fractures with a fracture normal parallel to the x_1-axis..... 36

2.1 Location in quarry from which the rock sample for coring was selected..... 49

2.2 Pulse-echo reflection system..... 51

2.3 Jones and Shipman surface grinder..... 52

2.4 Single core vacuum chuck 52

2.5 Vacuum pump..... 53

2.6 Pressure cell components..... 54

2.7 Pressure rig and lift 55

2.8 Transducer assembly..... 56

2.9 Example of pulsed-sine-wave traces generated 58

2.10 Measuring the length of the cylindrical core samples 60

2.11 Pressure cell in rig with three micrometer dials..... 61

2.12 Arenberg and Avtech P and S-pulse waveforms at different confining pressures..... 78

2.13 Avtech and Arenberg pulses to show the picking of the travel time difference 79

2.14 Flowchart outlining the methodology for calculating the normal and tangential fracture compliances 81

2.15 Whole samples: First and first multiple reflection off the rock/buffer rod interface..... 82

2.16 Whole samples: P and S-wave velocity versus confining pressure for both samples....84

2.17 Whole samples: Q_P^{-1} and Q_S^{-1} versus confining pressure for both samples....85

2.18 Cut samples: First and first multiple reflection off the rock/rock interface....86

2.19 Cut sample results versus confining pressure....88

2.20 Cut samples: Normal and tangential fracture compliance ratio versus confining pressure for both samples....89

2.21 Portland Pond Freestone grooved sample ensemble....91

2.22 Scanned image showing plan view of the bottom rock sample containing the grooves....91

2.23 Comparison of Q_P^{-1} from using the single and dual transducers....92

2.24 Grooved rock sample shortening versus confining pressure....93

2.25 Grooved sample results versus confining pressure....94

3.1 Limestone quarry wall at the borehole test site at Tytherington quarry....101

3.2 Map of the geology of the region....102

3.3 Plan view of the quarry indicating the location and strike of the boreholes....103

3.4 Fracture intersecting borehole as imaged by the optical televiewer log and interpretation thereof....105

3.5 Optical televiewer open fracture analysis of the three boreholes....115

3.6 Histograms showing the relative distribution of the bedding, open and calcite filled fractures in the three boreholes....116

3.7 Wireline geophysical logs obtained in all three boreholes....117

3.8 Wireline data and open fracture histogram correlation in BH 2....118

3.9 Wireline data and open fracture histogram correlation in BH 3....119

3.10 Wireline data and open fracture histogram correlation in BH 4 120

3.11 Analytical modelling to calculate the normal compliance from the compressional wave sonic data 121

4.1 Borehole electrical sparker source and hydrophone receivers 125

4.2 Acquisition geometry of the seismic crosshole survey at Tytherington 126

4.3 Tytherington common shot gather 127

4.4 Compressional wave velocity as a function of source and receiver depth 128

4.5 Horizontal difference velocities between BH 2 and BH 3 and the vertical compressional wave sonic interval velocity for BH 2 131

4.6 Backus average for BH 2 for all sonic velocity layer combinations 140

4.7 Backus average for BH 3 for all sonic velocity layer combinations 141

4.8 Backus average for BH 4 for all sonic velocity layer combinations 142

4.9 Cumulative P-wave velocity anisotropy for the three boreholes 143

4.10 Calculating the fracture density ε_f 144

4.11 Calculating the normal fracture compliance from the velocity anisotropy 145

5.1 Calibrating the receivers 148

5.2 Flowchart outlining the methodology followed in the amplitude processing 149

5.3 Analysis of the first arrival compressional wavetrain and choice of time window 151

5.4 Investigating the angular dependence of effective Q as well as the choice of the time window 152

5.5 Average stacked spectra of the three time windows 153

5.6 Forward modelling result assuming frequency independent Q 154

5.7 Frequency dependent Q from the average stacked zero offset spectra 155

5.8 Numerical modelling results in a media with discrete spatial distributions of fractures 158

6.1 Core analysis of a suite of samples from BH 20 162

6.2 Reskajeage common shot gather 163

6.3 Hydraulic transmissivity data for the two boreholes and the optimal seismic and electrical tomograms 166

6.4 Total compressional wave anisotropy ε_{res} as a function of the fracture density ε_f and dip θ of the imposed fracture on the anisotropic background medium 170

6.5 Calculating the normal fracture compliance from the group time delay 174

6.6 Reskajeage, amplitude analysis of a highly anisotropic fractured region and a high velocity, low anisotropy sandstone region 175

6.7 Modelling the transmission amplitudes using the linear slip theory 176

7.1 The scaling of fracture compliance from laboratory and field data 180

A1 Helium Porosimeter 189

A2 Reflection off the buffer rod/rock interface, and first reflection and first multiple reflection off the rock/rock interface 193

List of Tables

2.1 Petrographic data for the twenty Tytherington samples 65

2.2 Example showing how to correct the compressional wave velocity and attenuation for diffraction 76

2.3 Some physical properties of the perspex (lucite) buffer rod 77

2.4 Summary of the parameters as calculated from the whole acoustic data 83

4.1 Acquisition parameters for the seismic crosshole experiment at Tytherington quarry 124

6.1 P-wave velocity anisotropy resulting from introducing cracks, at an angle relative to the symmetry axis, into an anisotropic rock matrix 170

A.5 Benson and Kiyohara diffraction table 196

Chapter I

Introduction and Literature Review

1.1 Discontinuities in rock

The main objective of this research is to obtain experimental evidence of the validity and practical applicability of theoretical work on wave propagation through complex fractured media. Recent theoretical developments suggest that fracture compliance (or its inverse the fracture specific stiffness) is a key parameter when predicting the group time delay, reduction in frequency bandwidth and decrease in amplitude that a seismic wave can experience as it propagates through fractured rock. According to Hudson et al. (1996, 1997), the compliance is directly related to the microstructural details of the fracture surface, such as aperture, crack density and mean radius of weld. Fracture compliance is predicted to increase with increasing mean radius of weld and hence fracture dimension. However, the scaling effect of fracture compliance is still not well understood, as the field evidence in the literature is extremely sparse. Laboratory measurements give some indication of the scaling behaviour, but the question still remains as to how this parameter would up-scale for fracture lengths of metres or tens of metres. This thesis is principally an investigation of the scaling of fracture compliance using compressional and shear wave laboratory experiments on fractured core samples over a range of confining pressures, and also using field scale seismic crosshole and wireline log data.

The earth's upper crust is permeated by discontinuities such as joints, fractures and microcracks at all scales. These discontinuities might be aligned in one particular direction, randomly oriented, or consist of sets of aligned fractures which are oriented at fixed angles to each other. Furthermore, these fracture systems might be embedded in an

isotropic or anisotropic background medium, and might be open, partially open or sealed. The discontinuities normally increase the compliance of the intact rock mass, which will consequently result in a narrowing of the frequency bandwidth, and a reduction in the velocity and amplitude as the seismic wave propagates through the fractured rock mass. The specific stiffness of a fracture is the ratio between the seismic stress (which produces the elastic deformation of the asperities and voids in the fracture) and the seismic particle displacement across the boundary (units of stress/unit length) or the slope of the tangent to the stress displacement curve. The general understanding is that a fracture is a cluster of small cracks, and a fault is a cluster of fractures. The spatial aperture distribution and surface roughness are important parameters when considering single fractures, whilst fracture spacing, fracture orientation, spatial correlation among fractures and interconnectivity of fractures are all important for fracture networks. The normal experimental procedure at the field or the laboratory scale is to measure several properties of the fracture, like fluid flow through a fracture, mechanical deformation of a fracture, fracture geometry from borehole televiewers and field mapping, and the seismic response of a fracture in terms of velocity or attenuation.

Much attention has been paid to the properties of aligned cracks. Since discontinuities *in-situ* are subject to overburden pressure and tectonic stresses, they tend to be aligned. Cracks perpendicular to the maximum compressive stress are more likely to be closed, whereas those parallel to the maximum compressive stress are most likely to be open. Fractures that are open at the surface may be closed, or may not even exist at depth. Mineral deposition within the fracture (e.g. calcite in limestones) can also alter the fracture specific stiffness by filling in the void space, which will change the size and strength of the contact area. Seismic techniques provide the most promising means of

remotely sensing and characterising rock fractured properties, and the analytical theory of wave propagation through fractured rock is well developed.

Displacement versus normal and sometimes shear stresses has been studied using newly induced tensile fractures (Goodman, 1976; Swan, 1983) and natural fractures (Bandis et al., 1983; Raven and Gale, 1985; Pyrak-Nolte et al., 1990a). Goodman (1976), Bandis et al. (1983) and Pyrak-Nolte et al. (1990a) have drawn attention to the fracture specific stiffness as an important property of a fracture. The change in amplitude, and compressional and shear wave velocities across the displacement discontinuities, are proportional to the mechanical normal and tangential stiffness of the fracture, which in turn can be related to the geometric distribution of fracture aperture or void space at the fracture interface.

Lomize (1951) found that laminar flow between two glass plates depends on the cube of the separation (aperture) between the plates. In simple modelling, fluid flow is assumed to obey this cubic relationship. Pyrak-Nolte (1996) showed that fracture stiffness was inversely related to the cube root of flow. If this relationship holds, seismic measurements of fracture specific stiffness can provide an extremely valuable tool for predicting the hydraulic properties of a fractured rock mass, as it is the key link to inter-relating the physical properties of a fracture. However, it must be pointed out that the quantitative interrelationship between fracture specific stiffness and fluid flow is not unique, as the mechanical displacement depends on the amount and spatial distribution of apertures and contact area, whilst the fluid conductivity of a fracture will depend on the size and the spatial distribution of the joint apertures within the fracture. As the stress on the fracture increases, the apertures of the fracture will close up. This will increase the contact area

and decrease the connectivity of the void space. This in turn will result in a decrease in fluid flow, until the percolation limit is reached (i.e. a connected path across the fracture does not exist any more) resulting in a precipitous drop in flow (Zimmerman et al., 1990). To examine the hydraulic, mechanical and seismic response of a fracture, Pyrak-Nolte (1996) performed experiments on three quartz monzonite (Stripa granite) samples, and found that fractures which exhibit the most displacement, and therefore had the highest compliance, supported the most flow, and also that the flow path geometry was highly correlated where regions of large apertures have a high probability of being surrounded by other regions of large apertures, and vice versa (as also observed by Pyrak-Nolte and Morris, 2000). While the fracture geometry controls the interrelationship between fluid flow and mechanical displacements, the seismic method serves as a tool to access the fracture geometry remotely.

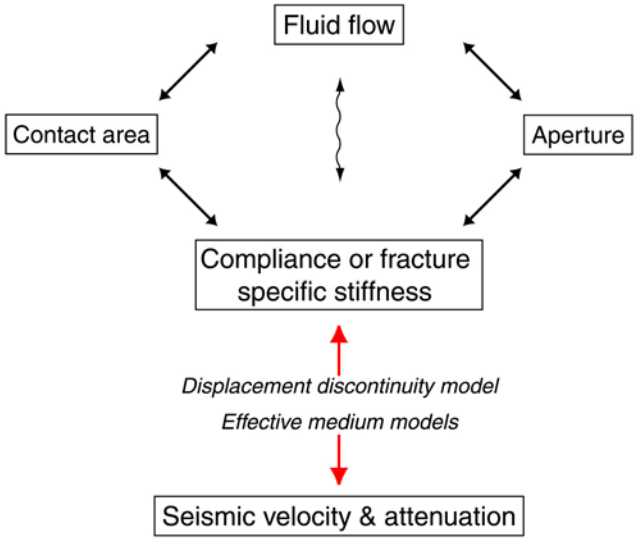


Figure 1.1: Fracture stiffness and fluid flow through a fracture are implicitly inter-related through the geometry of the fracture. Because fracture specific stiffness can be determined from seismic velocity and attenuation measurements, the hydraulic properties of a fracture can be investigated with seismic techniques (after Pyrak-Nolte, 1996).

The effects of fractures on seismic wave propagation are theoretically modelled by the displacement discontinuity theory or effective medium theories. The difference between

the displacement discontinuity models and effective medium models is that, in the displacement discontinuity model, the changes in frequency dependent group time delay and signal amplitude occurs at the fracture, whereas in the effective moduli method, the discreteness of the fracture is lost when the effects of the fracture are incorporated into effective moduli. Effective media models are strictly valid in the long wavelength limit, which assumes that the smallest wavelength of interest must be much larger than the crack dimensions or the sizes of the voids (apertures) under investigation. As new technology emerges and increasing attention is given to the development of methods to improve the resolution of subsurface structures, the situation will become more common in which the planar extent of the fractures, as well as the inter-fracture spacing, is large or comparable to the seismic wavelength in surface seismic exploration. Single fractures of large (infinite) planar extent cannot be represented by models of cracks small in length compared to the wavelength. Also, an effective modulus is neither correct nor appropriate when describing the wave propagation through fractured rock in which fracture spacing is of a magnitude comparable with, or even larger than, the seismic wavelength. It is essential that an appropriate model is used to investigate seismic wave propagation through complex fractured media. For seismic wavelengths much greater than the mean separation between asperities but less than the fracture spacing, the displacement discontinuity model has been suggested as an alternative to the elastic effective moduli method (Kendall and Tabor, 1971; Schoenberg, 1980).

King et al. (1986) conducted a crosshole experiment in which compressional and shear waves were propagated between four horizontal drill holes in a predominantly vertically jointed basaltic rock mass. The wavelength of the compressional waves was about 0.1 m, the spacing of the predominant jointing was 0.2 m - 0.5 m, and the distance between the

boreholes was approximately 3 metres. The waves with propagation paths across the fractures between the basalt columns were of smaller frequency bandwidth, smaller amplitude and lower velocity than those propagated in a direction parallel to the columns. They also observed that the effect of fractures on seismic wave amplitudes can be an order of magnitude greater that the effects on velocities. To model the amplitude spectra of the transmitted wave, Myer et al. (1995) applied the seismic displacement discontinuity theory to the same King et al. (1986) data and obtained a fracture compliance of Z = 2 x 10^{-12} m/Pa. They observed that their value was approximately an order of magnitude greater than had been observed in laboratory measurements on granitic rock by Pyrak-Nolte et al. (1990a) and concluded that the lower observed *in-situ* values might be due to scaling effects. Pyrak-Nolte et al. (1987) remarks that a typical change in velocity, caused by the presence of fractures as measured in the field at conventional seismic frequencies, is in the order of 5%. Using quasi-static or low frequency models, they showed that for P-waves normally incident on the fractures, the value in the following table of stiffness κ, the number of fractures per length n and frequencies would result in this 5% change in velocity:

n [fractures/metre]	0.01	0.1	1	10
κ [Pa/m]	10^{10}	10^{11}	10^{12}	10^{13}
Frequency [Hz]	100	1000	10 000	100 000

The table shows that if a frequency of 100 Hz is used, a fracture with a stiffness of $\kappa = 10^{10}$ Pa/m (compliance of $Z_N = 10^{-10}$ m/Pa) could be detected by virtue of its effect on reflected and transmitted amplitudes, whereas a frequency as high as 100 kHz would be required to detect fractures with a stiffness of $\kappa = 10^{13}$ Pa/m (or a compliance of $Z_N = 10^{-13}$ m/Pa). However, this scaling effect of fracture compliance is still not well

understood, and the evidence of the scaling behaviour, especially from field data, is at best inconclusive and incomplete. This research includes field and laboratory studies of the scaling behaviour of fracture compliance. In order to study fracture compliance *in-situ*, the objective was to build field-scale laboratories where information about rock fractures was well constrained, and to then interpret the seismic data using existing seismic wave theory.

1.2 Effective medium theories

The usual method for calculating the anisotropy in seismic velocities, caused by the presence of cracks or fractures, is to derive the effective elastic moduli for the rock mass. In doing this, the additional compliance of a dilute population of fractures or cracks is incorporated into an average strain, resulting in effective moduli for the fractured rock as a whole. Effective medium theories assume that the fracture will reduce the modulus of the rock (the larger the dynamic moduli, the stiffer the fracture) leading to a reduction in the seismic velocity. However, the location and cause of the reduction cannot be isolated.

Assuming an isotropic background matrix with a random non-interacting distribution of discontinuities, Eshelby (1957) first successfully solved the elastic problems of an infinite solid containing ellipsoidal inclusions. Based on Eshelby's classical theory, Wu (1966) developed a scheme to calculate the elastic moduli of a two-phase material containing a solid matrix and inclusions for three different crack aspect ratios: (i) penny-shaped where the aspect ratio shrinks to zero $d = \frac{c}{a} \to 0$; (ii) spherical where the aspect ratio is unity and (iii) needle-shaped, where the aspect ratio tends to infinity. Wu (1966) found that the penny-shaped inclusions had the largest effect in changing the elastic moduli. Bruner (1976), Henyey and Pomphrey (1982), and Yamamoto et al. (1981) presented a new self-

consistent scheme, whereby a small dilute proportion of the cracks is first introduced into the uncracked solid. Then, another small portion of cracks is introduced into the effective solid, with the effective elastic constants calculated in the first step, and new elastic constants are calculated again. This process is repeated until all the cracks are introduced.

Hudson, in a series of papers (1980, 1981, 1986, 1988, 1991), developed expressions for the effective elastic properties of a cracked solid accurate to second-order in crack density. First-order theories contain information on first-order statistics only (number density of the cracks); whereas second-order theories contain second-order statistics (extent of crack clustering and crack-crack interactions). A first order approximation means that the fracture compliance of one fracture, and hence its effect on seismic wave propagation, is not a function of the proximity of other fractures and there is therefore no mechanical interaction between the fractures. Hopkins et al. (1988) and Myer et al. (1995) have shown that this is true as long as the fracture spacing is not comparable to the spacing between the asperities. Also, it is assumed that the material on either side of the fracture is elastic, homogeneous and isotropic. A criticism of the Hudson (1980, 1981) second-order theory is that, it is unphysical for large crack densities, as the elastic stiffness increases rather than decreases, with an increase in crack density. In the long wavelength limit, Hudson (1980) showed that the effective elastic constants of a cracked solid can be expressed as:

$$c_{ipjq} = c^0_{ipjq} + c^1_{ipjq} + c^2_{ipjq} \tag{1.1}$$

where c^0_{ipjq} is the fourth-order elastic stiffness tensor of the matrix material without the cracks, c^1_{ipjq} and c^2_{ipjq} are the first-order and second-order corrections to the elastic

constants due to the presence of cracks. If the cracks are aligned perpendicular to the Z-axis, c^1_{ipjq} and c^2_{ipjq} have the following forms:

$$c^1_{ipjq} = -\frac{\nu a^3}{\mu_0} c^0_{k3ip} c^0_{l3jq} \overline{U}_{kl}(ka) \tag{1.2}$$

$$c^2_{ipjq} = \frac{1}{\mu_0} c^1_{iprs} c^1_{knjq} \chi_{rskn} \tag{1.3}$$

with $\chi_{rskn} = \frac{1}{15}\left[\delta_{rk}\delta_{sn}\left(4+\beta^2/\alpha^2\right) - \left(\delta_{rn}\delta_{sk}+\delta_{rs}\delta_{kn}\right)\left(1-\beta^2/\alpha^2\right)\right]$

where ν is the number density of cracks (number per unit volume), k is the wavenumber, μ_0 is the shear modulus of the rock matrix with P and S-wave velocities of α and β respectively. $\overline{U}_{kl}$ is the k^{th} component of the discontinuity in displacement across the crack due to unit imposed traction in the x_l-direction, integrated over the crack and normalized by μ_0 / a (Hudson, 1981). The non-dimensional diagonal quantity $\overline{U}_{kl}$ depends on the conditions of the crack face. In the case where the cracks are penny-shaped or highly oblate spheroids $\overline{U}_{11} = \overline{U}_{22}$. The crack conditions can be 'dry' (stress-free condition), 'fluid-filled' (shear traction is free, but the normal displacement is continuous), or 'filled with a weak material' (both normal and tangential displacements are continuous).

The elasticity stiffness or compliance tensor has four indices, two corresponding to the indices of stress σ and two to the indices of strain ε. Since both stress and strain are symmetric, the elasticity tensor can be simplified to a 6 x 6 matrix c_{pq} (Auld, 1990). The four subscripts of the stiffness tensor maps to two subscripts as follows:

ij (or kl)		p (or q)
11	→	1

22	→	2
33	→	3
23, 32	→	4
13, 31	→	5
12, 21	→	6

Therefore;

$$c^0_{ipjq} = \begin{bmatrix} \lambda+2\mu & \lambda & \lambda & 0 & 0 & 0 \\ \lambda & \lambda+2\mu & \lambda & 0 & 0 & 0 \\ \lambda & \lambda & \lambda+2\mu & 0 & 0 & 0 \\ 0 & 0 & 0 & \mu & 0 & 0 \\ 0 & 0 & 0 & 0 & \mu & 0 \\ 0 & 0 & 0 & 0 & 0 & \mu \end{bmatrix} \tag{1.4}$$

$$c^1_{ipjq} = -\frac{\varepsilon_f}{\mu} \begin{bmatrix} (\lambda+2\mu)^2 & \lambda(\lambda+2\mu) & \lambda(\lambda+2\mu) & 0 & 0 & 0 \\ \lambda(\lambda+2\mu) & \lambda^2 & \lambda^2 & 0 & 0 & 0 \\ \lambda(\lambda+2\mu) & \lambda^2 & \lambda^2 & 0 & 0 & 0 \\ 0 & 0 & 0 & 0 & 0 & 0 \\ 0 & 0 & 0 & 0 & \mu^2 & 0 \\ 0 & 0 & 0 & 0 & 0 & \mu^2 \end{bmatrix} D \tag{1.5}$$

$$c^2_{ipjq} = \frac{\varepsilon_f^2}{15} \begin{bmatrix} (\lambda+2\mu)q & \lambda q & \lambda q & 0 & 0 & 0 \\ \lambda q & \lambda^2 q/(\lambda+2\mu) & \lambda^2 q/(\lambda+2\mu) & 0 & 0 & 0 \\ \lambda q & \lambda^2 q/(\lambda+2\mu) & \lambda^2 q/(\lambda+2\mu) & 0 & 0 & 0 \\ 0 & 0 & 0 & 0 & 0 & 0 \\ 0 & 0 & 0 & 0 & X & 0 \\ 0 & 0 & 0 & 0 & 0 & X \end{bmatrix} D^2 \tag{1.6}$$

where $q = 15\left(\frac{\lambda}{\mu}\right)^2 + 28\left(\frac{\lambda}{\mu}\right) + 28$; $X = \frac{2\mu(3\lambda+8\mu)}{\lambda+2\mu}$; D is the diagonal matrix with diagonal entries $(U_{11}, U_{11}, U_{11}, 0, U_{33}, U_{33})$. Here the dimensionless fracture density ε_f, is given by:

$$\varepsilon_f = Na^3/V = 3\phi/4\pi d \tag{1.7}$$

with N the number of cracks of average radius a in volume V, ϕ is the porosity, and d is the crack aspect ratio. The cracks must be aligned, smooth faced, highly oblate spheroids (penny-shaped), isolated from one another and sparsely distributed through the matrix, with the seismic wavelength much larger than the crack dimensions. Crampin (1994) relates the fracture density parameter to the degree of fracturing of the intact rock in the crust. Sayers and Kachanov (1991) show that the results based on Hudson (1980, 1981) deviate markedly from other methods for calculating the elastic constants of cracked solids for fracture densities in excess of 0.15. Herwanger et al. (2004) showed in their calculations that the anisotropy increases approximately linearly with crack densities up to this value. For a thin crack filled with a weak material, with Lamé constants λ' and μ', Hudson (1981) obtained:

$$\overline{U}_{11} = \frac{16}{3}\left(\frac{\lambda + 2\mu}{3\lambda + 4\mu}\right)\frac{1}{1+M} \tag{1.8}$$

where,

$$M = \frac{4\mu'}{\pi d\mu}\left(\frac{\lambda + 2\mu}{3\lambda + 4\mu}\right) \tag{1.9}$$

$$\overline{U}_{33} = \frac{4}{3}\left(\frac{\lambda + 2\mu}{\lambda + \mu}\right)(1+K)^{-1} \tag{1.10}$$

$$K = \frac{k' + \frac{4}{3}\mu'}{\pi d\mu}\left(\frac{\lambda + 2\mu}{\lambda + \mu}\right) \tag{1.11}$$

where $k' = \lambda' + \frac{2}{3}\mu'$ is the bulk modulus of the weak material and d the crack aspect ratio.

Equations 1.8-1.11 can be used to model water-filled saturated thin cracks by putting $\mu' = 0$ and $k' = \lambda' \cong 2.25\text{x}10^{9}$ N.m^{-2} or $2.25\,\text{x}10^{9}$ Pa (bulk modulus of H_2O), which

then gives:

$$\overline{U}_{11} = \frac{16}{3}\left(\frac{\lambda + 2\mu}{3\lambda + 4\mu}\right) \quad \text{and} \quad \overline{U}_{33} = 0 \tag{1.12}$$

Equations 1.8 → 1.11 can also be used to model dry cracks by putting $\lambda' = \mu' = 0$, which then give:

$$\overline{U}_{11} = \frac{16}{3}\left(\frac{\lambda + 2\mu}{3\lambda + 4\mu}\right) \quad \text{and} \quad \overline{U}_{33} = \frac{4}{3}\left(\frac{\lambda + 2\mu}{\lambda + \mu}\right) \tag{1.13}$$

This corresponds to the 'drained' case, in which fluids can flow freely in and out of the fracture in response to the passage of the seismic wave, to ensure constant pore pressure. Thus, $\overline{U}_{11}$(water-filled) $= \overline{U}_{11}$(dry) and $\overline{U}_{33}$(water-filled) $\neq \overline{U}_{33}$(dry).

Schoenberg and Douma (1988) proposed a model to simulate the behaviour of a fracture system composed of large, closely spaced, aligned joints. The model admits any fracture system anisotropy: triclinic, monoclinic, orthorhombic or transversely isotropic, and is specified by the form of the 3 x 3 fracture system compliance matrix. The fracture system may be embedded in an anisotropic elastic background with no restriction on the type of anisotropy. In a transversely isotropic fracture system where the intact background is isotropic, there are four parameters describing the fractured system. Two for the background material (Lamé's parameters) and two for the fracture system (normal and tangential compliance: Z_N and Z_T). According to this theory Z_N and Z_T are determined by the following equation:

$$\begin{bmatrix} \Delta u_3 / H \\ \Delta u_2 / H \\ \Delta u_1 / H \end{bmatrix} = \begin{bmatrix} Z_N & 0 & 0 \\ 0 & Z_T & 0 \\ 0 & 0 & Z_T \end{bmatrix} . \begin{bmatrix} \sigma_{33} \\ \sigma_{22} \\ \sigma_{11} \end{bmatrix} \tag{1.14}$$

where H is the fracture interval width, which must be sufficiently large so that the fracture medium has the same total thickness of fractures in any thickness interval H. Here H must also be much smaller than the smallest wavelength of interest for the fracture medium to be replaced by a long wavelength equivalent medium. Assuming that there are N fractures in an interval of thickness H and that each fracture has the same properties, the total displacement Δu_i of the fracture system under stress σ_i can be expressed as:

$$\Delta u_i = N\delta_i \tag{1.15}$$

where δ_i is the mean displacement of the surfaces for a single fracture (Xu and King, 1992). Therefore, the normal Z_N and tangential Z_T compliances for a fracture system can be respectively expressed as a function of the normal $Z_N^{'}$ and tangential $Z_T^{'}$ compliances of a single facture:

$$Z_N = D_f Z_N^{'} \quad \text{and} \quad Z_T = D_f Z_T^{'} \tag{1.16}$$

where D_f is defined as the number fractures per unit length in the direction perpendicular to the fractures. Therefore, its inverse $1/D_f$ is the fracture spacing.

Hudson et al. (1996, 1997) relate the measured stiffnesses (or compliances) directly to the microstructural details of the fracture, such as aperture, crack density and mean radius of weld. The two fracture surfaces do not exactly conform, but are characterised by a random distribution of circular contacts, or welds. The equations for normal and tangential stiffness derived in Hudson et al. (1997) appear again in Worthington and Hudson (2000) but with minor modifications to cover the case of wet cracks:

$$Z_N = r^w \frac{4\mu}{\pi a}\left(1-\beta^2/\alpha^2\right)\left(1+\frac{2\left(r^w\right)^{1/2}}{\sqrt{\pi}}\right)+\frac{\kappa'+(4/3)\mu'}{\Delta} \qquad (1.17)$$

$$Z_T = r^w \frac{8\mu}{\pi a}\frac{\left(1-\beta^2/\alpha^2\right)}{\left(3-2\beta^2/\alpha^2\right)}\left(1+\frac{2\left(r^w\right)^{1/2}}{\sqrt{\pi}}\right)+\frac{(\mu')}{\Delta} \qquad (1.18)$$

where α, β and μ are the P and S-wave velocity and shear modulus (or rigidity of the rock), r^w is the proportion of the fracture surface area that consists of welded contact, a is the mean radius of the contact areas, μ' and κ' are the rigidity and bulk modulus of the fracture fill, and Δ is the mean aperture of the fracture. Re et al. (1997) investigated the variations in contact area as a function of joint size experimentally (in the laboratory) and numerically (assuming a fractal model), and observed that the contact area percentage decreased from 12% to 6% with increasing joint size. Brown and Scholz (1985) measured surface roughness of several fractures and determined that surface roughness was scale independent and fractal within a certain range of sizes. Assuming that fractures have fractal properties, as also suggested by Mandelbrot (1982), Yielding et al. (1992) and Xie (1993), one can relate fracture size to the mean radius of the contact area a for a fixed value r^w. The derivation includes the assumption that r^w is less than 0.2. If the fracture fill is fluid with a zero rigidity, then the shear stiffness is independent of fracture aperture. Consequently, the change of tangential stiffness with the scale of a fracture can be modelled by choosing suitable values of the mean radius of the contact area and the proportion of the fracture surface area in contact. If the bulk modulus of the fracture fill is set to the value for air at atmospheric pressure, then the second term in equation 1.17 is very small, and normal stiffness is also effectively independent of fracture aperture (this corresponds to the ‘drained’ case).

Liu et al. (2000) and Pointer et al. (2000) included the effects of fracture interconnectivity

and viscous flow of fluid in fractures. Hudson and Liu (1999) and Liu et al. (2000) suggested that published fracture models can broadly be classified into three groups:

(i) fracture is modelled as a planar distribution of small isolated areas of slip or cracks / isolated open areas on an otherwise welded fault / partial bond (Hudson et al., 1996 model); (ii) fracture is modelled as a planar distribution of imperfect facial contacts or rough surface / isolated areas of welded contact on an otherwise open fault / kissing bond (Hudson et al., 1997 model); (iii) fracture is modelled as a thin, continuous layer, filled with a soft material which is used to represent hydraulic fractures (Fehler, 1982 model). The basic assumption of effective medium theories used in these models, is that the mechanical response of a fracture with a complex structure, will be approximately the same as a fracture with circular cracks or welds. For all three fracture models the assumption that $\frac{Z_N}{Z_T} \approx 1$ generally holds true for dry fractures (as the Poisson's ratio is small); the resultant fractured medium is called a scalar fracture system by Schoenberg and Sayers (1995) and for liquid filled fractures $\frac{Z_N}{Z_T} \approx 0$. This implies that the $\frac{Z_N}{Z_T}$ ratio could, in theory, be used as an effective indicator of pore or fracture fluids (Liu et al., 2000).

Recently, Schoenberg and Sayers (1995) developed a method to include the effects of geologically realistic fractures on the seismic propagation through fractured rock, by writing the effective compliance tensor of the fractured rock as the sum of the compliance tensor of the unfractured background medium, and the compliance tensors for each set of parallel or aligned fractures within this homogeneous, isotropic background matrix. They concluded that the excess fracture compliance tensor represents the maximum amount of

information that can be obtained from seismic data, and that it is not possible to distinguish between microcracks and macrofractures.

The effective elastic compliance tensor $\tilde{S}$ of a rock containing fractures relates the average strain ε_{ij} over a representative volume V to the average stress components σ_{kl}:

$$\varepsilon_{ip} = \tilde{S}\sigma_{jq} = \left(\tilde{S}_b + \tilde{S}_f\right)\sigma_{jq} = \left(s^0_{ipjq} + s^f_{ipjq}\right)\sigma_{jq} \tag{1.19}$$

where s^0_{ipjq} is the 3 x 3 x 3 x 3 compliance tensor in the absence of fractures and s^f_{ipjq} is the tensor resulting from the extra compliance as a result of the fractures. If the fractures are not aligned, multiple fracture sets can be added easily in the compliance domain, by adding the additional compliances of each fracture set using equation 1.19. The compliance matrix for an isotropic background medium depends only on the two Lamé parameters λ_b and μ_b:

$$\tilde{S}_b = \begin{bmatrix} \frac{\lambda_b+\mu_b}{\mu_b(3\lambda_b+2\mu_b)} & -\frac{\lambda_b}{2\mu_b(3\lambda_b+2\mu_b)} & -\frac{\lambda_b}{2\mu_b(3\lambda_b+2\mu_b)} & 0 & 0 & 0 \\ -\frac{\lambda_b}{2\mu_b(3\lambda_b+2\mu_b)} & \frac{\lambda_b+\mu_b}{\mu_b(3\lambda_b+2\mu_b)} & -\frac{\lambda_b}{2\mu_b(3\lambda_b+2\mu_b)} & 0 & 0 & 0 \\ -\frac{\lambda_b}{2\mu_b(3\lambda_b+2\mu_b)} & -\frac{\lambda_b}{2\mu_b(3\lambda_b+2\mu_b)} & \frac{\lambda_b+\mu_b}{\mu_b(3\lambda_b+2\mu_b)} & 0 & 0 & 0 \\ 0 & 0 & 0 & \frac{1}{\mu_b} & 0 & 0 \\ 0 & 0 & 0 & 0 & \frac{1}{\mu_b} & 0 \\ 0 & 0 & 0 & 0 & 0 & \frac{1}{\mu_b} \end{bmatrix} \tag{1.20}$$

For a single set of rotationally invariant fractures in an isotropic background medium, the medium is transversely isotropic, with its symmetry axis perpendicular to the fractures. For a single set of fractures with normal parallel to the x_1-axis, i.e. $n_1 = \{1,0,0\}$ (see Fig. 1.2), the compliance (Eq. 1.20) now becomes:

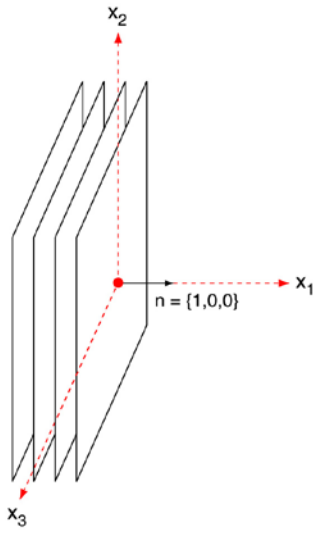


Figure 1.2: Schematic depiction of a single set of fractures with a fracture normal parallel to the x_1-axis.

$$\tilde{S} = \begin{bmatrix} \frac{\lambda_b+\mu_b}{\mu_b(3\lambda_b+2\mu_b)}+Z_N & -\frac{\lambda_b}{2\mu_b(3\lambda_b+2\mu_b)} & -\frac{\lambda_b}{2\mu_b(3\lambda_b+2\mu_b)} & 0 & 0 & 0 \\ -\frac{\lambda_b}{2\mu_b(3\lambda_b+2\mu_b)} & \frac{\lambda_b+\mu_b}{\mu_b(3\lambda_b+2\mu_b)} & -\frac{\lambda_b}{2\mu_b(3\lambda_b+2\mu_b)} & 0 & 0 & 0 \\ -\frac{\lambda_b}{2\mu_b(3\lambda_b+2\mu_b)} & -\frac{\lambda_b}{2\mu_b(3\lambda_b+2\mu_b)} & \frac{\lambda_b+\mu_b}{\mu_b(3\lambda_b+2\mu_b)} & 0 & 0 & 0 \\ 0 & 0 & 0 & \frac{1}{\mu_b} & 0 & 0 \\ 0 & 0 & 0 & 0 & \frac{1}{\mu_b}+Z_T & 0 \\ 0 & 0 & 0 & 0 & 0 & \frac{1}{\mu_b}+Z_T \end{bmatrix} \quad (1.21)$$

If $Z_N = Z_T = 0$ equation 1.21 reverts back to the isotropic case (Eq. 1.20). The value of fracture density is converted into a fracture compliance with units of Pa^{-1}. A stiffness matrix for a medium with a specified fracture density is obtained from Hudson (1980) or Crampin (1984), using equations 1.4 → 1.6, which can then be inverted to obtain the corresponding compliance matrix $\tilde{S}$. The excess compliance due to the fractures $\tilde{S}_f$ is $\tilde{S} - \tilde{S}_b$ (Eq. 1.21 – Eq. 1.20): Hence, normal fracture compliance: $Z_N = s_{11} - s_{22}$ and tangential fracture compliance: $Z_T = s_{55} - s_{44}$.

$$\Rightarrow \tilde{\tilde{S}}_f = \begin{pmatrix} Z_N & 0 & 0 & 0 & 0 & 0 \\ 0 & 0 & 0 & 0 & 0 & 0 \\ 0 & 0 & 0 & 0 & 0 & 0 \\ 0 & 0 & 0 & 0 & 0 & 0 \\ 0 & 0 & 0 & 0 & Z_T & 0 \\ 0 & 0 & 0 & 0 & 0 & Z_T \end{pmatrix} \tag{1.22}$$

If, however, the medium contains many sets of aligned fractures, assuming $Z_N = Z_T$, the fracture sets can be simplified into only three mutually perpendicular, rotationally invariant scalar fracture directions, which are the fracture components in the x_1, x_2 and x_3 directions in a 3D-coordinate system. The fractured medium is then orthorhombic.

In this case, the 6 x 6 compliance matrix $\tilde{\tilde{S}} = \tilde{\tilde{S}}_b + \tilde{\tilde{S}}_f$, in terms of Young's modulus E_b, Poisson's ratio ν_b with $\frac{1}{\mu_b} = \frac{2(1+\nu_b)}{E_b}$ may be written as:

$$\tilde{\tilde{S}} = \begin{bmatrix} \frac{1}{E_b}+\alpha_1 & -\frac{\nu_b}{E_b} & -\frac{\nu_b}{E_b} & 0 & 0 & 0 \\ -\frac{\nu_b}{E_b} & \frac{1}{E_b}+\alpha_2 & -\frac{\nu_b}{E_b} & 0 & 0 & 0 \\ -\frac{\nu_b}{E_b} & -\frac{\nu_b}{E_b} & \frac{1}{E_b}+\alpha_3 & 0 & 0 & 0 \\ 0 & 0 & 0 & \frac{2(1+\nu_b)}{E_b}+\alpha_2+\alpha_3 & 0 & 0 \\ 0 & 0 & 0 & 0 & \frac{2(1+\nu_b)}{E_b}+\alpha_1+\alpha_3 & 0 \\ 0 & 0 & 0 & 0 & 0 & \frac{2(1+\nu_b)}{E_b}+\alpha_1+\alpha_2 \end{bmatrix} \tag{1.23}$$

where α_1, α_2 and α_3 are the scalar compliances of fracture sets perpendicular to the x_1, x_2 and x_3 directions respectively.

Transverse isotropy can be implemented in the modelling as a special case by making the fractures very stiff ($\alpha_2 = \alpha_3$, $Z_N \leq 10^{-14}$ m/Pa) in the x_2 and x_3 directions (see Fig. 1.2).

1.3 Seismic theory of a displacement discontinuity

The elastic displacement discontinuity, linear slip, imperfect/loosely bonded, unbonded interface theory of Schoenberg (1980) models the effects of a fracture on seismic wave propagation by introducing a discontinuity in displacement (characterized by a specific stiffness) as a boundary condition in the seismic wave equation. A physical analog of the displacement discontinuity model is two elastic half spaces coupled by springs, in which the fracture specific stiffness is analogous to the spring constant per area for a certain spring distribution. Schoenberg (1980) has developed expressions for the seismic transmission and reflection coefficients across a partially open, (infinite) planar fracture, by assuming that traction across the interface is continuous, but displacement need not be. In this linear slip model, the displacement discontinuity vector $\Delta\vec{u}$ is linearly related to the traction vector $\vec{t}$:

$$\Delta\vec{u} = \begin{bmatrix} Z_T & 0 & 0 \\ 0 & Z_N & 0 \\ 0 & 0 & Z_T \end{bmatrix} \cdot \vec{t} \qquad (1.24)$$

where Z_N and Z_T are the normal and tangential compliances of the fracture. This model yields complex and frequency dependent reflection and transmission coefficients, group time delays and group velocities, and predicts that a fracture will delay as well as attenuate a seismic wave. For a purely elastic, transversely isotropic medium, composed of a set of parallel fractures, the displacement discontinuity model predicts a group velocity and transmitted wave amplitude that depends on the frequency ω of the wave, fracture specific stiffness κ, angle of incidence θ, density and elastic properties of the intact rock.

In applying the displacement discontinuity model for wave transmission across a single fracture, it is assumed that the seismic wavelength must be greater that the spacing

between the asperities of contact between the two surfaces of the planar fracture. The stiffness is also assumed to be uniform across the fracture plane. For waves normal to the displacement discontinuity, with the same material properties in both half spaces, the reflection and transmission coefficients for an incident P-wave are:

$$R_p(\omega) = \frac{\imath\omega}{-\imath\omega + 2(\kappa_z / Z_p)} \tag{1.25}$$

$$T_p(\omega) = \frac{2(\kappa_z / Z_p)}{-\imath\omega + 2(\kappa_z / Z_p)} \tag{1.26}$$

The group time delay can be used to predict the P and S-wave velocities in rock containing fractures (Pyrak-Nolte et al., 1987). For the transmitted wave the group time delay is:

$$t_g = \frac{d\theta_T}{d\omega} = \frac{2(\kappa_z / Z_p)}{\omega^2 + 4(\kappa_z / Z_p)^2} \tag{1.27}$$

where,

θ_T is the phase of the transmitted wave

$d\omega$ is the angular frequency of the compressional wave ($2\pi f$ or $2\pi / T$)

κ_z and Z_p are the normal fracture stiffness and seismic impedance respectively

By assuming that the specific stiffness of one fracture, and hence its effect on wave propagation, is not a function of the proximity of other fractures, the magnitude of the transmission coefficient for a wave propagating across a set of parallel fractures is simply $|T|^N$, where $|T|$ is the value of the transmission coefficient for a single fracture and N is the number of fractures (Pyrak-Nolte et al., 1990b).

This theory predicts that:

- A fracture behaves as a low pass filter with a cut-off frequency which is determined by the ratio of the specific stiffness of the displacement discontinuity to the seismic impedance of the half-spaces, passing only those frequencies of the wave which are lower than the characteristic frequency $\omega_c = 2\kappa / Z$, resulting in apparent attenuation.
- Energy is conserved in the displacement discontinuity, so that $|R(\omega)|^2 + |T(\omega)|^2 = 1$.
- The absolute value of the transmission coefficient $|T(\omega)|$ is a maximum at zero frequency, with the reflection coefficient $|R(\omega)|$ being zero at zero frequency.
- The group time delay is a maximum at zero frequency and decreases with increasing frequency.
- As the pressure on the fracture increases, the void space closes up, the stiffness tends to infinity, the fracture compliance and the reflection coefficient tend to zero, whilst the transmission coefficient approaches unity and the displacement discontinuity becomes equivalent to a welded interface, until (in the limit), the fracture becomes mechanically indistinguishable from the host rock, and the seismic waves propagates across the fracture without any modifications. As the stiffness tends to zero (fracture becomes more and more compliant), the displacement discontinuity reverts to the case of a free surface with all the energy being reflected off the interface.

Experiments performed by Myer et al. (1985) using artificial fractures of calculable stiffness, provided validation of the seismic displacement discontinuity theory for single fractures and normally incident compressional and shear waves. Pyrak-Nolte et al.

(1987a) studied the relationship between applied stress and normal fracture displacement across single natural fractures in laboratory specimens of quartz monzonite to a maximum uniaxial stress normal to the fracture of 85 MPa. Pyrak-Nolte et al. (1987) formulated an expression for group velocity for waves propagating at normal incidence to fractures and found that the theory correctly predicted experimentally measured values of group velocities from rock samples containing single fractures. Using both amplitude and velocity data, Pyrak-Nolte (1988) showed that the displacement discontinuity boundary conditions correctly predict the seismic response of dry natural fractures in rock, and was found to be consistent with the field measurements of King et al. (1986).

Pyrak-Nolte et al. (1990a) performed laboratory experiments using compressional and shear waves transmitted normal through the fracture plane of three different natural fractures in crystalline quartz monzonite, at effective axial stresses from 1.4 MPa to 85 MPa, under dry and saturated conditions, at room temperature. Amplitude spectra for the fractured specimens were predicted using the displacement discontinuity theory, and compared with those observed experimentally, by multiplying the experimentally observed spectra of the intact sample by the magnitude of the transmission coefficient predicted by the displacement discontinuity theory. Values of dynamic specific stiffness were chosen by trial and error until the best fit was obtained. In general: (a) the amplitudes were much more sensitive to changes in stress than the travel times; (b) an increase in stress resulted in significant increases in the high frequency content of the transmitted pulses; and (c) the increase in amplitudes and decrease in travel times with increasing stress were much greater for the fractured specimen than the intact specimen. They showed that, while it is observed that the displacements within a specimen containing a fracture are greater than that of an intact specimen without a fracture, it is

also observed that these additional displacements are concentrated in a region local to the plane containing the fracture. This observation gives rise to the notion that the additional displacements associated with the fracture can be represented as a discontinuity in the displacement field, and could thus be modelled successfully with Schoenberg (1980) using the ultrasonic body wave velocities (dynamic measurements).

Pyrak-Nolte et al. (1990b) extended the displacement discontinuity model for a single fracture to calculate the anisotropy in group velocities and amplitudes of seismic waves transmitted at oblique angles across multiple parallel fractures (with the material on either side of the fracture assumed to be elastic, homogeneous and isotropic), and again compared theoretical modelling with experimental observations. To simulate fracture surfaces, 31 sandblasted, laminated, mild steel plates, each 0.00318 m thick, were bolted together, and the block was then loaded biaxially. Compressional and shear wave group travel times and transmitted amplitudes were measured at angles of incidence of 0º (normal to the fractures) and 90º (parallel to the fractures) at loads of 15 kN and 30 kN and frequencies around 1 MHz. Comparison measurements were made on a solid steel cylinder. They found that: (i) the group velocity and peak-to-peak amplitude for the received P and S-waves at 0º incidence were much lower than that obtained for 90º incidence; (ii) for the 90º incidence, the P, S_v and S_h group velocities approached the group velocity as measured from the solid cylinder; (iii) the amplitudes and velocities were lower at 15 kN than the corresponding amplitudes and velocities at 30 kN, as the fractures were more open; and (iv) the P and S-wave pulses had higher velocities, frequencies and amplitudes for the solid steel cylinder than the laminated sample. These observations corresponded well with the decrease in group velocity, reduction in amplitude and change in frequency content predicted by the displacement discontinuity

model, and confirm the validity of the displacement discontinuity model for representing the seismic response of fractures.

1.4 Seismic attenuation

Two different mechanisms contribute to the estimate of attenuation. The intrinsic attenuation is due to the conversion of vibrational energy to heat within an inelastic medium. The scattering attenuation is due to the redistribution of the seismic energy within an inhomogeneous elastic medium, and may attenuate or enhance the seismic amplitudes. Separating the effects of intrinsic and scattering attenuation is largely an unresolved problem. Using synthetic data Richards and Menke (1983) studied the case where the scattering attenuation was greater than the intrinsic attenuation and showed that the total or effective attenuation Q_{eff}^{-1} was equal to the sum of the scattering and intrinsic attenuation:

$$\frac{1}{Q_{eff}} = \frac{1}{Q_i} + \frac{1}{Q_s} \tag{1.28}$$

where Q_i^{-1} and Q_s^{-1} are the intrinsic and scattering attenuation respectively.

The attenuative properties of the medium can be defined in terms of the quality factor Q as:

$$\frac{1}{Q} = -\frac{\Delta E}{2\pi E} \tag{1.29}$$

where $(-\Delta E)$ is the energy loss per cycle in a material with peak strain energy E. In the case of a single frequency propagating wave, the equation can be generalized to include the rate of loss of energy by converting to differential form:

$$\frac{1}{Q} = -\frac{1}{2\pi}\left(\frac{dE}{E}\right)\left(\frac{T}{dt}\right) = -\frac{1}{2\pi}\left(\frac{T}{E}\right)\left(\frac{dE}{dt}\right) \tag{1.30}$$

where T is the period of the propagating wave. This equation implicitly assumes that the wave is a plane wave and that there are no losses due to geometrical spreading. The reduction in energy is only due to the attenuative properties of the medium. Integrating equation 1.30 with respect to time gives:

$$E = E_0 e^{\frac{-2\pi t}{QT}} \tag{1.31}$$

where E_0 is the initial energy at time $t = 0$ and t is the travel time of the wave. If the response of the medium is linear, then the energy of the wave is proportional to the amplitude squared, and replacing T^{-1} with the frequency of the wave f gives:

$$A = A_0 e^{\frac{-\pi f t}{Q}} \tag{1.32}$$

This equation may also be expressed in terms of the distance x travelled by the wave and the velocity v of the medium:

$$A = A_0 e^{\frac{-\pi f x}{Qv}} = A_0 e^{-\alpha x} \tag{1.33}$$

where,

$$\alpha = \frac{\pi f}{Qv} \tag{1.34}$$

the attenuation coefficient of the medium. The assumption of a linear medium, in that the attenuation of a wave with a range of frequencies is equal to the sum of the attenuation of each single frequency component, leads to the generalization of equations 1.32 and 1.33 to all frequencies (Neep, 1995):

$$A(f) = A_0(f) e^{\frac{-\pi f t}{Q}} = A_0(f) e^{-\alpha x} \tag{1.35}$$

The above equations assume that both Q and velocity are independent of frequency. In order to satisfy the requirements of causality (no energy can arrive before zero time) velocity is assumed to vary with frequency (dispersion).

Toksöz et al. (1979), and Johnston and Toksöz (1980) have concluded that Q is independent of frequency over a range from 0.1 MHz - 1 MHz at elevated pressures and temperatures. However, Winkler and Nur (1982) and Winkler (1985) have shown that Q, particularly for partially saturated and saturated porous rock is frequency dependent. Spencer (1981), Tittman et al. (1984) and Jones (1986) have demonstrated that peaks of attenuation exist between the seismic and the sonic frequency bands. Raikes and White (1984) deduce a power law dependence of attenuation on frequency over a frequency band from 10 Hz to 375 Hz in Pierre Shale. Meissner (1983) concludes that Q is frequency dependent, based on a wide frequency band marine experiment with a variety of sources as well as laboratory data. Portsmouth, Worthington and Kerner (1993) and Portsmouth, Worthington and Neep (1993) performed a VSP and crosshole field study in a Carboniferous limestone field site in northern England, and suggested evidence of frequency dependent intrinsic Q. Sams et al. (1997) showed in a subsequent study that the compressional wave is frequency dependent with a peak in the attenuation in the sonic frequency band.

1.5 Summary of chapters

Chapter 2 covers a description of the experimental apparatus used for measuring normally incident compressional and shear wave reflection coefficients of fractures cut in cylindrical, homogeneous core samples. Compressional and shear wave velocity and attenuation measurements on limestone samples were performed in the laboratory at ultrasonic frequencies up to 60 MPa confining pressure. Theoretical expressions relating the reflection coefficients of a single fracture to the normal and tangential fracture compliances are calculated at ultrasonic frequencies using the linear slip theory of

Schoenberg (1980). Good agreement is noted between these results and experimental work done by Pyrak-Nolte et al. (1990a, 1990b).

In *Chapter 3*, a borehole test site in a Carboniferous limestone quarry, Tytherington, south-west England, is described. Three, 40 m vertical boreholes were drilled in-line with an inter-borehole spacing of 7 metres. Full waveform sonic, resistivity, natural gamma, formation density, caliper and optical televiewer wireline logs were obtained in all the holes. A clear relationship between the open fractures (as interpreted from optical televiewers logs), sonic velocity and resistivity was observed. The first arrival P-wave sonic velocity fluctuations were consistent over all three boreholes and attributed to the presence of open fractures. An upper and lower limit of normal fracture compliance was calculated from the group time delay the compressional sonic wave experienced as it propagated through the open fractures.

Chapter 4 covers the compressional wave crosshole experiments performed at the Tytherington quarry test site. A compressional seismic crosshole survey was carried out between the two outermost boreholes. The velocity and anisotropy results are presented, and the observed anisotropy, and associated fracture density, is used to calculate an upper and lower limit of normal fracture compliance which is compared with the results obtained from *Chapter 3*. This chapter also highlights the ambiguity that can arise when velocity and attenuation anisotropy results from the fabric of the rock matrix, as well as the superimposed open fractures.

Chapter 5 describes the amplitude studies performed on the data from the Tytherington quarry test site. The data show the attenuation of the compressional waves to be

dependent on frequency, and a parallel is drawn between the complexity of Tytherington data and synthetic data from a numerical study performed by Vlastos et al. (2003), which modelled the effect of discrete spatial distributions of fractures.

In *Chapter 6*, results from a major field experiment at a borehole test site in Cornwall (UK) as described in Herwanger et al. (2004) are briefly reviewed. The determination of fracture density for a hydraulically conducting fracture zone between two boreholes is described. Upper and lower normal fracture compliance limits are then obtained from the group time delay and the calculated fracture density. Additionally, the amplitude behaviour is also shown to be consistent with these compliance estimates.

Finally, in *Chapter 7*, the scaling behaviour of compliance is discussed. The compliance results from the laboratory experiment (ultrasonic frequencies) and the crosshole experiments at the two field sites (sonic/seismic frequencies) are compared with theoretical predictions and the discussion concludes with suggestions for further research.

Chapter II

Laboratory Acoustic Experiment

2.1 Introduction

This chapter is a description of laboratory work which was carried out at the **P**ostgraduate **R**esearch **I**nstitute of **S**edimentology (PRIS) at Reading University (UK). The purpose of the experiment was to obtain accurate laboratory estimates of the elastic properties of a single fracture at ultrasonic frequencies. Normal and tangential fracture compliance values as a function of confining pressure were calculated by relating the reflection coefficients of a compressional and shear wave at normal incidence on a fracture (cut perpendicular to the long axis of the core) to the linear slip theory of Schoenberg (1980).

Experiments were performed on cylindrical, homogeneous Portland Pond Freestone (Jurassic Limestone) and Carboniferous limestone core samples obtained from the field site at Tytherington quarry. Figure 2.1 shows the outcrop in the Tytherington quarry from which the rock sample for coring was selected. The Portland Pond Freestone provided a homogeneous, calibration rock specimen which was easily obtainable, easy to machine and had a constant velocity with increasing confining pressure. Velocity increase with increasing effective pressure has been attributed to cracks closing (Brace et al., 1966), with a constant velocity indicating little inherent cracking. These characteristics ensured that a single synthetic fracture would be the dominant feature influencing the seismic properties. Compressional and shear wave velocity and attenuation were measured over a range of pressures (from 5 MPa up to 60 MPa), at ultrasonic frequencies (0.6 MHz to 1.0 MHz), in a Triaxial Hoek cell (Hoek and Franklin, 1968), using the pulse-echo reflection

technique devised by Winkler and Plona (1982) and implemented by McCann and Sothcott (1992).

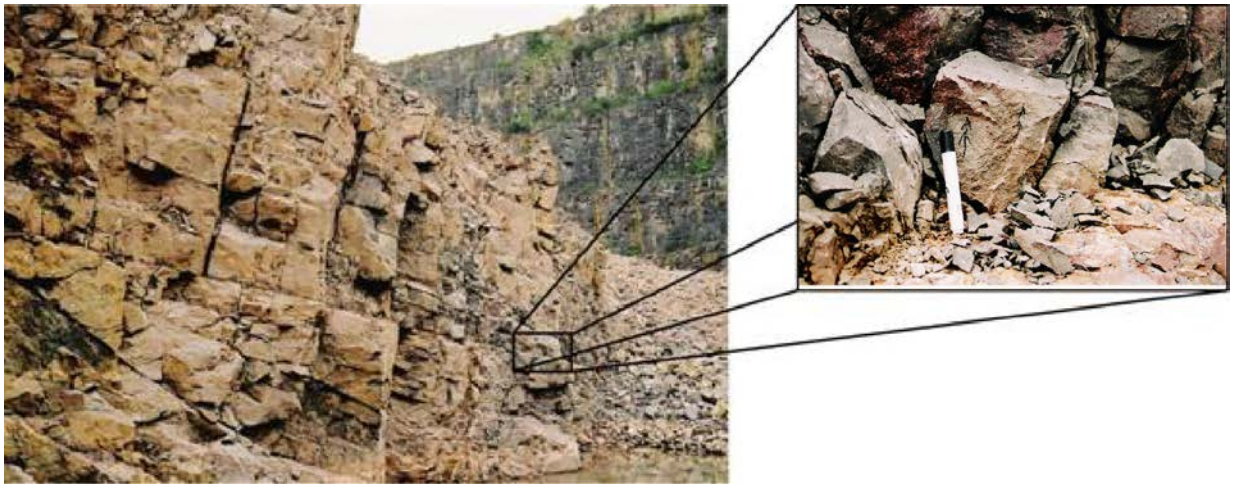


Figure 2.1: Location from which the rock sample for coring was selected. This *in-situ* sample was taken at a depth of 5 metres below the previous level, which corresponded with the top of the drilled boreholes at Tytherington quarry. The marker pen indicates scale. The black arrows on the sample indicate the exact orientation of the sample removed *in-situ*, and also the eventual long axis of the cylindrical core subsequently drilled from it. The core sample was placed in this orientation in the cell for acoustic measurements.

In the pulse-echo system the acoustics analysis of the rock is based on the reflections at the top and bottom of the sample. Any variation in the amplitude or spectral content of the source pulse due to the viscous transducer couplant, possible electronic variations, or impedance contrast between the buffer rod/rock and rock/buffer rod interfaces, would affect both reflections equally and would have no effect on the measurement of velocity and attenuation. The advantage of the method is that it is self-calibrating since whatever happens to the first pulse happens to the second one as well. The principal disadvantage of the method is that the velocity can be measured in only one direction - parallel to the long axis of the cylindrical core. As we were only interested in the normal and tangential compliance of a synthetic fracture perpendicular to the measurement direction, this

system limitation was not important. The precision of travel time measurements by this method was ±1 ns and the amplitudes were measured with a precision of ±0.01 mV.

A rock sample containing a fracture was sandwiched between perspex (lucite) buffer rods inside a hydraulic pressure cell. Velocity and attenuation were determined by comparing the picked travel times and the amplitudes of the pulses reflected off the top of the buffer rod/rock contact and the synthetic rock/rock (crack) interface. A compressional or shear wave transducer transmits a pulse through the perspex buffer rod into the rock sample which is then in turn reflected off the crack interface. The same transducer was used to receive the reflections from the buffer rod/rock interface at the top and from the rock/rock interface in the middle (Fig. 2.2). The reflected pulses were displayed on a digital oscilloscope for direct measurements of the travel times and amplitudes. The whole system comprising the steel housing of the transducer, the perspex buffer rods and the rock sample was enclosed in a rubber jacket and placed inside the pressure cell, applying a hydrostatic pressure up to 60 MPa. A feature of the high pressure cell is a hydraulic ram which extends from the inside to the outside of the chamber which remains in contact with the top of the transducer housing enabling uniaxial pressure to be applied. Travel time, amplitude and frequency measurements were then obtained with a digital oscilloscope, the traces were stored on computer and the pressure was increased to 60 MPa following the pressure sequence: 5 MPa, 10 MPa, 15 MPa, 20 MPa, 30 MPa, 40 MPa, 50 MPa and 60 MPa. The whole system was allowed to equilibrate at each pressure for a minimum of 30 minutes.

2.2 Sample preparation

Cylindrical core samples, 50 mm in diameter, of various lengths, were cut out of a

Portland Pond Freestone block and a Tytherington field sample (Fig. 2.1) using a diamond-tipped coring bit. The faces of the specimens were cut roughly parallel with a circular diamond edge saw and then lapped with a Jones and Shipman (Model 540) surface grinder, using different grade diamond wheels, to ensure end-face parallelism and flatness to an accuracy of ±0.005 mm (Fig. 2.3). A high degree of parallelism is crucial for two reasons (Sothcott, 1991):

(i.) Any lack of parallelism in the faces will result in breakage of the sample, as the stress pattern would be uneven in the high pressure ITR Triaxial Hoek cell.

(ii.) To obtain the sample acoustic velocity, both time and distance needs to be measured to a very high accuracy.

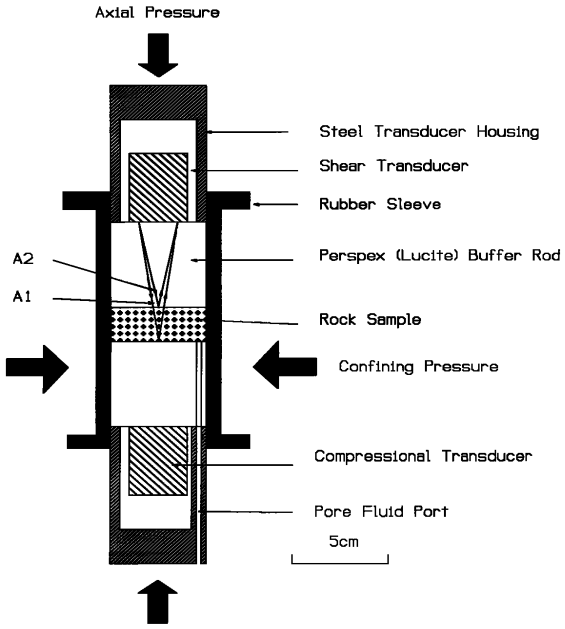


Figure 2.2: Schematic diagram showing the pulse-echo reflection system for measuring velocity and attenuation in the laboratory.

The single sample was held in place on the surface grinder by a vacuum chuck whilst grinding (Fig. 2.4). Afterwards, the sample was dried in an oven set at a constant 40º C for a day to remove the water used as a coolant in the cutting process. The oven dry core plugs were then further dried by placing the core samples in a steel chamber evacuated to

10^{-4} Pa (10^{-6} mbar) using a vacuum pump. This vacuum pump is an ensemble that consists of a rotary and diffusion pump unit (Fig. 2.5). The dried samples were then stored in an evacuated vacuum desiccator to ensure that the samples did not re-absorb any moisture from the atmosphere.



Figure 2.3: Jones and Shipman, model 540, surface grinder used to ensure end-face parallelism and flatness of the cylindrical core samples.

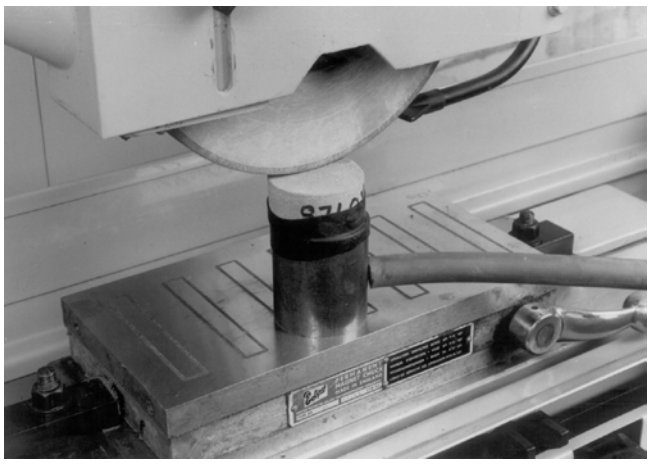


Figure 2.4: The single core vacuum chuck in operation. The chuck held the core sample firmly in place whilst lapping the edges on the surface grinder.

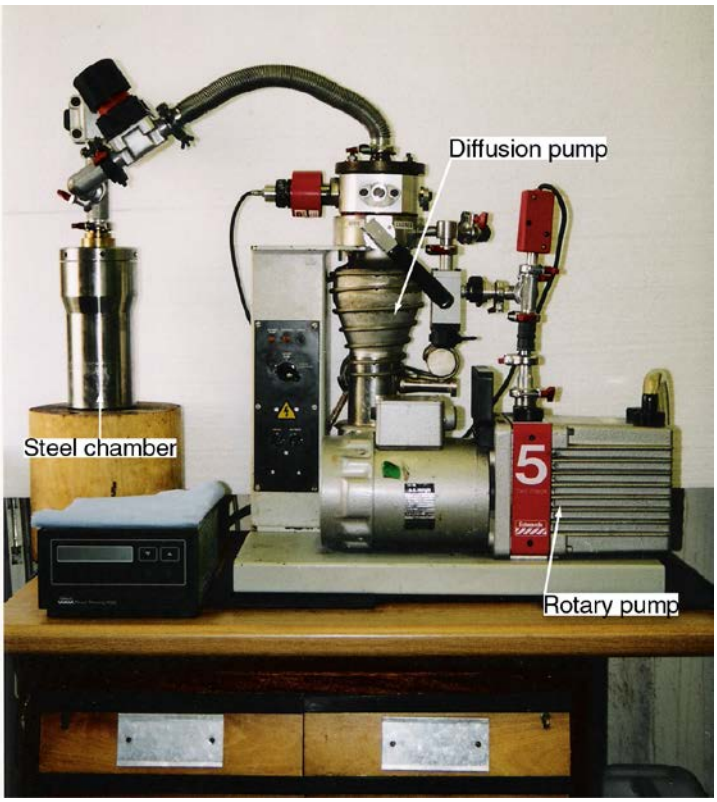


Figure 2.5: Vacuum pump used to dry the samples. The unit consists of a rotary pump and a diffusion unit. The vacuum pump is capable of evacuating the steel chamber to a pressure of up to 10^{-4} Pa ensuring completely dry samples.

2.3 Pressure cell and rig

The pressure cell used to exert a confining pressure onto the sample and the transducer assembly was an ITR Triaxial Hoek type cell. The maximum working pressure of the cell is 70 MPa and consists of a 160 mm diameter alloy steel tube, 270 mm long, with two internally fitted annular ring enclosures. A 5 cm internal diameter, cylindrical, thick, nitrile, rubber sleeve is housed within the cell, and encases the cylindrical core sample (Fig. 2.6).

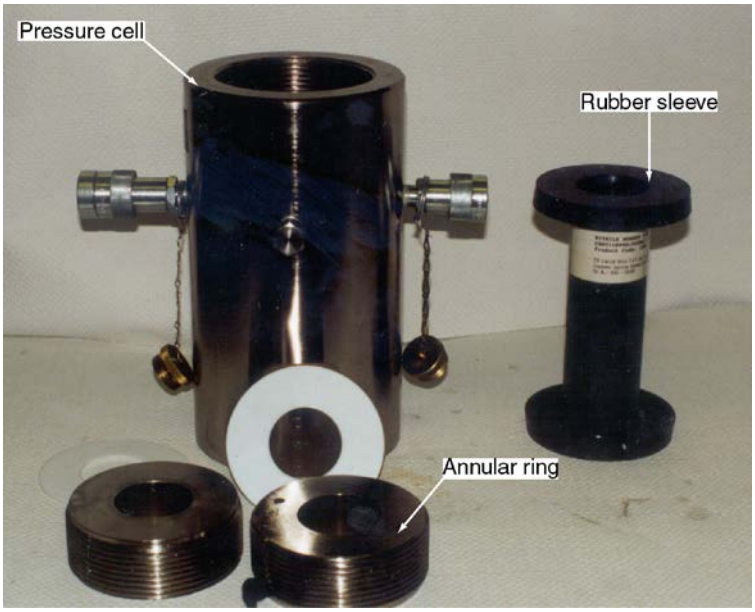


Figure 2.6: Pressure cell components used to exert a confining onto the sample (Courtesy of Mr. J. Sothcott, formerly at Reading University now at Southampton Oceanography Centre).

The oil reservoir between the rubber sleeve and pressure cell wall is filled with hydraulic oil. The whole system is pressurized by a single Enerpac P80 hand pump. The pump provides a confining pressure to the sample via the rubber sleeve, as hydraulic oil is pumped into the reservoir through a Pioneer High-flow port located either side of the pressure cell. The unused port is sealed off. An axial pressure via the transducer assembly is provided by an external ram attached to the top of the Enerpac pressure rig (Fig. 2.7). When loading a sample into the rig, it is crucial that the confining and axial pressure is

balanced before the system is pumped up to higher pressures. Failure to do so will result in the carefully prepared sample shattering under an uneven pressure distribution. The moving table of the rig is altered vertically with an Ezi-lift hoist and rests on two long pins inserted into the rig frame. The cell sits on four small alloy blocks held in position by four steel pins. It is further held firmly in place by two long hook bolts, which are secured by wing nuts, onto the moving table base assembly unit. A Budenberg pressure gauge, accurate to 0.25 MPa, was used to measure the effective pressure (confining pressure minus pore fluid pressure) on the sample.

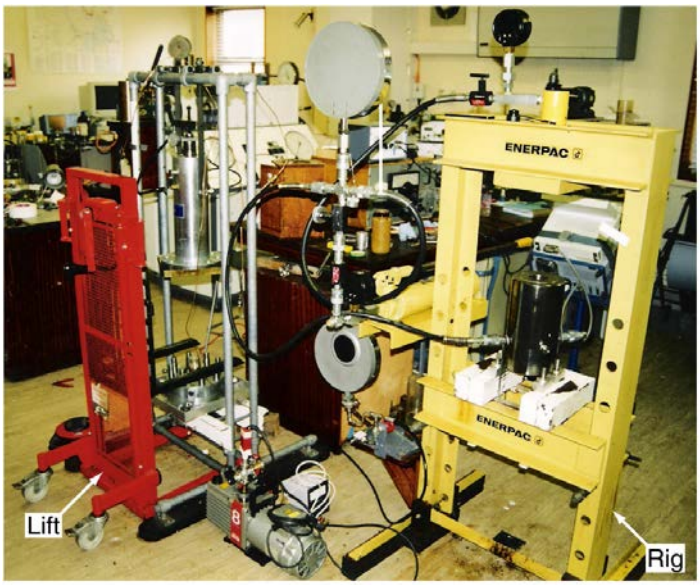


Figure 2.7: Enerpac pressure rig and Ezi-lift.

2.4 Transducers and transducer assembly

2.4.1 Single P and S-wave transducers

A Sonatest (Type SLE1-20) 20 mm diameter, compressional wave transducer and a Panametrics (Type V152) 25 mm diameter shear wave transducer, were used to generate the acoustic pulses. To ensure the efficient transfer of acoustic energy the transducers were cleaned with alcohol (methanol). The compressional wave transducer was coupled to the upper buffer rod with Ultragel couplant which is a water-based gel, whereas the

shear wave transducer was coupled with Panametrics shear wave couplant, which is a thick, viscous substance that resembles a mixture of honey and molasses that behaves as a solid at high frequencies. This couplant was also used for the dual P/S-wave transducer.

2.4.2 Dual P and S-wave transducers

A specially made Panametrics, 1 MHz, dual P/S, (Type D7105) unit (Fig. 2.8) was also used instead of single P and S-wave transducers. Using this dual transducer assembly enabled the lower rock sample to be made as long as possible (ensuring that the whole transducer assembly/rock sample and lower buffer rod still fitted into the rig). This led to the effective separation of the first reflected wavetrain energy off the rock/rock interface from subsequent first arrival reflected energy and multiple reflections off the bottom rock/buffer rod interface.

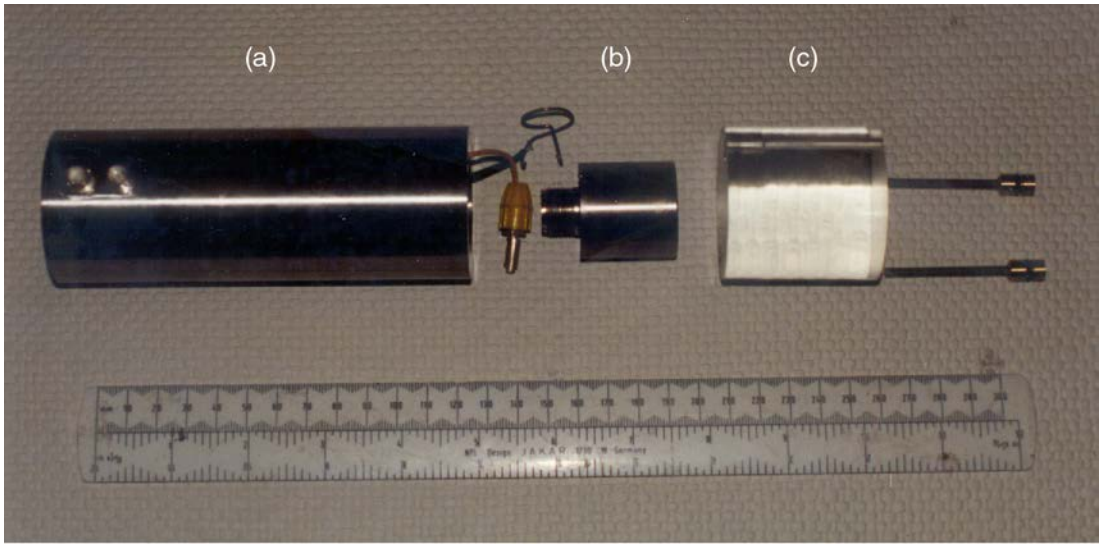


Figure 2.8: Transducer assembly. The assembly consists of (a) the transducer housing, (b) dual P/S-wave transducer and (c) a perspex buffer rod. The ruler indicates scale.

2.5 Pulse generators

The electrical signal driving the P and S-wave transducers was obtained from a pulse generator. Two types of pulse generators were used in the acoustic experiments to

generate single frequency and broadband pulses at ultrasonic frequencies:

(a) An Arenberg (Type PG 650C) pulse oscillator was used to generate a single, tone burst frequency, sinusoidal pulse, with a variable number of cycles, which then produces a flat–topped sinusoidal wavetrain. P-wave frequencies were typically ~0.9 MHz and generally higher than S-wave frequencies which were typically ~0.75 MHz.

(b) An Avtech (Type AVR-1-PW-C-P) pulse generator was also used to generate broadband pulses used for spectral analysis purposes. These pulses also aided in the picking of the correct travel times for reflections off the various interfaces using the Arenberg pulsed oscillator.

Figure 2.9 (a) shows an example of traces generated by the two generators with the top trace a typical broadband pulse and the bottom trace a typical single frequency pulse. The first pulse seen on each trace is the reflection from the top buffer rod/rock interface, the second, phase inverted pulse is from the lower rock/rock interface. Phase reversals will occur when there is an acoustic impedance contrast at the interface. In the rock/rock interface the air, which is of a lower velocity than the rock either side of the crack, allows for an impedance contrast, resulting in a phase reversal at the interface. Subsequent reflections are rock/rock multiples. The rock/buffer rod reflection can be seen much later in time, and is sometimes completely obscured or distorted by multiple reflections off the rock/rock interface. Figure 2.9 (b) shows the resulting power spectra for the broadband pulse (left) and the single frequency pulse (right). This clearly demonstrates that using a single frequency pulse allows the frequency to be measured with certainty.

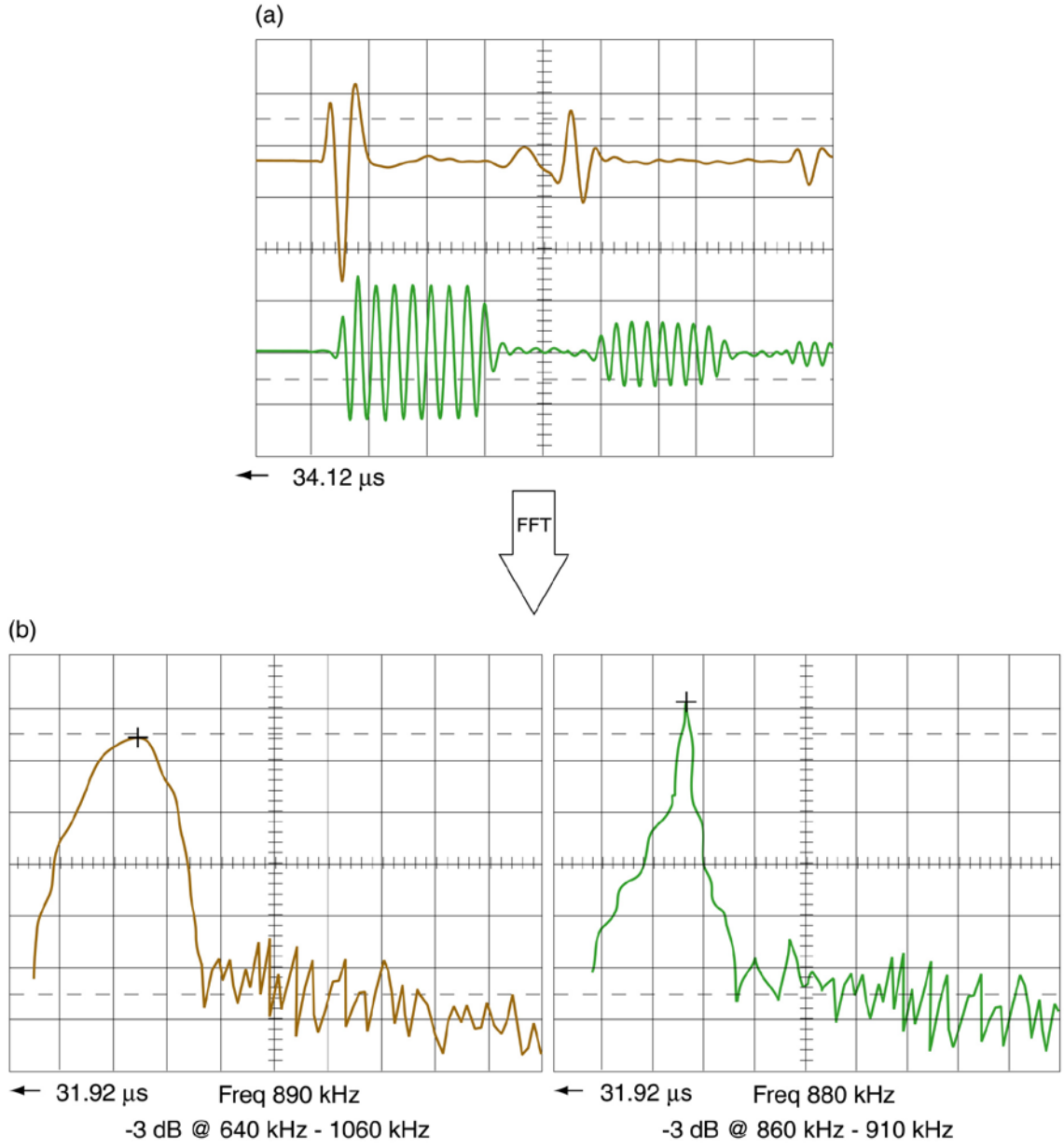


Figure 2.9: Example of pulsed-sine-wave traces generated. (a) The upper trace is a broadband pulse whilst the lower trace is a single frequency pulse; (b) Colour coded power spectra of the traces in (a). The settings of the oscilloscope were identical for each trace; the horizontal frequency axis is scaled from 0 Hz to approximately 4 MHz. The broadband spectrum (left trace) contains a wide range of frequencies from 640 kHz to 1060 kHz, whilst the single frequency spectrum (right trace) shows a narrower frequency content (860 kHz to 910 kHz).

2.6 Data acquisition and storage

The pulse train was left to settle first, and in each time and amplitude measurement, 1000 signals were summed and averaged to maximize the signal-to-noise ratio. This pulse train was gated to remove the input signal and displayed on a LeCroy (9400A) digital oscilloscope.

Measurements of the arrival times [μs], peak amplitude [mV] and frequency [kHz] of the 3rd positive cycle (peak) from the reflection (or echo) off the base of the top buffer rod, and the 3rd negative cycle (trough) from the reflection off the rock/rock interface were made. This technique eliminated the vagaries of first break picking. In picking the travel time on the oscilloscope the 3rd peak/trough under investigation was isolated and displayed with maximum amplification and a large offset (small T/div). The peak then became a sharply defined point and could be picked to the nearest nanosecond. The arrival times of the top (buffer rod/rock) interface and the middle (rock/rock) interface were measured and recorded twice at each pressure whilst the amplitudes and frequencies were measured once.

Signals were stored as binary files on floppy disc using an IBM computer. These binary files were later converted to ASCII format with LabView^{TM} and plotted in Matlab^{TM} for subsequent quality control and spectral analysis. Two single frequency traces were stored, one trace being the P-wave and the other being the S-wave with each trace containing the buffer/rock, rock/rock and rock/buffer interface reflections as a minimum. In addition, six broadband traces were stored, three for the P-wave and three for the S-wave respectively showing the reflection off the buffer rod/rock interface, the rock/rock interface and a trace containing all reflections (buffer rod/rock, rock/rock, rock/rock multiples, rock/buffer rod

and rock/buffer rod multiples). The start-time-delay [μs], gain [mV/div] and time-per-division [μs] were also recorded for all signals.

2.7 Core sample length measurements

The core length measurements were taken with a digital micrometer, capable of measuring to an accuracy of ±1 μm (Fig. 2.10 (a)). The core plug lengths at room pressure and temperature were averaged over 7 measurements at the positions shown in figure 2.10 (b).

(a) (b)



Figure 2.10: Measuring the length of the cylindrical core samples. (a) Digital micrometer; (b) The length recorded is an average length of 7 measurements taken at the numbered positions.

Another feature of the system is that the decrease in the length of the sample due to the increase in the applied pressure, could be monitored during the experiment i.e. whilst the sample was in the rig. Due to rig allocation time, the length versus pressure measurements were only taken for the grooved sample experiment (see section 2.18). The measurements could be taken accurately to ±0.01 mm with three dial micrometers. Two stainless steel rings are attached with tightening screws, to the top and the bottom of the transducer housings respectively. Welded to the rings, in the same plane, are three arms angled at 120° relative to each other which act as supports for three taught cables, from the micrometers, running between the top and bottom transducers (Fig. 2.11). The micrometers are calibrated to zero. As the pressure increases the buffer rock ensemble

shortens and the cables move downwards, resulting in a movement of the three micrometer needles. The values can then be read off conveniently from the dials. As one is only interested in the shortening of the rock sample from one pressure increment to the next, the shortening in the buffer rods need to be subtracted from the shortening of the buffer rod/rock ensemble. This results in the required shortening of the rock sample only.

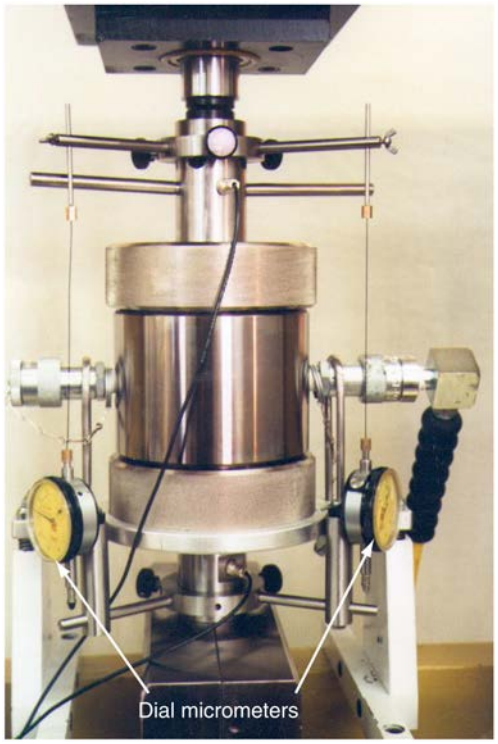


Figure 2.11: Pressure cell in rig with three micrometer dials angled at 120º relative to one another around the cell. Two yellow face micrometer dials can be seen to the front left and right of the cell respectively. A third micrometer is at the back of the cell obscured from view.

2.8 Measuring the bulk volume

For regular shaped cores like the small, cylindrical Portland Pond Freestone core samples, the bulk volume was determined from the length and diameter measurements on the core, made with the digital micrometer (see section 2.7). The bulk volume is simply equal to $\pi r^2 h$, with r and h, the radius and height of the core cylinder respectively.

To determine the bulk volume of the irregular Tytherington samples the Archimedes principle was applied. The small, oven dried, Tytherington core chips, were stored in a vacuum desiccator evacuated with a Charles Austin DA7-C pump. They were removed and individually weighed on a Sartorius Analytic balance to an accuracy of ±0.0001 g. Using a small paint brush the weighed chip was coated with wax and left to dry before weighing it again. Coating the sample with wax, ensured that when it was submerged it was completely watertight. A glass beaker containing deoxygenated H_2O, was then put on the scale and the scale was calibrated to zero. The waxed sample was immersed in the H_2O and the weight was recorded again. The wax weight could then be calculated by deducting the sample weight from the waxed sample weight and the bulk volume of the wax (V_W) could then be calculated by dividing the wax weight by the wax density knowing that $\rho_{wax} = 0.9983$ g/cm^3.

The bulk volume of the waxed sample could be calculated from:

$$V_{WS} = \frac{W_{WS} - W_{WI}}{\rho_{Fl}} \tag{2.1}$$

where,

V_{WS} = bulk volume of waxed sample [cm^3]

W_{WS} = waxed sample weight [g]

W_{WI} = waxed sample immersed weight [g]

ρ_{H_2O} = density of deoxygenated H_2O (0.9982 g/cm^3) [g/cm^3]

Finally, the bulk volume of the sample could be calculated by subtracting the bulk volume of the wax from the bulk volume of the waxed sample:

$$V_S = V_{WS} - V_W \tag{2.2}$$

where,

V_S = bulk volume of sample only [cm^3]

V_{WS} = bulk volume of waxed sample (wax + sample) [cm^3]

V_W = bulk volume of wax only [cm^3]

2.9 Measuring the bulk density

Many seismic modelling and interpretation schemes require, as a minimum, the P-wave velocity v_P, S-wave velocity v_S and the bulk density ρ_B. However, velocity is often not very well related to porosity, and therefore also not to density (Mavko et al., 1998). Bulk density and compressional and shear velocities were needed for the calculation of the acoustic impedances of the rock samples. These acoustic impedances were then used to calculate the normal and tangential compliance values of the crack interface, using the theory of Schoenberg (1980). The bulk density is related to the bulk volume as follows:

$$\rho_B = \frac{W_S}{V_S} \tag{2.3}$$

where,

ρ_B = bulk density of sample [g/cm^3]

W_S = weight of sample [g]

V_S = bulk volume of sample as calculated from equation 2.2 [cm^3]

2.10 Determination of porosity using the Helium Porosimeter

The wide range of densities of sedimentary rock is primarily due to variations in porosity. The bulk density used in calculating the normal and tangential compliance is a function of

porosity ϕ. Density is a simple volumetric average of the rock constituent densities and is closely related to porosity (Mavko et al., 1998) by:

$$\rho_B = \rho_{Fl}\phi + (1-\phi)\rho_M \tag{2.4}$$

where,

ρ_B, ρ_{Fl} and ρ_M = bulk, pore fluid and matrix density respectively

Helium Porosimetry was used to determine the porosity of the homogeneous, Portland Pond Freestone and Tytherington field samples. The Helium Porosimetry methodology is explained in detail in an internal Reading University document prepared by Mr. D. M. Thornley. A summary of the methodology is given in the Appendix (Appendix A.3). An average porosity from six samples of Portland Pond Freestone, of $\phi_{n=6}$ = 12.97% was obtained, compared with a value of ϕ = 13.73% supplied by the quarry owners.

Table 2.1 summarises the measured/calculated values from the Archimedes bulk volume experiment, pore, and grain volume, bulk density and porosity for 20 Tytherington rock samples. The porosities are very low (< 5%) with the exception of samples (2A, 3C and 6C). The higher values might be due to the samples having cracks in them as these samples contained obvious visible fossils and were weathered and brittle. Porosity affects the effective elasticity, and is an important factor in determining the velocities of sedimentary rocks (Sheriff and Geldart, 1999). The low porosity measured from the Tytherington samples implies that the bulk density correction would be minor as $\rho_M \to \rho_B$ when $\phi \to 0$ (Eq. 2.4). These measurements are not crucial to the calculation of the normal and tangential compliance values. However, they do demonstrate that the bulk porosity will have a negligible effect on the bulk volume deformation, and therefore also on the compressional and shear wave velocities (Fig. 2.16).

No.	Sample ID	W_S [g]	V_P [cm^3]	V_G [cm^3]	V_B [cm^3]	ρ_B [g/cm^3]	ϕ [%]
1	1A	1.5254	0.008	0.549	0.556	2.742	1.40
2	1B	2.2420	0.013	0.805	0.818	2.740	1.60
3	1C	2.0761	0.006	0.743	0.749	2.772	0.84
4	2A	3.3820	0.121	1.214	1.335	2.534	9.05
5	2B	3.6712	0.034	1.365	1.399	2.623	2.44
6	2C	2.1478	0.005	0.805	0.811	2.649	0.67
7	3A	4.4212	0.077	1.621	1.698	2.603	4.54
8	3B	3.3114	0.052	1.229	1.281	2.585	4.07
9	3C	1.6658	0.059	0.590	0.649	2.566	9.08
10	4A	2.1401	0.015	0.776	0.790	2.708	1.84
11	4B	2.7985	0.020	1.016	1.036	2.700	1.97
12	4C	1.8198	0.011	0.662	0.673	2.704	1.57
13	5A	2.9248	0.027	1.064	1.091	2.680	2.49
14	5B	1.1115	0.014	0.404	0.419	2.656	3.36
15	5C	3.5693	0.021	1.313	1.334	2.676	1.58
16	5D	1.5446	0.024	0.556	0.581	2.660	4.16
17	6A	2.7834	0.012	1.035	1.046	2.660	1.10
18	6B	1.9964	0.030	0.719	0.749	2.666	4.02
19	6C	1.6672	0.040	0.588	0.628	2.653	6.39
20	6D	1.0237	0.012	0.374	0.385	2.658	2.99
						$\langle 2.662 \rangle_{n=20}$	

Table 2.1: Petrographic data for the 20 Tytherington samples. The average bulk density ρ_B for $n = 20$ is 2.662 g/cm^3.

2.11 Transmission losses

When an acoustic pulse arrives at an interface separating two media with different elastic properties (different acoustic impedances) a proportion of the energy will be reflected and the rest of the energy (assuming infinite Q), will be transmitted through the interface.

The amplitudes of the reflected and transmitted waves are calculated from Zoeppritz's equations (Telford et al., 1990; Aki and Richards, 2002) which reduce to a very simple form at normal incidence.

The reflection coefficient from the perspex buffer rod to the rock sample, at normal incidence, is given as:

$$R_{BR} = \frac{Amp_1}{Amp_0} = \frac{Z_R - Z_B}{Z_R + Z_B} = \frac{\rho_R v_R - \rho_B v_B}{\rho_R v_R + \rho_B v_B} \qquad (2.5)$$

The transmission coefficient from the perspex buffer rod to the rock sample, at normal incidence, is given as:

$$T_{BR} = \frac{Amp_2}{Amp_0} = \frac{2Z_B}{Z_R + Z_B} = \frac{2\rho_B v_B}{\rho_R v_R + \rho_B v_B} \qquad (2.6)$$

where,

ρ = density of the buffer rod or rock

v = seismic velocity of the buffer rod or rock

Amp_0, Amp_1 and Amp_2 = amplitudes of the original, reflected and transmitted part of the wave respectively

The transmission loss [dB] is calculated from the amplitude ratio of the reflection off the base of the rock sample A_2 (rock/buffer rod contact) and the top of the rock sample A_1 (buffer rod/rock) contact. As $A_2 = A_0 T_{BR} T_{RB} R_{RB}$ and $A_1 = A_0 R_{BR}$

And also,

$T_{BR} T_{RB} = 1 - R_{BR}^2$ (see section A.1 in the Appendix)

It follows that the transmission losses arising from the impedance contrast between the buffer rods and sample are given by:

$$dB_{loss} = 20 \log_{10} \left| \left(\frac{A_0 T_{BR} T_{RB} R_{RB}}{A_0 R_{BR}} \right) \right|$$

$$= 20 \log_{10} \left| \left(- \frac{A_0 \left(1 - R_{BR}^2\right) R_{RB}}{A_0 R_{RB}} \right) \right|$$

$$= 20 \log_{10} \left| \left(1 - R_{BR}^2\right) \right|$$

$$= \left(\frac{20}{\ln 10} \right) \ln \left| \left(1 - R_{BR}^2\right) \right|$$

$$= 8.686 \ln \left| \left(1 - R_{BR}^2\right) \right| \qquad (2.7)$$

where,

R_{BR} = reflection coefficient at the buffer rod/rock interface

2.12 Diffraction correction

Diffraction corrections arise from the interference between the elementary waveforms transmitted from each point on the transducer and are a function of the frequency, transducer diameter and path length. The net result is a change in the phase of the observed signal, which gives rise to an apparent decrease in the travel time, and thus to a higher velocity in the sample. Wave diffraction is also responsible for a decrease in the

amplitude of the signal, resulting in an apparent higher attenuation in the sample. Both effects become more pronounced with decreasing frequency (McCann and Sothcott, 1992).

In calculating the velocity and attenuation in the pulse-echo method it is assumed that the waves generated by the ultrasonic transducers are planar. The finite diameter faces of the ultrasonic transducers produced waves that were neither spherical nor plane. It is therefore imperative to correct the reflections for frequency dependent diffraction effects (beam spreading) before calculating the normal and tangential compliances from the reflection coefficients of the crack interface. McCann and Sothcott (1992) concluded from measurements on an aluminium alloy and sandstone rock samples that the variations in reproducibility of specimen orientation, pressure and particularly the diffraction corrections for the finite size of the transducer, degraded the velocity accuracy to ±0.3% and the attenuation accuracy to ±0.1 dB/cm, at a frequency of 0.85 MHz, and a pressure of 60 MPa, within a 95% confidence interval. All the error bars on the subsequent figures in this chapter were calculated based on these error estimates of velocity and attenuation.

Papadakis (1972) calculated the phase and attenuation corrections by treating the transducer as a finite diameter circular piston. The amplitude and phase difference between the wavefield along the axis of the transducer, and the wavefield from a plane wave source could then be computed. Papadakis (1966) and Papadakis et al. (1973) calculated and produced graphs of the phase shift and the amplitude change arising from diffraction of a P-wave signal in terms of a distance, S, normalised by the Fresnel length:

$$\frac{2r^2}{\lambda} \tag{2.8}$$

where,

r = transducer radius [m]

λ = wavelength [m]

Benson and Kiyohara (1974) produced tabulated values of loss due to diffraction in dB as a function of the parameter S (Appendix A.5). Although these values strictly only apply to a compressional wave piston transducer, radiating into an infinite medium, the same correction was used for shear waves because diffraction corrections for shear waves have not yet been published. Best (1992) demonstrated that for the pulse-echo system the bottom reflection for P and S-waves lies well into the far-field or Fraunhofer region. In the dual transducer assembly the two active elements were not circular but semicircular so their radii for calculation of the diffraction correction could not be straightforwardly expressed. The effective radius of each of the dual P and S-wave transducers was 0.9 cm which is smaller than the single element shear and compressional transducers. This led to a larger scaled distance S, (from Eqs. 2.10 and 2.11) and as a consequence of this, also to a larger eventual diffraction correction. Klimentos and McCann (1990) and Green and Wang (1991), have shown that the diffraction corrections of Benson and Kiyohara (1974) are reliable for P and S-waves travelling through solids. McCann and Sothcott (1992) also carried out experiments with non-attenuating materials of known velocities (aluminium and brass) and found that the table of phase diffraction corrections for compressional waves gave good predictions of shear wave diffraction effects. The tabulated data of amplitude loss were therefore used to correct pulse-echo data for diffraction effects. The S-wave diffraction corrections for both velocity and attenuation are smaller than the P-wave diffraction corrections, as the S-waves have smaller wavelengths than the P-waves resulting in the near-field or Fresnel region extending further into the rock sample. Best (1992) has documented the theoretical diffraction corrections applied to the pulse-echo

system where the normalised distance S, is calculated from:

$$S = \frac{z\lambda}{r^2} = \frac{z\nu}{r^2 f} \tag{2.9}$$

where,

z = distance from the source [m]

λ = wavelength [m]

ν = velocity of the wave [m/s]

f = frequency [Hz]

For the pulse-echo method the values for S at the top and base reflections are calculated from:

$$S_T = \frac{0.1(\nu_{PB})}{r^2 f} \tag{2.10}$$

$$S_B = \frac{[0.1(\nu_{PB})] + 2L_R\nu_R}{r^2 f} \tag{2.11}$$

where,

S_T = normalized distance of the reflection from top of sample

S_B = normalized distance of reflection from the bottom of the sample

ν_{PB} = velocity of the perspex buffer rod; ν_P = 2763 m/s and ν_S = 1376 m/s

L_R = length of the rock sample [m]

ν_R = velocity of the rock sample [m/s]

2.12.1 Diffraction correction for travel time

The diffraction correction for the difference in travel time between the top and base reflections, using Benson and Kiyohara (1974) (Appendix A.5), is calculated from:

$$\Delta t = \frac{\phi(S_B) - \phi(S_T)}{2\pi f} \tag{2.12}$$

where,

Δt = travel time diffraction correction or increment in travel time due to diffraction [μs]

ϕ = phase shift at distance S [rad]

f = frequency [MHz]

The corrected travel time is then calculated from:

$$t_C = t_M + \Delta t \tag{2.13}$$

where,

t_C = corrected travel time [μs]

t_M = measured travel time [μs]

The sample density was obtained from the Helium Porosimetry measurements. Some physical properties of the perspex (lucite) buffer rod are given in table 2.3. The flowchart (Fig. 2.14) includes a series of processing steps that correct the raw data for extrinsic transmission losses and diffraction effects. Other intrinsic effects include interference from sidewall reflections, mode conversions and rock sample/buffer rod shortening at elevated pressures but have been shown not to be significant within the pulse echo system, at frequencies greater than 0.4 MHz for transducers with diameter of 2.5 cm (Best, 1992; Jones, 1995; Hennah, 2004).

In the grooved sample experiment (to be described in section 2.18) the shortening versus pressure for the sample has been observed for the whole pressure range from 5 MPa to 60

MPa. The true length of the rock sample between the buffer rods could be calculated accurately by subtracting the average length measurements from the three dial micrometer readings at every pressure from the original measured length at room pressure. This is the combined length change of the rock and buffer ensemble at a specific pressure. A calibration experiment monitoring the length change (using the dial micrometers) of the buffer rod, under an increase in pressure, has been performed. Knowing the buffer rod length change one can then calculate the length change correction to the rock sample by subtracting the combined buffer and rock length change from the calibrated buffer length change at every specific pressure. This correction (negative) is then added to the measured length of the rock sample at room pressure at every measured pressure from 5 MPa through to 60 MPa which gives the true actual rock sample length. Knowing this length one can then calculate the compressional and shear wave velocities (not corrected for diffraction/beam spreading) for a single frequency measurement:

$$v_{P/S}(f) = \frac{2L_R}{\langle \Delta t \rangle} \tag{2.14}$$

where,

$v_{P/S}(f)$ = compressional or shear velocity, which is a function of frequency [m/s]

L_R = length of rock sample [m]

$\langle \Delta t \rangle$ = average two-way travel time through the rock sample [s]

Using equations 2.10 → 2.12, the diffraction correction for the difference in travel time between the top and base (crack) reflections could then be calculated. Table 2.2 shows the procedure followed in correcting the calculated dry, Portland Pond Freestone, 50 mm cut sample, compressional velocity for diffraction effects at 60 MPa effective pressure. The same procedure applies to the shear velocity diffraction correction. Note: $\langle f \rangle_P$ indicates

the average compressional wave frequency calculated from the reflections off the buffer/rock and the synthetic crack interface respectively. The compressional and shear wavelengths can then be calculated using the diffraction corrected v_p and v_s velocities, and their average corresponding frequencies of the reflections off the buffer rod/rock and rock/rock interfaces respectively:

$$\lambda_P \text{ (@ 60 MPa)} = \frac{v_P}{\langle f \rangle_P} = \frac{4728}{877455} \approx 5.4 \text{ mm} \qquad \text{and}$$

$$\lambda_S \text{ (@ 60 MPa)} = \frac{v_S}{\langle f \rangle_S} = \frac{2690}{863555} \approx 3.1 \text{ mm}$$

2.12.2 Diffraction correction for attenuation

The frequency dependent attenuation coefficient α [dB/cm], again using Benson and Kiyohara (1974) (Appendix A.5), is calculated from:

$$\alpha(f) = \frac{8.686}{2L_R} \ln\left(\frac{A_1}{A_2}\right) \tag{2.15}$$

where,

L_R = length of rock sample [cm]

A_1 = amplitude of first buffer rod/rock reflection [mV]

A_2 = amplitude of second rock/buffer rod reflection [mV]

The quality factor Q, is then derived from the relationship:

$$Q = \frac{\pi f}{v\alpha} \tag{2.16}$$

where,

α = attenuation coefficient [dB/cm]

v = wave velocity [cm/μs]

f = wave frequency [MHz]

The presence of interfering pulses, such as those arising from scattering and mode conversions, distort the characteristic flat-top of the pulse and acts as a sensitive visual test of the reliability of the final attenuation results.

The diffraction correction (loss per unit length due to diffraction) for attenuation is calculated from:

$$\Delta\alpha = \frac{\alpha(S_B) - \alpha(S_T)}{2L_R} \tag{2.17}$$

where,

$\Delta\alpha$ = attenuation diffraction correction [dB/cm]

α = loss at distance S [dB]

L_R = length of rock sample [cm]

The corrected attenuation is then calculated from:

$$\alpha_C = \alpha_M - \Delta\alpha \tag{2.18}$$

where,

α_C = corrected attenuation [dB/cm]

α_M = measured attenuation coefficient [dB/cm]

2.13 Experimental data

Figure 2.12 shows an example of traces generated by the two generators travelling through the whole Portland Pond Freestone sample at different confining pressures.

Figures 2.12 (a) and (c), shows the broadband, Avtech, pulses and figures 2.12 (b) and (d), their corresponding single frequency, Arenberg, pulses. The vertical scale is in millivolts.

The first pulse seen on each trace is the reflection from the top buffer rod/rock interface. The second phase inverted pulse is from the lower rock/buffer rod interface. Subsequent much lower amplitude reflections are the rock/buffer rod multiples. The red arrows indicate the picked travel times, with the connecting blue dotted line showing a similar positive slope on both the reflections off the buffer rod/rock interface and the rock/buffer rod interface, with an increase in confining pressure. The same trend is observable for both the broadband and single frequency P and S-waveforms.

For all the recorded traces, the difference in travel time between the top and bottom reflections for the S-waveforms were larger than the corresponding travel time difference of the P-waveform at the same confining pressure. The amplitudes of the single frequency S-waveforms were generally *smaller* than the amplitudes of the single frequency P-waveforms, whilst the amplitudes of the S-waveforms, from the broadband frequency measurements, were *larger* than the broadband frequency P-waveforms, at the same confining pressures.

Velocity diffraction correction	
Uncorrected v_P [m/s] (Eq. 2.14)	4564
$\langle f \rangle_P$ [Hz]	877455
S_T (Eq. 2.10)	3.88751
S_T phase correction (ϕ)	0.79437
S_B (Eq. 2.11)	6.36300
S_B phase correction (ϕ)	1.08270
Diffraction correction (Eq. 2.12)	0.05229
Corrected v_P [m/s] (Eqs. 2.13 and 2.14)	4728

Attenuation diffraction correction	
*Uncorrected α [dB] (Eq. 2.15)	0.87784
S_T (Eq. 2.10)	3.95693
S_T phase correction (ϕ)	3.73830
S_B (Eq. 2.11)	10.58705
S_B phase correction (ϕ)	10.34300
Diffraction correction (Eq. 2.17)	0.66162
Corrected α [dB] (Eqs. 2.15 and 2.18)	0.21622

Benson and Kiyohara		
S	ϕ	α
0.0	0.00000	0.00000
0.1	0.07602	0.61488
.	.	.
3.6	0.75772	3.35980
3.7	0.77640	3.48390
3.8	0.79437	3.61020
3.9	0.81165	3.73830
4.0	0.82826	3.86770
4.0	0.82826	3.86770
.	.	.
6.0	1.05950	6.41140
6.1	1.06750	6.52930
6.2	1.07520	6.64610
6.3	1.08270	6.76180
6.4	1.09000	6.87640
6.5	1.09710	6.98990
.	.	.
.	.	.
10.0	1.25930	10.34300

Table 2.2: Correcting the compressional wave velocity and attenuation for diffraction. Exactly the same methodology is followed in correcting the shear wave velocity and attenuation for diffraction. *Note: The attenuation here has already been corrected for transmission losses using equation 2.7.

ρ [kg/m^3]	1183.55
Upper perspex buffer rod length [cm]	5
P/S transducer radius [cm]	0.9
v_P (perspex buffer) [m/s]	2763
v_S (perspex buffer) [m/s]	1376

Table 2.3: Some physical properties of the perspex (lucite) buffer rod.

2.14 Picking the travel time difference

In calculating the normal and tangential compliance values of the fracture, it was crucial to calculate the velocity, and therefore travel time, through the rock sample very accurately. Some single frequency reflections exhibited a slow rise time, which made identification of the third peak/trough pair on the single frequency pulses slightly more difficult. The broadband pulses aided in the picking of the correct travel time difference between buffer rod/rock and rock/buffer rod interfaces, when the whole samples were used, or the buffer rod/rock and rock/rock interfaces when the cut samples were used.

As an example, figure 2.13 shows the two types of pulses generated for two P-waves travelling through a whole Portland Pond Freestone sample at 20 MPa confining pressure. The reflection off the top of the buffer rod/rock interface can clearly be isolated from the reflection off the bottom rock/buffer rod interface. The travel time difference Δt, between the top and bottom reflections from the broadband pulse, were used as a guide in identifying the third peak/trough pair in the corresponding single frequency pulse at the same confining pressure. This then ensured that the third peak/trough pair was clearly identified and picked at every pressure change. The pulse width could be changed on the Arenberg pulse generator, isolating reflections and multiples. The pulse interference was more pronounced in the faster Tytherington cut sample.

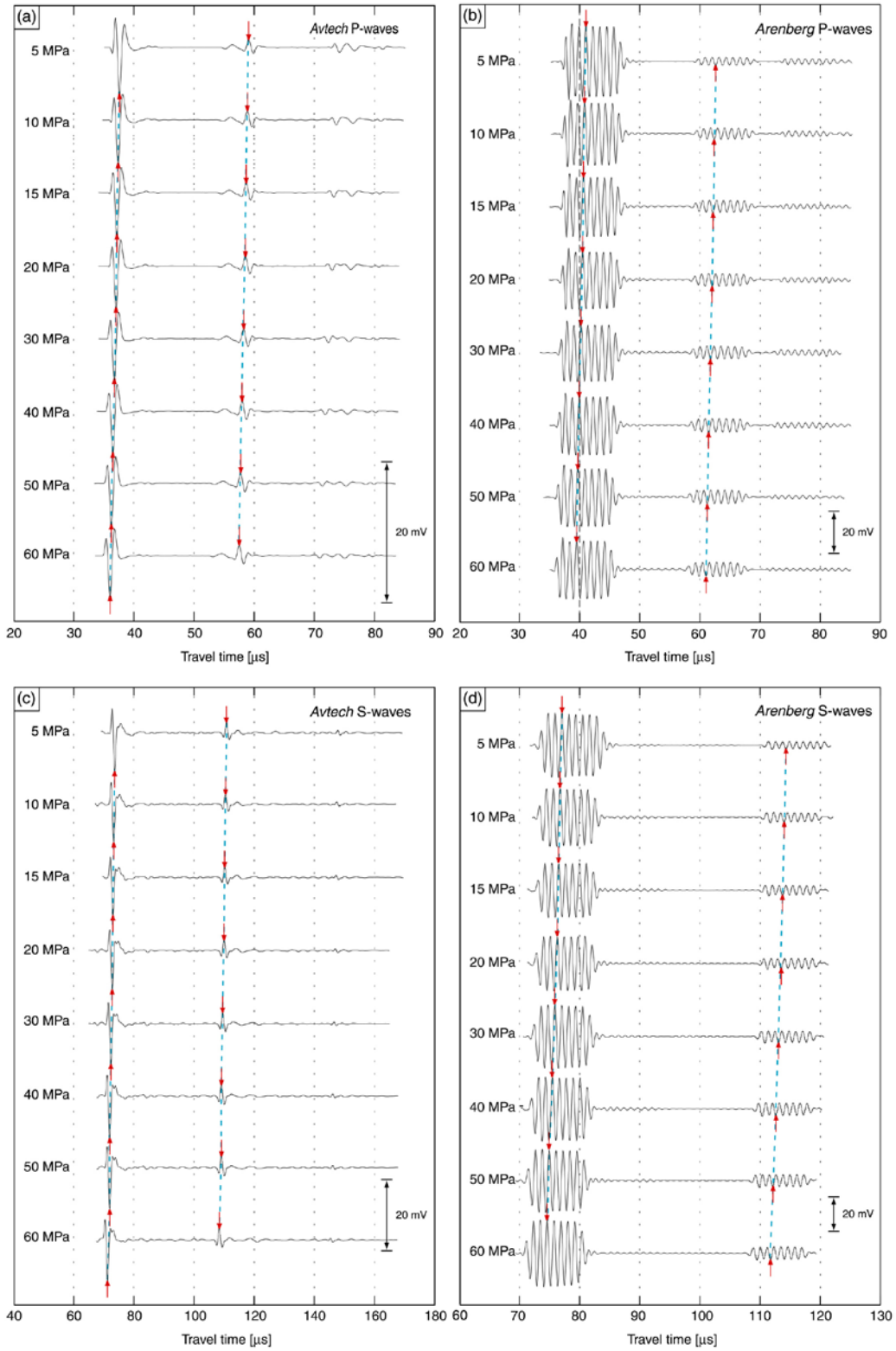


Figure 2.12: Portland Pond Freestone, whole sample, Arenberg and Avtech P and S-pulse waveforms at different confining pressures. (a) Avtech P-waves; (b) Arenberg P-waves; (c) Avtech S-waves; (d) Arenberg S-waves.

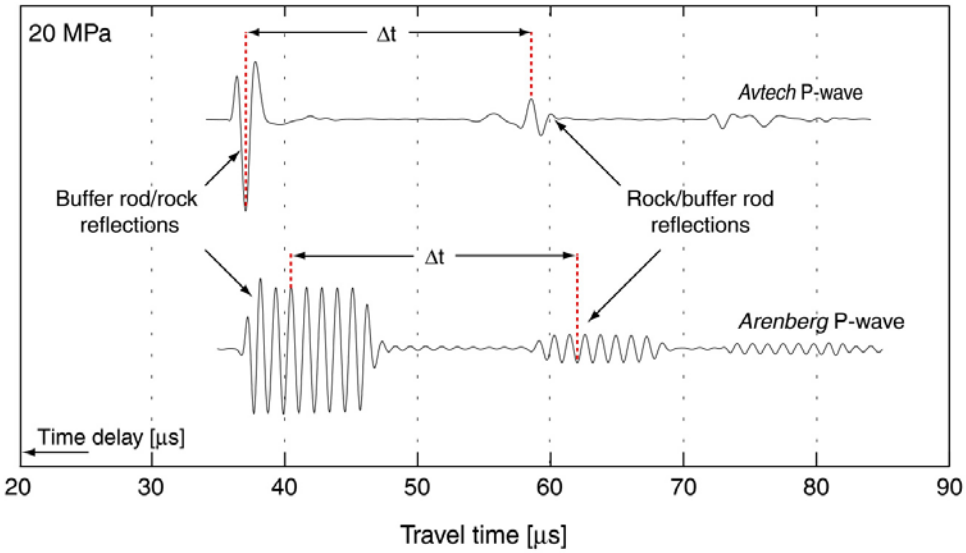


Figure 2.13: Top, broadband (Avtech) and bottom, single frequency (Arenberg) pulses generated for two P-waves travelling through the whole Portland Pond Freestone sample at 20 MPa confining pressure. The time delay [μs] of the two pulses differed, hence the horizontal shift in time relative to each other.

2.15 Methodology: Procedure to calculate Z_N and Z_T

Figure 2.14 is a simplified, logical flowchart for compressional waves, outlining the precise methodology followed to calculate the normal and tangential compliance values of the fracture interface from the compressional and shear wave acoustic data. In this flowchart, text in between the text boxes represents *procedures*, or actual calculations performed, whilst text contained within the text boxes represents the *results* from the procedures. Note that exactly the same procedure was followed to calculate the tangential compliances of the fracture from the S-wave data. The methodology is exactly the same for the whole and cut samples up to the dotted line in the flowchart. To obtain an average sample P-wave velocity (second text box from top of flowchart), two travel time values per interface were recorded for the reflections. This enabled 2 difference travel time values δ_1 and δ_2 (between the bottom and the top for a whole sample and between the crack and the top for a cut sample) to be calculated.

The left hand column below this dotted line outlines the calculations needed to calculate a Q_P value from the *whole* Pond Freestone or Tytherington sample, and was measured first. After obtaining a Q_P and Q_S value from both the Pond Freestone and Tytherington whole specimen, both core samples were cut in two with the bottom sample longer than the top sample. This was in order to optimize the reflection events in time, off the top buffer rod/rock interface ($A_0 \rightarrow A_1$) from the subsequent reflections off the rock/rock interface ($A_0 \rightarrow A_2$) and subsequent rock/rock multiples ($A_0 \rightarrow A_3$) – see figure 2.18. The calculated Q value (Q_P in this case) from the *whole* sample, then serves as input into the right hand column of the flowchart where it is used, in the corresponding *cut* sample, to correct the reflection coefficient of the crack for Q_P. This reflection coefficient is then used in Schoenberg (1980) – using equation A4 in the Appendix - to calculate the normal compliance value Z_N (for a compressional wave) for the crack interface.

2.16 Whole samples

Acoustic measurements were performed on the Portland Pond Freestone and Tytherington whole and cut core samples. Figure 2.15 shows the dimensions and experimental setup of the whole sample experiments.

2.16.1 Results and discussion

Table 2.4 summarizes the parameters as calculated from the measured, whole, Portland Pond Freestone acoustic data. Figure 2.16 shows the compressional and shear wave velocity versus confining pressure, as calculated from the whole Portland Pond Freestone (a) and Tytherington field sample (b) experiment. The Portland Pond Freestone and the Tytherington field sample both had virtually constant compressional and shear wave velocities with an increase in pressure, which indicates little inherent micro-cracking.

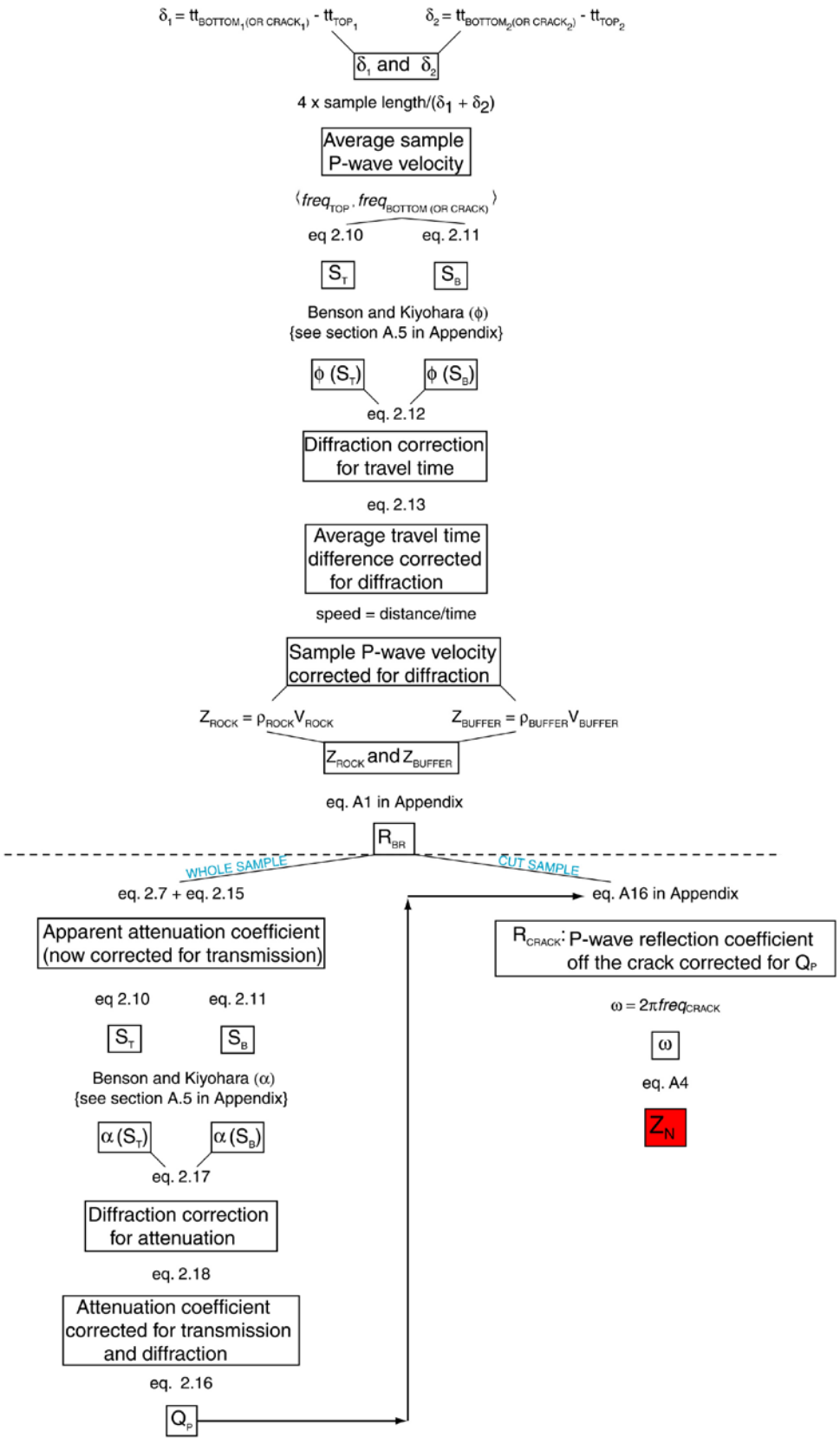


Figure 2.14: Flowchart outlining the methodology followed in calculating a normal fracture compliance value Z_N from the compressional wave data. The same methodology is followed for calculating Z_T from S-waves. $\langle\ \rangle$ indicates the arithmetic average.

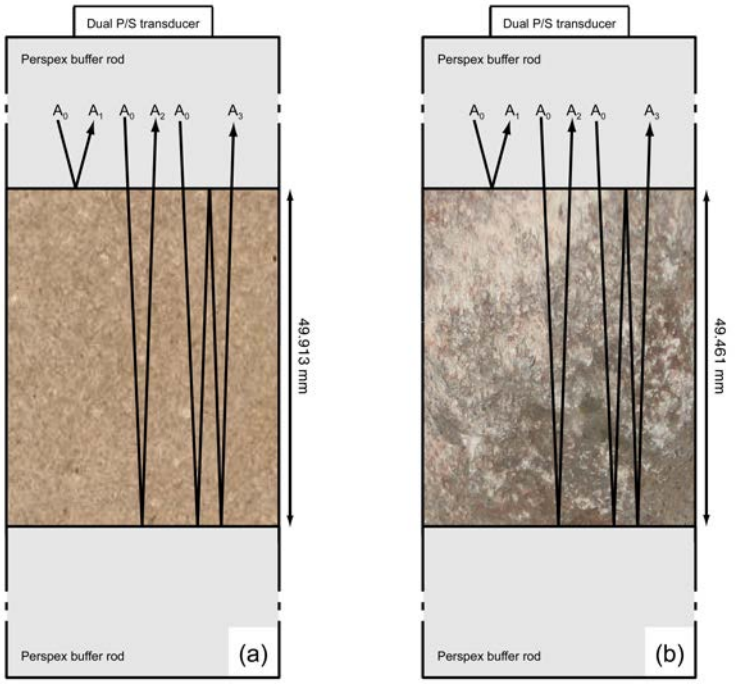


Figure 2.15: Whole samples used for calculating Q_P and Q_S values versus confining pressure needed for correcting the reflection coefficient amplitudes of the rock/rock interface for Q. (a) Portland Pond Freestone sample; (b) Tytherington field sample.

The sharp increase in compressional and shear velocity from 5 MPa to 10 MPa confining pressure indicate a transducer/buffer rod or buffer rod/rock (or both) contact problem. This problem completely resolved itself for confining pressures in excess of 10 MPa. The differential compressional and shear wave Portland Pond Freestone velocities between the maximum and minimum pressures, are smaller then the sensitivity of the instrument. This shows the excellent choice of Portland Pond Freestone as a calibration rock specimen. Figure 2.17 (a) and (b) shows the inverse compressional and shear Q values versus confining pressure for the whole, Pond Freestone and the Tytherington field sample respectively, after correcting the amplitudes for both diffraction and transmission. The Pond Freestone Q_P^{-1} and Q_S^{-1} values both decrease with an increase in confining pressure, with the Q_P^{-1} gradient steeper than the Q_S^{-1} gradient. The higher the confining pressure the

	Portland Pond Freestone sample							
	Confining pressure [MPa]							
	5	10	15	20	30	40	50	60
v_P [m/s]	4614	4619	4620	4619	4620	4623	4625	4627
Q_P^{-1}	0.0177	0.0091	0.0062	0.0053	0.0050	0.0052	0.0048	0.0043
$\langle f \rangle_P$ [kHz]	857.650	865.060	877.460	877.460	862.060	862.060	859.100	862.060
v_S [m/s]	2671	2673	2673	2673	2676	2679	2677	2679
Q_S^{-1}	0.0133	0.0094	0.0083	0.0086	0.0082	0.0074	0.0082	0.0081
$\langle f \rangle_S$ [kHz]	892.850	875.790	877.460	875.870	896.070	877.460	894.450	880.670
v_P / v_S	1.73	1.73	1.73	1.73	1.73	1.73	1.73	1.73
	Tytherington field sample							
	Confining pressure [MPa]							
	5	10	15	20	30	40	50	60
v_P [m/s]	5922	6352	6352	6361	6370	6383	6397	6410
Q_P^{-1}	0.0176	0.0084	0.0034	0.0017	0	0.0015	0	0
$\langle f \rangle_P$ [kHz]	871.120	862.060	878.950	863.560	862.060	777.460	863.560	891.260
v_S [m/s]	3378	3413	3416	3417	3420	3423	3427	3431
Q_S^{-1}	0.0090	0.0103	0.0094	0.0092	0.0080	0.0074	0.0077	0.0071
$\langle f \rangle_S$ [kHz]	813.760	863.560	892.850	892.850	891.260	889.110	894.450	892.850
v_P / v_S	1.76	1.87	1.86	1.87	1.87	1.87	1.87	1.87

Table 2.4: Summary of the parameters as calculated from the whole acoustic data. $\langle f \rangle_P$ indicates the average compressional wave frequency as calculated from the two reflections off the top buffer rod/rock and rock/rock interface respectively.

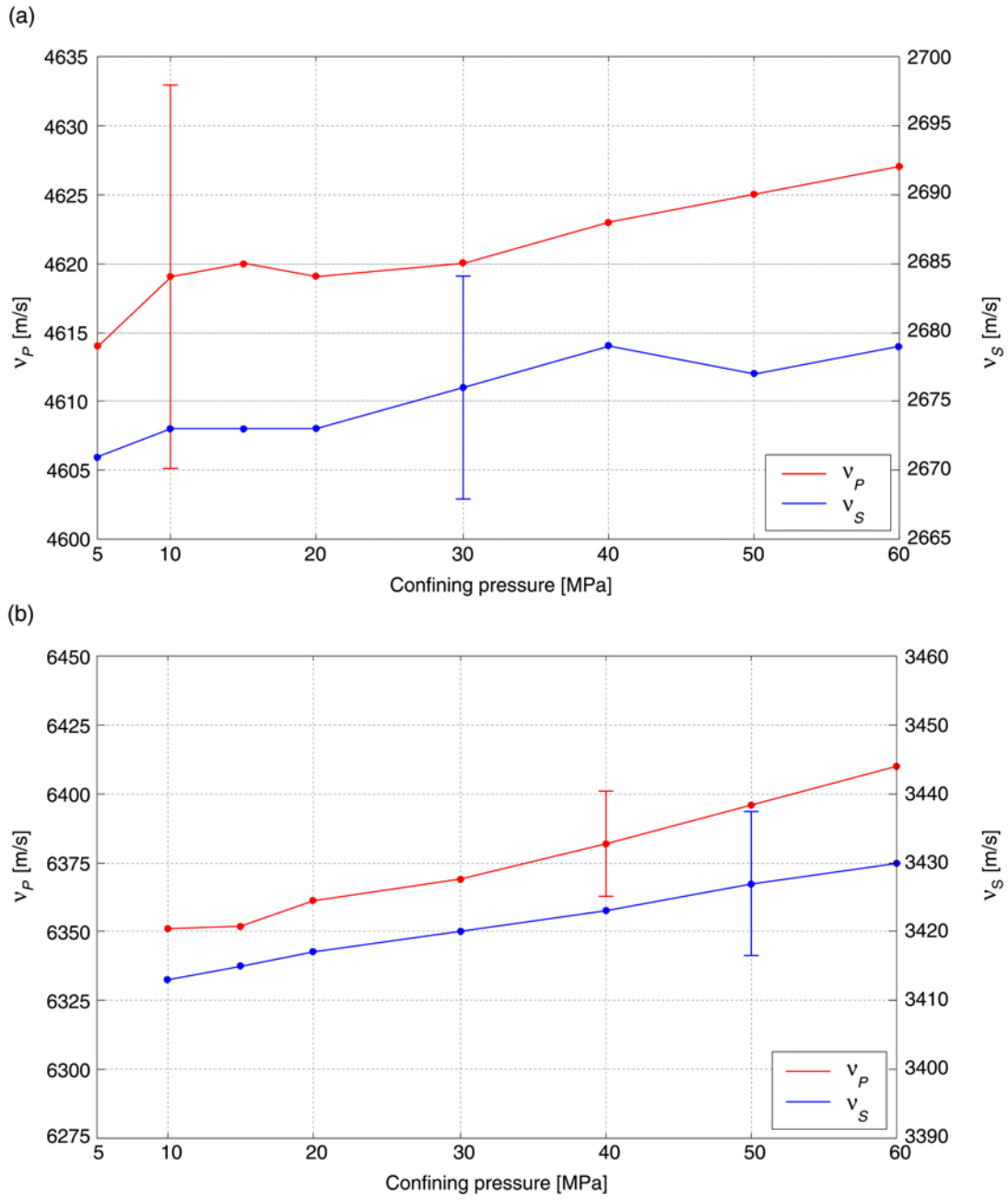


Figure 2.16: Whole sample compressional v_P and shear v_S wave velocity versus confining pressure; (a) Portland Pond Freestone and (b) Tytherington field sample.

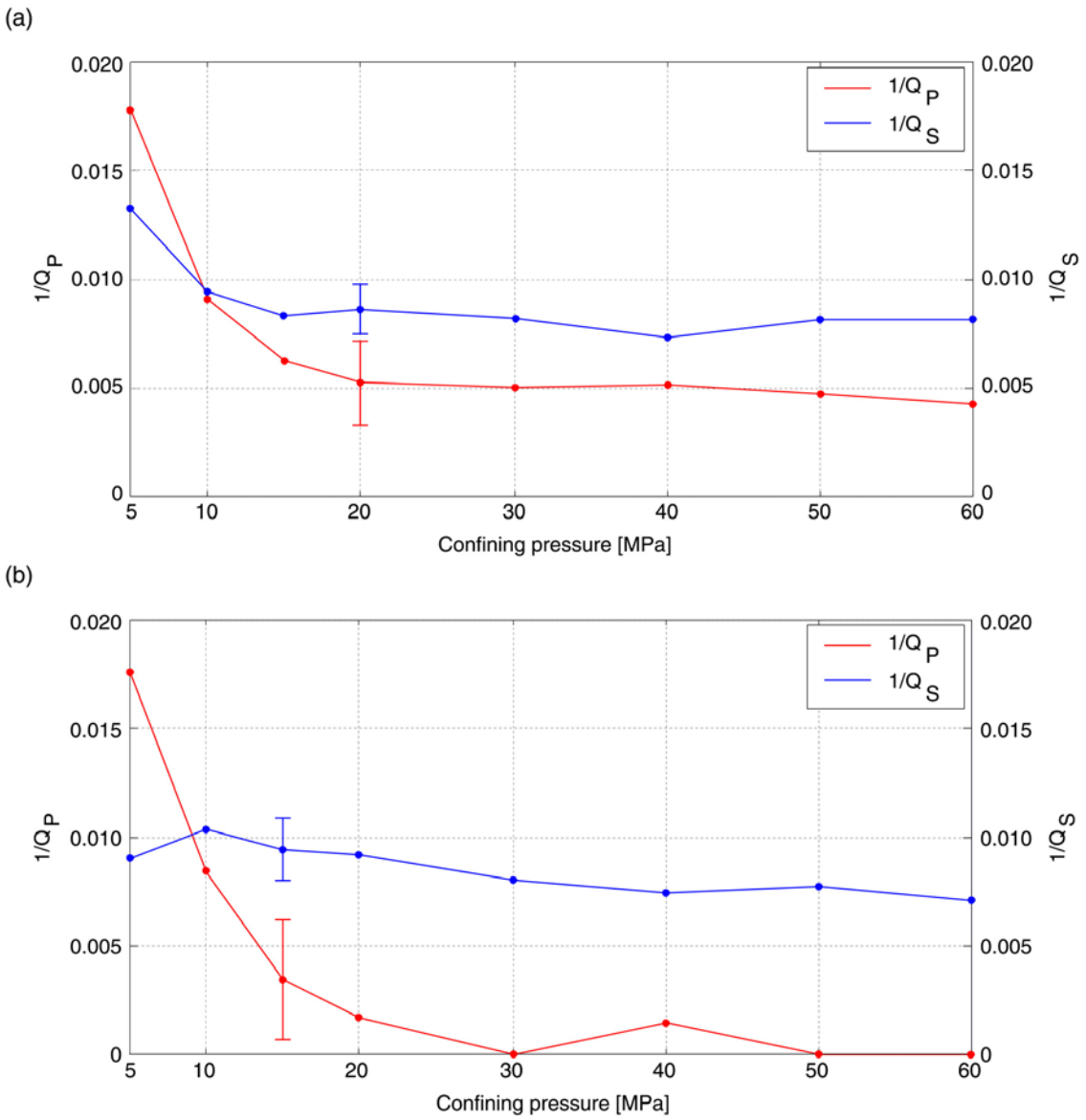


Figure 2.17: Whole sample Q_P^{-1} and Q_S^{-1} versus confining pressure; (a) Portland Pond Freestone and (b) Tytherington field sample.

lower the Q_P^{-1} and Q_S^{-1} values and thus the lower the attenuation, as attenuation is directly proportional to the inverse of the quality factor (Eq. 2.16). The intrinsic Q of both samples increases (Q^{-1} decreases) with pressure and is effectively infinite, especially in the case of the Tytherington sample, for confining pressures in excess of 15 MPa. The zero values of Q_P^{-1} at 30 MPa, 50 MPa and 60 MPa, for the Tytherington sample, correspond to a low signal/noise ratio which make any quantitative measurement of Q_P^{-1}

very difficult. It has been qualitatively surmised, since the work of Birch and Bancroft (1938a, 1938b), that the increase in quality factor with pressure is due to the closure of micro-cracks.

2.17 Cut samples

The same whole core samples were then cut and reassembled, and the experiment was repeated. Figure 2.18 shows the dimensions and experimental setup of the cut sample experiment.

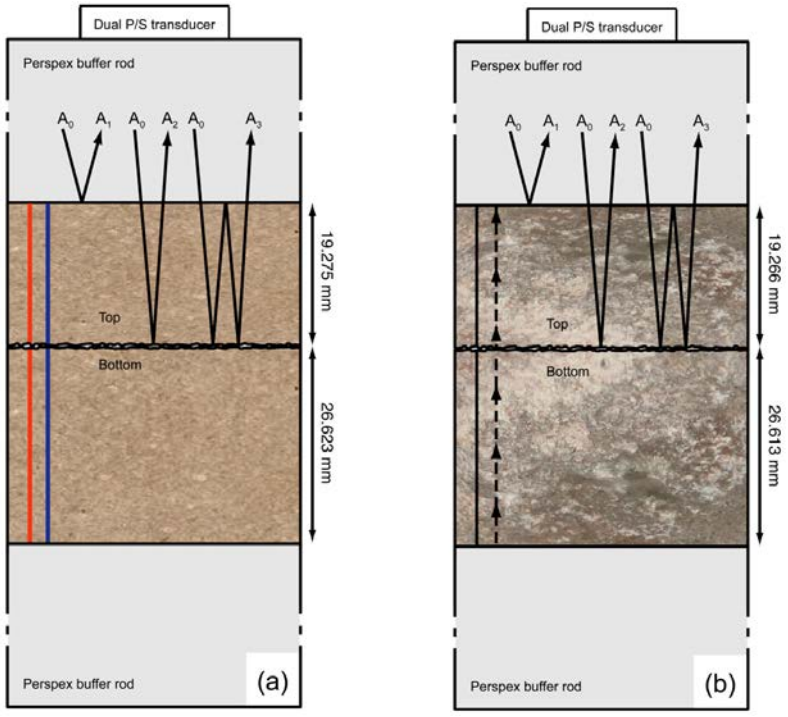


Figure 2.18: Cut samples used for calculating the normal Z_N and tangential fracture compliance Z_T values from reflections off the crack; (a) Portland Pond Freestone sample and (b) Tytherington field sample.

2.17.1 Results and discussion

Figure 2.19 shows the compressional and shear wave velocity versus confining pressure, from the cut Portland Pond Freestone (a) and Tytherington field sample (b) experiment. Both show an increase in compressional and shear wave velocities as the fracture is

closing-up under pressure. The velocity increase with a fracture is greater than that of an intact specimen without a fracture. As we know that the velocities for the intact specimen, for both samples, are virtually constant for all confining pressures, this increase must be due to the fracture itself. As the reflection coefficient is complex in the displacement discontinuity model (Eq. 1.25), there is a possibility that the velocity differences, between the cut and the uncut samples, could be ascribed to the phase difference due to the cut interface. This effect, however, was found to be negligible. The compressional and shear wave reflection coefficients of the fracture interface, versus confining pressure, for the two specimens are shown in figure 2.19 (c) and (d). There is a decrease in the compressional and shear wave reflection coefficient with an increase in confining pressure for both samples, with the change more pronounced for the Tytherington sample probably due to a slightly higher degree of inherent micro-cracking. As the fracture closes-up under an increase in confining pressure an increasing amount of energy is transmitted through the fracture whilst less energy is reflected off the interface.

Finally, figure 2.19 (e) and (f) shows the normal Z_N and tangential Z_T fracture compliance for both samples (calculated using Eq. A4 in the Appendix). Values of compliance varied between approximately 0.5 - 4.5 x 10^{-14} m/Pa. These results are consistent with the laboratory measurements of Pyrak-Nolte et al. (1990a), performed on different natural fractures in crystalline quartz monzonite and Pyrak-Nolte et al. (1990b) for experiments on parallel laminated steel plates. The Pond Freestone and Tytherington normal and tangential fracture compliance ratios versus confining pressure are plotted in figure 2.20. The Z_N / Z_T ratio is essentially constant for all pressures for both the Pond Freestone and Tytherington samples with average values of 0.46 and 0.43 respectively.

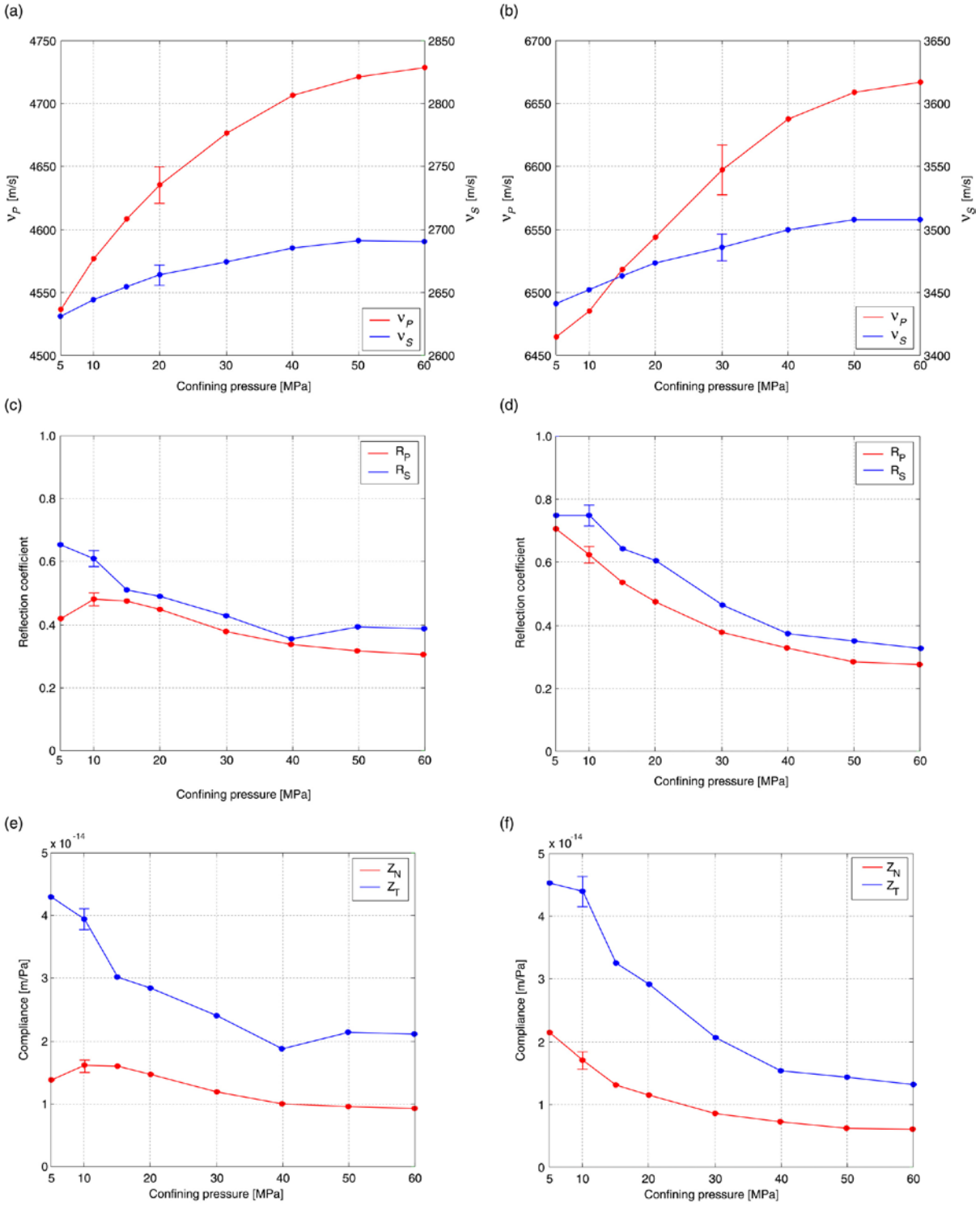


Figure 2.19: Results for the cut samples versus confining pressure. The left column relates to the Portland Pond Freestone sample, whilst the right column relates to the Tytherington field sample. (a) and (b) – Compressional v_P and shear v_S wave velocity; (c) and (d) – Compressional R_P and shear R_S wave reflection coefficients; (e) and (f) – Normal Z_N and tangential Z_T fracture compliance.

The Z_N / Z_T ratio has only recently emerged as a potentially significant pore, or fracture fluid indicator, and is a subject of ongoing research. The Z_N / Z_T ratio is sensitive to the microstructural properties of the fracture as well as the fracture infill. It has been assumed that $Z_N / Z_T \approx 1$ for dry fractures, as the Poisson's ratio σ is small and typically $0.1 \le \sigma \le 0.25$, and $Z_N / Z_T \approx 0$ for liquid filled fractures (Liu et al., 1996; Liu et al., 2000). Pyrak-Nolte et al. (1990a) obtain laboratory estimates of Z_N / Z_T between 0.2 and 0.5 for a dry natural fracture in quartz monzonite (their sample E35). In the normal and tangential stiffness expressions (see Eqs. 1.17 and 1.18) developed by Hudson et al. (1997), if the bulk modulus of the fracture fill is set to the value for air at atmospheric pressure ('drained case'), one gets for limestones $0.79 \le Z_N / Z_T \le 0.86$ (by assuming from Mavko et al. (1998) that $1.72 \le \nu_P / \nu_S \le 2.04$). Liu and Li (2000) show that the Z_N / Z_T ratio is directly related to the Thomsen (1986) anisotropic parameters and thus can be estimated from seismic data.

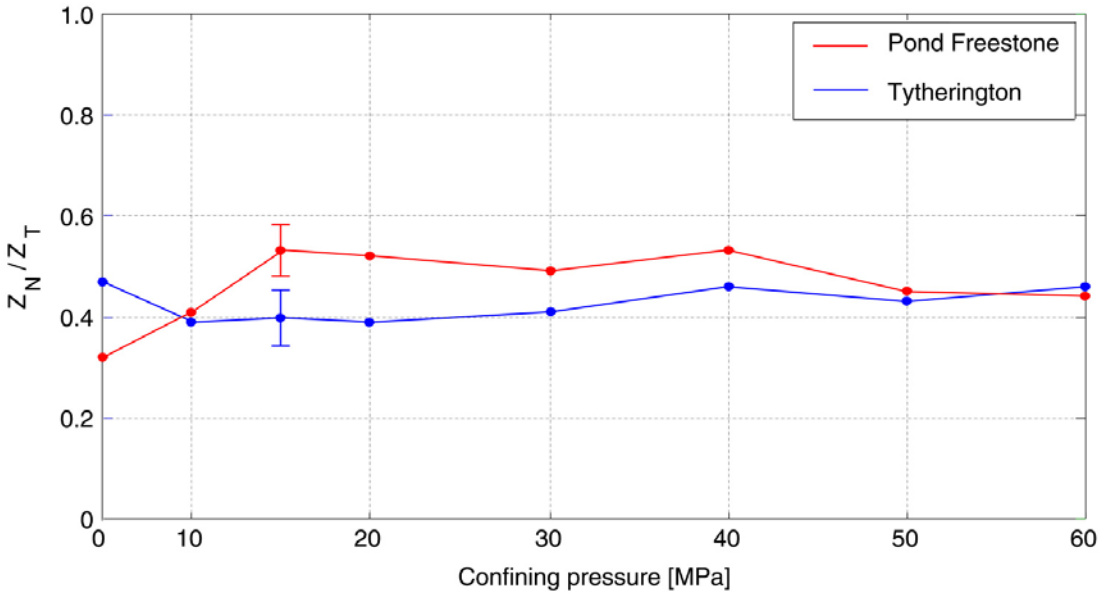


Figure 2.20: Pond Freestone and Tytherington normal Z_N and tangential Z_T fracture compliance ratio versus confining pressure.

An interesting observation is that the Z_N / Z_T ratio results from this study are consistent with the laboratory estimates obained by Pyrak-Nolte et al. (1990a). These experimentally obtained values seem to be inconsistent with theoretical predictions by Liu et al. (1996), Liu et al. (2000) and Hudson et al. (1997).

2.18 Grooved sample

In order to investigate possible added complexities due to irregular interfaces a separate additional fracture interface was cut perpendicular to the core axis of the Portland Pond Freestone sample ('grooved' sample).

Figure 2.21 shows the dimensions and experimental setup of the grooved sample experiment. In this experiment, normally incident P and S-wave pulses were generated using single P and S-wave transducers either side of the fracture (as opposed to a single dual P and S-wave transducer unit on top of the top buffer rod used for the whole and cut Portland Pond Freestone and Tytherington samples). The P-wave transducer was at the bottom of the ensemble, whilst the S-wave transducer was at the top. In order to minimize scattering of energy off the grooves, the size of the rugosity had to be smaller than the P and S-pulse wavelengths ($\lambda_P \approx 5$ mm and $\lambda_S \approx 3$ mm respectively from section 2.12.1). Using a precision circular saw, evenly spaced, parallel tramlines, 0.3 mm deep, 0.5 mm wide, with a groove spacing of 0.5 mm, were cut into the lower Portland Pond Freestone rock (Fig. 2.22). Although the compressional and shear wave velocities of the Pond Freestone sample were lower than the compressional and shear wave velocities of the Tytherington sample the reflections off the buffer rod/rock and rock/rock interfaces were still sufficiently well spaced in time to allow for them to be picked accurately as separate events.

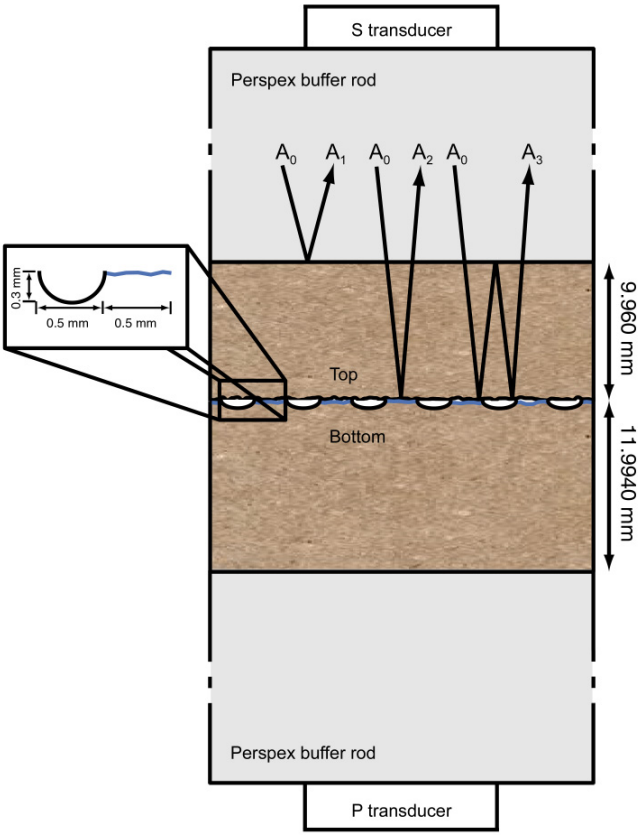


Figure 2.21: Portland Pond Freestone grooved sample ensemble, as used in the rig with the corresponding dimensions of the grooves.

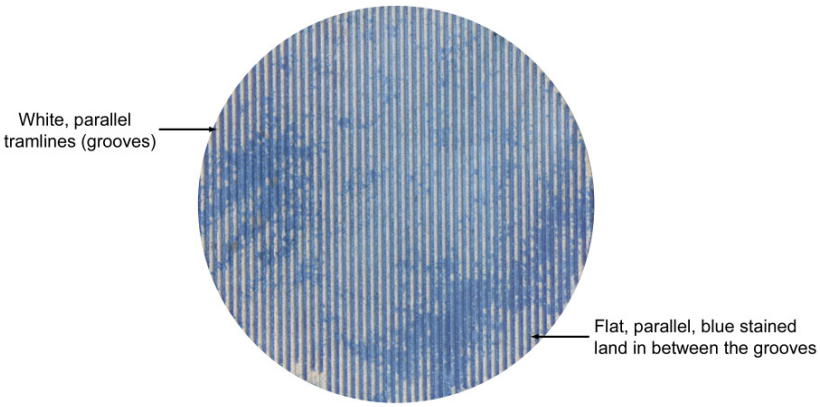


Figure 2.22: Scanned image showing plan view of the bottom rock sample containing the grooves. Blue ink was used to show the grooves more clearly.

The single transducer assembly could be used in this experiment. The diffraction correction for the single P and S-wave transducers was more accurate than the diffraction correction as calculated for the dual P and S-wave transducer experiment. Figure 2.23 shows the difference in Q_P^{-1} values as calculated from the single P-wave transducer and dual P and S-wave transducer respectively. The reflection coefficients at every pressure were corrected for diffraction, transmission losses from the impedance contrast of the buffer rod and sample, and also corrected for Q. The Q_P and Q_S values were calculated using single P and S-wave transducers placed either side of a whole Portland Pond Freestone sample.

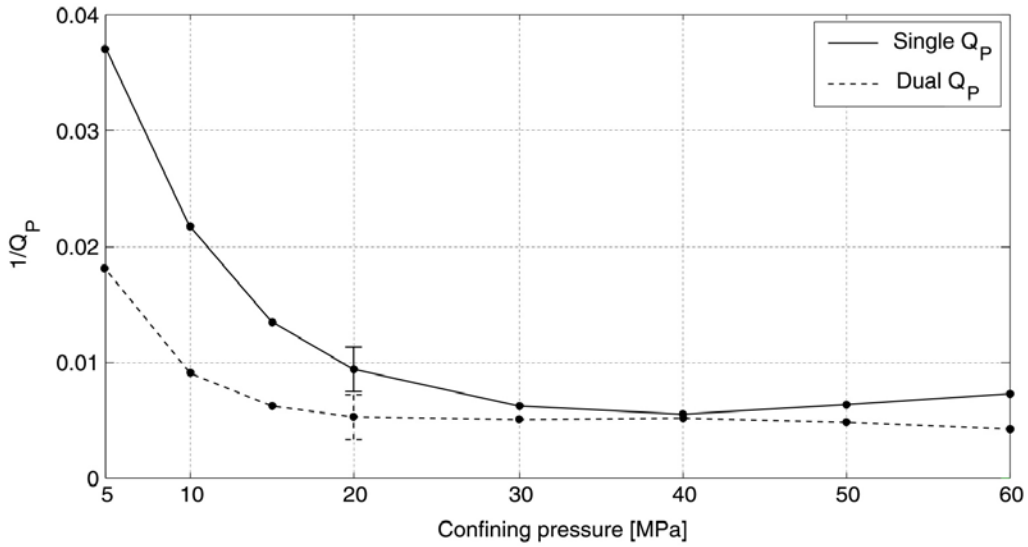


Figure 2.23: Comparison of the calculated Q_P^{-1} from using the single P-wave transducer (dotted line) and dual P and S-wave transducer (solid line) versus confining pressure.

2.18.1 Results and discussion

Figure 2.24 shows the shortening in length of the rock ensemble within the rig as, measured by the 3 dial micrometers, as the confining pressure was increased from 5 MPa to 60 MPa. Failure of the grooves occurred as the confining pressure was increased from 30 MPa to 40 MPa. The error bars correspond to the dial micrometer measurements taken to an accuracy of ±0.01 mm.

Figure 2.25 shows the results for the grooved Portland Pond Freestone sample versus confining pressure. McCann and Sothcott (1992) concluded that the 95% confidence interval of the velocity for the pulse-echo system, incorporating all measurement errors and corrections, is ±0.3% at 0.85 MHz. This percentage equates to ±15 m/s around the mean of the compressional velocity of 4850 m/s over the pressure range (and will be lower for the shear wave velocity). With these confidence limits in mind, there was a decrease, albeit a relatively slight one, in the compressional and shear wave velocity with increasing confining pressure (Fig. 2.25 (a)).

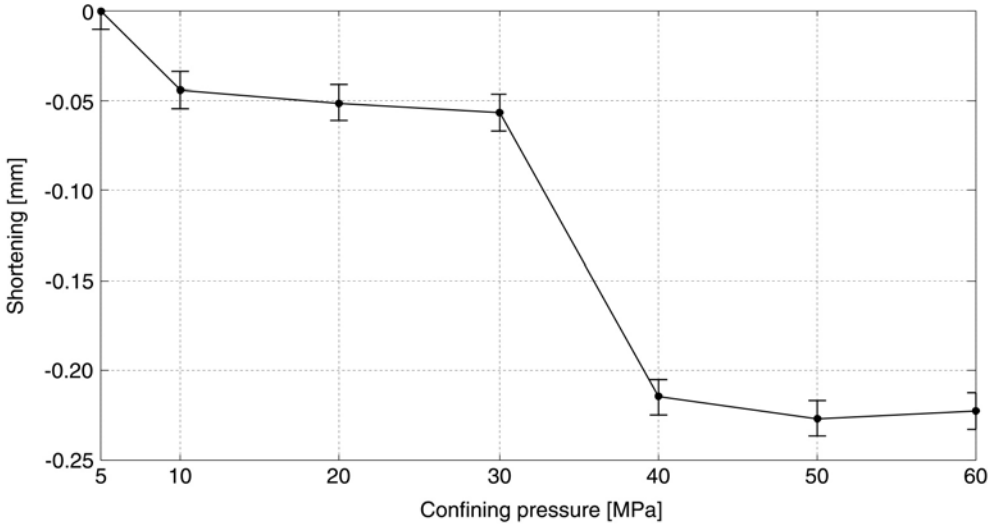


Figure 2.24: Grooved Portland Pond Freestone rock sample shortening versus confining pressure.

Both the compressional and shear wave reflection coefficients and corresponding calculated normal and tangential compliances exhibit a positive trend from 5 MPa to 40 MPa, from where the values then gradually decrease with confining pressures in excess of 40 MPa (Fig. 2.25 (b) and Fig. 2.25 (c)). It was observed, after removing the grooved sample from the rig, that the grooves were almost completely destroyed, with powder clearly visible in the areas between the grooves and within the remaining grooves themselves. The compliance increase over an increase in confining pressure up to 40 MPa

might be due to the fact that the fracture was gradually disintegrating as the pressure was increased. As the pressure was raised, the powder dust that formed at the crack interface resulted in the crack becoming more complaint. The decrease in P and S-wave reflection coefficient versus confining pressures greater than 40 MPa indicates that an increasing amount of energy is transmitted through the rock/rock interface as the fracture is closing under the increase in confining pressure. This then leads to a decrease in the corresponding calculated, normal and tangential compliance values for pressures in excess of 40 MPa.

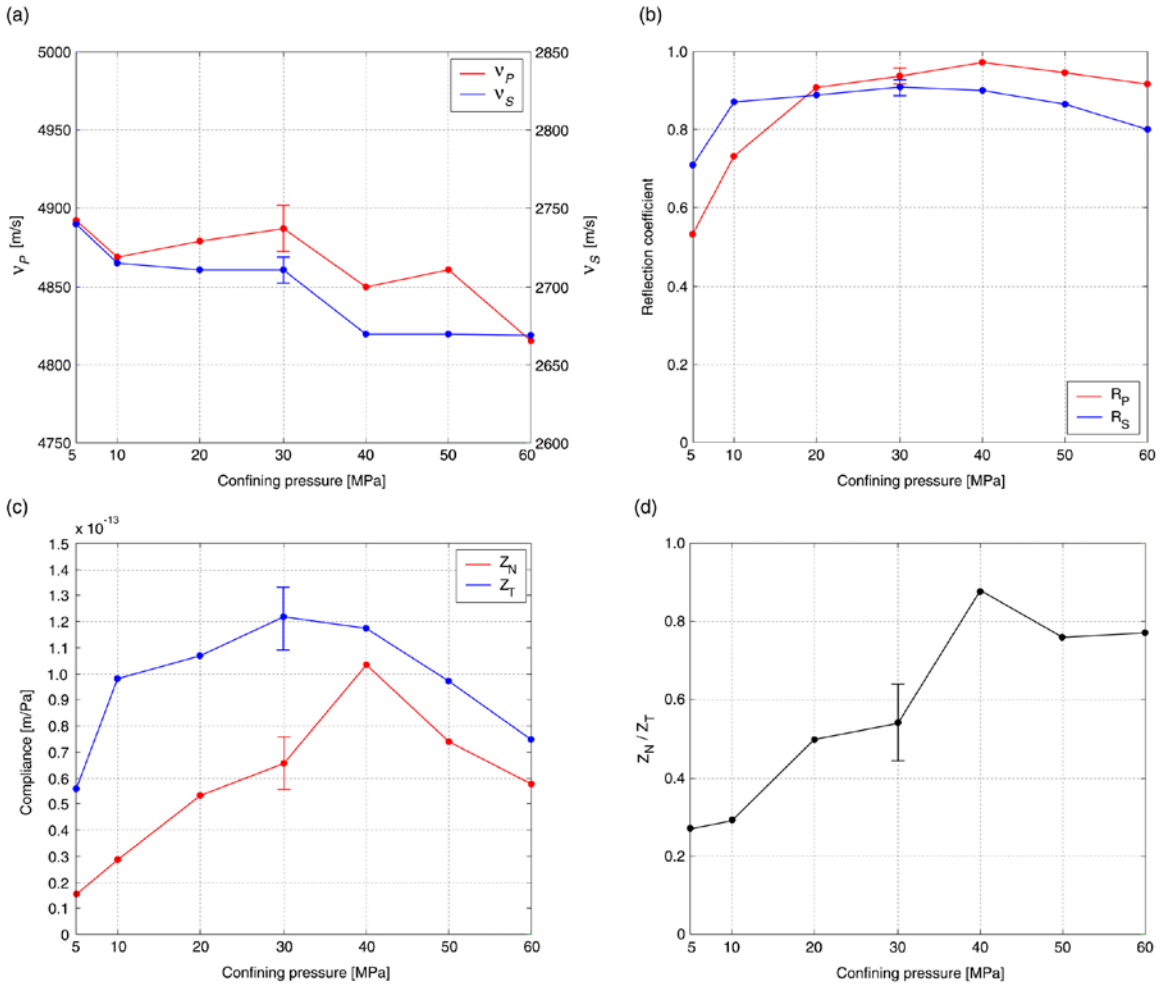


Figure 2.25: Results for the grooved Portland Pond Freestone sample versus confining pressure. (a) Compressional v_P and shear v_S wave velocity; (b) P-wave R_P and S-wave R_S reflection coefficients; (c) Normal Z_N and tangential Z_T fracture compliance; (d) Z_N / Z_T ratio.

Figure 2.25 (d) shows how the normal and tangential fracture compliance ratio changes with confining pressure. It is interesting to note that the Z_N / Z_T ratio dramatically increases from 30 MPa to 40 MPa confining pressure, which is where the fracture disintegrates. As the pressure increased, the grooved fracture approached a microscopic fracture model as opposed to the macroscopic planar fracture model represented by a single planar cut through a rock specimen. In addition to the macroscopic scale fracture model represented by the Pond Freestone and Tytherington cut samples, this result gives an insight into the microscopic behaviour of fractures or how fracture compliance might behave at different geometric scales within the shallow subsurface. It shows that the changes in compliance might be hard to predict if fracture surfaces have disintegrated at some time in the past.

In this chapter the normal and tangential fracture compliance, and fracture properties in general, have been investigated at ultrasonic frequencies in the laboratory. In order to investigate how fracture compliance would up-scale to conventional field scale frequencies, field scale experiments were then performed at two separate field test sites.

Chapter III

Tytherington Quarry - Wireline Data

3.1 Introduction

In order to investigate fracture properties at the field scale, a field test site was constructed in a Carboniferous limestone quarry at Tytherington, near Bristol in southwest England.

There are very few fracture compliance values in the open literature, with no experimental evidence for values of fracture compliance much in excess of $Z = 2 \times 10^{-12}$ m/Pa (Myer et al., 1995). Values calculated from the Tytherington field site experiment should provide the data needed to predict the scaling effect of fracture compliance with fracture dimension, from the field scale (observed with kilohertz range frequencies), to the laboratory scale (observed with ultrasonic range frequencies).

In this chapter the Tytherington quarry field test site is described. Firstly, the location of the quarry will be discussed, and the regional and site geology of the area will be outlined. Secondly, a detailed fracture analysis will be given based on subsurface mapping of the quarry wall and wireline data obtained from three boreholes. Thirdly, a clear correlation between the full waveform far-field sonic data, the open fractures as interpreted from optical televiewer logs, the short normal resistivity and the compressional wave sonic interval velocity, will be shown. Fourthly, a compressional wave, normal compliance value will be calculated from the effective group time delay or the delay a wave experiences in crossing a set of fractures (Pyrak-Nolte et al., 1987).

In order to investigate the spatial extent of the fracture network with depth, three, in-line, vertical boreholes were drilled 40 metres deep and 7 metres apart with a rotary percussion drill bit (Fig. 3.1). The water table was visible in the boreholes at approximately 1 - 2 metres below the surface. The uppermost portion of every hole was cased to stabilise the highly fractured top few metres. The lengths of the casings are depicted by the solid black lines observed in the top portion of every hole in figure 3.1. The first borehole that was drilled was labelled BH 1, but this hole collapsed and was never used. The next three boreholes were labelled BH 2, BH 3 and BH 4 respectively. All subsequent studies at the site were performed using just these three holes.

A detailed mapping survey of the quarry was carried out by the author, with the aid of Dr. John Cosgrove from Imperial College London.

A wireline geophysical logging survey was also carried out in all the boreholes by Robertson Geologging Ltd. The following wireline logs were obtained in all the holes: Near and far-field full waveform sonic, resistivity, natural gamma, caliper and optical televiewer. A comprehensive fracture analysis was performed based on the interpretation of the optical televiewer data. In addition, a formation density log was obtained for BH 2. The nominal frequency of the piezoelectric transducers, used in the sonic tool, was 23 kHz.

The boreholes were drilled approximately perpendicular to a sub-vertical wrench fault set (see par. 3.3.1), approximately normal to the layering of the bedding. Hence, a two dimensional geometry could be assumed for the compressional wave crosshole survey. This survey will be discussed in chapters 4 and 5.

3.2 Geographical location and geology of Tytherington quarry

3.2.1 Geographical location

The Tytherington quarry field site is situated approximately 1 km northwest of Tytherington village in Gloucestershire, southwest England. The quarry is approximately 15 km north-northeast of Bristol, and approximately 12 km east of the Bristol channel. The site is at an elevation of about 30 metres above Ordinance Datum (AOD). Figure 3.2 shows the regional geology of the area with the location of the quarry indicated. Figure 3.3 is a plan view of the quarry and the surrounding areas, indicating the relative location and strike of the boreholes in Ordnance Survey National Grid coordinates as 366400E/188900N and N10ºE respectively.

3.2.2 Geology

Regional geology

The highly fractured Carboniferous (345 - 280 My) rocks are associated with the Coal Measures sequence, and are positioned on the western limb of a north-south trending syncline. The Coal Measures outcrop as an inlier surrounded by Triassic and younger rocks which lie with a marked unconformity above them. The Coal Measures in the district span the stratigraphic Westphalian and lowermost Stephanian (Green, 1992).

The regional strike of the Carboniferous beds is east-west, which is thought to be the result of Variscan folding associated with the closing of the Variscan Ocean and the formation of the east-west trending Variscan belt, which formed as a result of the collision and welding together of Gondwanaland to the south and Laurasia to the north. The Carboniferous beds in which the quarry is situated form the gently inclined southward dipping beds of a large asymmetric northern facing fold which is now partially

covered by overlying Triassic and Jurassic beds. The site is situated on the northern margin of the Variscan belt and as a result the deformation is characterised by both brittle and ductile behaviour (Cosgrove, 2001).

Site geology

The scale of the folding that affects the rocks of the quarry is too large for them to be seen directly in the field. A variety of fractures occurs including: (i) Extensional fractures (joints), which form normal to the bedding and are restricted to individual competent beds; (ii) Shear fractures (faults), which are not restricted to individual competent beds. These fractures form either at a low angle to the bedding, or as vertical shear fractures which cut through the sedimentary succession, often for tens of metres. Large differential stresses, that are the difference between the maximum and minimum compressive stress, favour the formation of shear fractures, whilst low differential stresses favour the formation of extensional fractures. Fractures are often formed at the same time as folding, and the orientation of these fractures is intimately related to the stress field generating the fold and hence the geometry of the fold. One of the effects of stressing an anisotropic system, such as a succession of well bedded sediments, is that the principal stresses are rotated into positions either parallel or normal to bedding. This is because the relatively weak bedding planes cannot support a large shear stress. Thus during folding, as the layers become steepened on the limbs of the growing fold, the principal compression continues to follow the layering. The orientation of the fold (north-south trending syncline) indicates that the causative compression or principal compressive stress σ_1, was acting horizontally in an east-west direction (here σ_1, σ_2 and σ_3 are the maximum, intermediate and minimum principal stresses respectively). σ_2 or σ_3 could be assumed to be vertical.

If σ_2 was assumed to be vertical:

- at low differential stresses extensional fractures would open against the least principal stress direction (σ_3). These **joints** would be vertical and have an east-west strike,
- at high differential stresses, shear fractures or **faults** would be vertical and strike 30º north and 30º south of the east-west principal compression. These would be classified as wrench faults. A wrench fault is a type of strike-slip fault in which the fault surface is vertical and the fault blocks move sideways past each other. The presence of slickensides or scratch marks on wrench fault fracture surfaces at Tytherington quarry is evidence that fractures accommodated shear motion.

If σ_3 was assumed to be vertical:

- at low differential stresses, joints would open in the vertical direction and would be horizontal,
- at high differential stresses the faults would be north-south striking, and dipping at 30º to bedding. These would be classified as thrust faults, which are reverse faults in which the fault plane had a very shallow dip, where the hanging wall has moved up the fault surface relative to the footwall. Thrust faults can occur in areas of compression.

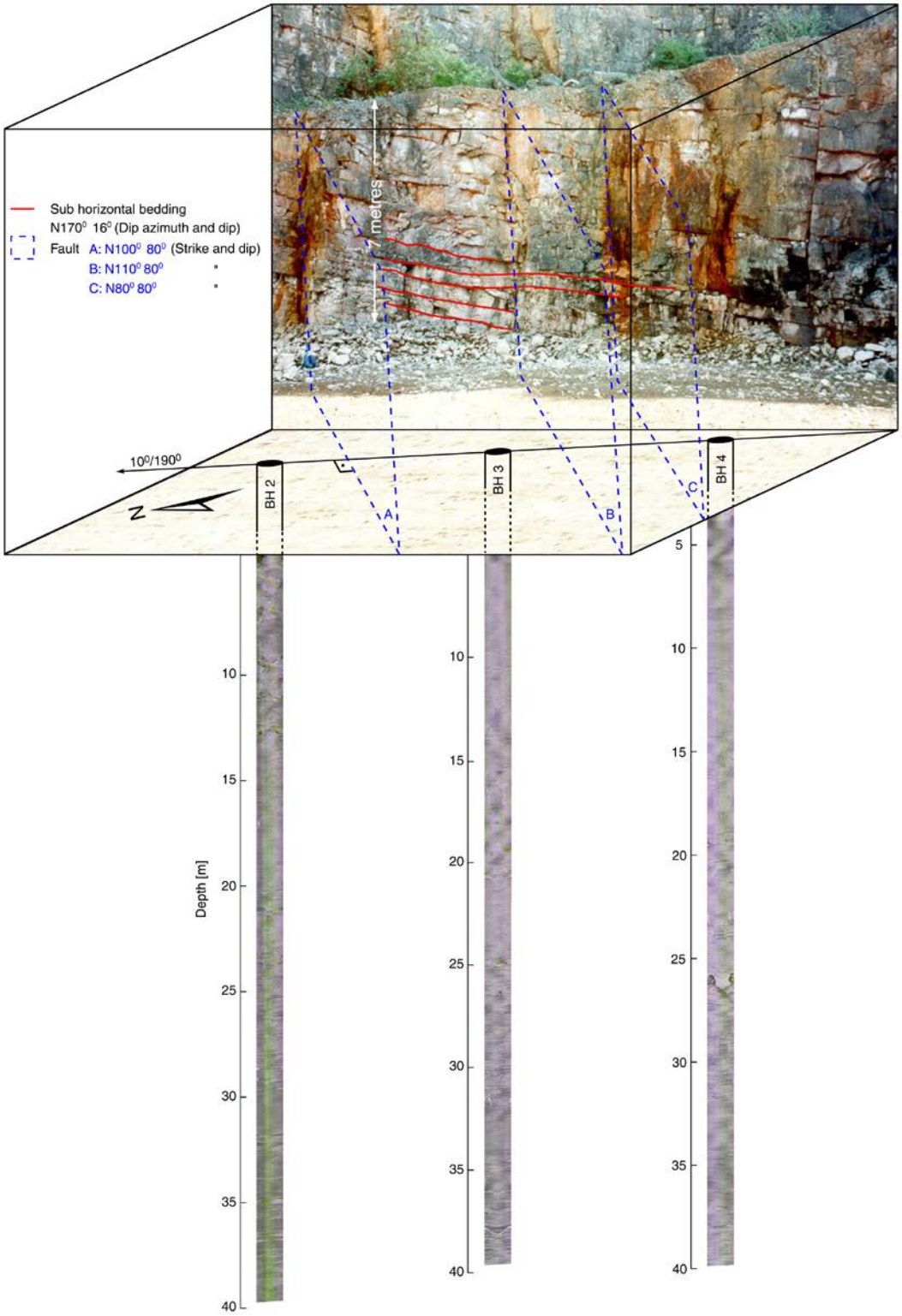


Figure 3.1: Limestone quarry wall at the borehole test site showing the major identified fractures and orientation of the boreholes (striking N10ºE). Unrolled optical televiewer images were projected onto each borehole. Some sub-horizontal bedding planes, with a respective dip azimuth and dip direction of N170º and 16º, are indicated in red. The sub-vertical fault planes of the two identified wrench fault sets (set 1: A and B and set 2: C) are indicated in blue.

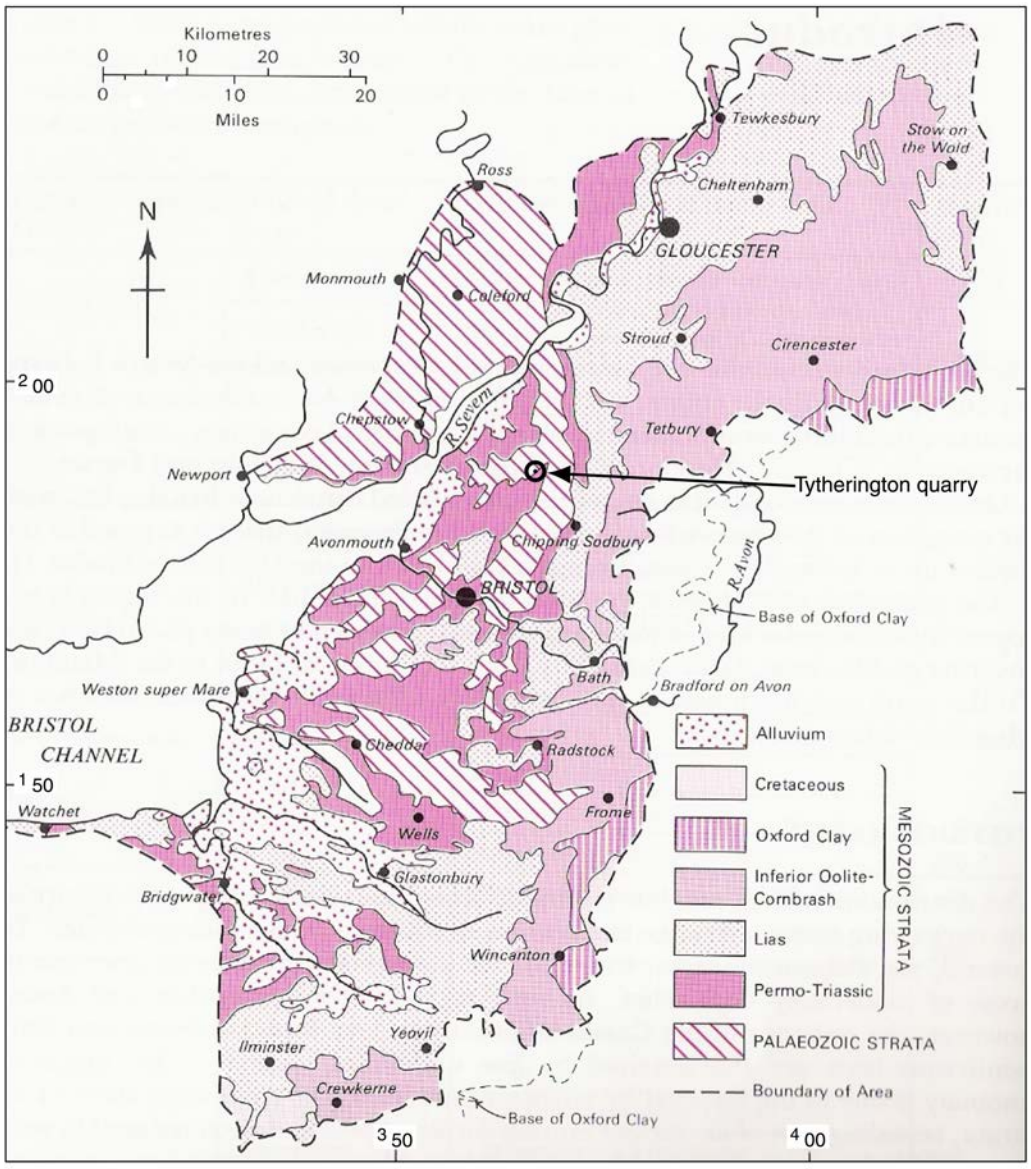


Figure 3.2: Map of the geology of the region.

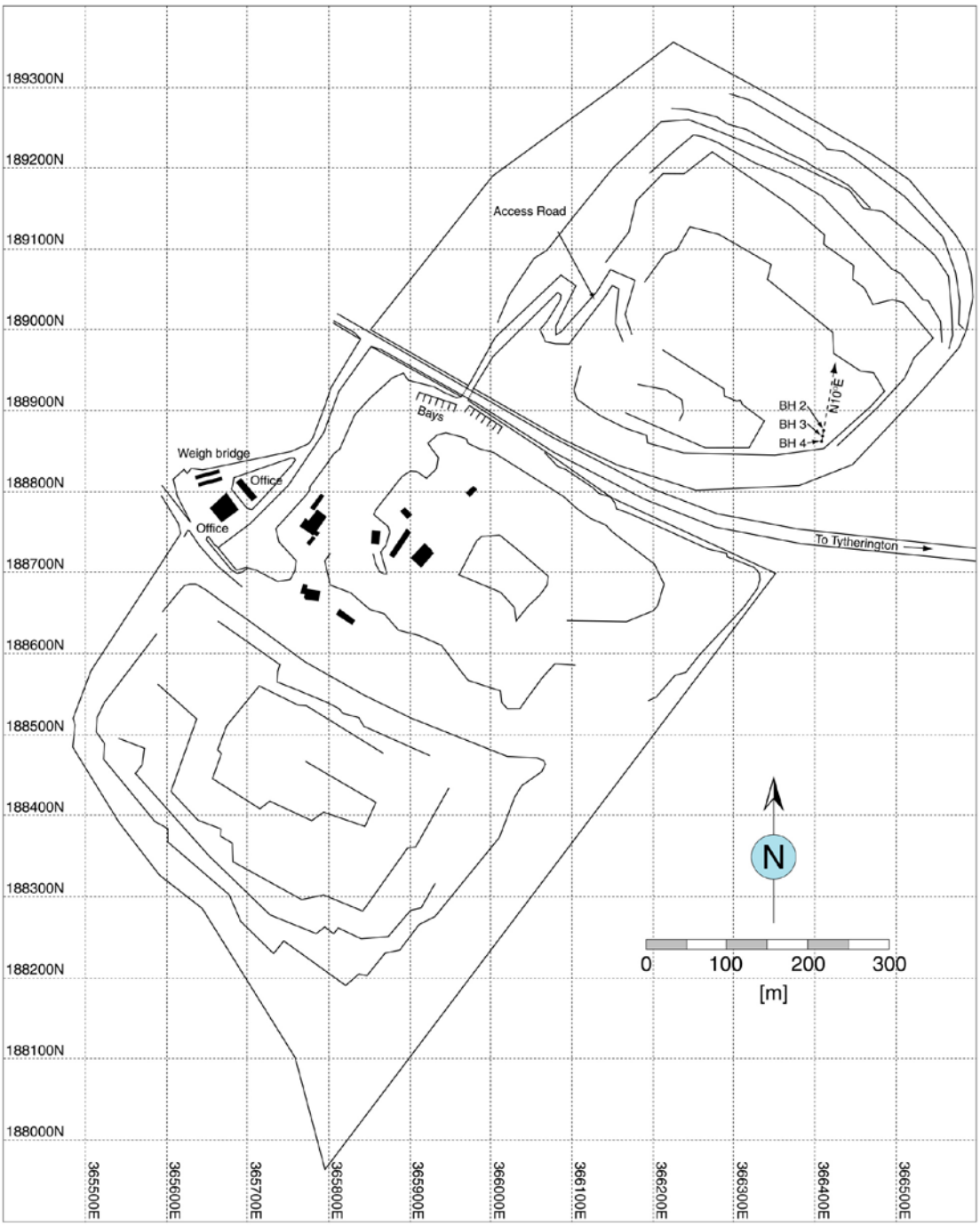


Figure 3.3: Plan view of Tytherington quarry indicating the location and strike of the boreholes. Three, in-line, 40 metre deep, vertical boreholes were drilled. These boreholes were labelled as BH 2, BH 3 and BH 4 respectively.

3.3 Fracture analysis

3.3.1 Fracture orientation from mapping

The following fractures were clearly identified in the Tytherington quarry wall (see Fig. 3.1):

- **Bedding**. Bedding planes may be extremely smooth planar surfaces or extremely irregular due to the formation of stylolite formation. Beds have a true dip of 16º to N170º.

- **Bedding constrained joints**. These joints are often termed 'brickwork' joints and form normal to bedding. In Tytherington quarry these joints were observed to be dipping at approximately 65º and striking north-south.

- **Vertical wrench faults**. Two sets of vertical wrench faults striking N60ºE and N120Eº respectively were identified.

The pronounced sub-vertical wrench faults, with an average fracture frequency of 0.25 fractures/metre, and the sub-horizontal bedding, with a fracture frequency of 0.5 fracture/metre can be seen clearly in figure 3.1.

3.3.2 Fracture orientation from optical televiewer log

Optical Televiewer (OPTV) logs can sometimes provide a more representative description of fractures than core, as the fractures are viewed *in-situ*, whereas core taken to the surface would be subjected to stress relief fractures. Core logging is expensive. Factors such as incomplete borehole core recovery and the fact that the orientation of the

core itself is sometimes not preserved when bringing the core barrel to the surface, can all severely complicate the fracture analysis (Haller and Porturas, 1998).

A continuous, high resolution, 360º image of the borehole wall is obtained by lowering a camera, contained within the optical televiewers probe, down the borehole. The OPTV probe contains three component magnetometers and accelerometers, and an internal orientation module to record well deviation and well azimuth. This optical televiewer image can then be viewed either as an unrolled image oriented North-East-South-West-North (NESWN) or as an image wrapped onto the external surface of the core of nominal borehole diameter (Fig. 3.4).

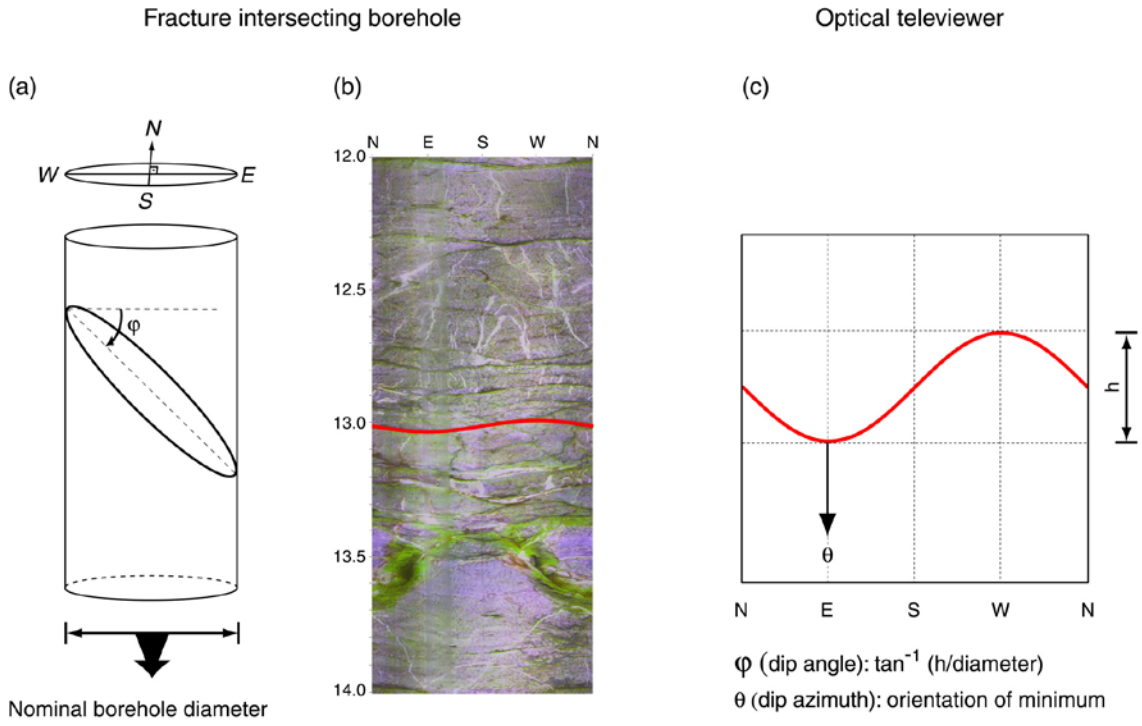


Figure 3.4: Fracture intersecting borehole as imaged by the optical televiewer log and its associated interpretation giving a good indication of the fracture orientation within the column of the borehole. (a) Schematic depiction of the digitised open fracture shown in red in (b) at approximately 13 metres depth down BH 2; (b) An unrolled image of the highly fractured region between 12 m – 14 m in BH 2; (c) Image analysis of open fracture in (b), showing the methodology for calculating the dip angle and dip azimuth from the image (after Zemanek et al., 1970).

Sinusoidal bedding and fracture features were identified manually during the digitising feature picking process, where the planar features on the imagery were labelled by their appearance, in much the same way as one would do in outcrop mapping in the field. Fractures are labelled as:

- **Bedding**. When repeated parallel traces occur which are often parallel with colour banding and associated with textural changes.

- **Open fractures**. Dark traces, reflecting little of the incident light.

- **Veins**. As the traces are within a limestone matrix, white traces, or traces paler than the surrounding rock, are assumed to be calcite filled.

Figure 3.5 shows the lower hemisphere, equal area, stereographic projections of the open fracture distribution, from the OPTV analysis, for the three boreholes, as red circles. The process of an equal area projection is rather like peeling the skin off the lower hemisphere, flattening it out and then shrinking it to a circle (Priest, 1985). Also shown for every borehole is a corresponding dip azimuth/dip/depth plot. Reading off the dip and dip azimuth of a specific identified open fracture from the stereographic projection, one can then relate this to its position or depth down the borehole using the right hand, corresponding diagram. This analysis allows for a complete three dimensional visualisation of the fractures within the column of the borehole. The top, middle and bottom rectangles relate to BH 2, BH 3 and BH 4 respectively. In total, 45 open fractures were identified for the BH 2, 42 for BH 3 and 24 for BH 4. In the stereographic projections of the identified open fractures (Figs. 3.5 (a), (c) and (e)), the dip decreases

radially outwards and reaches a minimum of 0º when the fracture was identified as horizontal. Therefore, the centre of the circle represents a vertical fracture plane with a dip of 90º. The fracture azimuth is related to rotation about the circle centre. The 12 o'clock position on the perimeter of the circle represents a dip azimuth of 0º (north), the 3 o'clock position a dip azimuth of 90º (east) and so forth. The strike of the plane containing the boreholes (N10ºE), is shown in green on all of these plots. Figures 3.5 (b), (d) and (f) are the corresponding dip, dip azimuth, and depth down the borehole of figures 3.5 (a), (c) and (e) respectively.

Hubbert and Willis (1957) and Zoback and Zoback (1980) point out that fractures at depth in the earth are probably most commonly oriented vertically, parallel to the maximum compressive overburden stress which is vertical. However, in the shallow subsurface the fractures tend to be horizontal, as the maximum stress is due to horizontal compression, with the overburden pressure effectively zero at the surface. Hudson and Harrison (1997) point out that, from the worldwide *in-situ* stress dataset (Hoek and Brown, 1980), at depths likely to be encountered in civil engineering (approximately 0 - 500 m) in 92% of the case studies the magnitude of the mean horizontal stress exceeds that of the vertical stress component, and that at typical mining depths (approximately 0 – 1000 m) the same trend applies. The average vertical compressional wave velocity (Figs. 3.8 – 3.10) is approximately 5500 m/s, which is 500 m/s less than the horizontal velocity (as shown later in Chapter 4, section 4.5). It is concluded from all these observations that the vertical velocity is reduced by the relatively high compliance of sub-horizontal fractures. Sub-vertical fractures would appear to be stiffer, resulting in horizontal velocities that are close to the value for the un-fractured rock. At these shallow depths, it would not be unusual for the horizontal stress to be two or three times larger than the

vertical stress (Hudson and Harrison, 1997). Therefore the rocks at Tytherington are assumed to be transversely isotropic with a sub-vertical axis of symmetry.

Histograms of the open, calcite filled fractures and bedding, or lithological banding, down the three boreholes are shown in figure 3.6. The bedding and calcite filled fractures are far more numerous than the open fractures for all the holes throughout the depth interval of the boreholes. Note also that the open fracture density decrease markedly with depth below 20 metres.

3.3.3 Wireline logging

The physical properties of the rocks surrounding the boreholes were measured by geophysical wireline logging. The wireline logs obtained in all the holes are shown in figure 3.7. The resistivity decrease towards the bottom of the hole corresponds to a progressive increase in natural gamma, indicating an increase in the clay content with depth. This is especially evident in all holes below 28 metres, where the average sonic velocity is also much lower than the velocity for the top of the holes.

The caliper log indicates variations in the borehole diameter, which might indicate possible fracture zones. All the holes are relatively smooth with the exception of 10 m – 14 m down borehole 2 where a large number of open fractures were identified from the OPTV analysis (Fig. 3.4b and Fig. 3.6). In particular, at a depth of 13 and 16 metres down borehole 2, 9 and 8 open fractures/metre were identified respectively, which clearly correlates with a local enlargement in the caliper log at the same depth. Also, there is an anomalously large caliper value at approximately 25 metres in BH 4. This disturbance in

the borehole diameter is believed to be associated with one of the large sub-vertical wrench faults intersecting the borehole at this depth.

The formation density log was only recorded for BH 2. This log gives an average value of $\rho \approx 2.60$ g/cm^3, calculated from 338 values which is the entire recorded depth interval from 3.34 m – 37.13 m. This correlates very well with the average bulk density calculated in the laboratory, from the Helium Porosimetry measurements for the 20 Tytherington field samples (see Table 2.1).

The solid blue lines in figure 3.7 are the sonic velocities for the respective boreholes. Plotted here is the 3rd moving average, compressional wave interval velocity which was calculated from the picked, first arrival compressional wave energy, on the near and far-field full waveform sonic traces. Due to the fact that the near and far-field full waveform sonic waveforms were recorded every 0.2 metres, the 3rd moving average of the velocity was chosen to smooth the data to the resolution of the distance between the two receivers (0.4 metres). The distance between the two receivers (Rx_1 and Rx_2) is divided by the compressional wave travel time difference recorded at the two receiver positions. Only the lower transmitter (Tx_1) was used in the survey. The recording lengths for the waveforms were 1920 μs, which corresponds to a sampling interval of 4 μs at 480 samples/trace.

3.4 Correlation between the open fractures and the wireline data

As shear waves do not propagate in fluids, a P-wave source produces an S-wave through mode conversions at the borehole wall (P → S). This S-wave, in turn, is converted back into a P-wave (S → P) which is then recoded at the receiver. The high frequency P-wave,

travelling in the formation arrives first (usually with very low amplitude), to be followed by a higher frequency, stronger shear wave, and then a lower frequency, very high amplitude Stoneley wave travelling along the borehole wall (Sheriff and Geldart, 1999). Fracture interfaces or discontinuities would also be responsible for additional mode conversions, lowering the reliability with which shear wave data can be picked from compressional wave surveys. As a consequence of this, it was decided not to pick the shear arrivals from the compressional wave sonic data. In order to calculate a tangential compliance with confidence from the sonic data, a true S-wave source would be required.

Figures 3.8 - 3.10 show the correlation between the far-field full waveform sonic, interval sonic, and resistivity logs with the open fracture histogram log, for all depths above 28 metres, since 95% of the identified open fractures were identified in this zone (Fig. 3.6). The profiles correlate well with the macroscopic fracture histogram log, with the interval sonic velocity range consistent over all three boreholes which proves that the fractures are *not* seismically transparent. Zones of low electrical resistivity coincide with low sonic velocity and high fracture density, with an obvious associated decrease in far-field full waveform sonic amplitudes over the same interval and vice versa. This amplitude decrease was also evident in the near-field full waveform sonic dataset.

The highly attenuated far-field full waveform sonic amplitudes evident over the entire recording time interval from 0 μs – 1920 μs, between 0 - 6 metres in BH 3 (Fig. 3.9), correspond to the highly fractured subsurface rock due to continuous subsurface blasting in the quarry. The caliper log was not deployed in this portion of the boreholes.

3.5 Calculating a fracture compliance from the compressional wave sonic data

In the preceding sections it was shown that the open fractures have a definite and clear influence on the sonic and other wireline data. This result enables one to confidently calculate a compressional wave, sonic, normal compliance value from this limestone field test site, by attributing the fluctuations in sonic velocity to the presence or absence of open fractures.

From the sonic velocity logs obtained from BH 2, BH 3 and BH 4 (Figs. 3.8 - 3.10) it is assumed that the mean velocity fluctuation from approximately 5.25 km/s to 5.75 km/s was due to the open fractures. Knowing that the spacing between the two receivers on the sonic sonde is 0.4 metres, one can then calculate a group time delay associated with this sonic velocity differential of 0.5 km/s. This is the time delay the compressional wave experiences on crossing a set of fractures. As a first order approximation, ignoring the interaction between the fractures, the group time delay is calculated as follows:

$$t_g = tt_{slow} - tt_{fast} \qquad (3.1)$$

$$= \frac{0.4}{5.25} - \frac{0.4}{5.75}\ \frac{m}{km/s}$$

$$= \underline{0.0066}\,\text{ms}$$

where,

tt_{slow} and tt_{fast} are the travel times of the slow and fast compressional wave in the presence or absence of open fractures respectively

Thus, the velocity change of 0.5 km/s, over a distance of 0.4 metres, corresponds to a group delay of the order 0.0066ms.

From the open fracture histograms (Figs. 3.8 – 3.10) it can be seen that there are, on average, between 2 and 4 open fractures over the 0.4 metre distance between the two sonde receivers. Hence, the time delay per fracture is: $0.0017 \text{ ms} \leq t_g \leq 0.0033 \text{ ms}$

Knowing the density, compressional wave velocity, transmitted frequency and incident angle of the compressional wave incident on a set of fractures, one can calculate the normal compliance from the phase delay which is related to the group time delay by equation 1.27. Assuming $Z_N = Z_T$, figure 3.11a shows how the group time delay of a compressional wave travelling through a set of fractures, at normal incidence, varies with normal compliance and frequency (using Schoenberg, 1980). Input parameters v_P = 6150 m/s and ρ = 2600 g/cm^3 were obtained from the Tytherington core samples, whilst v_S was assumed to be $\frac{v_P}{1.88}$ (mean v_P / v_S ratio from Mavko et al., 1998). The stiffer the fracture (i.e. the smaller the compliance), the smaller the group time delay. In the limit where the stiffness is infinite (zero compliance) the group time delay is, as expected, zero for all frequencies. The more compressible the fractures, the more it is responsible for delaying the wave pulse as it travels through the formation. Figure 3.11b is a profile of figure 3.11a at 23 kHz, the nominal frequency of the piezoelectric transducers in the sonde, but for a range of angles (θ). Here, θ is the angle between the wave vector and the axis of symmetry. Under this convention, θ = 0º for a transversely isotropic (TI) background medium with a vertical symmetry axis (VTI) when the incident wave is normally incident on the TI medium. Thus, in figure 3.11b, 0º is equivalent to the normal incidence wave in figure 3.11a at 23 kHz. A compliance interval is calculated by allowing for different P-wave incident angles, from $\theta = 0°$ to $\theta = 20°$, to the open fracture dips at Tytherington. In figure 3.11b, the lower limit of normal fracture compliance ($\theta = 0°$) at a

specific time delay is shown in blue, whilst the corresponding upper limit of compliance ($\theta = 20°$) is shown in green.

It is estimated that the normal compliance of the fractures for BH 2 is:

$$Z_N = 2.27 - 2.37\,\text{x}10^{-13}\ \text{m/Pa}\ @\ t_g = 0.0017\ \text{ms} \qquad \text{and}$$

$$Z_N = 6.38 - 7.41\,\text{x}10^{-13}\ \text{m/Pa}\ @\ t_g = 0.0033\ \text{ms}$$

Thus, within the $\pm 20^{\circ}$ tolerance of the open fracture dips, it is estimated that the normal fracture compliance as calculated from the sonic compressional wave data, from the three boreholes, at the Tytherington quarry field test site is:

$$Z_N = \left(4.84 \pm 2.57\right)\text{x}10^{-13}\ \text{m/Pa}$$

3.6 Discussion

Thompson (1966) found zones of high fracture density adjacent to principal slip faces in granites. These were believed to have developed during slip events, which led to additional microcracking of the matrix surrounding the slip faces. The presence of slickensides on the sub-vertical wrench faults in our field site is evidence that these slip events also occurred at Tytherington at some point in the quarry's geological past. Mechanical and chemical alteration of rock adjacent to macroscopic fractures plays an important role in reducing the *in-situ* velocities. The increase in travel time and group time delay which a seismic wave experiences, would not only be due to the macroscopic open fractures, but would be a combined effect of the open fractures and the altered zone surrounding the fractures. Moos and Zoback (1983) investigated the effect of macroscopic fractures on compressional and shear wave velocities in granitic rock, and concluded that, although the presence of macrofractures had a marked effect on the sonic

velocities, the degree of *in-situ* fracturing could not be unambiguously estimated from the sonic velocities because of the importance of composition and microcracks. In the light of this argument, it is concluded that, the upper limit of normal fracture compliance from our field site can be stated with relative certainty, whilst the lower limit is less reliable due to the sonde sampling a combined effect of the chemical alteration, microcracking and open fractures. This issue will be discussed further in Chapter 7.

In this chapter a value for compressional wave fracture compliance at sonic frequencies (~20 kHz) from the Tytherington quarry field site was obtained by attributing the group time delay of the seismic wave to the open fractures. This normal compliance value was higher than values obtained from the laboratory estimates (frequencies ~850 kHz) from the field core sample. In the following chapter, the estimation of normal fracture compliance from crosshole data (frequencies ~2 kHz) from the same field site is described.

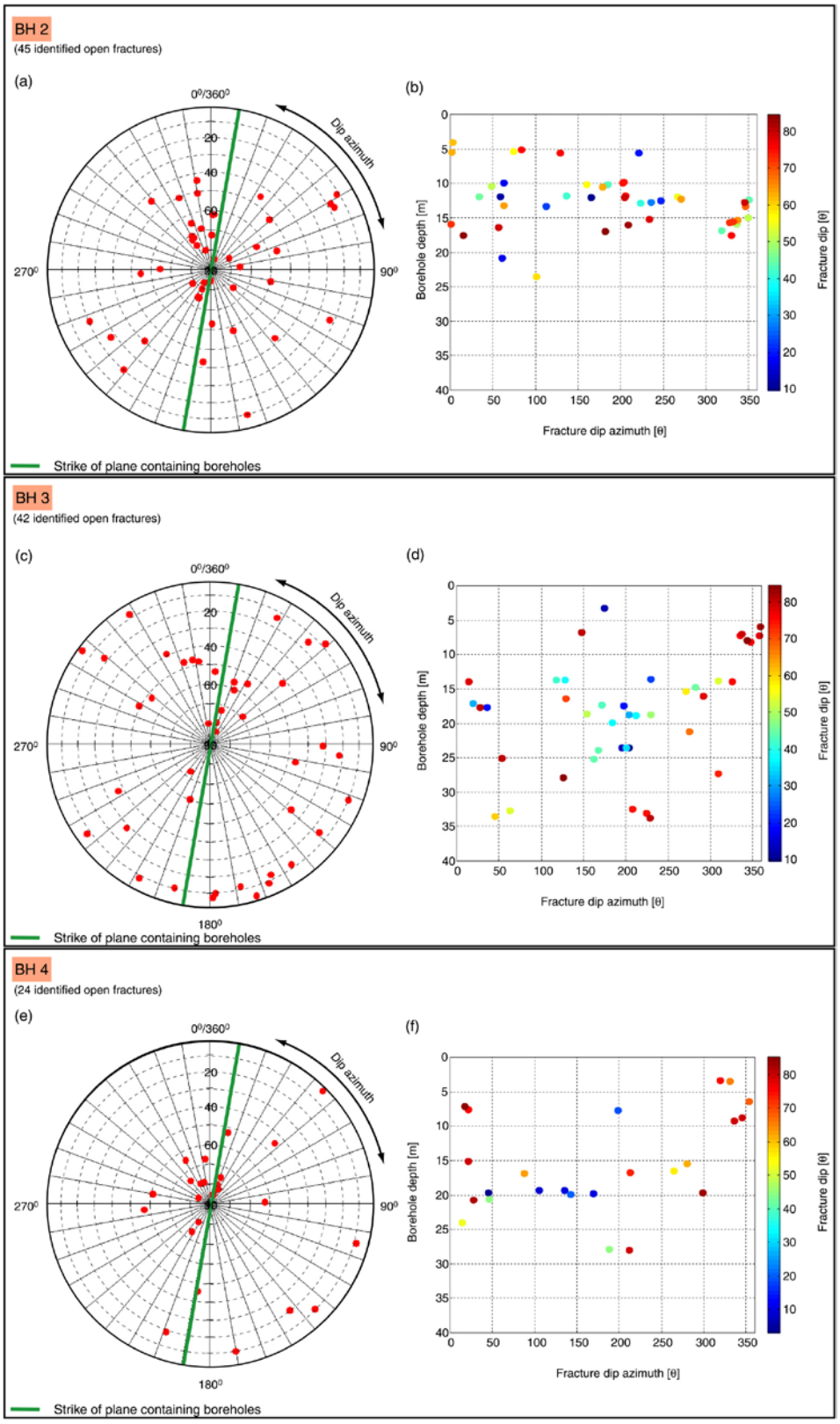


Figure 3.5: Optical televiewer open fracture analysis of BH 2, BH 3 and BH 4 at Tytherington quarry. (a), (c) and (e) are the equal area, stereographic projections of BH 2, BH 3 and BH 4 respectively; figures (b), (d) and (f) are the corresponding dip, dip azimuth and depth plots of (a), (c) and (e) – see text for details.

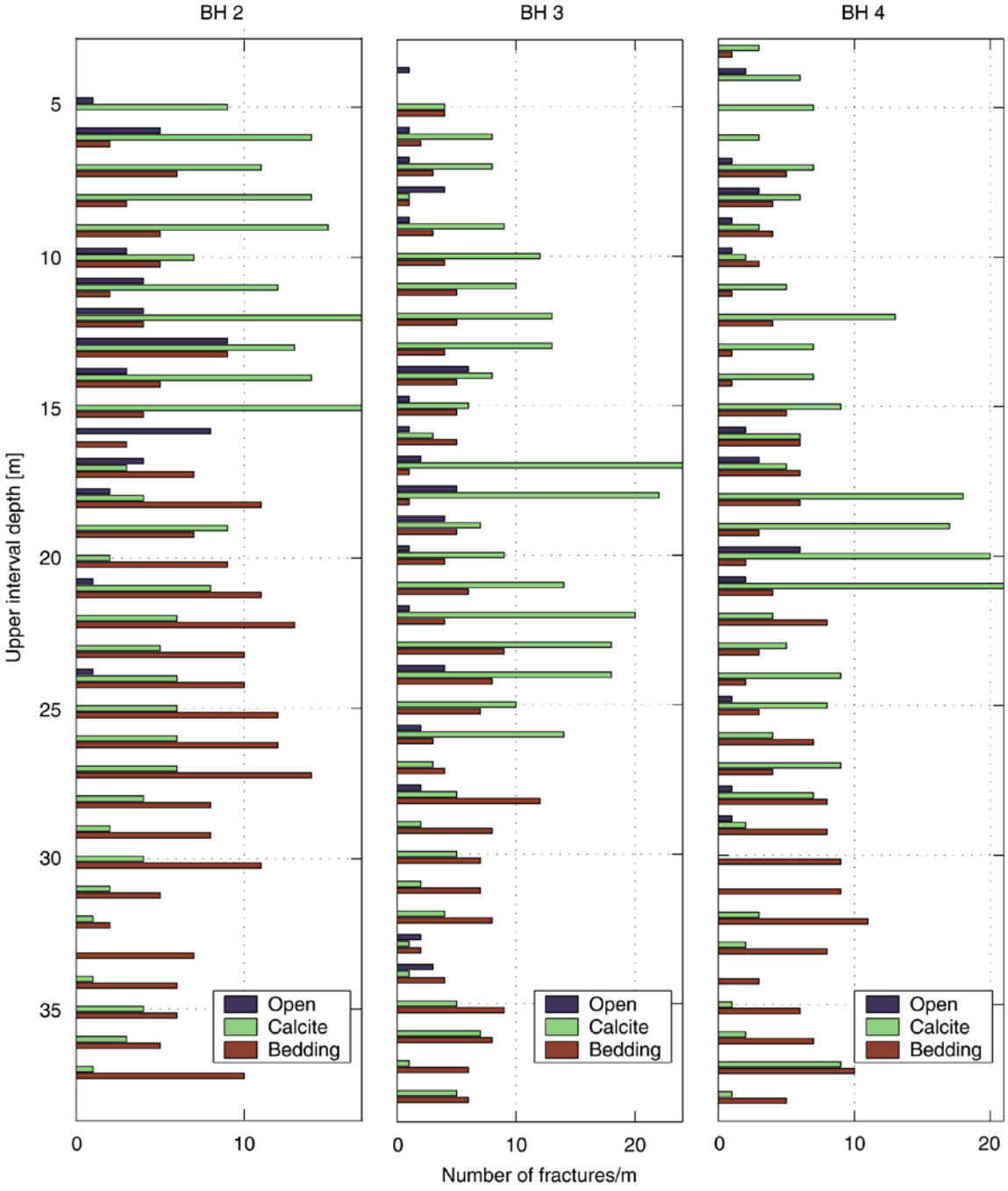


Figure 3.6: Histograms showing the relative distribution of the bedding, open and calcite filled fractures in the three boreholes from the optical televiewer data analysis.

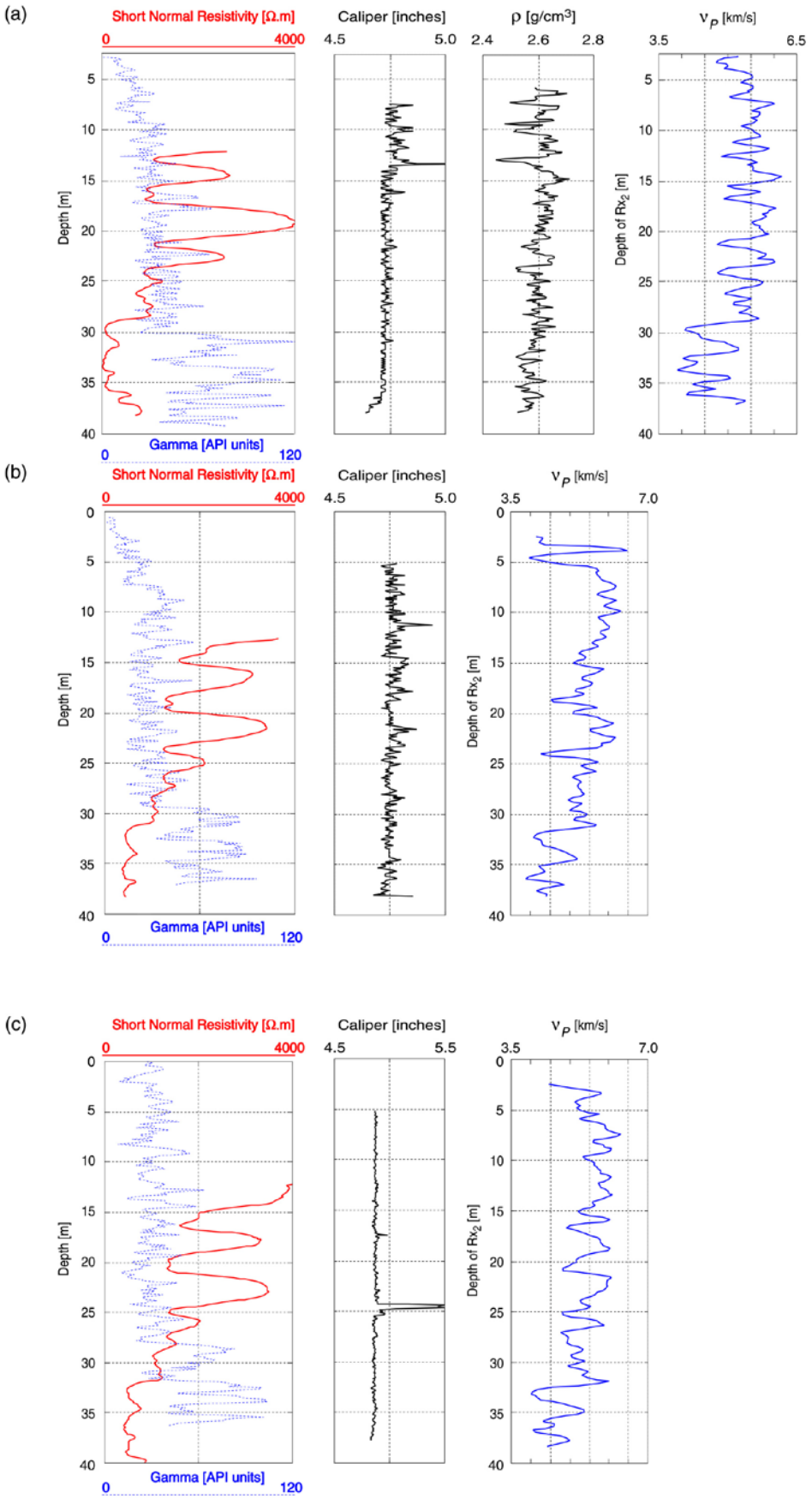


Figure 3.7: Wireline geophysical logs obtained in all the boreholes. (a) BH 2; (b) BH 3; (c) BH 4.

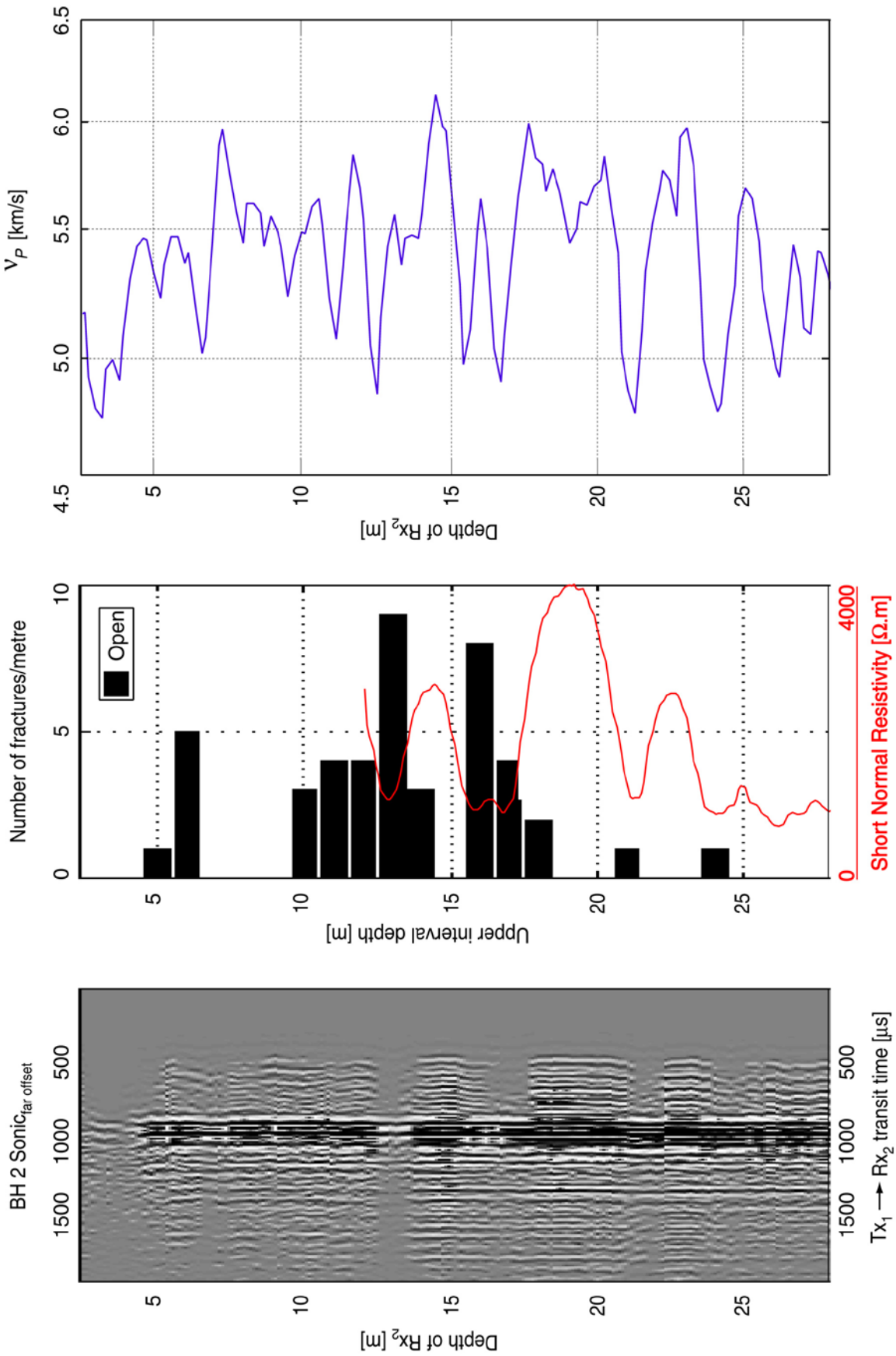


Figure 3.8: Correlation between the far-offset full waveform sonic, interval sonic, and electrical resistivity logs with the open fracture histogram log, for all depths above 28 metres in BH 2.

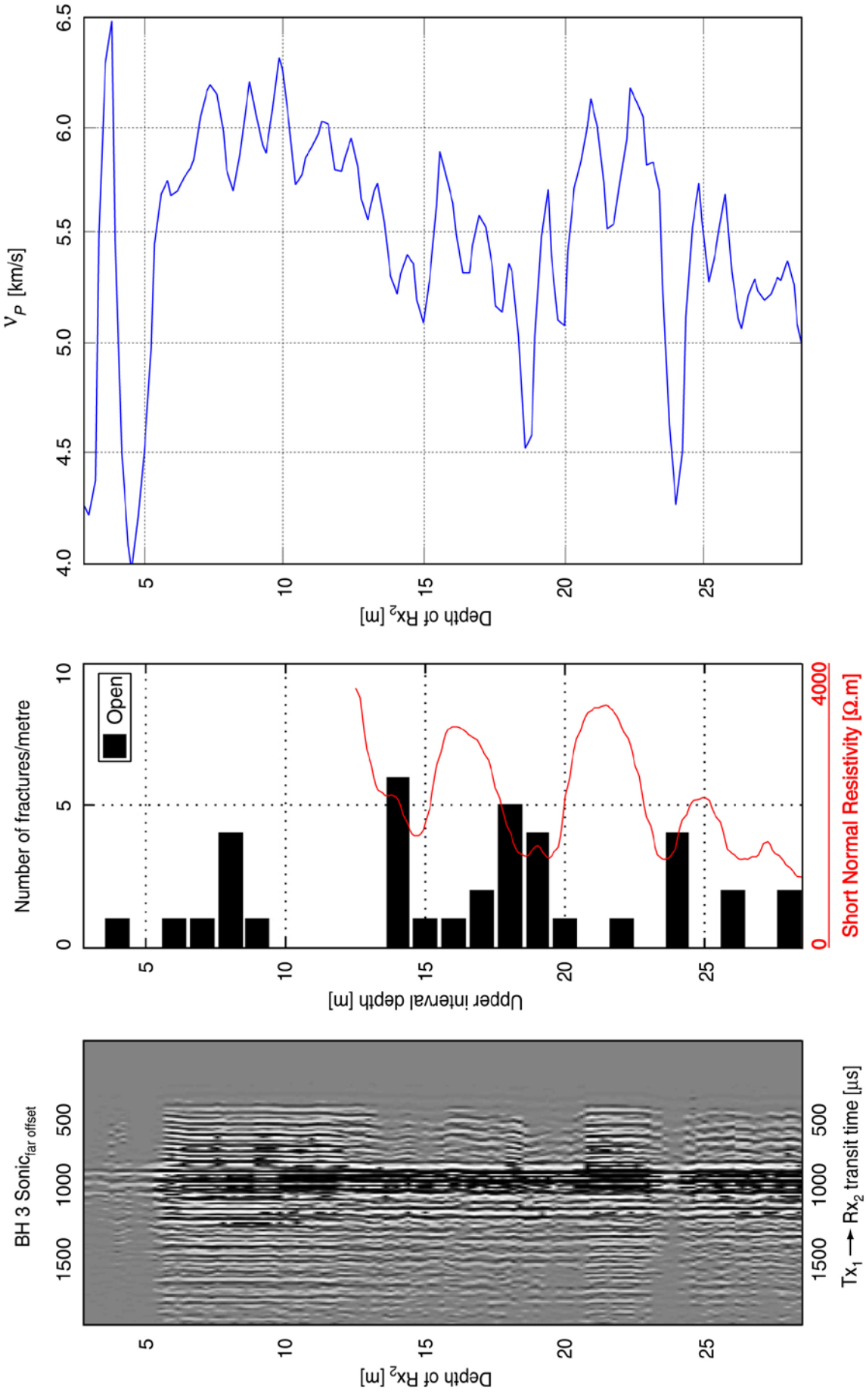


Figure 3.9: Correlation between the far-offset full waveform sonic, interval sonic, and electrical resistivity logs with the open fracture histogram log, for all depths above 28 metres in BH 3.

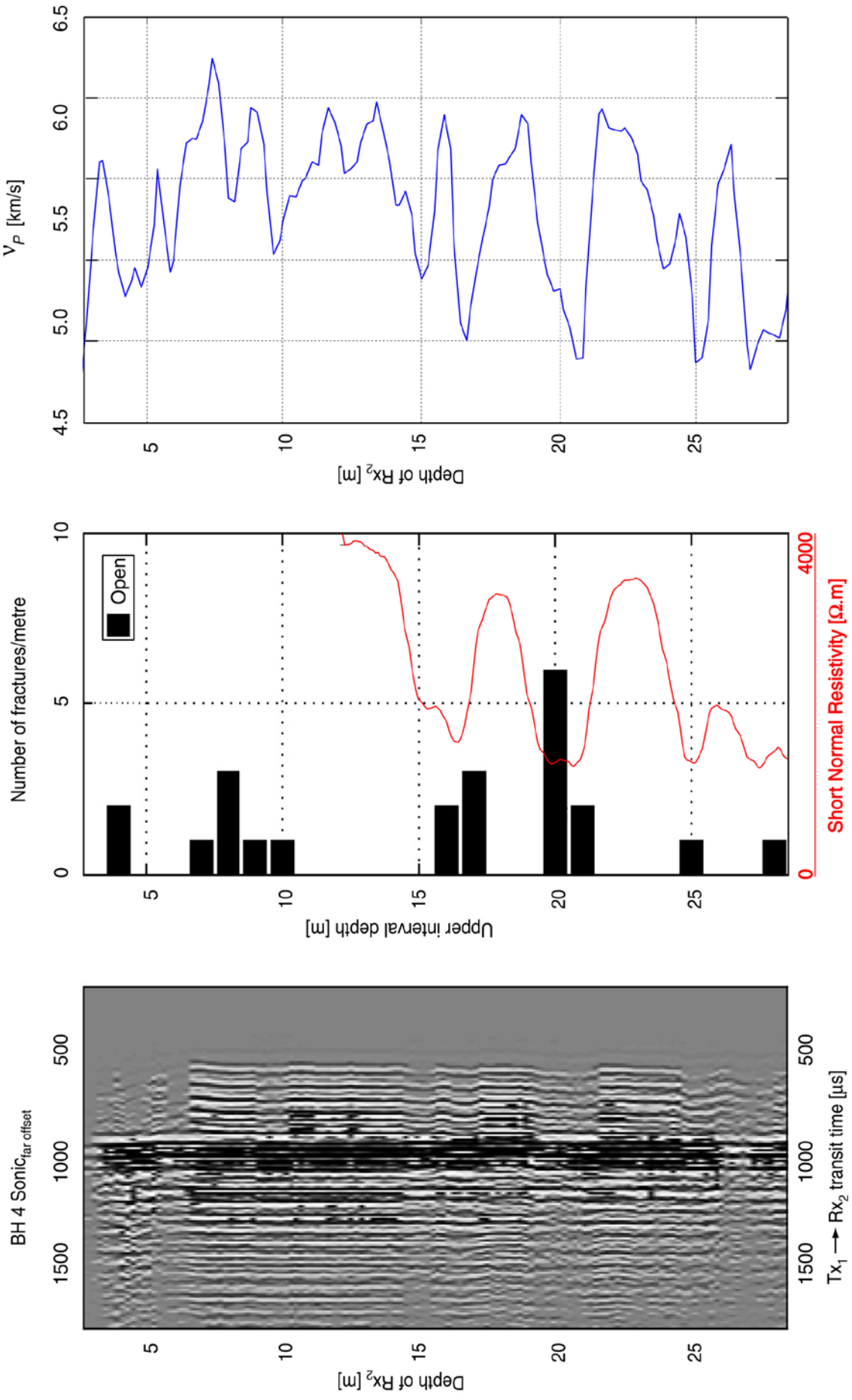


Figure 3.10: Correlation between the far-offset full waveform sonic, interval sonic, and electrical resistivity logs with the open fracture histogram log, for all depths above 28 metres in BH 4.

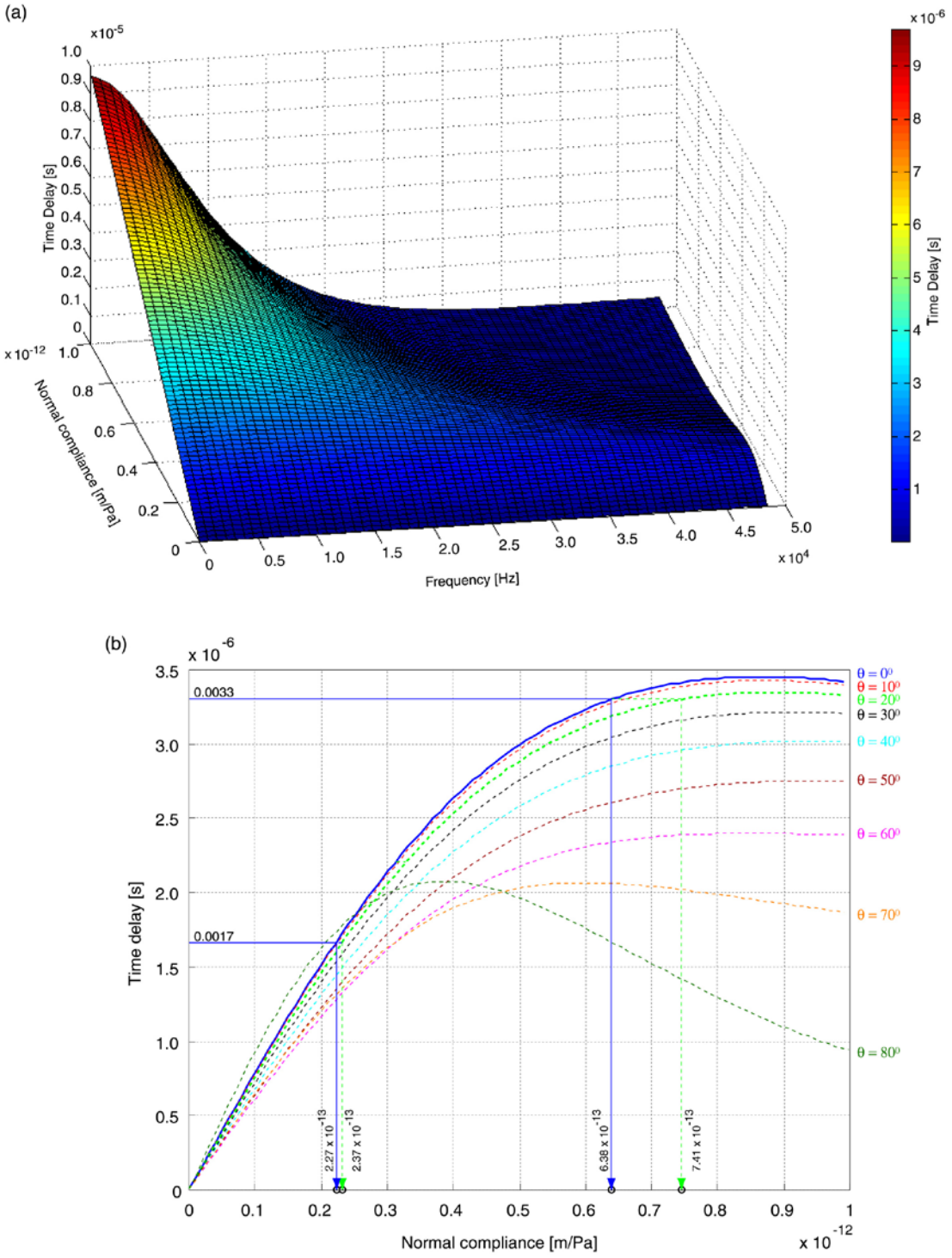


Figure 3.11: Analytical modelling to calculate the normal fracture compliance from the compressional wave sonic data, assuming $Z_N = Z_T$. (a) Theoretical calculation of normal fracture compliance versus frequency and group time delay due to fractures, as calculated for a wave normally incident on a set of fractures; (b) Normal fracture compliance versus group time delay for a wave transmitted at a frequency of 23 kHz, at a range of angles (here $\theta = 0°$ represents a normally incident P-wave).

Chapter IV

Tytherington Quarry - Crosshole Travel Time Data

4.1 Introduction

In this chapter equivalent media theories are used to calculate fracture compliance values for the same scale of fractures as in Chapter 3. The crosshole experiment is described, and the compressional wave velocity anisotropy is calculated from the interval sonic data and crosshole seismic data between BH 2 and BH 4, allowing for dispersion. This velocity anisotropy, as observed in the fractured region above 28 metres in the three boreholes, is a function of the intrinsic anisotropy, lithology or bedding induced anisotropy and open fracture related anisotropy (from microcracks and macrofractures). The bedding/lithology and the intrinsic anisotropy are subtracted from the total anisotropy leaving the anisotropy related to the open fractures only. An upper and lower limit of normal fracture compliance is then calculated and this estimate is compared with the value from the previous chapter.

4.2 Acquisition parameters

A seismic compressional wave crosshole survey was carried out at Tytherington quarry in November 2001. A borehole electrical sparker source was deployed in BH 4 at depths between 6 m and 38 m at an increment of 2 m (Fig. 4.1). The sparker source created a seismic pulse by applying a large voltage (5 kV) between a spark candle and a cage in a chamber filled with salt water. A 10 channel BGS (British Geological Survey) hydrophone chain with a 1 metre receiver spacing and a 12 channel OYO (OYO Geospace Corporation) hydrophone chain with a 2 metre receiver spacing was deployed in BH 3 and

BH 2 respectively. A summary of the acquisition parameters is shown in table 4.1. Figure 4.1 (b) shows the 12 channel hydrophone string used in BH 2.

This geometry enabled a seismic wave to be recorder by two similar recording instruments as the wave propagated in-line between BH 3 and BH 2. This eliminated associated source radiation pattern and coupling uncertainties. The waveforms were recorded on a 24 bit Geometrics StrataView seismograph which enabled 24 channels to be recorded simultaneously. The Nyquist frequency, $f_{Nyquist} = \frac{1}{2\Delta t}$, with a sampling interval of 62.5 μs was 8 kHz. No analogue filters were applied in the field before digitising the seismic signal. Channels 3 - 12 were used for the 10 channel BGS hydrophone chain in BH 3, with the remaining channels (channels 13 - 24) used for the 12 channel OYO hydrophone chain in BH 2.

The crosshole survey was carried out in two stages. In the first stage the first shot was fired in the bottom of BH 4 at a depth of 38 metres with the first phones (channel 3) on the BGS chain and channel 24 on the OYO chain at a depth of 38 m down BH 3 and BH 2 respectively. For the next shot, the BGS hydrophone string in the BH 3 was moved up by 1 metre intervals whilst the hydrophone string in BH 2 remained fixed. This process was repeated until the last phone (channel 12) in BH 3 reached a depth of 12 metres and the source reached a depth of 6 metres. In the second stage, the BGS and OYO strings were moved up with the last BGS phone (channel 12) and the last OYO phone (channel 13) at 6 metres down BH 3 and BH 2 respectively. For the subsequent shots, the hydrophone chain in BH 3 was lowered by 1 metre intervals whilst the hydrophone chain in BH 2 again remained fixed. This procedure produced good angular coverage ($0° \leq \theta \leq 66°$), and two hydrophones in-line with the source for every shot position. Figure 4.2 is a schematic

diagram illustrating the acquisition geometry showing an example of a common vertical source receiver offset gather (zero offset in this case) and a common shot gather with the shot at 38 metres down BH 4. Assuming straight rays, the dip angle θ is calculated simply using arctan $\frac{\Delta z}{\Delta x}$. $\theta = 0°$ indicates zero offset, horizontal or straight across rays.

Tytherington Seismic Experiment – Acquisition Parameters	
Source	BGS Mini-Sparker
Signal Centre Frequency	2000 Hz
Recording Unit	Geometrics StrataView R24
Receivers	10 channel BGS hydrophone chain 12 channel OYO hydrophone chain
Sampling Interval	62.5 μs
Record length	128 ms
Source spacing	2 m
Source positions	BH 4; 6.0 – 38.0 m 17 source positions
Receiver spacing	BGS: 1 m OYO: 2 m
Receiver positions	OYO – BH 2; 6.0 – 38.0 m 17 receiver positions
	BGS – BH 3; 6.0 – 37.0 m 32 receiver positions

Table 4.1: Acquisition parameters for the seismic crosshole experiment at Tytherington quarry.

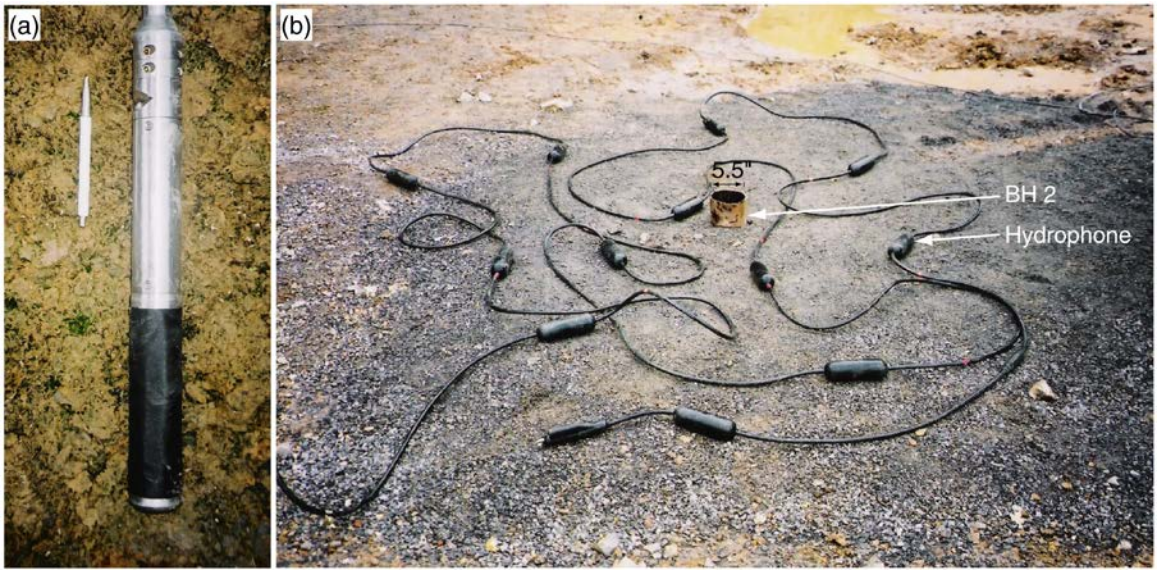


Figure 4.1: Crosshole source and receivers. (a) Borehole electrical sparker source used in BH 4; (b) 12 channel hydrophone string deployed in BH 2. The diameter of the borehole casing (shown as 5.5 inches) indicates scale. The receiver spacing on this hydrophone string was 2 metres.

4.3 Picking of the travel times

The aim of the data processing was to increase the visibility of the first arrival of the seismic energy, whilst at the same time ensuring that the signal characteristics were maintained. The dataset was imported into Promax^{TM} and the geometry of the survey was manually created in the processing flows. This enabled the data to be sorted in a variety of ways, aiding greatly the picking of the first arrival travel times. Using different gathers during the travel time picking process helps to ensure consistency in the travel time picks (Pratt and Sams, 1996). For this purpose the data were picked by sorting the data iteratively in common source gathers, common offset gathers and common receiver gathers, and readjusting the first break picks using a pre-determined gain setting. Global scaling was applied in order to conserve relative amplitudes. Using this methodology, approximately 280 first arrival compressional wave travel times were picked from the dataset with accuracy better than 0.2 ms, which corresponds to ~3 samples.

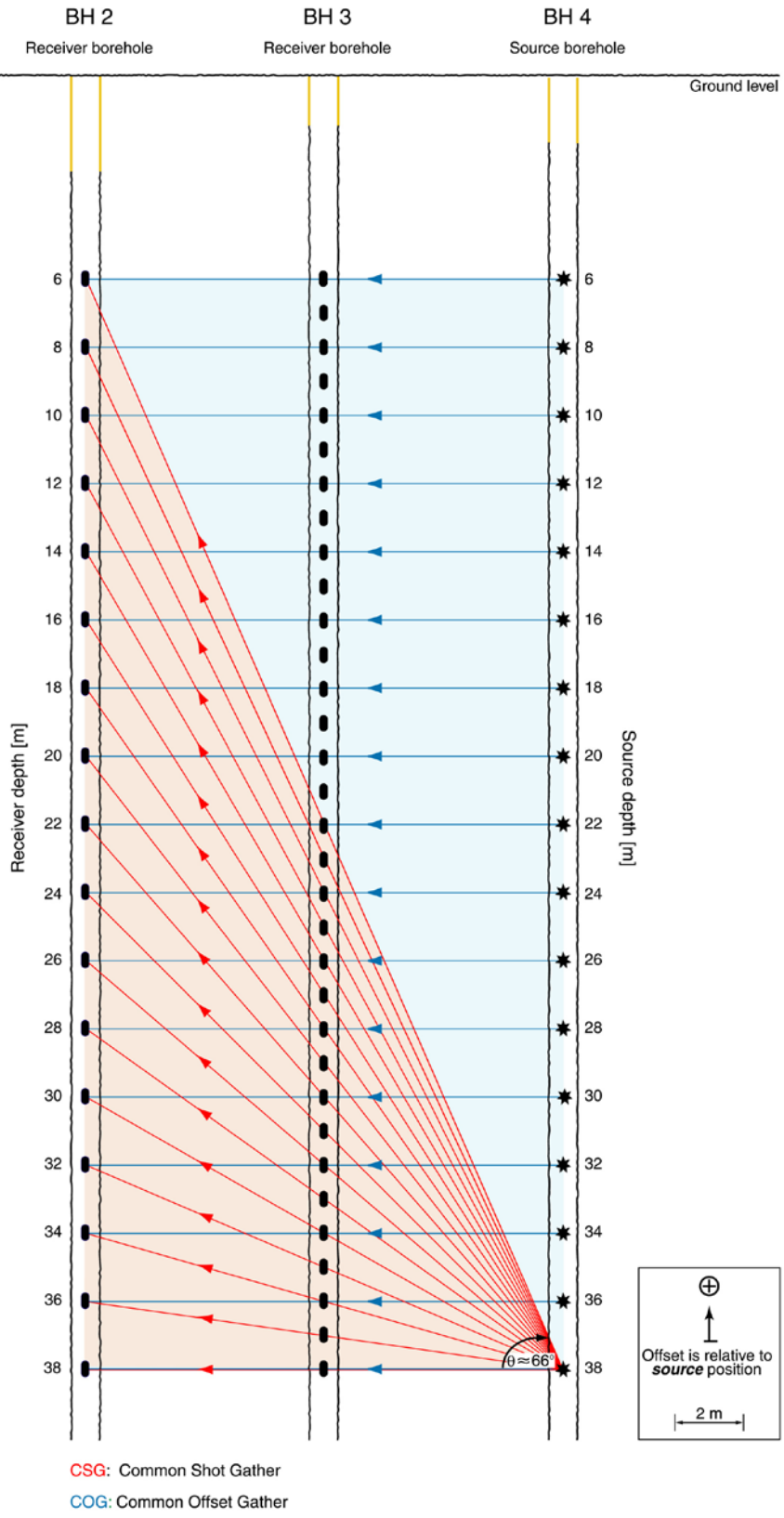


Figure 4.2: Schematic diagram illustrating the acquisition geometry. An example of a zero offset, common offset gather (COG) is shown in blue. Here positive offsets are equivalent to ray paths with negative gradients and vice versa. A common shot gather (CSG) with the sparker source at 38 metres down BH 4 is shown in red.

Three shots were recorded for every source position down BH 4. Having more than one recorded trace at every depth interval allowed for the removal of spurious traces at the processing stage without the danger of upsetting the data continuity. Some of the traces contained a DC component which was removed prior to stacking. The data were filtered with an Ormsby bandpass filter with corner frequencies of 50 Hz and 100 Hz at the lower end of the passband, and 5 kHz and 6 kHz at the upper end of the passband. The three signals from a fixed shot position were stacked to improve the signal to noise ratio. An example of a common shot gather between the two furthest boreholes is shown in figure 4.3. The source in BH 4 was at a depth of 20 metres. The hydrophone chain was deployed in the upper fractured region of BH 2, with the hydrophone receivers from 6 m to 28 m with a 2 m increment.

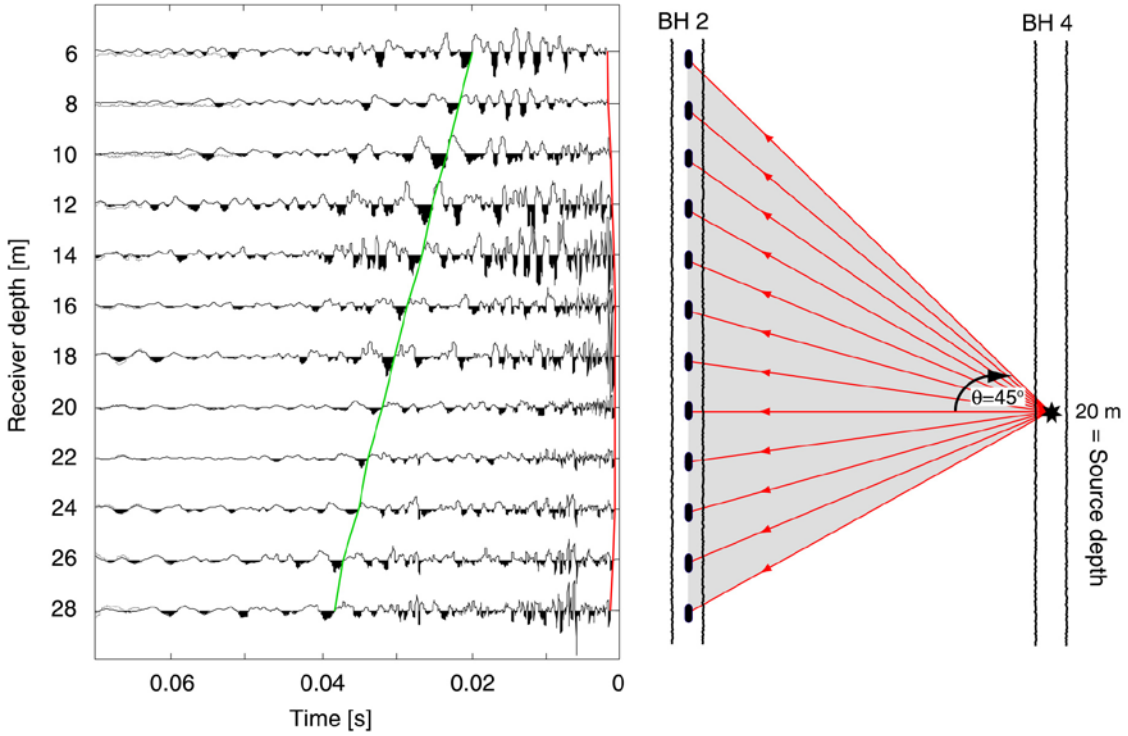


Figure 4.3: Tytherington common shot gather with the source in BH 4 (at a depth of 20 metres) and the OYO hydrophone chain in BH 2 (with receiver depths ranging from 6 m to 28 m).

A complex coda is a notable feature of these data but the first arrival could be traced very easily through the seismogram (shown in red). S-waves could not be identified unambiguously. Hardin et al. (1987) attribute the generation of tube waves to open fractures, a change in lithology or a change in the borehole diameter. High amplitude, low frequency later arrival tube waves are also evident in the common shot gather (shown in green) and are characterised by linear moveout.

4.4 Evidence of anisotropy

Figure 4.4 shows the compressional wave velocity variation between BH 4 and BH 2 from the crosshole survey calculated by assuming straight rays. Any line perpendicular to the x-axis represents a common receiver gather whilst and any line perpendicular to the y-axis indicates a common shot gather. All common offset gathers in this plot will be lines parallel to the line y = x.

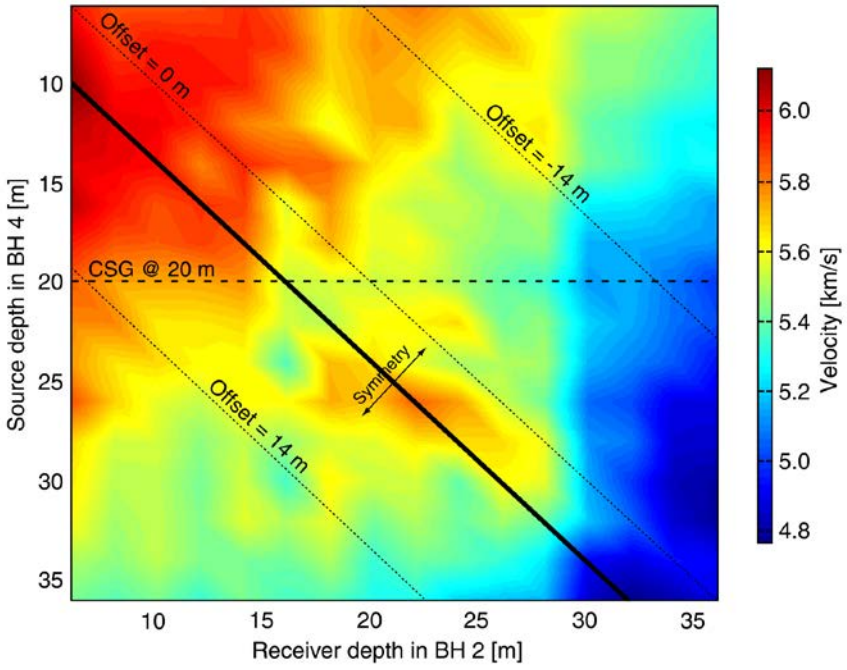


Figure 4.4: Compressional wave velocity as a function of source depth (in BH 4) and receiver depth (in BH 2) from the crosshole survey between BH 4 and BH 2.

From the straight-across, zero offset rays, a decrease in velocity with depth can be seen, which is wholly consistent with the sonic velocities from the wireline logs. The lowest velocity is again observed in the zone below 28 metres, which is within the shale-rich region. Transverse isotropy is indicated by a symmetric decrease of velocity either side of a common offset gather line. A clear symmetry in the data in figure 4.4, about a common offset gather of 4 metres, corresponds to the dip of the bedding at the test site. It was shown in Chapter 3 that the bedding at Tytherington dips at 16º towards 170º (i.e. approximately from BH 2 towards BH 4). This dip would be responsible for a tilted symmetry axis if one were to assume a transversely isotropic medium.

4.5 Calculating the anisotropy

The next procedure was to look at the difference travel times i.e. shooting in BH 4 and measuring simultaneously in BH 2 and BH 3. This is a way of eliminating any possible error in the source trigger, unknown receiver time delay and source function variation at different depths down the borehole. The solid red line in Figure 4.5 shows the arithmetic mean over a 4 metre interval calculated from the straight across, horizontal difference velocities between the two boreholes. Also shown is the mean vertical compressional sonic interval velocity for BH 2, averaged over the same depth interval. A way of describing the anisotropy, or velocity dependence on angle, is to use the Thomsen (1986) anisotropy parameter ε, which is the fractional difference of the P-wave velocity perpendicular and parallel to the symmetry axis in the limit of weak anisotropy. The phase angle is the angle between the wavefront normal and the symmetry axis:

$$\varepsilon = \frac{v_P(90°) - v_P(0°)}{v_P(0°)} \tag{4.1}$$

From figure 4.5 it can be seen that the average horizontal difference velocity, at ~2 kHz,

in the top of the borehole (above 25 metres), is in the region of 6100 m/s, whilst the average vertical sonic velocity over the same interval, at ~23 kHz, is in the region of 5500 m/s. This velocity difference between the horizontal and vertical velocities occurs within the region of higher fracture intensity observed from the OPTV analysis, as described in Chapter 3, and corresponds to an ε of 11%. This is consistent with anisotropy values reported in the literature by Pratt and Chapman (1992), Pratt et al. (1993) and Kragh et al. (1996) for near surface fractured rocks.

4.5.1 Modelling the velocity dispersion

The well known relationship (Eq. 4.2) derived by Futterman (1962) was used to show that the velocity difference described in the last section is not due to dispersion effects.

$$\frac{c(\omega_1)}{c(\omega_2)} = 1 + \frac{1}{\pi Q}\ln\left(\frac{\omega_1}{\omega_2}\right) \tag{4.2}$$

where,

$c(\omega_1)$ and $c(\omega_2)$ = the velocities of the body wave at frequencies ω_1 and ω_2

Q = quality factor

Futterman (1962) showed that velocity dispersion for seismic body waves is small. Dispersion or the distortion of the wave train in which the velocity of the wave varies with frequency has been attributed to several mechanisms (Winkler and Murphy III, 1995), but is directly related to seismic attenuation. A Q value of 25 was used in the modelling. This value was based on the compressional wave quality factor (Q_P^{-1}) values calculated from the whole Tytherington field sample in the laboratory (Table 2.4) and the average Q value as calculated in Chapter 5 (shown in Fig. 5.7). Using equation 4.2, with $Q = 25$, one obtains: v_P (@ 23 kHz) = 1.031 v_P (@ 2 kHz). In other words, if one corrects

2 kHz data to be comparable with 23 kHz data the velocity will increase. This result is plotted as a dashed red line in figure 4.5.

This clearly shows that velocity dispersion has a minimal effect on the velocities over the seismic/sonic frequency range (even for a Q value as low as 25). The velocity difference between the horizontal and vertical velocities is therefore predominantly a function of open fractures, microfractures and lithology.

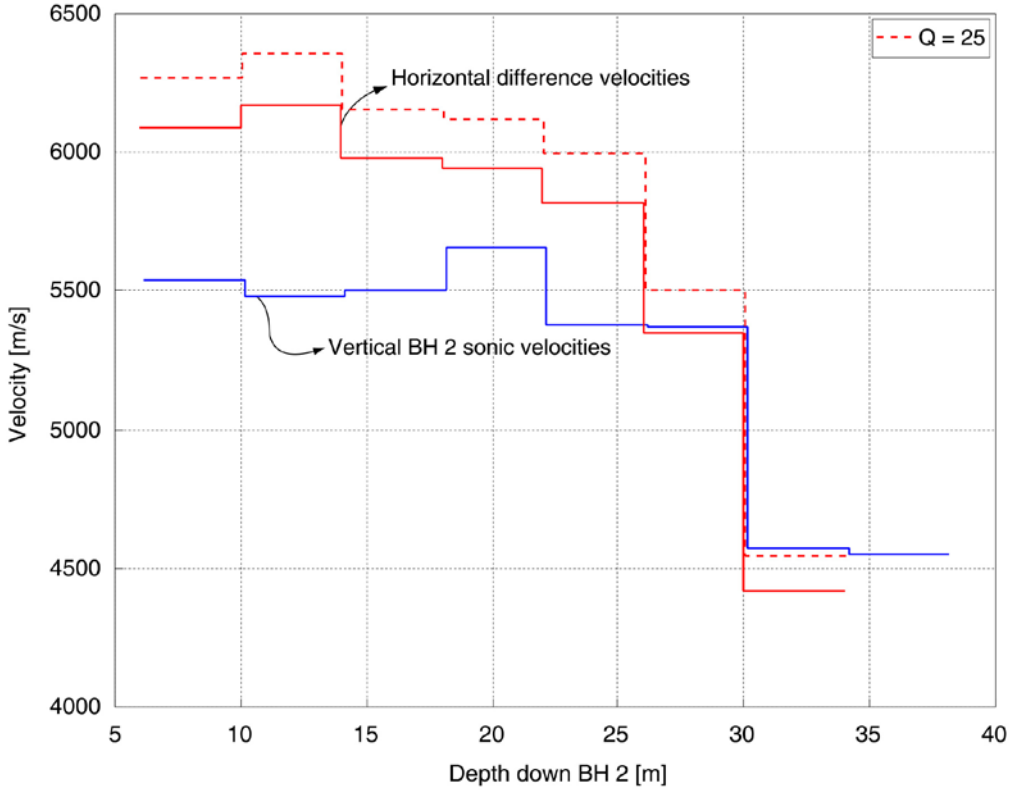


Figure 4.5 Horizontal difference velocities between BH 2 and BH 3 (solid red line) and the vertical compressional wave sonic interval velocity for BH 2 (solid blue line) versus the depth in metres down BH 2. The red dashed line is the horizontal difference velocities corrected for dispersion assuming a Q value of 25.

4.6 Estimating the lithology induced anisotropy

Backus (1962) developed an essentially zero frequency averaging technique whereby a finely layered stratified medium with homogeneous isotropic or transversely isotropic

layers can be replaced with a single, smooth, transversely isotropic long wavelength equivalent medium. In this theory it is assumed that the materials are linear elastic, there are no sources of intrinsic energy dissipation such as friction or viscosity, and the layer thickness must be much smaller than the wavelength - a rule of thumb is that the wavelength must be at least 10 times the layer thickness (Mavko et al., 1998).

In equivalent medium theories, it is assumed that the seismic wavelength used to characterise the subsurface is much larger than the fractures, and that the wavelength samples an average effect of the rock properties. At Tytherington, the crosshole wavelength $\lambda = \frac{v_P}{f} \approx \frac{6000 m/s}{2000 Hz} = 3$ m, and since at most 10 fractures/m was observed in the most heavily fractured region in BH 2, BH 3 and BH 4 (1 fracture every 0.1 metres) the equivalent medium theory was assumed to be valid for this site at crosshole frequencies.

Hsu et al. (1988) used a Backus averaging scheme to estimate the anisotropy parameters from high resolution sonic logs for several window lengths. They underline the fact that the equivalent medium theory, assuming isotropic layers, underestimates the true anisotropy in the presence of layering finer than the log sampling or in the presence of strong intrinsic anisotropy. However, these factors were not an issue in our field site. The low API gamma values (~20 API) recorded in the fractured region, above 28 metres in all the boreholes (Fig 3.7), suggests that this region consists of essentially clean limestone. Evidence for the isotropic character of the limestone is discussed below.

A compressional wave sonic velocity was calculated from the first arrival near and far-field sonic waveforms which were recorded every 0.2 metres down the three boreholes.

Assuming that every calculated sonic velocity represented the isotropic P-wave velocity of a 0.2 m thick layer in a layered sequence, the effective anisotropy of the sequence could be calculated. This methodology allowed for the calculation of the lithology or bedding contribution to the total observed anisotropy, as calculated from the crosshole experiment using equation 4.1. It was assumed throughout the analysis that the layer thickness was 0.2 metres, the density ρ = 2.6 g/cm^3 and that v_P / v_S = 1.88. BH 2 had 181 calculated sonic interval velocities whilst BH 3 and BH 4 had 182 sonic velocities. The effective anisotropic elastic constants could be computed using, in the extreme cases, only a *single* layer at a time or the cumulative response of *all* the layers down the borehole. The elastic constants were computed for all the layer combinations between these 2 extremes i.e. $2 \rightarrow 180$ for BH 2 and $2 \rightarrow 181$ for BH 3 and BH 4 using a sliding window down the boreholes with a 1 layer increment. These elastic constants were then used to calculate an effective horizontal and vertically propagating P-wave velocity, v_{PH} and v_{PV}. These values could then be used to calculate the effective anisotropy due to the layering. Figures 4.6 – 4.8 shows the result of the modelling for BH 2, BH 3 and BH 4 respectively. In the first extreme case, when the effect of single layer at a time is calculated, the result (v_{PH} and v_{PV}) is the original sonic interval log as shown in figure 3.7. As expected, the model is very sensitive when a small number of layers is used. The second extreme, where the effective anisotropic elastic constants are calculated using all the layers, resulted in all the horizontal layers of different velocities being replaced by a single apparent velocity parallel v_{PH} and perpendicular v_{PV} to the layering. The plot depth down the borehole is halfway between the sliding window distance.

Figure 4.9 shows profiles of the cumulative P-wave velocity anisotropy calculated from

the v_{PH} and v_{PV} values for the three boreholes using 25 layers at a time. This corresponds to a sliding window distance of 5 metres (25 x 0.2 m = 5 m). The profiles are also shown as a vertical colour coded line (BH 2 – blue; BH 3 - black and BH 4 – green) on the v_P anisotropy plots in figure 4.6 (c), figure 4.7 (c) and figure 4.8 (c). The average for the fractured region above 28 meters in all the boreholes is shown in red in figure 4.9. From this analysis it is concluded that the layer induced anisotropy is approximately of the order 1%.

The Thomsen (1986) anisotropy parameter ε (Eq. 4.1), is the gross P-wave velocity anisotropy as sampled by the crosshole P-wave, as it travels through the rock mass from source to receiver, and may result from open fracture anisotropy, layering or bedding induced anisotropy, and intrinsic anisotropy of the host rock. Unfortunately, no intrinsic velocity anisotropy studies were performed on the Tytherington quarry samples. In a separate study, King and Shams-Khanshir (1998) performed studies on 31 mm diameter, cylindrical limestone samples from preserved core obtained from boreholes drilled in a Carboniferous Limestone series in northern England. Specimens were cored in directions parallel and perpendicular to the vertical axis of the limestone bedding. They showed that the intrinsic velocity anisotropy, calculated from 34 limestone samples in the laboratory under *in-situ* stress conditions, was small, approximately 0.5% (porosities to 12%). Since there is no evidence of any anisotropic fabric in the clean limestone at Tytherington, it is assumed that intrinsic anisotropy will not be greater than 0.5%.

In the preceding sections it was proved that the effective total velocity anisotropy observed at the Tytherington test site is approximately 11%. Also, by using a Backus averaging method, it was shown that the lithology contribution to the total velocity

anisotropy is approximately in the order of 1%. The intrinsic velocity anisotropy value is assumed to be approximately 0.5% from King and Shams-Khanshir (1998) and Thomsen (1986). Thus it is concluded that the remainder of the P-wave velocity anisotropy observed at Tytherington is due to the open fractures in the region between the boreholes. The P-wave velocity anisotropy due to open fractures is the total velocity anisotropy, minus the bedding (lithology) induced anisotropy, minus the inherent intrinsic fabric velocity anisotropy, i.e. 11% - 1% - 0.5% $\approx$ 10%.

4.7 Calculating the fracture density ε_f

The theory described by Hudson (1980, 1981) and Crampin (1984), for dry fractures, has been used to estimate what the fracture density ε_f would be with a Thomsen epsilon anisotropy ε of 10% and the associated fracture compliance as described in section 1.2. Here `dry` means setting the bulk modulus and the rigidity of the fluid in the fractures to zero, which physically represents the condition when pore fluid can flow freely in or out of the fractures to maintain constant pore pressure. Under these conditions the elastic constants are independent of the crack aspect ratio.

Figure 4.10 (a) shows a common receiver gather at a depth of 6 metres down BH 2 used to calculate the difference travel times between BH 3 and BH 2. Figure 4.10 (b) shows the group velocities, calculated from the difference travel times (green dots), versus the modelled phase velocity variation with angle between the wave vector and the symmetry axis in a TI medium (in red). Also shown on the same plot is the group velocity (dotted green) calculated from the phase angle (Thomsen, 1986). The average BH 2 sonic velocity, shown in blue, is calculated from 81 velocities obtained in the most heavily fractured section of this borehole from 6 m to 22 m, with an increment of 0.2 m. Fitting

the phase velocity curve to the measured difference velocities perpendicular and parallel to the TI symmetry axis was achieved by modelling the dry cracks with a fracture density of ε_f = 0.035 with input parameters v_P = 6100 m/s, $v_S = v_P/1.88$ and ρ = 2.6 g/cm^3. v_P and v_S are the respective compressional and shear wave velocities propagating through the solid containing the aligned fractures. Liu et al. (1991) and Liu et al. (1993), reports that fracture densities of this order are not uncommon in near surface (<60 m) rocks.

4.8 Calculating the normal compliance

The limits of the normal compliance at seismic frequencies are calculated in two different ways. (Note: The input parameters were again assumed to be v_P = 6100 m/s, $v_S = v_P/1.88$ and ρ = 2.6 g/cm^3). Firstly, a fracture compliance is calculated by using equation 1.23 (Schoenberg and Sayers, 1995) and secondly, a compliance value is calculated from the fracture density ε_f.

The Tytherington OPTV open fracture analysis revealed that the earth is approximating to a transversely isotropic media with a sub-vertical axis of symmetry. Since the crosshole survey is conducted within a two dimensional plane, no assumptions could be made for α_3 as it was out of the survey plane (see Fig. 1.2). Transverse isotropy is modelled by making the fractures very stiff ($\alpha_2 = \alpha_3$, $Z_N \leq 10^{-14}$ m/Pa) in the x_2 and x_3 directions and allowing α_1 to vary in the x_1 direction. Figures 3.8 - 3.10 shows that the maximum compressional wave sonic velocities above 28 metres in BH 2, BH 3 and BH 4 are v_P = 6100 m/s, v_P = 6300 m/s and v_P = 6250 m/s respectively. Arguably, these velocities represent that of homogeneous limestone without any fractures at sonic frequencies.

These velocities correspond well with measurements on two separate, intact, homogeneous, cylindrical Tytherington core samples under confining pressures from 5 MPa - 60 MPa. For sample 1: v_P = 6150 ± 15 m/s and for sample 2: v_P = 6325 ± 10 m/s. The average horizontal compressional wave crosshole velocity for the top region of the borehole was shown to be approximately 6100 m/s (Fig. 4.5). Thus, the maximum vertical sonic velocities and the horizontal crosshole velocities are approximately equivalent to that of homogeneous limestone (from laboratory measurements). These facts suggest that the approximation of $\alpha_2 = \alpha_3$ is not unreasonable and seems entirely plausible from observations of the quarry wall. Having proven in section 4.6 that approximately 10% of the compressional wave velocity anisotropy is open fracture related, enables one to proceed to calculate a normal fracture compliance from the compressional wave seismic crosshole data, at a dominant frequency of ~2 kHz, using equation 1.23. Using this methodology, from figure 4.11, the normal fracture compliance which corresponds to an open fracture related P-wave velocity anisotropy of 10% is: Z_N = 2.6 x 10^{-12} Pa^{-1}. The open fracture histograms in figures 3.8 – 3.10, in Chapter 3, revealed between 2 – 4 fractures over the 0.4 metre distance between the two receivers of the sonde, i.e. between 5 – 10 fractures/metre. Using equation 1.16 (Xu and King, 1992), the normal compliance of a single fracture at this site is estimated as:

$$\frac{2.6x10^{-12}}{10} \leq Z_N \leq \frac{2.6x10^{-12}}{5}$$

$$\Rightarrow 2.6\text{x}10^{-13} \leq Z_N \leq 5.2\,\text{x}10^{-13} \text{ m/Pa}$$

By assuming that the test site is transversely isotropic, having shown that the calculated fracture density value ε_f of 0.035 (Hudson, 1980, 1981; Crampin, 1984) is open fracture related, allows one to calculate a fracture compliance value from the fracture density (Eq.

1.22). For dry cracks with input parameters v_P = 6100 m/s; ρ = 2600 g/cm^3 and $v_S = \frac{v_P}{1.88}$, the normal compliance of the open fractures at ~2 kHz is: $Z_N = 2.5x10^{-12}$ Pa^{-1} which corresponded with a compressional wave anisotropy of 10%. Again using equation 1.16 (Xu and King, 1992), the normal compliance of a single fracture at this site is estimated as:

$$\frac{2.5x10^{-12}}{10} \leq Z_N \leq \frac{2.5x10^{-12}}{5}$$

$$\Rightarrow 2.5\text{x}10^{-13} \leq Z_N \leq 5.0\,\text{x}10^{-13} \text{ m/Pa}$$

Thus, the normal fracture compliance of the open fractures at a dominant frequency of ~2 kHz at the Tytherington field site is:

$$Z_N = (3.90 \pm 1.35)\,\text{x}10^{-13} \text{ m/Pa}$$

This value is wholly consistent with the normal fracture compliance value obtained from the compressional wave sonic wireline data in Chapter 3, which was $Z_N = (4.84 \pm 2.57)$ x10^{-13} m/Pa. As it is assumed that the sub-horizontal open fractures are the most compliant, the tangential compliance Z_T value is not critical at normal incidence.

4.9 Conclusion

In Chapters 3 and 4 the same scale of fractures has been investigated and the normal fracture compliance has been estimated in a number of different ways to increase confidence in the error estimates. A value for compressional wave normal compliance at seismic frequencies (~2 kHz) has been calculated, and it was shown to be similar to that

obtained from the wireline sonic velocities at borehole sonic frequencies (~23 kHz). The following chapter is a description of a separate study performed at Tytherington to investigate the effect of the fractures on seismic transmission amplitudes.

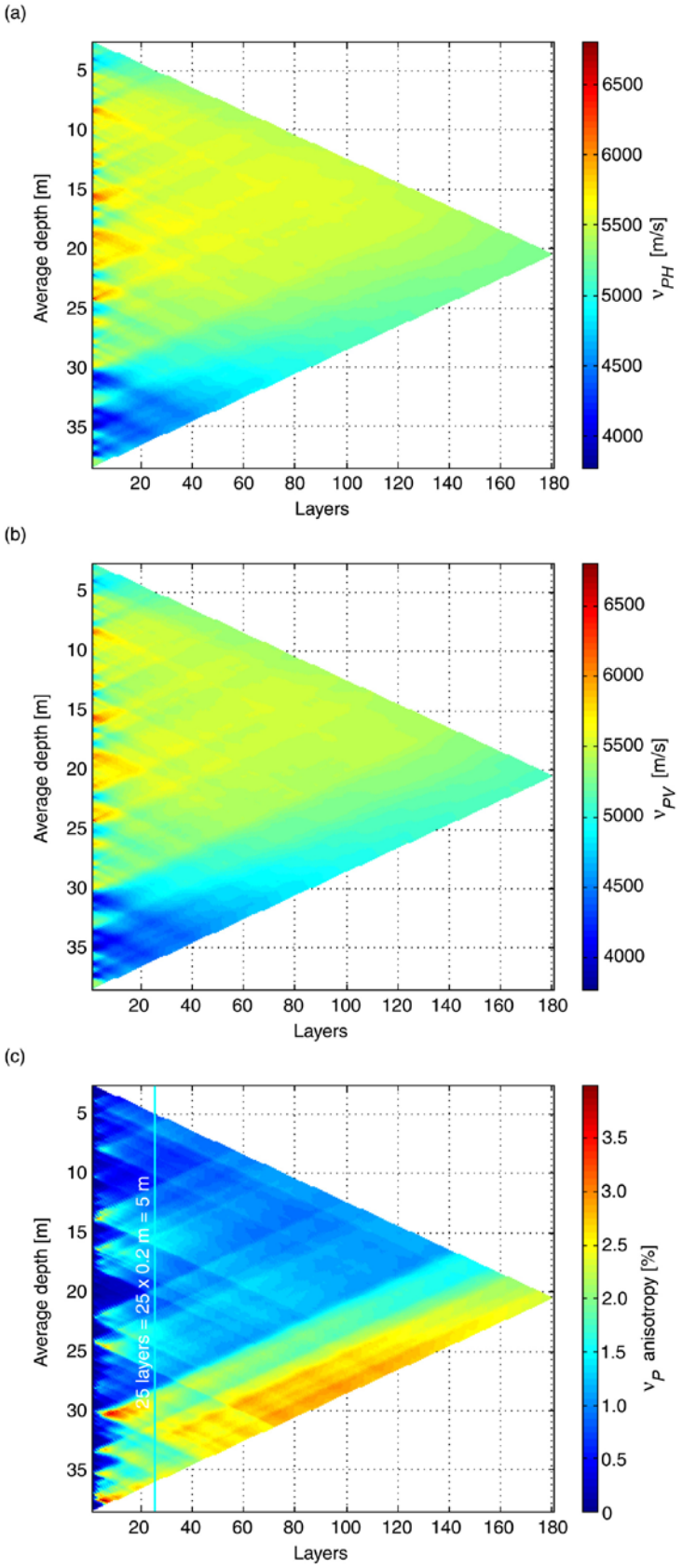


Figure 4.6: Backus average for BH 2 for all sonic velocity layer combinations. (a) Horizontal propagating P-wave; (b) Vertically propagating P-wave; (c) P-wave velocity anisotropy calculated using (a) and (b).

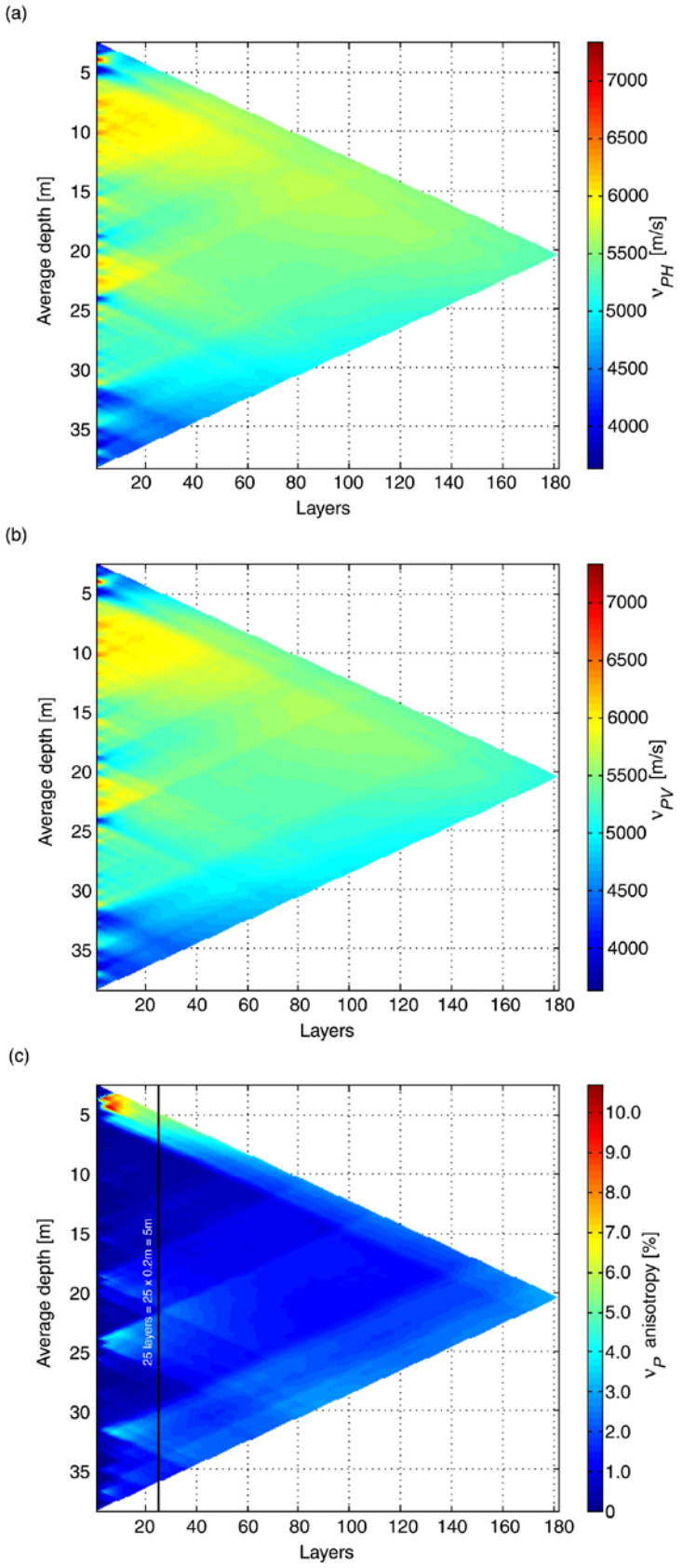


Figure 4.7: Backus average for BH 3 for all sonic velocity layer combinations. (a) Horizontal propagating P-wave; (b) Vertically propagating P-wave; (c) P-wave velocity anisotropy calculated using (a) and (b).

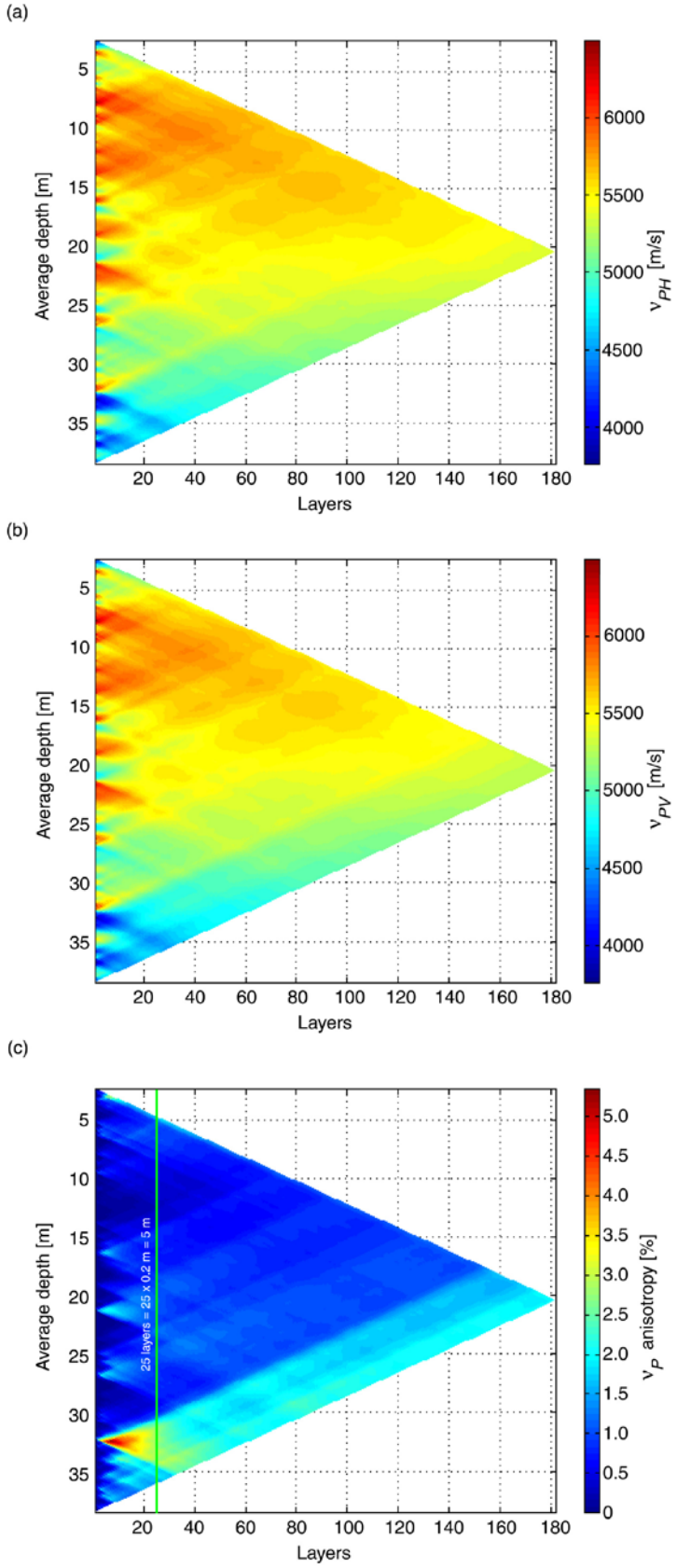


Figure 4.8: Backus average for BH 4 for all sonic velocity layer combinations. (a) Horizontal propagating P-wave; (b) Vertically propagating P-wave; (c) P-wave velocity anisotropy calculated using (a) and (b).

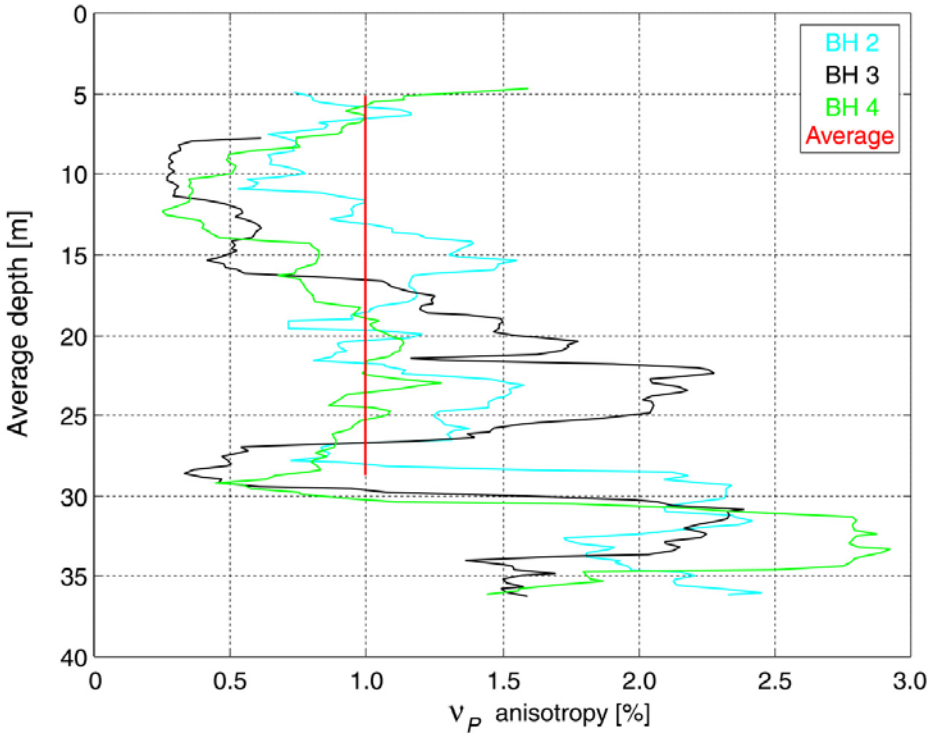


Figure 4.9: Cumulative P-wave velocity anisotropy for the three boreholes using 25 layers at a time.

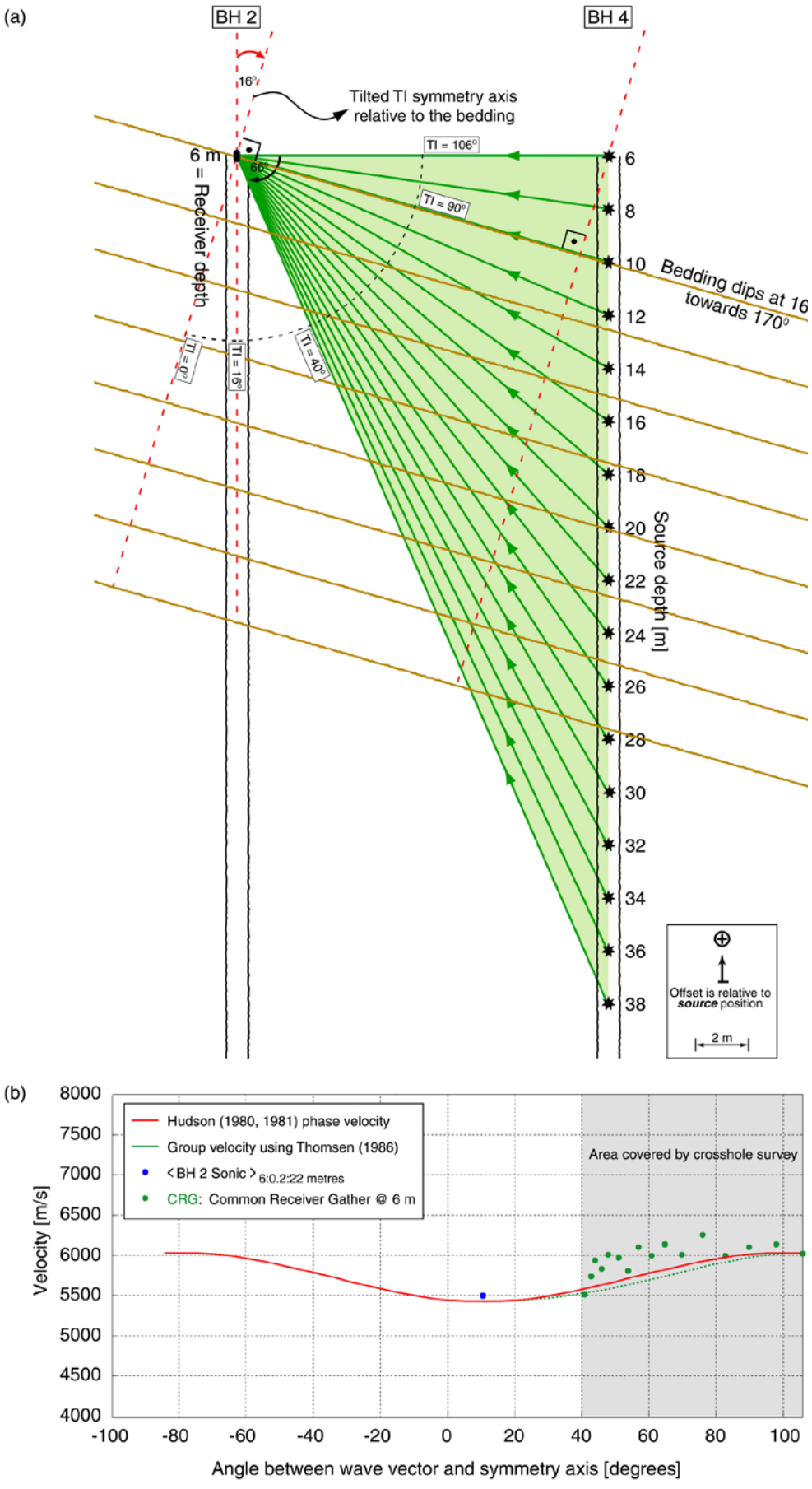


Figure 4.10: Calculating the fracture density. (a) Common receiver gather at a depth of 6 metres down BH 2 used to calculate the difference travel times between BH 3 and BH 2. Superimposed is the geometry of the tilted transversely isotropic (TI) symmetry axis relative to the bedding (dipping at 16° towards 170°); (b) Group velocities calculated from the difference travel times (in green), versus the theoretical phase velocity variation, versus angle between the wave vector and the symmetry axis in a TI medium (in red). The group velocity (dotted green) is shown for the positive angles only. The average (81 velocities) sonic velocity in BH 2 between 6 m and 22 m is shown in blue.

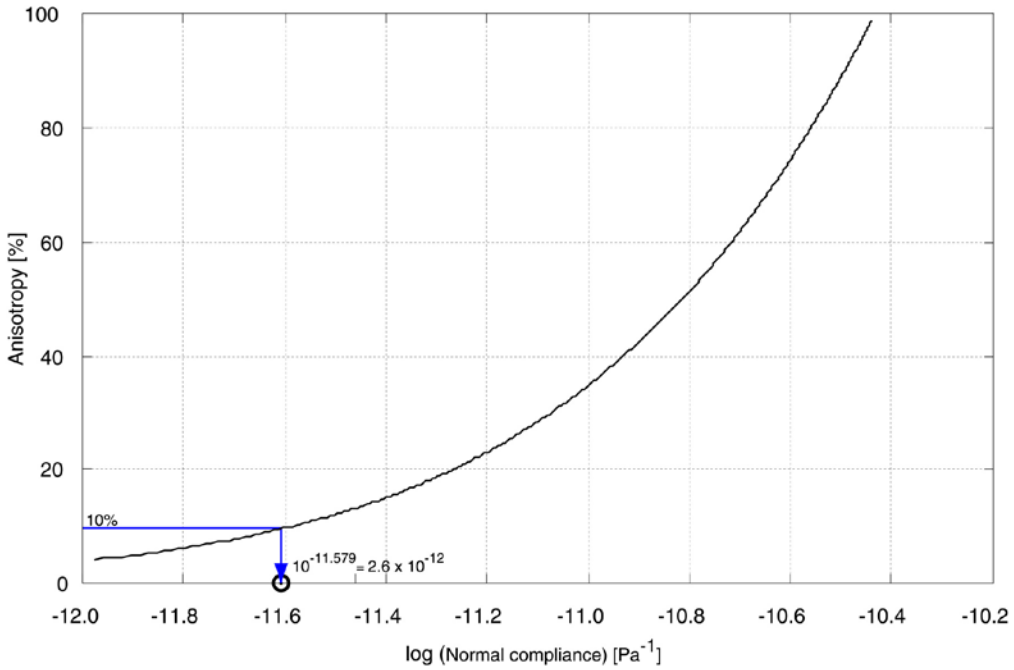


Figure 4.11: Analytical modelling performed to calculate the normal fracture compliance value, by assuming that the 10% anisotropy observed at the Tytherington field test site in the top 28 metres is open fracture related (Schoenberg and Sayers, 1995). It is assumed here that $Z_N = Z_T$.

Chapter V

Tytherington Quarry - Crosshole Amplitude Study

5.1 Introduction

It is well established that fractures in rock can have a significant effect on wave attenuation. In fact, most proposed attenuation mechanisms, such as friction across the surfaces of microcracks, microscopic flow (Biot 1956a, 1956b), inter-crack squirt flow (Mavko and Nur, 1975; O'Connell and Budiansky, 1977), intra-crack flow (Mavko and Nur, 1979), and scattering, are associated with microcracks and/or macrofractures.

This chapter is a description of the compressional wave amplitude studies at Tytherington quarry, which were performed to investigate the effect of fractures on seismic transmission amplitudes. The main purpose of this study was to investigate the possible frequency dependence (or frequency independence) of Q_P, and to then obtain a reasonable compressional wave Q_P estimate at this test site. A spectral averaging technique, performed over different time windows, was employed for this purpose. An anisotropic seismic wave attenuation analysis was also carried out to investigate the possibility of Q_P being dependent on angle.

5.2 Receiver calibration

Before any systematic and accurate amplitude analysis between two boreholes could be performed, it was necessary to first calibrate the receivers by observing how the recorded signal differed when recorded at the same depth with different hydrophones (OYO and

BGS). The only required assumption was that the sparker source was repeatable as was observed over the 102 shots fired during the crosshole survey.

The source was deployed in BH 2 at a constant depth of 26 metres whilst the OYO and BGS hydrophone strings were deployed in BH 3 at a depth interval 16:2:30 metres. Three shots were recorded for each hydrophone string which were later stacked. This allowed for the comparison of 8 stacked recordings at the same position with 2 different hydrophone strings. The sampling interval was 125 μs, resulting in a Nyquist frequency of 4 *kHz* . Figure 5.1 shows the stacked amplitude spectra (solid curves) up to the Nyquist frequency over this depth interval for the two instruments. The high frequency fall-off is due to an anti-aliasing filter applied to the data, attenuating all frequencies above a corner frequency of ~2.5 kHz, avoiding contamination of the spectrum with frequencies above the Nyquist. The red and blue dotted curves are 3rd order polynomials, fit in a least squares sense, to the BGS and OYO stacked spectra. It can be seen that the curves are virtually identical which indicates that the response of the two different tools were consistent over the bandwidth of the data.

5.3 Spectral processing

It was assumed that the rock mass in between the boreholes was spatially heterogeneous. Factors such as the internal saturation, porosity, permeability and microstructure of the rock grains and fractures may be the cause of the complex coda, which was also pointed out in Chapter 4. Consequently, it was extremely difficult to isolate the first compressional arrival wavelet. The analysis was performed instead on the first arrival compressional wavetrain with a much longer window length. This procedure allowed for averaging techniques (stacking) to be employed effectively using different vertical

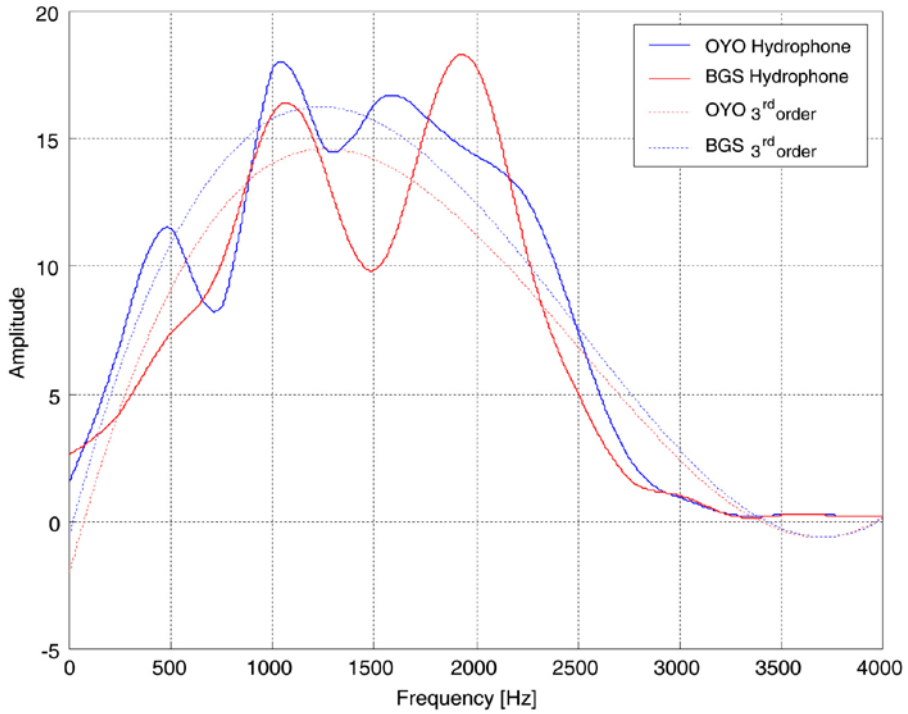


Figure 5.1: Stacked amplitude spectra of the OYO and BGS hydrophone receivers for identical ray paths. The source was in BH 2 at a depth of 26 metres. The OYO and BGS hydrophone receivers were deployed alternatively at a depth of 16 metres to 30 metres in BH 3, with an interval spacing of 2 metres. The corresponding dotted colour coded curves are least squares fit, 3rd order polynomials and are virtually identical over the bandwidth.

source-receiver offset gathers and different time window lengths as the compressional wave propagated in-line between BH 3 and BH 2. The source was deployed in BH 4 and the BGS and OYO hydrophones strings were deployed in BH 3 and BH 2 respectively as described in Chapter 4. As mentioned before, this geometry enabled difference amplitudes to be measured between two similar recording instruments, rather than isolated recording events containing associated source radiation pattern and coupling uncertainties.

Figure 5.2 is an outline of the methodology followed in obtaining an effective Q estimate from the crosshole survey, from the recorded first arrival P-wavetrain. To investigate any

angular dependence of the attenuation, the crosshole data were first sorted into common source-receiver offset gathers, and the traces were then horizon flattened to 10 ms (the preset trigger delay) using the first arrival P-wave energy picks. Care was taken in selecting the time window to only select the first arrival P-wavetrain energy contained within the recorded wavefield, and not energy from other recorded waves such as shear waves, head waves, guided waves and borehole generated tube waves. A filter was then constructed based on the selected time window. To improve the resolution of the amplitude spectrum in the frequency domain, the filtered traces were padded with zeros either side of the filtered window in the time domain before applying a Fast Fourier Transform. The spectra were stacked in the frequency domain to obtain a mean statistical average effect of the fractures on the ray paths within the specific common offset gather, which is necessary to give a stable estimation of the attenuation (Neep et al., 1996). A geometrical spreading correction was finally applied to account for the difference in propagation distance between the two boreholes.

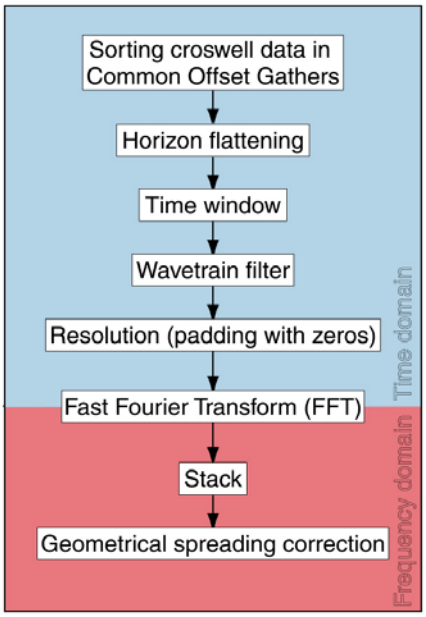


Figure 5.2: Flowchart outlining the methodology followed in the amplitude processing.

Figure 5.3 (a) shows a horizon flattened, zero offset gather from 10 ms - 70 ms as recorded with an OYO hydrophone string deployed in BH 4 with the sparker source in BH 2 from 6 m - 38 m with a 2 m interval spacing. The high amplitude, low frequency tube wave with a linear moveout, ultimately limiting the width of the time window, is shown in green. Figure 5.3 (b) is an enlarged section of the time window corresponding to the red rectangle between 10 ms and 20 ms in Figure 5.3 (a) showing the character of the first arrival compressional wavetrain energy used in the analysis. The tube wave arrival can clearly be seen at approximately 19 ms at a receiver depth of 6 metres down the borehole. The compressional wavetrain time windows, of different lengths, are shown to the left of the data. It can be seen that the corner of the time windows are 10-10-12-13 ms (green), 10-0-13-14 ms (blue) and 10-10-14-15 ms (red) respectively. The upper-end of the time window is indicated by colour coded dotted lines on the zero offset gather showing the effective selected wavetrain.

Figure 5.4 shows the result of an investigation into the angular dependence and the effect of the choice of the time window on the stacked amplitude spectra. The data were sorted into common ray angle gathers with ray angles of +45º, 0º and -45º, and the processing was carried out as outlined in Figure 5.2. The result was the stacked spectra for the BGS (solid lines) and the OYO (dotted lines) hydrophone strings using the three different time windows at three different ray angles. The shape and the magnitude of the respective stacked BGS/OYO spectral ratios are consistent over the bandwidth for the different ray angles. This anisotropic attenuation analysis shows that there is no observed angular dependence of Q between the boreholes and also that the spectra are relatively insensitive to the choice of the time window. For this reason any subsequent amplitude spectral analysis was performed using the stacked zero offset common ray angle spectra (Fig. 5.4

(b)). Figure 5.5 shows the average BGS (red) and OYO (blue) stacked spectra of the three time windows from the zero offset common ray angle gather shown in figure 5.4 (b). The error bars on the average BGS and OYO spectra correspond to the amplitude deviation of the respective stacked spectra at a sampling interval of ~38 Hz. The maximum energy is at approximately 2 kHz, which is the dominant source signal centre frequency.

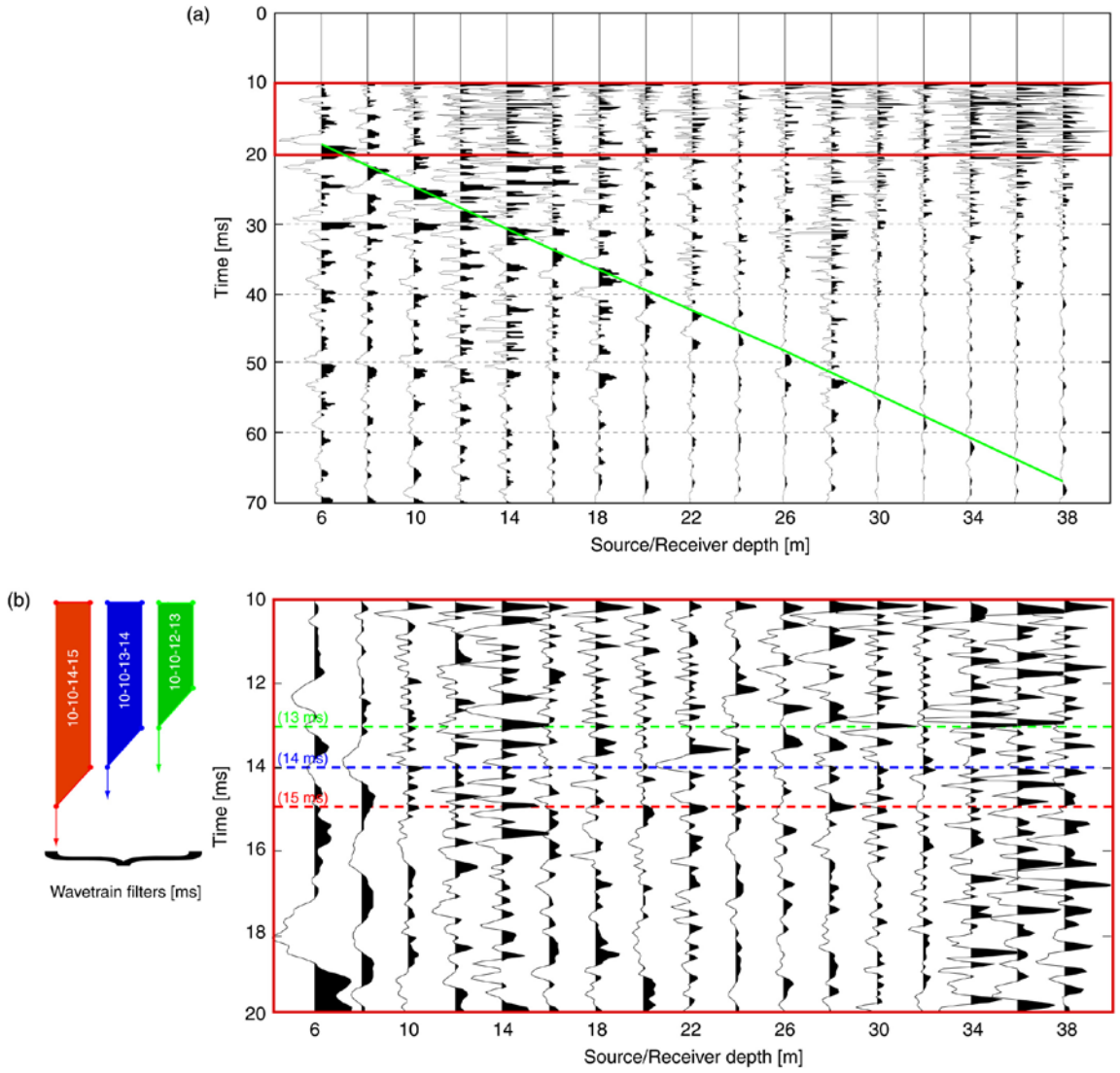


Figure 5.3: Analysis of the first arrival compressional wavetrain (horizon flattened). (a) A zero offset gather with the source and the OYO hydrophone string deployed in BH 2 and BH 4 respectively. The high amplitude, low frequency tube wave, ultimately limiting the width of the time window, is shown in green; (b) Enlarged time window corresponding to the red rectangle between 10 ms and 20 ms in (a) with the time domain filters used on the left.

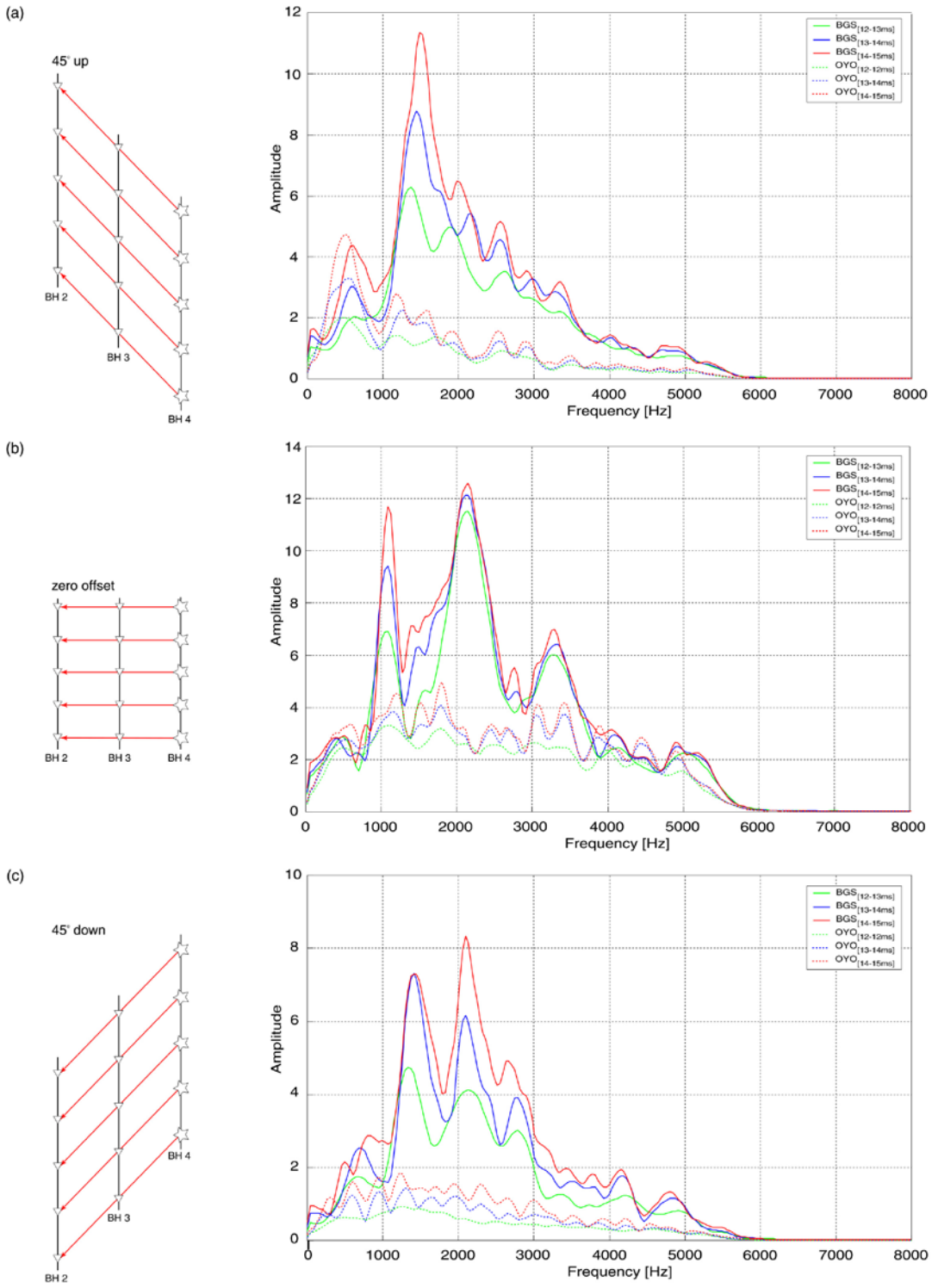


Figure 5.4: Spectra of the stacked common ray angle gathers sorted with respect to vertical source-receiver offsets to investigate the angular dependence of effective Q as well as the choice of the time window. (a) Offset = +14 m; resulting in ray angles of +45º; (b) Zero offset common ray angle gather; (c) Offset = -14 m; resulting in ray angles of -45º. The sketches on the left in (a), (b) and (c) depict the source-receiver geometries used to obtain the spectra on the right.

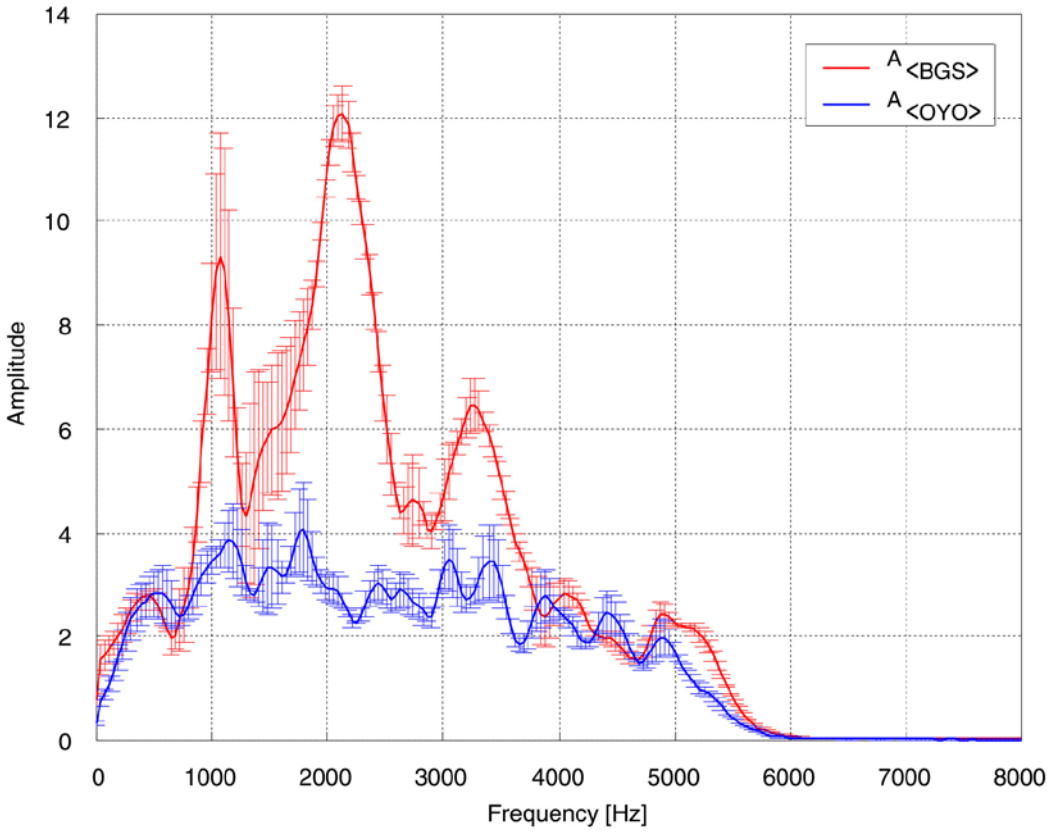


Figure 5.5: Average BGS and OYO stacked spectra of the three time windows from the zero offset common ray angle gather shown in figure 5.4 (b).

5.4 Q dependence on frequency

No consensus has been reached on whether Q is frequency dependent or not within the seismic frequency band (10 Hz – 10 kHz). The possibility of the Q being independent of frequency was first investigated. On this assumption, in terms of the distance travelled by the wave x, and the velocity of the medium v:

$$A_{OYO}(f) = k_x A_{BGS}(f) e^{-\pi f \Delta t / Q} = k_x A_{BGS}(f) e^{-\pi f x / Qv} = k_x A_{BGS}(f) e^{-\alpha x} \qquad (5.1)$$

where,

$\alpha = \dfrac{\pi f}{Qv}$ = the attenuation coefficient [dB/cm]

k_x = the frequency independent geometric factor that allows for the changes in pulse magnitude with the distance of propagation due to spherical divergence

Computation of the spectra of the wavelet and evaluation of the natural logarithmic ratio yields an equation of a straight line over a finite frequency range:

$$\ln\left(\frac{A_{OYO}}{A_{BGS}}\right) = -\frac{\pi\Delta t}{Q} f + \ln k_x \qquad (5.2)$$

Figure 5.6 shows the results of the forward modelling performed in which the OYO amplitude spectra is predicted from equation 5.1, by assuming Q values as shown in the legend. The solid lines are the average stacked zero offset spectra, and the dotted lines are the predicted OYO spectra. This shows that the constant frequency assumption fails to predict the observed spectral behaviour between BH 3 and BH 2 at the Tytherington quarry field site, and the likely possibility of Q being frequency dependent was therefore further investigated.

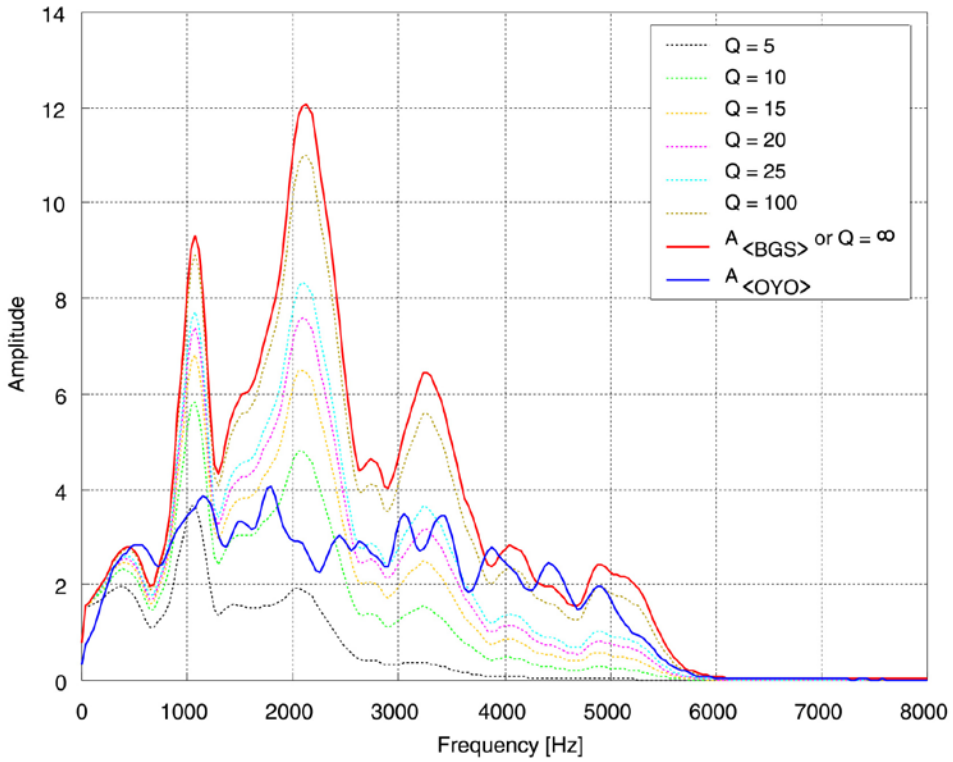


Figure 5.6: Forward modelling result assuming frequency independent Q. The solid lines are the average stacked zero offset spectra, and the dotted lines are the predicted OYO spectra from the BGS spectra assuming constant Q values, as shown in the legend.

A separate study was performed in which no assumptions were made about the frequency dependency of Q. Using the real, stacked BGS and OYO zero offset spectra in equation 5.2, ensuring that the log spectral ratio is zero at zero frequency, (by eliminating the $\ln k_x$ term), Q^{-1} was then plotted against frequency for 1 kHz $\leq f \leq 4$ kHz (Fig. 5.7). The constant $\ln k_x$ term acts only as a DC shift that does not affect the slope of the curve and therefore does not affect the value of Q. For frequencies approximately below 1 kHz errors become very large because one is measuring the effect as sampled by a fraction of one seismic wavelength. The upper limit represents the crosshole Nyquist frequency. The error limits were defined by:

$$Error_{\pm} : \ln\left(\frac{A_{OYO} \mp \mathrm{E}}{A_{BGS} \pm \mathrm{E}}\right) = -\frac{\pi \Delta t}{Q} f \qquad (5.3)$$

where,

E = minimum or maximum error value of OYO or BGS error bar (see Fig. 5.5)

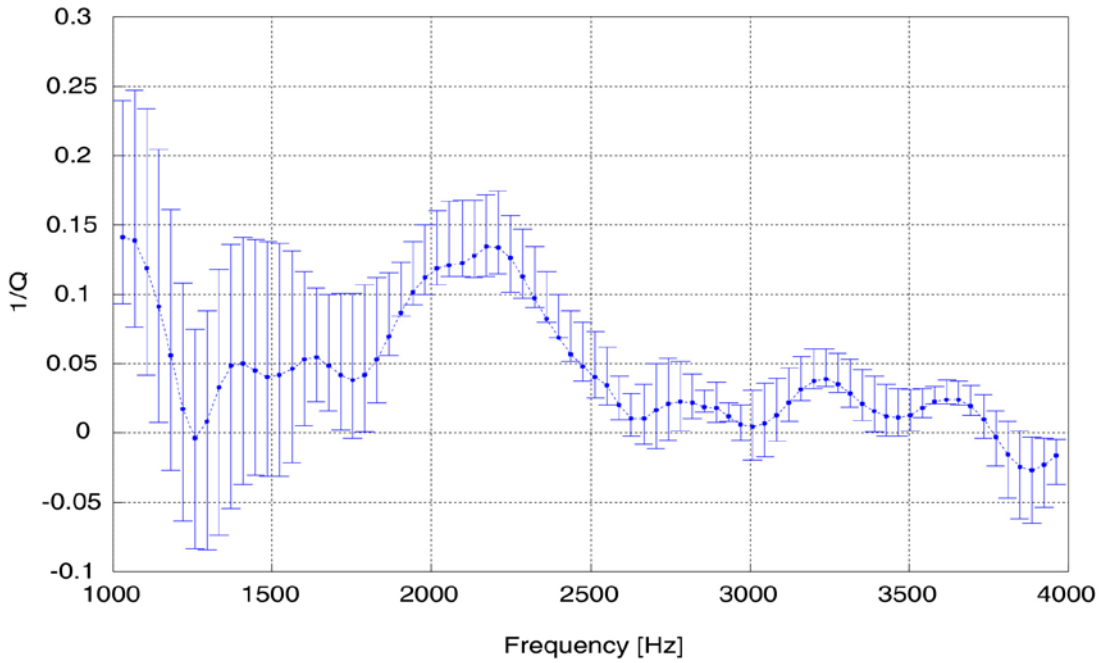


Figure 5.7: Frequency dependent Q from the average stacked zero offset spectra.

5.5 Discussion

This anisotropic attenuation analysis shows that there is no observed angular dependence of Q in the limestone site at Tytherington quarry. The Q values (Fig. 5.7) obtained are consistent with published results of Q from Carboniferous rocks within the investigated frequency range. King and Shams-Khanshir (1998) reported Q values in the range $14 \leq Q < 28$ from measurements on 34 limestone samples from a Carboniferous limestone field site in northern England. These values were also consistent with the isotropic intrinsic Q estimates ($Q \approx 20$) from a crosshole survey for the same site using spectral ratio averaging techniques (Portsmouth et al., 1993). However, it is far from certain that the causal attenuation mechanism is the same in all these studies.

The dependence of Q with frequency (Fig. 5.7) is very unlikely to be a mesoscopic-scale effect (scales greater than grain sizes but smaller than the seismic wavelengths) as described by Pride et al. (2004). Nor is it likely to be a squirt flow effect (fluid flow from crack to pore) as postulated by Sams et al. (1997). Both these phenomena predict variations in Q with frequency that are normally distributed over several decades. Measurements of Q on samples from Tytherington quarry, described in Chapter 2, have shown that the intrinsic compressional wave Q is greater than 70 (Fig. 2.17). It is therefore proposed that scattering attenuation might be a dominant mechanism controlling the observed attenuation seen in the data at this field site.

Vlastos et al. (2003) modelled the effect of different fracture spatial distributions, different fracture scale lengths compared to the seismic wavelength and also a fractal distribution of fracture sizes, on seismic wave propagation through the rock mass, by treating the fractures as highly compliant slip interfaces. They concluded that fracture

clustering results in high local fracture densities, which can cause energy to be trapped in certain areas, severely increasing the complexity of the wavefield by introducing resonant peaks into the Fourier spectra. Figure 5.8 shows how different distributions affect multiple scattering. The character of the wavelets and the amplitude spectra closely resembles that seen at the Tytherington field site. The frequency here is lower than the crosshole seismic frequencies from the Tytherington field survey, but by assuming that fractures are fractal, it is plausible to assume that their numerical code would predict the same effect at frequencies in the region of ~2 kHz. They also point out that effective medium theories must be used with caution, since scale lengths and fracture spatial distributions are not properly treated in such theories.

This study highlights the problems that can occur when modelling and interpreting seismic attenuation data. Pride et al. (2004) conclude that the squirt mechanism produces a great deal of attenuation at ultrasonic frequencies used in laboratory measurements but is incapable of explaining the level of loss ($10^{-2} < Q^{-1} < 10^{-1}$) within the seismic band of frequencies ($1 - 10^{4}$ Hz). In contrast, mesoscopic-scale models easily produce enough attenuation to explain the level of loss in seismic field data and the rate at which the mesoscopic-scale fluid pressure equilibrates is a strong function of the permeability of the porous material. The rate at which microcracks equilibrate with the main pores in squirt flow is on the other hand not permeability dependent. This leaves open the possibility of extracting permeability information from the frequency dependence of seismically measured Q. However, at the present time, techniques that can reliably separate the intrinsic and scattering attenuation are generally not available.

In the following chapter I return to the main theme of this thesis and estimate an additional field scale normal fracture compliance value from a different field site located in Cornwall (UK). The hydraulically conductive open fractures at this test site resulted in a significant increase in transmission travel times, and were associated with an anomalously high compressional wave velocity anisotropy (>30%).

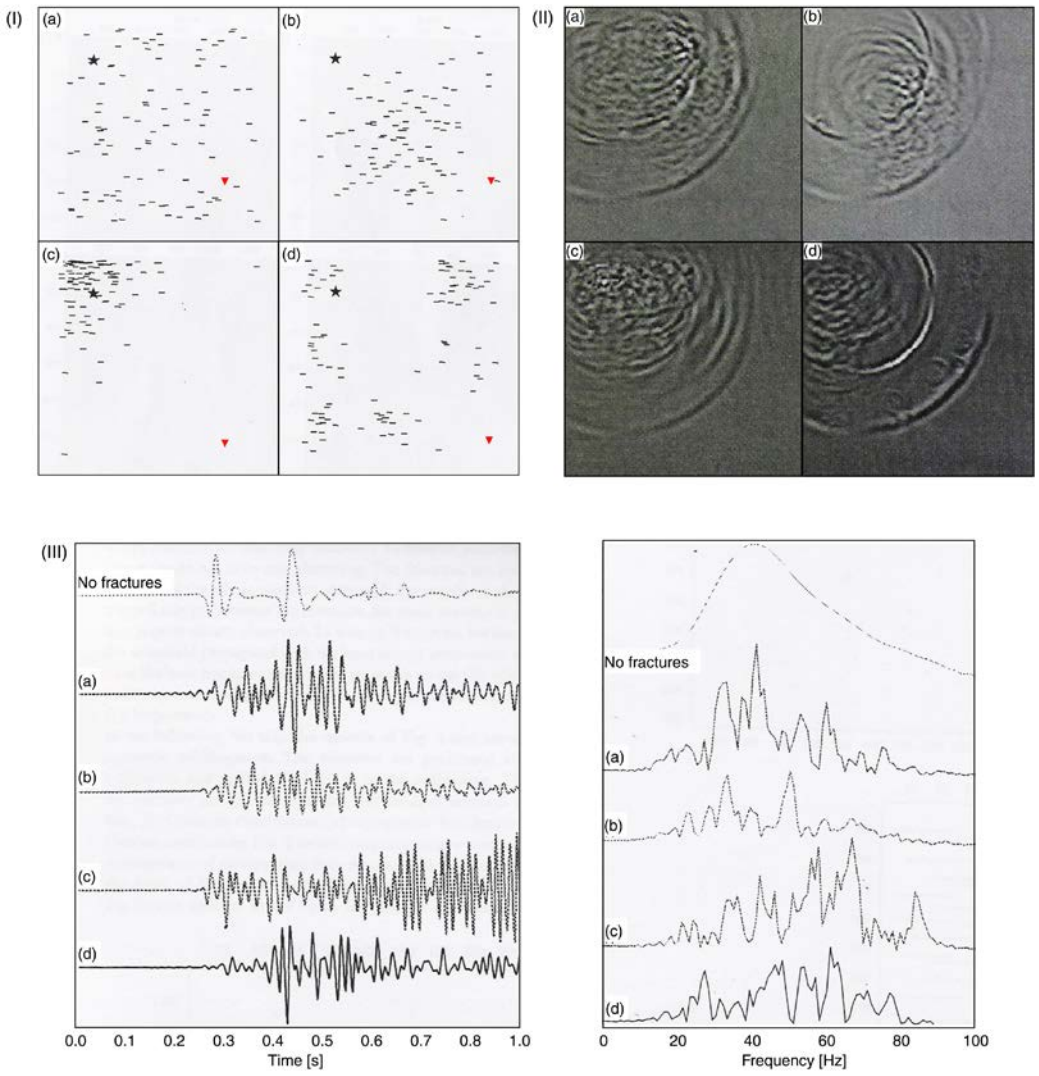


Figure 5.8: Numerical modelling results in a media with discrete spatial distributions of fractures (after Vlastos et al., 2003). (I) Different modelled spatial distributions: (a) Uniform, (b) Gaussian, (c) Exponential, (d) Gamma distribution. The source (star) and receiver (triangle) is also shown; (II) Snapshots (a) to (d) correspond to fracture distributions (a) to (d); (III) Synthetic seismograms and corresponding spectra for fracture distributions (a) to (d) for the x-component of motion, which are recorded at the positions of the red triangles.

Chapter VI

Reskajeage Quarry

6.1 Introduction

The field data presented in this chapter were acquired at a previous Imperial College field test site. The research formed part of a major hydro-geological research programme centred on the characterisation of fracture networks and the modelling of groundwater flow through fractured rock. The hydrological program was funded by United Kingdom Nirex Limited (Nirex) and the field scale experiments were undertaken by AEA Technology and Dr. J. V. Herwanger as part of his graduate studies at Imperial College London.

In this chapter, the work carried out by Herwanger (2001) is briefly described (section 6.2). Work related to this study is then described in section 6.3 and beyond. A fracture compliance is calculated from the open fracture related fracture density ε_f obtained from modelling a low velocity, high anisotropy zone as aligned open fractures within an anisotropic rock matrix with an inherent rock fabric anisotropy of 20% (Hudson, 1991). In addition, a fracture compliance is also obtained by attributing the fluctuations in the crosshole velocity in this fractured zone to open fractures (using Eq. 1.27). Furthermore, as a check to see whether the amplitude behaviour could be explained by the compliance estimates calculated from the transmission travel times, a fracture compliance is calculated from modelling the transmission amplitudes.

6.2 Reskajeage test site

The Reskajeage quarry borehole test site in Cornwall (UK) was developed for the purpose of understanding the nature of fluid-flow in a fracture dominated hydrogeological environment. Large amounts of hydrological and geological data have been acquired at this site (Baker et al., 1999; Jefferies et al., 2000; Holton and Jefferies, 2001). The site was chosen because of the high density of water conducting fractures at shallow depth (10 m - 30 m) beneath the quarry floor. Two, unlined, near vertical boreholes (designated BH 19 and BH 20) have been drilled approximately 25 m apart, to depths up to 300 m into the Mylor Slate Formation, a marine metasediment of Upper Devonian age. The formation comprises a variable succession of medium- to dark-grey slates with silty laminae, thinly-bedded, fine-grained sandstones, coarse-grained turbiditic sandstones, fine-grained massive sandstones and black mudstones. The lithological description of the rocks shows a vanishingly small porosity, confining the dominant fluid flow and permeability of the rock mass to the heterogeneous distribution of open fractures.

Many open fractures, in addition to sealed, predominantly quartz cemented veins, have been identified from fully oriented core and impression packing. The predominant fracture set strikes NE - SW, moderately dipping (~30º) to the SE, which is approximately the direction from BH 20 to BH 19. These fracture planes cut the bedding at angles of 10º – 20º. The average open fracture frequency, calculated on the basis of 1 m intervals down BH 19 and BH 20 was ~1.5 fractures/m with up to 8 fractures/m recorded in highly fractured regions. A sandstone unit between 50 m and 70 m depth in BH 20 was particularly sparsely fractured. A second fracture set strikes E - W, with a gentle or moderate dip to the north, and a smaller number of steeply dipping fractures strike broadly NNE - SSW. As at Tytherington, the vertical plane through BH 19 and BH 20 at

Reskajeage is at right angles to the strike of both the bedding planes and the dominant fracture sets, which is some justification for obtaining two-dimensional crosshole resistivity and seismic data.

To derive hydraulic transmissivity logs a single double packer system has been employed with an interval spacing of 5 m in the shallow part of the boreholes and a 1 m spacing in the deeper part of the boreholes (Jefferies et al., 2000). The observed transmissivities, as a function of depth for the boreholes BH 20 and BH 19, are plotted as bar-charts in figures 6.3 (a) and (f), with each bar representing the transmissivity from one single injection experiment. Note that the cube-root ($\sqrt[3]{T}$) of the observed transmissivities is plotted. This is a convenient graphical scaling device, as transmissivity is proportional to the third power of average fracture aperture or 'openness' of the fracture along the fracture plane as shown by Brown (1987).

Using a pulse transmission technique, compressional wave velocities were also measured for a suite of core samples from BH 20, at ambient temperature and pressure at a frequency of 0.8 MHz, by Dr. J. Khazanehdari at Reading University, **P**ostgraduate **R**esearch **I**nstitute of **S**edimentology (PRIS). The errors for the vertical and azimuthal velocity measurements were 3% and 4% respectively (Dr. J. Khazanehdari, personal communication, April 4, 2005). The arrows against the depth axis in figure 6.3 (b) indicate the location of the core samples that have been analysed. The core samples analysed had porosities of less than 3% and negligible permeabilities of less than 0.01 mD. Velocity measurements were also obtained for both dry and saturated samples at elevated effective pressures up to 60 MPa at room temperature. Negligible differences were observed between these results and the results obtained under ambient conditions,

suggesting an almost complete absence of microcracks for these samples. Figure 6.1 shows the azimuthal velocity anisotropy, calculated from two orthogonal horizontal directions, and the vertical\horizontal velocity anisotropy. From figure 6.1 it can be seen that the average inherent vertical\horizontal velocity anisotropy is approximately 20% ($\varepsilon = \frac{v_{Fast} - v_{Slow}}{v_{Slow}} = 0.2$). The low value of the vertical\horizontal anisotropy at 53 m corresponds to a sample from the fine-grained, massive sandstone unit. The anisotropy is attributed to the preferred orientation of the micas, based on X-ray diffraction analyses of a number of core samples.

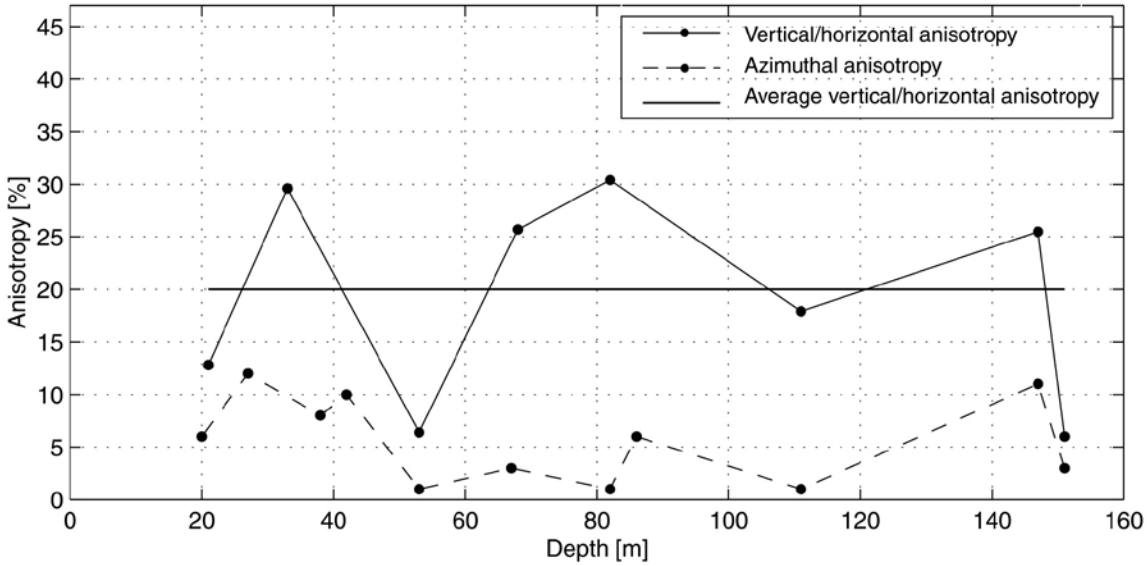


Figure 6.1: Core analysis of a suite of samples from BH 20. Velocity anisotropy of laboratory core samples versus depth down BH 20. Note the average vertical/horizontal anisotropy of 20% (Herwanger et al., 2004).

A seismic crosshole experiment was carried out between the two boreholes using a 48-channel hydrophone chain (BH 19) and an electrical sparker source (BH 19) by Herwanger (2001). Figure 6.2 shows one common shot gather. The first arrival compressional wave could be picked to a high degree of accuracy. The pronounced borehole tube-waves with linear moveout originating from the first arrival curve are

generated when the direct compressional wave impinges on a dominant discontinuity in the receiver borehole (BH 20). These depths correspond to regions of relatively high hydraulic transmissivity. Clusters of these events in BH 20 occur between 15 m and 30 m, at 45 m, between 70 m and 75 m and at 105 m. Figure 6.3 (b and c) shows the optimal seismic velocity and anisotropy tomograms obtained with tomographic inversion code developed by Dr. R. G. Pratt from Queens University, Canada. Details of the inversion algorithm and methodology is not included since they are well documented in a number of papers including Chapman and Pratt (1992), Pratt and Chapman (1992), Pratt et al., (1993), Pratt and Sams (1996) and Kragh et al. (1996). The inversion result showed that the velocity structure of the rock at this test site was both inhomogeneous and anisotropic.

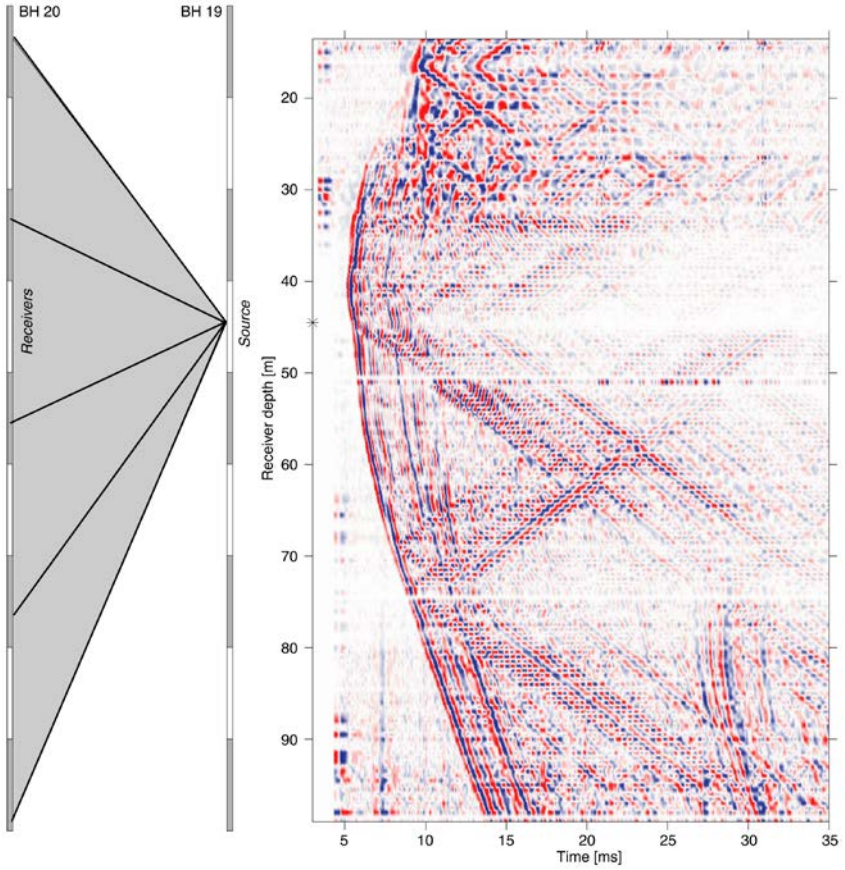


Figure 6.2: Reskajeage common shot gather. The source depth is at 44.5 m, indicated by an asterisk. Receiver depths range from 13.5 m to 99.0 m (172 traces). The sketch on the left depicts the source-receiver geometry. The illuminated region is shaded in grey. The first arrival energy can be clearly identified along the whole data set with a central frequency ~1.5 kHz (Herwanger et al., 2004).

In addition, an electrical crosshole survey was also performed between the two boreholes with a current electrode in BH 19 and a potential electrode in BH 20 using a pole-pole configuration. Figure 6.3 (d and e) shows the optimal electrical conductivity and electrical anisotropy tomograms obtained with tomographic inversion code. Computational issues are described in Pain et al., (2002) and a description of the algorithm and the inversion of the field data are presented in detail in Herwanger (2001) and Herwanger et al., (2004).

All subsequent analyses will be based on the data as shown in figure 6.3. In this figure, a fine-grained massive sandstone unit can be observed in BH 20 between 50 m and 70 m depth, and is identifiable as a zone with a high seismic velocity, near-zero seismic anisotropy, low electrical conductivity and a small electrical anisotropy. It also appears to thin towards BH 19. A band of low seismic velocity, high electrical conductivity, very high seismic anisotropy (most values in excess of 30%) and large electrical anisotropy can be seen between approximately 25 m – 40 m in BH 20 and 30 m – 50 m depth in BH 19, and is associated with relatively high values of hydraulic transmissivity in both boreholes. This corresponds to a dip of $\arctan\left(\frac{\Delta z}{\Delta x}\right) = \arctan\left(\frac{15m}{25.7m}\right) \approx 30°$, which is the dip of the dominant fracture set. A prominent band of high electrical anisotropy dips from approximately 35 m in BH 20 to 55 m in BH 19. In general, areas of high electric anisotropy coincide with seismically anisotropic areas, and an anti-correlation between electric conductivity and seismic velocity is observed, which is consistent with the observed fracturing or layering.

The percentage anisotropy for depths ≥ 50 m is fairly constant, with the zone of moderately high anisotropy values between 80 m and 100 m in BH 20, not nearly as distinct as the very high anisotropy zone in the upper-part of the boreholes. The seismic

velocity anisotropy observed below 50 m seems to be mainly attributed to the inherent anisotropy of the rock with a mean anisotropy value in the order of 20%, and it seems, therefore, that the observed anisotropy in this region can be largely explained in terms of the rock fabric.

6.3 Fractures in an anisotropic background medium

In order to interpret the prominent, very high seismic velocity anisotropy dipping zone in the fractured upper-part of the boreholes, it was assumed that seismic anisotropy was a superposition of the inherent anisotropy of the rock, and the anisotropy calculated for either dry or saturated open fractures. This anisotropy calculated for either dry or saturated fractures, was then assumed to be the contribution of the open fracture set to the total resultant seismic anisotropy in the highly fractured zone at this site.

The wavelengths of the Reskajeage field data were between 2 m and 5 m. It seems realistic to assume that the 8 identified open fractures per meter are within the bounds of the long wavelength assumption. The estimated parameters are therefore valid for a homogeneous, anisotropic, long wavelength equivalent medium.

Hudson (1991) showed that inherent material anisotropy is equivalent to a distribution of hypothetical cracks embedded in an isotropic background medium. The effect of microfractures in an anisotropic solid may then be calculated by imposing the hypothetical and real cracks, at any arbitrary angle, on an isotropic matrix. If an anisotropic material contains a distribution of cracks, then the net effect is equivalent to an isotropic material, with elastic constants c^0, containing two sets of cracks.

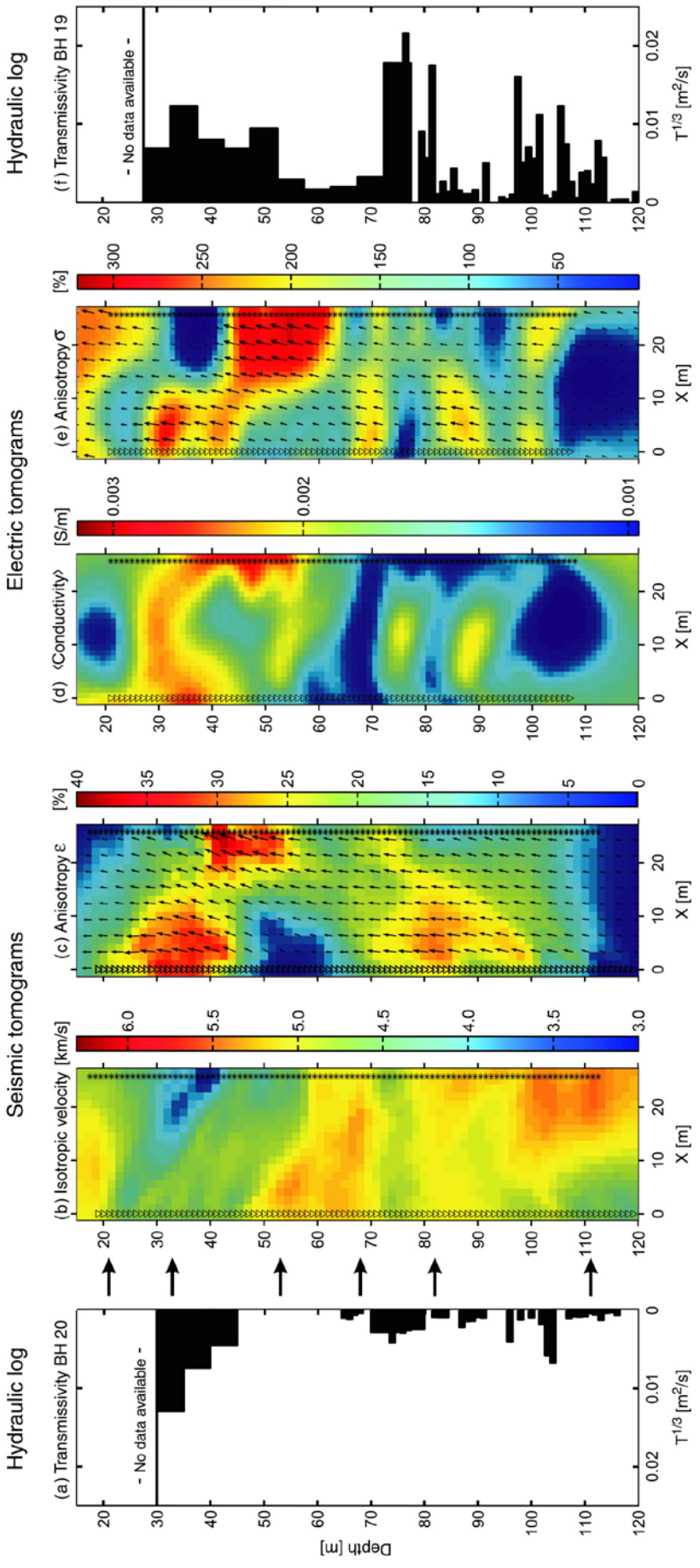


Figure 6.3: Hydraulic transmissivity data for the two boreholes and the optimal seismic and electrical tomograms. (a) and (f) are the transmissivity plots (cube root) for BH 20 and BH 19 respectively; (b) Isotropic velocity tomogram; (c) Seismic anisotropy tomogram; (d) Average electrical conductivity tomogram; (e) Electrical anisotropy tomogram. The direction of the arrows, on (c) and (e), indicate the directions of the symmetry axes of the assumed TI symmetry, whilst the length is proportional to the anisotropy. The source and receiver locations are depicted by asterisks (BH 19) and inverted triangles (BH 20), in figures (b) to (e) (Herwanger et al., 2004).

The hypothetical set gives rise to a first-order correction term c^1, with the second real set of cracks giving rise to a first-order correction term $\hat{c}^1$. The first-order correction due to the hypothetical and real cracks according to Hudson (1990) is: $c^1 + \hat{c}^1$ and the second order correction is then:

$$c^2 = \frac{1}{\mu_0}\left(c^1 + \hat{c}^1\right)\chi\left(c^1 + \hat{c}^1\right) \tag{6.2}$$

where,

$$\chi_{rskn} = \frac{1}{15}\left[\delta_{rk}\delta_{sn}\left(4 + \beta^2/\alpha^2\right) - \left(\delta_{rn}\delta_{sk} + \delta_{rs}\delta_{kn}\right)\left(1 - \beta^2/\alpha^2\right)\right] \tag{6.3}$$

with α, β and μ_0 the compressional wave velocity, shear wave velocity and shear modulus of the rock matrix respectively. The overall elastic constants correct to second order are:

$$c = c^0 + c^1 + \hat{c}^1 + \frac{1}{\mu_0}\left(c^1 + \hat{c}^1\right)\chi\left(c^1 + \hat{c}^1\right) \tag{6.4}$$

This is the elastic stiffness tensor of the anisotropic material with one set of randomly orientated fractures. After rotating the elastic stiffness tensor so that the x_3-axis lies along the axis of symmetry, as for VTI media in Thomsen (1986), one can then calculate the Thomsen (1986) anisotropy parameter ε using:

$$\varepsilon = \frac{c_{11} - c_{33}}{2c_{33}} \tag{6.5}$$

with c_{11} and c_{33}, two of the five elastic constants that define a medium with hexagonal symmetry.

The theory described by (Hudson, 1980, 1981) and Crampin (1984) is used to obtain a value of anisotropy of 20%, which is the mean value of the core samples, attributable to the rock fabric, and also the mean value of the anisotropic tomogram (Fig. 6.3 (c)). This

was achieved by modelling dry cracks with a fracture density of ε_f = 0.065. The input parameters v_P = 5500 m/s and ρ = 2400 g/cm^3 were obtained from the core data, whilst v_S was assumed to be $\frac{v_P}{1.7}$ m/s. These are the hypothetical cracks. From this calculation an effective medium with an inherent material anisotropy of 20% is obtained, which then serves as the anisotropic background medium into which the real fracture set is introduced.

In order to model the predominant, moderately dipping (~30º), open fracture set described in section 6.2, equation 6.2 is used to determine the elastic constants of a fractured anisotropic medium. Here $\hat{c}^1$ is the first-order correction term for a set of parallel dry fractures, and θ is the dip angle relative to the normal of the symmetry axis of the anisotropic background medium. Fracture densities are calculated up to ε_f = 0.1 as, again, the Hudson (1980, 1981) theory is not violated up to this value for the fracture density (Sayers and Kachanov, 1991). As the bedding planes dip at 10º - 15º to the SE, and the dominant hydrologically conducting fracture planes dip at approximately 30º in the same direction, the dominant open fracture set cuts the bedding planes at angles of approximately 10º to 20º.

Also, as recommended by Mavko et al. (1998), the theory of Brown and Korringa (1975) and Mukerji and Mavko (1994) is then used to calculate the elastic constants of the corresponding water saturated fractures in the anisotropic medium:

$$S_{ijkl}^{(dry)} - S_{ijkl}^{(sat)} = \frac{\left(S_{ij\alpha\alpha}^{(dry)} - S_{ij\alpha\alpha}^{0}\right)\left(S_{kl\alpha\alpha}^{(dry)} - S_{kl\alpha\alpha}^{0}\right)}{\left(\beta_{dry} - \beta_0\right) + \left(\beta_f - \beta_0\right)\phi} \tag{6.6}$$

where,

$$\beta_{dry} = S^{(dry)}_{\alpha\alpha\beta\beta} \frac{1}{K_{dry}}$$

$$\beta_0 = S^{0}_{\alpha\alpha\beta\beta} \frac{1}{K_0}$$

$$\beta_f = \frac{1}{K_f}$$

and $S^{(sat)}_{ijkl}$ the predicted saturated rock compliance, $S^{(dry)}_{ijkl}$ and S^{0}_{ijkl} the compliances of the dry rock and the mineral material, β_f and β_0 the compressibility of the pore fluid and mineral material and ϕ the porosity.

Figure 6.4 shows the total resultant P-wave anisotropy ε_{res}, which is the anisotropy from the background, and the anisotropy from the imposed dipping fracture set, for $0° \leq \theta \leq 35°$ and an imposed dipping fracture density $0.01 \leq \varepsilon_f \leq 0.1$ for dry (Fig. 6.4 (a)) and saturated fractures (Figs. 6.4 (b) – (d)). Case 'A' is the condition of dry fractures. Cases 'B', 'C' and 'D' are the results of applying the Brown and Korringa (1975) water saturation correction for fracture porosity values of ϕ = 0.05, 0.01 and 0.001 respectively. Fracture porosity is not reliably estimated in these experiments, so these values simply represent a plausible range. Also, the black dots (marked as 1 to 3 on each plot) are the Herwanger et al. (2004) resultant anisotropy values for θ = 0º (nr. **1**), θ = 10º (nr. **2**) and θ = 20º (nr. **3**) as outlined in table 6.1. It can be seen that there is considerable uncertainty in the anisotropy estimates. This uncertainty would increase if one were to include additional fracture sets with different orientations. However, the calculations show that values of total resultant P-wave velocity anisotropy near to or greater than 0.3 could be caused, at this site, by a fracture zone with a fracture density ε_f of 0.07 within a rock matrix with an inherent fabric anisotropy of 20%.

	1: θ = 0º	**2**: θ = 10º	**3**: θ = 20º
Case 'A' (dry)	0.40	0.38	0.34
Case 'B' (saturated; ϕ = 0.05)	0.36	0.34	0.30
Case 'C' (saturated; ϕ = 10^{-2})	0.28	0.27	0.25
Case 'D' (saturated; ϕ =10^{-3})	0.22	0.21	0.20

Table 6.1: Values of total resultant P-wave velocity anisotropy calculated for four scenarios of introducing cracks at an angle of θ relative to the symmetry axis into an anisotropic rock matrix (Herwanger et al., 2004).

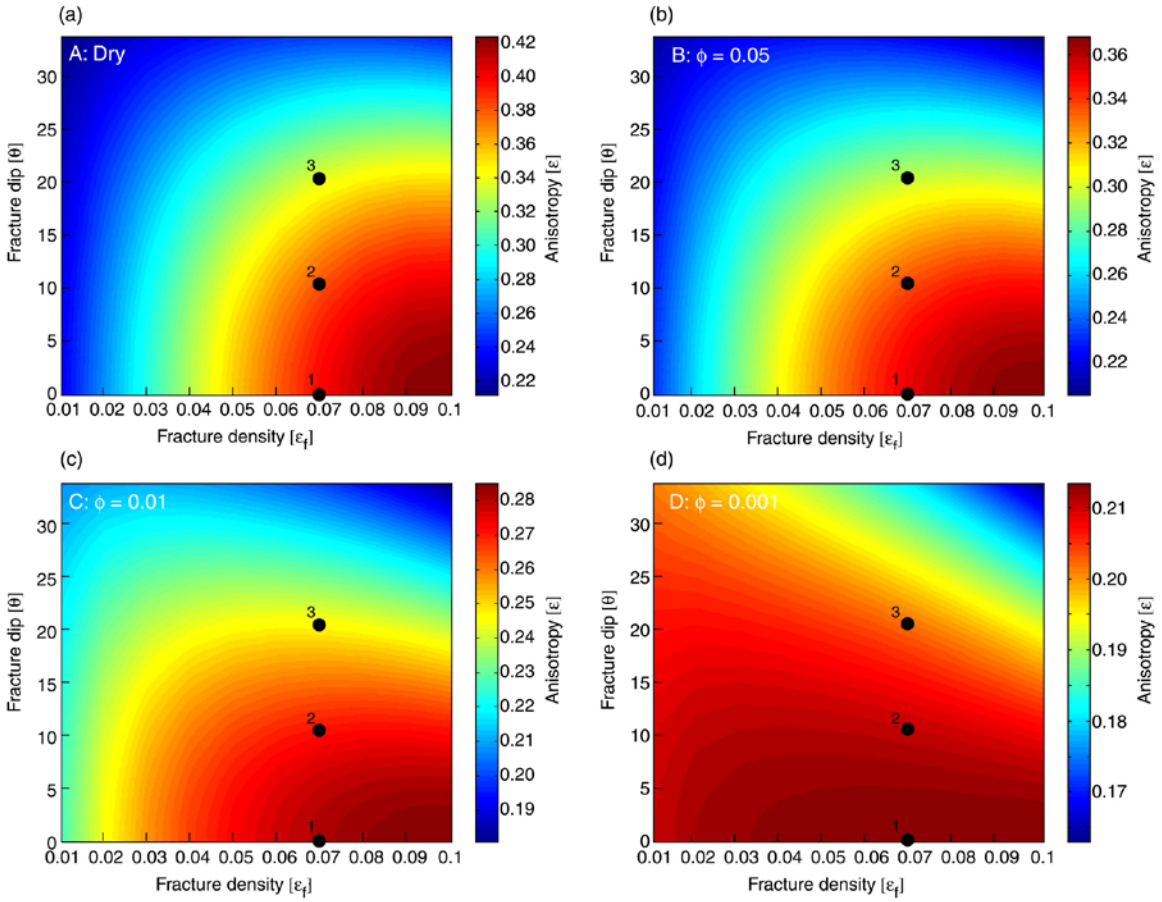


Figure 6.4: Total compressional wave anisotropy ε_{res}, as a function of the fracture density ε_f and dip θ of the imposed fracture on the anisotropic background medium. (a) Dry fractures; (b) Saturated fractures with ϕ = 0.05; (c) Saturated fractures with ϕ = 10^{-2}; (d) Saturated fractures with ϕ = 10^{-3}. See text for details.

6.4 Calculating the compliance and modelling the transmission amplitudes

6.4.1 Compliance from travel times

Assuming this value of ε_f = 0.07 to be open fracture related enables one to calculate a normal compliance for this field site using the Hudson (1980, 1981) or Crampin (1984) theory, again with input parameters: v_P = 5500 m/s; ρ = 2400 g/cm^3 and $v_S = \frac{v_P}{1.7}$ m/s for dry cracks in a TI medium following the approach outlined in section 1.2. The normal compliance of the open fractures at ~2 kHz was: $Z_N = 6.62 \text{ x} 10^{-12}$ Pa^{-1}, which corresponded with a P-wave velocity anisotropy of 22%. Furthermore, as the borehole observations revealed up to 8 - 10 open fractures/m in the highly fractured shale rich-region, the normal compliance of a single fracture at this site was estimated to be:

$$\frac{6.62x10^{-12}}{10} \leq Z_N \leq \frac{6.62x10^{-12}}{8}$$

$$\Rightarrow 6.62 \text{ x} 10^{-13} \leq Z_N \leq 8.28 \text{ x} 10^{-13} \text{ m/Pa}$$

Alternatively, the fluctuations in the crosshole velocity due to the presence or absence of open fractures are responsible for a group time delay as the pulse is transmitted through the fractured region (Pyrak-Nolte et al., 1987). From figure 6.3 (b) it can be seen that the velocity for the highly fractured region between approximately 25 m - 40 m BH 20 and 30 m – 50 m in BH 19 varies between approximately 3.0 km/s (dark blue) to approximately 4.7 km/s (green), which incidentally, is also the average velocity of all the rays between each source receiver pair (Herwanger, 2001). Over a distance of approximately 15 m the group time delay will be: $t_g = tt_{slow} - tt_{fast} = \frac{15}{3.0} - \frac{15}{4.7} \frac{m}{km/s} \Rightarrow$ 1.81 ms. As a first order approximation, 8 - 10 open fractures/m $\Rightarrow$ 120 - 150 open fractures over as 15 m interval. Hence, the group time delay per fracture is:

$\frac{1.81}{150} \leq t_g \leq \frac{1.81}{120} \Rightarrow 0.012$ ms $\leq t_g \leq 0.015$ ms. From the Pyrak-Nolte et al. (1987) group time delay theory (Eq. 1.27), this equates to a normal fracture compliance (Fig. 6.5 (a)) of:

$$1.90 \text{ x} 10^{-12} \leq Z_N \leq 2.44 \text{ x} 10^{-12} \text{ m/Pa}$$

It is important to point out that the Pyrak-Nolte et al. (1987) group time delay equation for a single, normally incidence transmitted P-wave (Eq. 1.27) has two roots, giving two values of normal compliance for any one value of group time delay (Fig. 6.5 (b)). These higher values of normal fracture compliance correspond to very low transmission coefficients (Eq. 1.26), with $T_p(\omega) \approx 0.2$ at the Reskajeage crosshole frequencies (~2 kHz), which is not observed. Also, these higher values of normal compliance are anomalously large and are not consistent with the observed velocity anisotropy from the crosshole data.

By combining the error limits from the two approaches it is therefore estimated that the normal compliance for the open fractures at the Reskajeage site is within the following range:

$$6.62 \text{ x} 10^{-13} \leq Z_N \leq 2.44 \text{ x} 10^{-12} \text{ m/Pa}$$

This value is higher than the normal fracture compliance value obtained from the Tytherington field site for reasons that will be discussed in the final chapter

6.4.2 Modelling the transmission amplitudes

An amplitude study was also performed in order to investigate whether the amplitude behaviour could be explained by the compliance estimates calculated using the travel

times in the previous section.

Figure 6.6 (a) shows the zero offset, common ray angle gather, between BH 20 and BH 19 at this test site. The first arrival energy can be clearly traced through the seismogram, but the first arrival for the shallow receivers above 40 m is much more attenuated, with a distinctly lower frequency than that observed for the deeper receivers. A shift in the dominant frequency can be observed in the amplitude spectra from approximately ~1 kHz for the shallow receivers, to ~2 kHz for the deeper receivers (Fig. 6.6 (b)). For the modelling, zero offset P-wavelets were then extracted from these two regions at depths indicated by the arrows in figure 6.6 (a). The first wavelet (blue), was extracted at a depth of approximately 30 m, which was within the highly anisotropic fractured zone, whereas the second wavelet (red), was extracted at a depth of approximately 55 m, which was within the high velocity, low anisotropy, hydraulically tight sandstone zone. The corresponding colour coded wavelets are shown in figure 6.7 (a). The solid red and blue curves in figure 6.7 (b) shows the amplitude spectra resulting from performing a Fast Fourier Transform of the extracted wavelets. Also shown in this plot are the transmitted amplitude spectra (dotted lines) resulting from filtering the data at ~55 m depth, with a transmission response function obtained by assuming a fixed compliance per fracture of $Z_N = Z_T = 1\text{x}10^{-12}$ m/Pa, for a variable amount of fractures $N = \{40, 80, 120, 150\ 180\}$, using the linear slip model of Schoenberg (1980). It is assumed here that the wave is normally incident on the fractures and that the magnitude of the transmission coefficient for a wave propagating across a set of N parallel fractures is $|T|^N$. A normal compliance of $1\text{x}10^{-12}$ m/Pa per fracture was chosen as it was the mean normal fracture compliance obtained from the travel times in section 6.4.1. It can be seen that a reasonable match to the spectra at a depth of ~30 m is obtained for approximately N = 120 to 150 fractures.

Under these assumptions it has been shown that the observed amplitude behaviour is consistent with the compliance limits obtained from the transmission travel times.

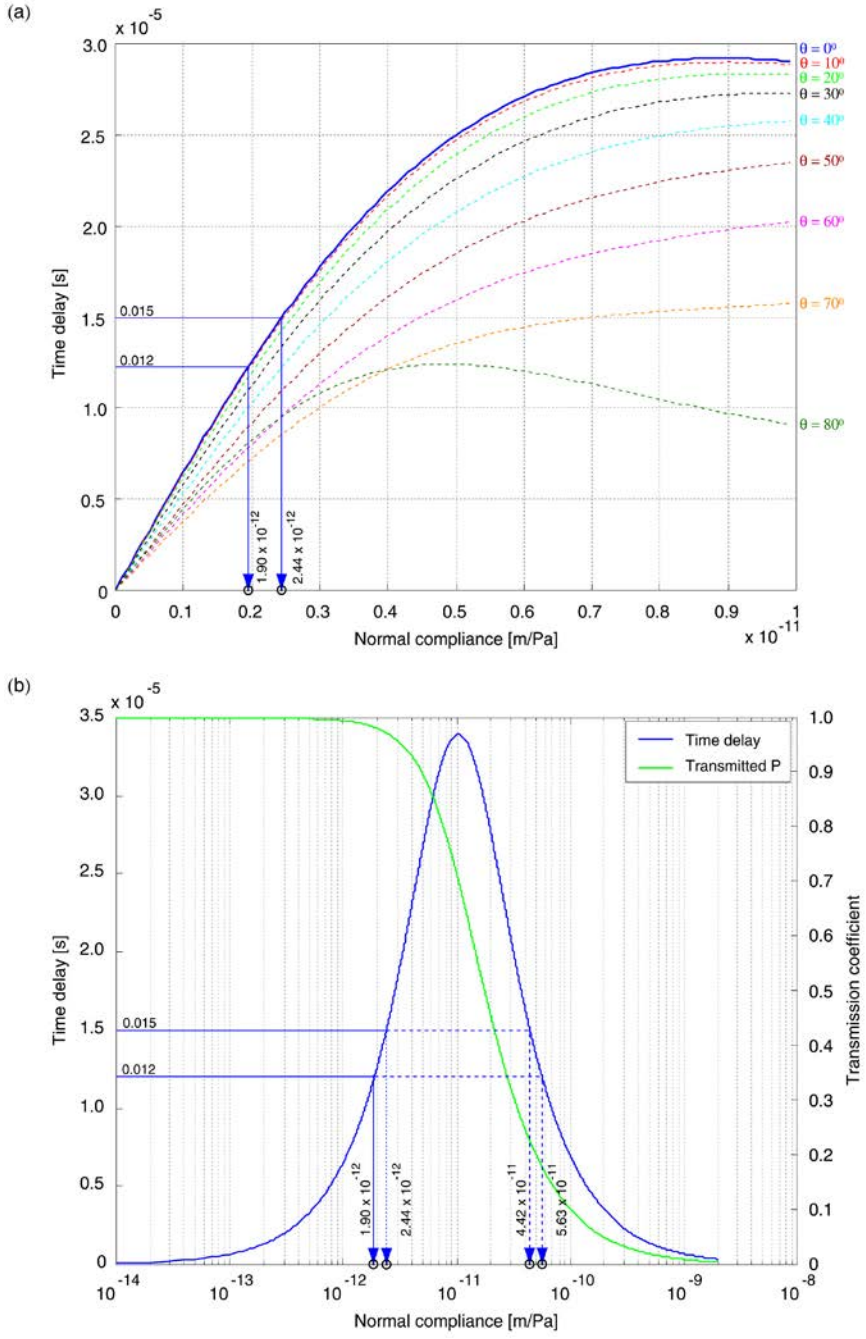


Figure 6.5: Calculating the normal fracture compliance from the group time delay, assuming $Z_N = Z_T$. (a) Normal compliance versus group time delay for a wave transmitted at a frequency of 2 kHz, at a range of angles ($\theta = 0°$ represents a normally incident P-wave); (b) Theoretical group time delay (blue) and transmission coefficient (green) curves using the Pyrak-Nolte et al. (1987) formulation for a normally incident P-wave on a single fracture at a frequency of 2 kHz.

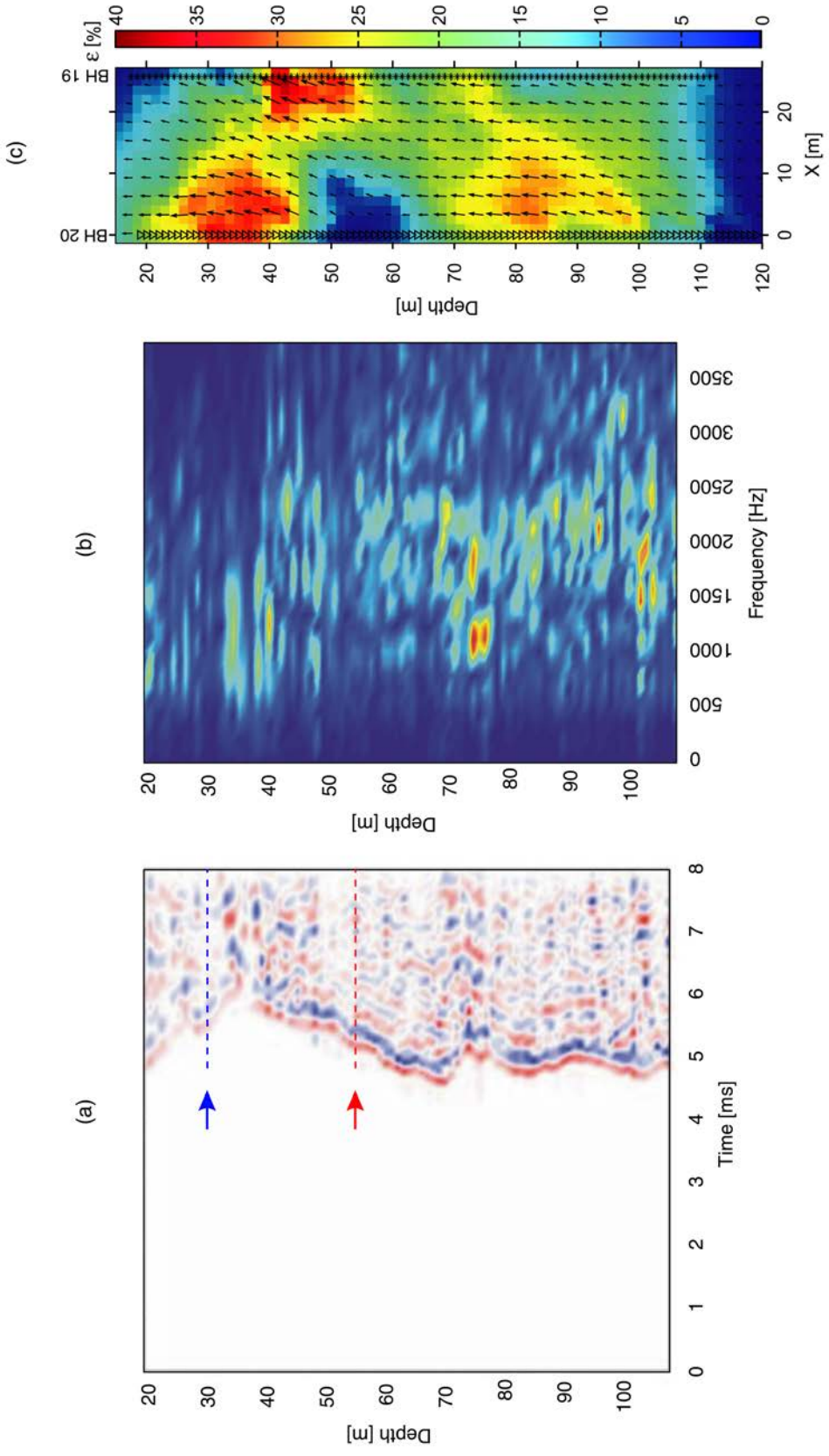


Figure 6.6: (a) Zero offset common ray angle gather with the blue and red arrows indicating the highly anisotropic fractured region and high velocity, low anisotropy sandstone region respectively; (b) Amplitude spectra of (a); (c) Seismic anisotropy tomogram (Lubbe and Worthington, 2003).

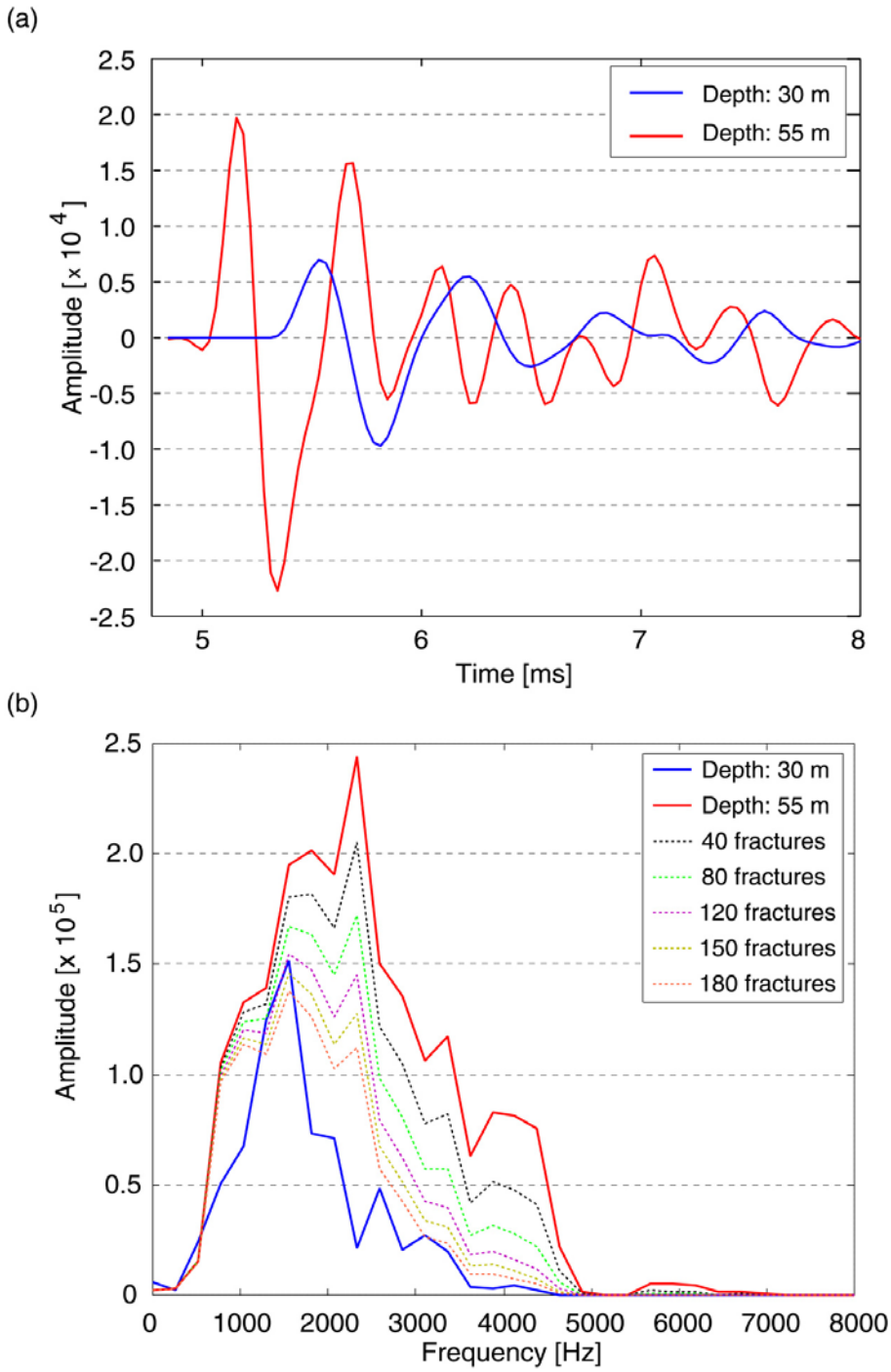


Figure 6.7: Modelling the transmission amplitudes using the linear slip theory. (a) Two P-wavelets were extracted at the positions indicated by the arrows in Figure 6.6 (a). One from the highly anisotropic zone at a depth of 30 m (blue) and another from the high velocity, low anisotropy sandstone zone at a depth of 55 m (red); (b) Amplitude spectra of (a), indicated by the solid blue and red spectra, as well as the transmitted frequency spectra (dotted lines) resulting from filtering the data with a transmission response function assuming N parallel fractures. It is assumed that the wave is normally incident on the fractures and that $Z_N = Z_T = 1 \text{x} 10^{-12}$ m/Pa.

Chapter VII

Conclusions and Suggestions for Further Research

Fracture compliance is a profoundly important earth parameter and yet very few reliable estimates exist. The seismic visibility of fractures depends on the magnitude of their normal and tangential compliance and how these quantities vary with the scale of the fracture and depth of burial. It has been shown in this thesis that laboratory scale estimates of fracture compliance are of the order 10^{-14} m/Pa. If this value is applicable to mesoscale fractures (scale lengths of metres to tens of metres) then they would be totally seismically invisible at seismic exploration frequencies (10 - 200 Hz). Crampin and Chastin (2003) have argued that this is indeed the case, and that crustal seismic anisotropy must be due to micro-porosity and grain-scale microfractures. The reason why there are so few values of the compliance of field scale fractures is simply because the experiments are very difficult to perform. Much preliminary work is required to ensure that the region of the earth to be studied is sufficiently well understood so that the seismic attributes can be reliably related specifically to the fractures. In this thesis, order of magnitude estimates of fracture compliance have been obtained, with error bounds governed by the uncertainty in the normal to tangential fracture compliance ratio. The aim was to determine whether there was any evidence of fracture compliance scaling with fracture size.

7.1 Conclusions

The main conclusion of this thesis is summarised in figure 7.1 which shows the results of laboratory and field estimations of the compliance of fractured rock, from this thesis (shown in blue) and obtained from literature (shown in red), versus increasing estimated fracture length. The black dotted line is the theoretical prediction by Hudson et al. (1997)

for tangential compliance, and also, if the fracture is filled with a weak material, for normal compliance assuming a variable average weld radius a and r^w = 0.1 (10% area in welded contact). The horizontal axis is diagrammatic, since it is not possible to measure any parameter that accurately represents the size of the fracture. The progression from log to crosshole to seismic simply reflects an order of magnitude estimate of the lengths of the fractures. By relating the weld radius to fracture size, it is implicitly assumed that fractures have fractal properties as suggested by Mandelbrot (1982), Brown and Scholz (1985), Yielding et al. (1992) and Xie (1993).

The vertical bar labelled (1) bounds the range of normal fracture compliance values from the laboratory experiments on samples of Portland Pond Freestone and Carboniferous limestone described in *Chapter 2*. This bar is a function of confining pressure, with the top of the bar corresponding to a confining pressure of 5 MPa, whilst the bottom of the bar corresponds to a pressure of 60 MPa. Compliance values were obtained by measuring the reflection coefficient of the fracture for compressional and shear waves, and using the displacement discontinuity theory of Schoenberg (1980). Values ranging between $0.5 \text{x} 10^{-14} \leq Z_N \leq 4.5 \text{x} 10^{-14}$ m/Pa were obtained and always decreased with increasing confining pressure. The normal to tangential compliance ratio Z_N / Z_T was approximately 0.4 and was independent of applied stress.

The range of compliance values labelled (2) was calculated from the laboratory results of Pyrak-Nolte et al. (1990a). These authors presented laboratory results of normal and shear stiffness from single natural fractures in three samples of quartz monzonite, for a range of applied uniaxial stresses from 1.4 to 85 MPa. Their estimates were obtained by trial and error modelling of the transmitted compressional and shear wave amplitude spectra using

the displacement discontinuity theory of Schoenberg (1980). This vertical bar bounds the range of normal compliance values for all three samples under dry and saturated conditions, at all applied axial stresses. The top of the bar corresponds to a uniaxial stress of 1.4 MPa whilst the bottom of the bar corresponds to a stress of 85 MPa.

The bar (3) bounds the range of the normal fracture compliance values from the Tytherington field site, as described in *Chapter 3*, from compressional wave sonic wireline data at a frequency ~23 kHz, and from the open fracture related velocity anisotropy calculated from the crosshole survey in *Chapter 4*. Firstly, by assuming $Z_N = Z_T$, in *Chapter 3*, using the theory of Schoenberg (1980) and Pyrak-Nolte et al. (1987), I attributed the fluctuations in the compressional wave sonic wireline data to the presence or absence of open fractures, which allowed me to calculate a normal fracture compliance from the group time delay the pulse experienced as it was transmitted through the fractured region. Here, due to uncertainties in fracture dips, I allowed for the incidence angle to vary between $\theta = 0°$ (normal incidence) to $\theta = 20°$ relative to the symmetry axis. The estimated normal fracture compliance obtained in this way was $Z_N = (4.84 \pm 2.57) \text{x} 10^{-13}$ m/Pa. In *Chapter 4*, I used the theory developed by Schoenberg and Sayers (1995) to determine values of vertical and horizontal excess open fracture compliance that result in a reduction of ±500 m/s in the vertical velocity. Following this methodology, I estimated the normal compliance of a single fracture at this site to be between $2.5 \text{x} 10^{-13} \leq Z_N \leq 5.0 \text{x} 10^{-13}$ m/Pa. Secondly, also in *Chapter 4* as an alternative calculation, this time making no assumptions about the $Z_N = Z_T$ ratio, I used the Hudson (1980, 1981) and Crampin (1984) theory and modelled the open fracture related fracture density ε_f of 0.035 (compressional wave velocity anisotropy of 10%), and estimated the

normal compliance of a single fracture at this site to be between $2.6\text{x}10^{-13} \leq Z_N \leq 5.2\,\text{x}10^{-13}$ m/Pa. Thus, for the open fractures at the Tytherington site, a realistic bound of normal fracture compliance was, in effect, determined by the compressional wave sonic wireline data which ranged between $Z_N = (4.84 \pm 2.57)\text{x}10^{-13}$ m/Pa.

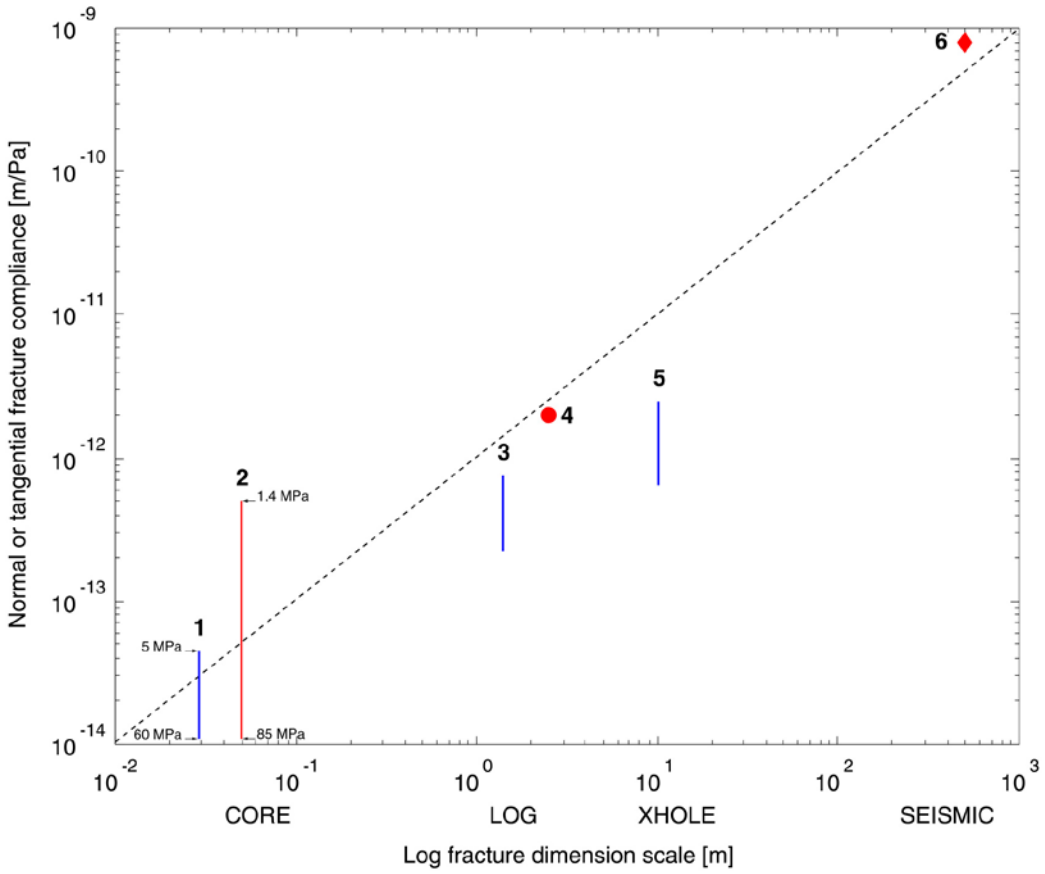


Figure 7.1: The scaling of fracture compliance from laboratory and field data. The two values (nos. 4 and 6) and vertical bar (no. 2), shown in red, are from literature, whilst the vertical bars (nos. 1, 3 and 5), shown in blue, are from this research. The black dotted line is the theoretical prediction by Hudson et al. (1997) for tangential compliance and also, if the fracture is filled with a weak material, for normal compliance assuming a variable average weld radius a and r^w = 0.1 (10% area in welded contact).

The data point labelled (4) is the Myer et al. (1995) fracture compliance estimation of $Z = 2\,\text{x}10^{-12}$ m/Pa. They obtained this value by modelling the transmission amplitudes

with the seismic displacement discontinuity theory using the King et al. (1986) crosshole dataset (as described in section 1.1).

The vertical bar (5) bounds the range of normal fracture compliance values from the Reskajeage field site as described in *Chapter 6*. Firstly, again making no assumption about the Z_N / Z_T ratio, I used the Hudson (1980, 1981) and Crampin (1984) theory and the modelled open fracture related fracture density ε_f of 0.07 (P-wave velocity anisotropy of 22%) obtained from the highly fractured shale rich-region, and estimated the normal compliance of a single fracture at this site to be between $6.62\text{x}10^{-13} \leq Z_N \leq 8.28\,\text{x}10^{-13}$ m/Pa. Secondly, by assuming $Z_N = Z_T$ and attributing the fluctuations in the crosshole data to the presence or absence of open fractures, using the theory of Schoenberg (1980) and Pyrak-Nolte et al. (1987), I was able to calculate a normal fracture compliance between $1.90\text{x}10^{-12} \leq Z_N \leq 2.44\,\text{x}10^{-12}$ m/Pa. Thirdly, following the methodology of Pyrak-Nolte et al. (1990a, 1990b) and Myer et al. (1995), I then modelled the observed attenuation from the compressional wave transmission amplitudes in the highly anisotropic open fractured zone with the Schoenberg (1980) displacement discontinuity theory, and obtained a reasonable fit to the calibration spectra assuming N = 120 to 150 parallel fractures each with a normal fracture compliance of $Z_N = 1.0\,\text{x}10^{-12}$ m/Pa. This value was consistent with the normal fracture compliance values obtained from the crosshole travel time data. Thus, for the open fractures at the Reskajeage site, a realistic bound of normal fracture compliance of $6.62\text{x}10^{-13} \leq Z_N \leq 2.44\,\text{x}10^{-12}$ m/Pa was estimated. This value was higher than the normal fracture compliance value obtained from the Tytherington field site, as the

hydraulically conducting open fractures at Reskajeage, were of larger scale in comparison.

Data point (6) was taken from Worthington and Hudson (2000) and represents a tangential fracture compliance estimate of $Z_T = 1.1\text{x}10^{-9}$ m/Pa. This value was obtained from VSP data for a major fault zone (1 – 2 km depth), intersecting a well at an angle of approximately $50°$. This experiment differs from the other five experiments because it was never claimed to be an experimental determination of fracture compliance, since no sufficiently detailed knowledge of the transmission path was available. The aim of the experiment was to demonstrate that low seismic Q, apparently associated with a major fracture zone, could be attributed to apparent attenuation mechanisms such as Rayleigh scattering and the low pass filtering effect of partially sealed interfaces rather than intrinsic attenuation. A notable feature of these estimates is that Q was constant over a wide frequency band from about 10 to 150 Hz. Also, a peak in the attenuation was clearly associated with the depth interval where the borehole intersected the major fracture zone. Worthington and Hudson (2000) interpreted these Q data using displacement discontinuity modelling after Schoenberg (1980) combined with the theory in Hudson et al. (1997). Their analysis highlighted the importance of shear compliance when modelling compressional wave transmission across a fault. The work also highlighted the critical importance of shear compliance and the theoretical possibility of Z_N / Z_T being close to zero, since the normal compliance of a fracture at 2 km depth would be vanishingly small.

Laboratory and field estimates of fracture compliance have been calculated in this thesis for a range of fracture sizes. Compliance has been shown to increase with the scale of the fractures. By assuming the possibility of fractal scaling of fracture parameters, this

scaling behaviour is consistent with theoretical predictions by Hudson et al. (1997) for shear compliance and also, if the fracture is filled with a weak material, for normal compliance.

7.2 Suggestions for Further Research

In order to relate the measured compliance from seismic data directly to the microstructural detail of the fracture using analytical expressions derived by Hudson et al. (1997), it is vital to obtain estimates for Z_N / Z_T from experimental data. This is an area of intense current interest because of its conceptual and practical importance (Liu et al., 1996; Schoenberg, 1998; Liu and Li, 2000; Liu et al., 2000) as the potential benefits are in terms of estimation of fluid flow, permeability anisotropy and pressure prediction in hydrocarbon reservoirs.

To some degree natural fracture systems may not be consistent with conventional equivalent medium theories. They do not appear as dilute, randomly spaced, disconnected, or ideal shapes, nor are they weak scatterers or always smaller than the seismic wavelength. These restrictions should be borne in mind when applying equivalent medium theories (MacBeth, 1995).

In the displacement discontinuity theory of Schoenberg (1980) or the velocity discontinuity theory (Pyrak-Nolte et al., 1990a), in general, the ratio of the normal to shear compliances is dependent on the fracture interior boundary conditions, in particular the fluid types. Simple, analytic expressions linking fracture compliances to pore fluid, and to fracture induced P and S-wave anisotropic measurement characterised by the

Thomsen (1986) parameters, have been developed by Liu and Li (2000). As this ratio is linked to the Thomsen (1986) parameters it can, in theory, be obtained from seismic data.

A need exists to test these theories, firstly in the laboratory, as these experiments are in principle easier to perform than field experiments, and then to up-scale to conventional field exploration frequencies to test the reliably with which seismic data from the laboratory, wireline log and large scale field surveys can be compared.

Shear wave field experiments through fractured rock need to be designed to predict the scaling behaviour of tangential compliance with fracture size. An insightful laboratory experiment to test the empirical formulation of Liu and Li (2000) and Schoenberg (1998) would be to propagate P and S-waves through cut and reassembled rock samples, cored from the same homogeneous rock type, with fracture planes cut at a range of angles to the long axis of the cylindrical core. The fractures could be either dry, filled with water or filled with other substances of differing viscosities such as oil, brine, gas etc. To simulate *in-situ* hydrocarbon reservoir conditions these experiments can be performed over a range of confining pressures. The different fractures could be sealed with silicone rubber and could be filled before deploying them in the rig. The travel time, amplitude and frequency content of the transmitted P or S-waves could be recorded either side of the fracture. A normal Z_N and tangential Z_T fracture compliance value could then be calculated at every pressure interval by modelling the transmission amplitudes (Pyrak-Nolte et al., 1990a; Myer et al., 1995) using the displacement discontinuity theory of Schoenberg (1980), or the velocity discontinuity theory (Pyrak-Nolte et al., 1990a; Yoshioka and Kikuchi, 1993). The velocity discontinuity theory would be more suited for viscous interfaces. Yoshioka and Kikuchi (1993) have shown that high stresses occurring at the points of

contact of two fault faces might lead to inelastic behaviour in the solid material during the transmission of elastic waves within the shallow subsurface, complicating the prediction of normal and tangential fracture compliance (see grooved sample experiment in *Chapter 2*). These experiments can be compared with the variation of P-wave transmission coefficient with frequency and incident angle (Worthington and Hudson, 2000) and also with field experiments by Majer et al. (1997) who have injected gas into a natural fracture system located between two vertical boreholes and observed significant seismic attenuation. The modelled normal and tangential compliances could be used to calculate a Z_N / Z_T ratio over a confining pressure interval for the dry or fluid filled fracture at a certain angle. In this way, a suite of Z_N / Z_T values could be obtained at different pressures, incident angles and fluid types. The Z_N / Z_T ratio could then be compared with analytical expressions (Liu and Li, 2000; Schoenberg, 1998) relating Z_N / Z_T to the Thomsen anisotropic parameters and the proposed potential fluid indicator capability of Z_N / Z_T could also be tested.

Additionally, in order to investigate the dependence of the reflection and transmission coefficients on the frequency of the wave in the displacement discontinuity theory of Schoenberg (1980), the scaling behaviour of compliance also needs to be investigated for fractures of discrete sizes over a range of frequencies in the field and the laboratory (Pyrak-Nolte and Nolte, 1992).

Appendix

A.1 Proof that: $T_{BR}T_{RB} = 1 - R_{BR}^2$

Zoeppritz's equations for normal incidences (Telford et al., 1990):

$$R_{BR} = \frac{Z_R - Z_B}{Z_R + Z_B} \tag{A1}$$

where R_{BR} = reflection coefficient; buffer rod → rock

$$T_{BR} = \frac{2Z_B}{Z_R + Z_B} \tag{A2}$$

where T_{BR} = transmission coefficient; buffer rod → rock

$$T_{RB} = \frac{2Z_R}{Z_R + Z_B} \tag{A3}$$

where T_{RB} = transmission coefficient; rock → buffer rod

Thus, for a single reflection off the crack (rock/rock interface), assuming infinite Q, using the right hand side and equation A1:

$$RHS = 1 - R_{BR}^2$$

$$= 1 - \left(\frac{Z_R - Z_B}{Z_R + Z_B} \right)^2$$

$$= \frac{(Z_R + Z_B)^2}{(Z_R + Z_B)^2} - \left(\frac{Z_R^2 - 2Z_R Z_B + Z_B^2}{(Z_R + Z_B)^2} \right)$$

$$= \frac{4Z_R Z_B}{(Z_R + Z_B)^2}$$

Using the left hand side and equations A2 and A3 gives:

$$LHS = T_{BR}T_{RB}$$

$$= \left(\frac{2Z_B}{Z_R + Z_B}\right)\left(\frac{2Z_R}{Z_R + Z_B}\right)$$

$$= \frac{4Z_R Z_B}{(Z_R + Z_B)^2}$$

$$\therefore LHS = RHS$$

$$\Rightarrow \underline{T_{BR}T_{RB} = 1 - R_{BR}^2}$$

A.2 Calculating Z_N or Z_T from the reflection coefficients of the fracture using the displacement discontinuity theory

From the displacement discontinuity or linear slip theory of Schoenberg (1980):

$$R = -\frac{Z_1 - Z_2 - i\omega\eta Z_1 Z_2}{Z_1 + Z_2 - i\omega\eta Z_1 Z_2}$$

where,

$|R|$ = observed reflection coefficient; R_P if a compressional wave transducer was used or R_S if a shear wave transducer was used

η = Z_N if calculating a normal compliance or Z_T if calculating a tangential compliance

Z = acoustic impedance; ρv_P or ρv_S depending on the type of transducer used

$\omega = 2\pi f$

In the case that the material on either side of the fracture is the same:

$$Z_1 = Z_2 = Z$$

$$\Rightarrow R = \frac{i\omega\eta Z^2}{2Z - i\omega\eta Z^2} = \frac{i\omega\eta Z}{2 - i\omega\eta Z}$$

The absolute values of the reflection coefficient of the rock/rock interface are measured. The Schoenberg (1980) theory however produces complex reflection coefficients. To obtain absolute values for the reflection coefficients one needs to calculate the absolute value of the complex reflection coefficients.

$$\Rightarrow |R| = \left| \frac{i\omega\eta Z}{(2 - i\omega\eta Z)} \right|$$

$$= \left| \frac{i\omega\eta Z}{(2 - i\omega\eta Z)} \times \frac{(2 + i\omega\eta Z)}{(2 + i\omega\eta Z)} \right| = \left| \frac{2i\omega\eta Z - \omega^2\eta^2 Z^2}{4 + \omega^2\eta^2 Z^2} \right|$$

$$= \left| -\frac{\omega^2\eta^2 Z^2}{4 + \omega^2\eta^2 Z^2} + \left(\frac{2\omega\eta Z}{4 + \omega^2\eta^2 Z^2} \right) i \right|$$

Also: $|a - bi| = (a^2 + b^2)^{1/2}$

$$\therefore |R|^2 = \left(-\frac{\omega^2\eta^2 Z^2}{4 + \omega^2\eta^2 Z^2} \right)^2 + \left(\frac{2\omega\eta Z}{4 + \omega^2\eta^2 Z^2} \right)^2$$

$$\frac{\omega^4\eta^4 Z^4}{(4 + \omega^2\eta^2 Z^2)^2} + \frac{4\omega^2\eta^2 Z^2}{(4 + \omega^2\eta^2 Z^2)^2} = \frac{\omega^4\eta^4 Z^4 + 4\omega^2\eta^2 Z^2}{(4 + \omega^2\eta^2 Z^2)^2}$$

$$\frac{\omega^2\eta^2 Z^2 (4 + \omega^2\eta^2 Z^2)}{(4 + \omega^2\eta^2 Z^2)^2} = \frac{\omega^2\eta^2 Z^2}{4 + \omega^2\eta^2 Z^2}$$

$$\Rightarrow |R|^2 (4 + \omega^2\eta^2 Z^2) = \omega^2\eta^2 Z^2$$

$$\therefore \omega^2\eta^2 Z^2 |R|^2 - \omega^2\eta^2 Z^2 = -4|R|^2$$

$$\therefore \eta^2 (\omega^2 Z^2 |R|^2 - \omega^2 Z^2) = -4|R|^2$$

$$\therefore \eta^2 = \frac{4|R|^2}{\omega^2 Z^2 - \omega^2 Z^2 |R|^2}$$

$$\eta = \frac{2|R|}{\left(\omega^2 Z^2 - \omega^2 Z^2 |R|^2\right)^{1/2}}$$

$$\therefore \eta = \frac{2|R|}{\omega Z (1 - |R|^2)^{1/2}} \tag{A4}$$

A.3 Helium Porosimetry

The porosimeter does not give a direct measurement of porosity but measures the grain volume of a rock or core, using a technique based on the principle of Boyle's Law expansion of helium gas. A schematic of the instrument is shown in figure A1.

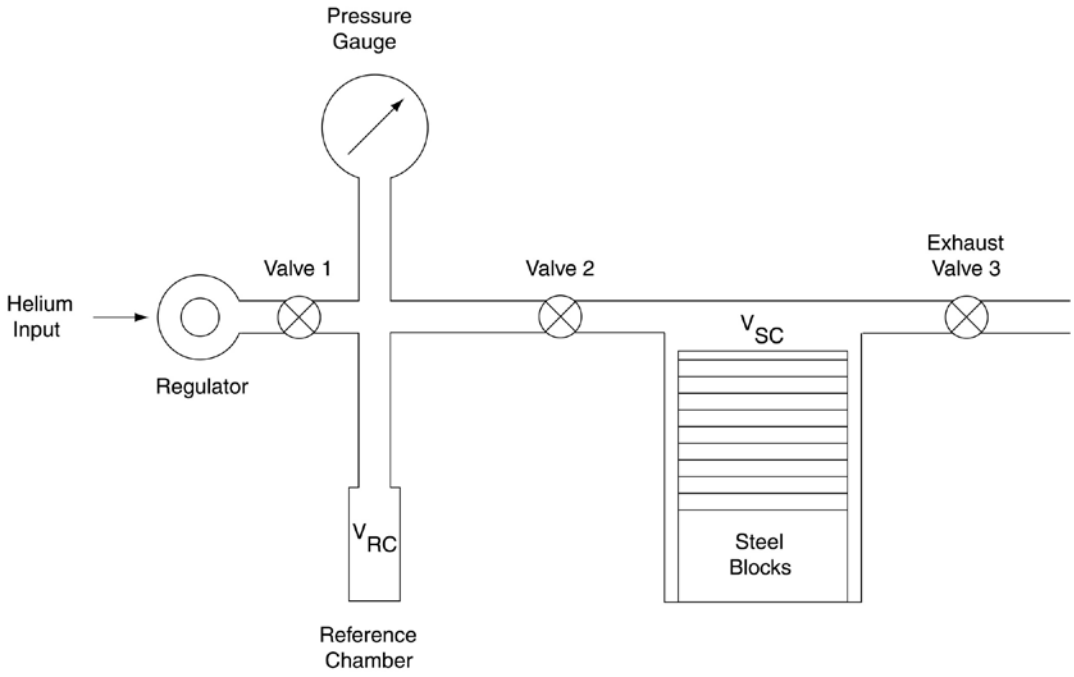


Figure A1: Schematic diagram showing the Helium Porosimeter for measuring the porosity.

The sample cell makes a leak tight seal when loaded into the porosimeter. A sample, which has previously been weighed and had its dimensions taken, is placed into the sample cell. Steel filler plugs of known volume are used fill any space not occupied by the sample. The sample cell is then positioned onto the base of the piston block on the

porosimeter. The piston block is raised and the sample cell is forced upwards against a steel block to create pressure tight sample chamber. Helium gas is introduced through valve 1 into a reference volume chamber of known fixed volume. The helium pressure is measured with a gauge pressure transducer which measures the pressure *above* atmospheric pressure. Valve 1 is then closed and the pressure in the reference volume chamber is recorded (~95 to 100 lb/in^2), with the sample cell being at atmospheric pressure. Valve 2 is opened and the helium gas expands into the sample cell. The pressure is recorded when it has reached a constant value. A thermocouple, located in the steel block at the top of the sample chamber, is used to measure the sample temperature. Valve 3 is opened to release the helium gas and then all valves are closed. The piston block is then lowered and the sample is removed from the sample cell. The equilibrium pressure measured after opening valve 2 is proportional to the volume of solid material present in the sample cell. The instrument is calibrated using the same procedure as above but using the stainless steel filler plugs covering a range of known volumes. Plotting the filler block volume versus its measured inverse expanded pressure (i.e. pressure measured with valve 2 open or P_{RC+SC} lb/in^2) would result in a straight line. The steel filler plug volume is predicted and compared with the actual volume of the steel filler blocks in the sample chamber. As the stainless steel filler blocks occupy free space within the sample chamber, this volume is analogous to the grain volume of an actual sample within the sample chamber. Also, as the temperature usually increases during the period of calibration, the expanded pressure for each point is corrected, or normalised to, the reference volume temperature T_0 at the initial calibration. P and T are the standard pressure (atmospheric pressure = 14.7 lb/in^2) and temperature (0º C = 273.15 K) respectively. To convert the pressure above atmospheric pressure, as measured by the pressure transducer, to absolute

pressure one needs to add 14.7 lb/in^2 to the pressure measured by the pressure transducer i.e. lb/in^2 (*absolute*) = lb/in^2 (*measured*) + 14.7 lb/in^2.

$$P_{RC\{corrected\}} = \left(\frac{\left(P_{RC} + 14.7lb/in^2\right)\left(T_0\,°C + 273.15K\right)}{T_{RC} + 273.15K} \right) - 14.7lb/in^2$$

$$P_{RC+SC\{corrected\}} = \left(\frac{\left(P_{RC+SC} + 14.7lb/in^2\right)\left(T_0\,°C + 273.15K\right)}{T_{RC+SC} + 273.15K} \right) - 14.7lb/in^2$$

where,

$P_{RC\{corrected\}}$ = corrected pressure of the reference chamber only [lb/in^2]

$P_{RC+SC\{corrected\}}$ = corrected pressure of the reference chamber and the sample cell [lb/in^2]

T_{RC} = temperature of reference chamber volume [K]

T_{RC+SC} = temperature of reference chamber and sample cell volume [K]

T_0 = temperature of reference chamber volume, at initial calibration, using stainless steel filler blocks [K]

The reference and sample chamber volumes are known for a range of stainless steel filler plug combinations. These parameters are used to calculate the grain volume of the real samples:

$$V_G^{'} = \frac{P_{RC+SC(corrected)}\left(V_{RC} + V_{SC}\right) - P_{RC(corrected)}V_{RC}}{P_{RC+SC(corrected)}} \qquad \text{(A5)}$$

where,

$V_G^{'}$ = grain volume of sample and filler block [cm^3]

V_{RC} and V_{SC} = reference chamber and sample cell volume respectively [cm^3]

The stainless steel filler blocks that have been inserted into the sample chamber to fill up the free space, adds to the final calculated grain volume and needs to be subtracted to obtain the grain volume of the rock sample only.

$$V_G = V_G^{'} - V_{FB} = (V_G + V_{FB}) - V_{FB} \tag{A6}$$

where,

V_G = grain volume of rock sample only [cm^3]

V_{FB} = total volume of stainless steel filler blocks [cm^3]

Knowing the bulk volume, as calculated with equation 2.2 (see Chapter 2, section 2.8), the porosity is then calculated as follows:

$$\phi = \frac{V_P}{V_S}$$

$$= \frac{(V_S - V_G)}{V_S} \text{ x } 100\% \tag{A7}$$

where,

V_P, V_G and V_S = pore, grain and bulk volume of the sample respectively [cm^3]

ϕ = porosity

A.4 Calculating the reflection coefficients of the crack from the acoustic data

A.4.1 Correcting the reflection coefficient of the crack interface (R_{CRACK}) for Q

Assuming A_2 is already corrected for transmission and diffraction (see Fig. A2):

$$R_{CRACK} = \frac{A_2}{A_1}$$

$$\Rightarrow A_2 = R_{CRACK} A_1 e^{-\alpha 2x} \tag{A8}$$

where,

α = the attenuation coefficient [dB/cm]

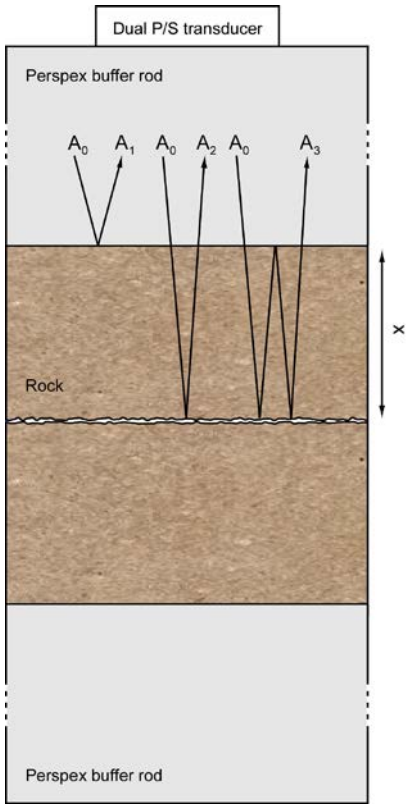


Figure A2: Schematic diagram showing the reflection off the buffer rod/rock interface ($A_0 \rightarrow A_1$) and also the first reflection ($A_0 \rightarrow A_2$) and the first multiple reflection ($A_0 \rightarrow A_3$), off the rock/rock (crack) interface.

Also, from equation 2.16 (see Chapter 2, section 2.12.2):

$$Q = \frac{\pi f}{\alpha v}$$

$$\Rightarrow \alpha = \frac{\pi f}{Q v} \tag{A9}$$

Substituting equation A9 into equation A8 gives:

$$A_2 = R_{CRACK} A_1 e^{-\frac{\pi f}{Qv} 2x}$$

$$\Rightarrow R_{CRACK} = \frac{A_2}{A_1} e^{+\frac{\pi f}{Qv} 2x} \tag{A10}$$

A.4.2 Correcting the first reflection off the crack interface for transmission and Q

Assuming A_2 is already corrected for diffraction, one can correct the reflection off the crack for transmission:

$$A_1 = A_0 R_{BR} \tag{A11}$$

$$A_2 = A_0 T_{BR} R_{CRACK} T_{RB} \tag{A12}$$

Dividing equation A11 by equation A12:

$$\frac{A_2}{A_1} = \frac{T_{BR} T_{RB} R_{CRACK}}{R_{BR}} \tag{A13}$$

But $T_{BR} T_{RB} = \left(1 - R_{BR}^2\right)$ (see section A.1)

$$\Rightarrow A_2 = \frac{A_1 R_{CRACK} \left(1 - R_{BR}^2\right)}{R_{BR}} \tag{A14}$$

$$\Rightarrow R_{CRACK} = \frac{A_2 R_{BR}}{A_1 \left(1 - R_{BR}^2\right)} \tag{A15}$$

Now, correcting the reflection coefficient of the crack for Q:

$$\Rightarrow R_{CRACK} = \frac{A_2 R_{BR} e^{\frac{\pi f}{Qv} 2x}}{A_1 \left(1 - R_{BR}^2\right)} = \frac{A_2 R_{BR} e^{\frac{\pi f t}{Q}}}{A_1 \left(1 - R_{BR}^2\right)} \tag{A16}$$

where t = the two way travel time [μs]

A.4.3 Correcting the first multiple reflection off the crack interface for transmission and Q

Assuming A_3 is corrected for diffraction, one can correct the first multiple reflection off the crack for transmission:

$$A_3 = A_0 T_{BR} R_{CRACK} R_{RB} R_{CRACK} T_{RB}$$

$$= A_0 T_{BR} R_{CRACK} \left(-R_{BR}\right) R_{CRACK} T_{RB} \tag{A17}$$

Dividing equation A17 by equation A11:

$$\frac{A_3}{A_1} = -T_{BR}T_{RB}R_{CRACK}^2 \tag{A18}$$

Strictly speaking $R_{RB} = -R_{BR}$ (signal polarity reversal), but since we are only concerned with the absolute value of the reflection coefficient, this would not make a difference in the calculation of the compliance values.

$$\therefore R_{CRACK} = \sqrt{\frac{A_3}{A_1 T_{BR} T_{RB}}} \tag{A19}$$

But again, $T_{BR}T_{RB} = \left(1 - R_{BR}^2\right)$ (see section A.1)

$$\Rightarrow R_{CRACK} = \sqrt{\frac{A_3}{A_1(1 - R_{BR}^2)}} \tag{A20}$$

Now, correcting the first multiple reflections off the crack for Q:

$$\Rightarrow R_{CRACK} = \left(\sqrt{\frac{A_3}{A_1(1 - R_{BR}^2)}}\right) \cdot e^{\frac{\pi f 4x}{Qv}} = \left(\sqrt{\frac{A_3}{A_1(1 - R_{BR}^2)}}\right) \cdot e^{\frac{2\pi ft}{Q}} \tag{A21}$$

where again t is the two way travel time [μs]

A.5 Benson and Kiyohara (1974) diffraction table

	S = 0.0 to 5.0		
	S	***φ***	***α***
1	0.0	0.00000	0.00000
2	0.1	0.07602	0.61488
3	0.2	0.11011	0.86482
4	0.3	0.14118	1.05830
5	0.4	0.16049	1.20960
6	0.5	0.18141	1.34500
7	0.6	0.20561	1.56080
8	0.7	0.22505	1.54100
9	0.8	0.25341	1.77940
10	0.9	0.25281	1.91260
11	1.0	0.26593	1.85040
12	1.1	0.29792	1.85800
13	1.2	0.33002	2.01080
14	1.3	0.35059	2.23920
15	1.4	0.35848	2.45390
16	1.5	0.35840	2.59970
17	1.6	0.35635	2.66300
18	1.7	0.35686	2.65820
19	1.8	0.36220	2.61090
20	1.9	0.37286	2.54510
21	2.0	0.38830	2.47890
22	2.1	0.40756	2.42340
23	2.2	0.42961	2.38480
24	2.3	0.45355	2.36550
25	2.4	0.47864	2.36590
26	2.5	0.50430	2.38500
27	2.6	0.53010	2.42120
28	2.7	0.55573	2.47270
29	2.8	0.58095	2.53760
30	2.9	0.60562	2.61420
31	3.0	0.62963	2.70090
32	3.1	0.65292	2.79610
33	3.2	0.67544	2.89850

	S = 5.1 to 10.0		
	S	***φ***	***α***
52	5.1	0.97502	5.30190
53	5.2	0.98569	5.42920
54	5.3	0.99601	5.55550
55	5.4	1.00600	5.68090
56	5.5	1.01560	5.80530
57	5.6	1.02500	5.92870
58	5.7	1.03400	6.05100
59	5.8	1.04280	6.17220
60	5.9	1.05130	6.29230
61	6.0	1.05950	6.41140
62	6.1	1.06750	6.52930
63	6.2	1.07520	6.64610
64	6.3	1.08270	6.76180
65	6.4	1.09000	6.87640
66	6.5	1.09710	6.98990
67	6.6	1.10400	7.10230
68	6.7	1.11070	7.21360
69	6.8	1.11720	7.32380
70	6.9	1.12350	7.43290
71	7.0	1.12970	7.54090
72	7.1	1.13570	7.64790
73	7.2	1.14150	7.75380
74	7.3	1.14720	7.85870
75	7.4	1.15280	7.96250
76	7.5	1.15820	8.06530
77	7.6	1.16340	8.16720
78	7.7	1.16860	8.26800
79	7.8	1.17360	8.36780
80	7.9	1.17850	8.46670
81	8.0	1.18320	8.56460
82	8.1	1.18790	8.66160
83	8.2	1.19240	8.75770
84	8.3	1.19690	8.85280

Benson and Kiyohara diffraction table (continue)

34	3.3	0.69717	3.00700
35	3.4	0.71813	3.12070
36	3.5	0.73830	3.23850
37	3.6	0.75772	3.35980
38	3.7	0.77640	3.48390
39	3.8	0.79437	3.61020
40	3.9	0.81165	3.73830
41	4.0	0.82826	3.86770
42	4.1	0.84425	3.99800
43	4.2	0.85963	4.12890
44	4.3	0.87443	4.26030
45	4.4	0.88868	4.39170
46	4.5	0.90241	4.52310
47	4.6	0.91563	4.65430
48	4.7	0.92838	4.78500
49	4.8	0.94067	4.91530
50	4.9	0.95252	5.04490
51	5.0	0.96397	5.17380

85	8.4	1.20120	8.94700
86	8.5	1.20550	9.04040
87	8.6	1.20960	9.13280
88	8.7	1.21370	9.22450
89	8.8	1.21760	9.31520
90	8.9	1.22150	9.40510
91	9.0	1.22530	9.49420
92	9.1	1.22900	9.58250
93	9.2	1.23270	9.67000
94	9.3	1.23620	9.75670
95	9.4	1.23970	9.84260
96	9.5	1.24320	9.92780
97	9.6	1.24650	10.01200
98	9.7	1.24980	10.09600
99	9.8	1.25300	10.17900
100	9.9	1.25620	10.26100
101	10.0	1.25930	10.34300

Bibliography

Aki, K., and Richards, P. G., 2002, Quantitative seismology: University Science Books, California, 2nd ed.

Auld, B. A., 1990, Acoustic fields and waves in solids: Vols. I and II, Robert E. Krieger Publication Co., Malabar, Florida.

Backus, G. E., 1962, Long-wave elastic anisotropy produced by horizontal layering: Journal of Geophysical Research, **67**, 4427-4440.

Baker, A. C., Holton, D., Jefferies, N. L., and Watkins, V. M. B., 1999, Hydraulic testing in boreholes 17, 19 and 20 at Reskajeage Quarry, Cornwall: AEA Technology Report AEAT/ERRA-0089.

Bandis, S. C., Lumsden, A. C., and Barton, N. R., 1983, Fundamentals of rock joint deformation: International Journal of Rock Mechanics and Mining Science & Geomechanics Abstracts, **20**, No. 6, 249-268.

Benson, G. C., and Kiyohara, O., 1974, Table of integral functions describing diffraction effects in the ultrasonic field of a circular piston source: Journal of the Acoustical Society of America, **55**, 184-185.

Best, A. I., 1992, The prediction of the reservoir properties of sedimentary rocks from seismic measurements: Ph.D. thesis, University of Reading.

Biot, M. A., 1956a, Theory of propagation of elastic waves in a fluid saturated porous solid. I. Low-frequency range: Journal of the Acoustical Society of America, **28**, 168-178.

—— 1956b, Theory of propagation of elastic waves in a fluid saturated porous solid. II. Higher frequency range: Journal of the Acoustical Society of America, **28**, 179-191.

Birch, F., and Bancroft, D., 1938a, The effect of pressure on the rigidity of rocks I: Journal of Geology, **46**, 59-87.

—— 1938b, The effect of pressure on the rigidity of rocks II: Journal of Geology, **46**, 113-141.

Brace, W. F., Paulding, B. W., and Scholz, C., 1966, Dilatancy in the fracture of crystalline rocks: Journal of Geophysical Research, **71**, 3939-3953.

Brown, R. J. S., and Korringa, J., 1975, On the dependence of the elastic properties of a porous rock on the compressibility of the pore fluid: Geophysics, **40**, No. 4, 608–616.

Brown, S. R., 1987, Fluid flow through rock joints: the effect of surface roughness: Journal of Geophysical Research, **92**, 1337-1347.

Brown, S. R., and Scholz, C. H., 1985, Closure of random elastic surfaces in contact: Journal of Geophysical Research, **90**, 5531-5545.

Bruner, W. M., 1976, Comment on “Seismic velocities in dry and saturated solids” by R. J. O’Connell and B. Budiansky: Journal of Geophysical Research, **81**, 2573-2576.

Chapman, C. H., and Pratt, R. G., 1992, Traveltime tomography in anisotropic media – I: Theory: Geophysical Journal International, **109**, 1-19.

Cosgrove, J., 2001, A brief review of the geological setting and structural geology of the Tytherington quarry: Hanson Tytherington Quarry.

Crampin, S., 1984, Effective anisotropic elastic constants for wave propagation through cracked solids: Geophys. J. R. Astr. Soc., **76,** 135-145.

Crampin, S., 1994, The fracture criticality of fractured rocks: Geophysical Journal International, **118**, 428-438.

Crampin, S., and Chastin, S., 2003, A review of shear wave splitting in the crack-critical crust: Geophysical Journal International, **155**, 221-240.

Eshelby, J. D., 1957, The determination of the elastic field of an ellipsoidal inclusion, and related problems: Proc. R. Soc. Lond., A241, 376-396.

Fehler, M., 1982, Interaction of seismic waves with a viscous liquid layer: Bull. Seism. Soc. Am., **72**, 55-72.

Futterman, W. I., 1962, Dispersive body waves: Journal of Geophysical Research, **67**, 5279 -5291.

Goodman, R. E., 1976, Methods of Geological Engineering, West Publishing, St. Paul, MN, 170-173.

Green, D. H., and Wang, H. F., 1991, Shear wave diffraction loss for circular plane-polarized source and receiver: Journal of the Acoustical Society of America, **90,** 2697-2704.

Green, G. W., 1992, British Regional Geology, Bristol and Gloucester region: British Geological Survey, 3rd edition.

Haller, D., and Porturas, F., 1998, How to characterize fractures in reservoirs using borehole and core images: case studies. In: Harvey, P. K. & Lovell, M. A. (Eds.), Core-Log Integration, Special Publication of the Geological Society of London, **136,** 249-259.

Hardin, E., Cheng, C., Paillet, F., and Mendelson, J., 1987, Fracture Characterization by Means of Attenuation and Generation of Tube Waves in Fractures Crystalline Rock at Mirror Lake, New Hampshire: Journal of Geophysical Research, **92**, No B8, 7989-8006.

Hennah, S., 2004, Broadband acoustic attenuation mechanisms and their relationship to petrophysical properties: Ph.D. thesis, University of Reading.

Henyey, F. S., and Pomphrey, N., 1982, Self-consistent elastic moduli of a cracked solid: Geophysical Research Letters, **9**, 903-906.

Herwanger, J. V., 2001, Seismic and Electric Crosshole Tomography for Fracture Detection and Characterization: Ph.D. thesis, Imperial College of Science Technology and Medicine, University of London.

Herwanger, J. V., Pain, C. C., Binley, A., de Oliviera, C. R. E., and Worthington, M. H., 2004, Anisotropic Resistivity Tomography: Geophysical Journal International, **158**, No. 2, 409-425.

Herwanger, J. V., Worthington, M. H., Lubbe, R., Binley, A., and Khazanehdari, J., 2004, A comparison of cross-hole electrical and seismic data in fractured rock: Geophysical Prospecting, **52**, 109-121.

Hoek, E., and Brown, E. T., 1980, Underground Excavations in Rock: Institution of Mining and Metallurgy, London.

Hoek, E., and Franklin, J. A., 1968, Simple triaxial cell for field or laboratory testing of rock: Transactions of the Institution of Mining and Metallurgy, A22-A26.

Holton, D., and Jefferies, N. L., 2001, Fracture network modelling of groundwater flow at Reskajeage Quarry, Cornwall: AEA Technology Report AEAT/R/ENV/0201.

Hopkins, D. L., Myer, L. R., and Cook, N. G. W., 1988, Seismic wave attenuation across parallel multiple fractures as a function of fracture stiffness and spacing: Eos Trans. AGU, **69,** No. 44, 1427.

Hubbert, M. K., Willis, D. G., 1957, Mechanics of hydraulic fracturing: Trans. Soc. Petrol. Engrs., **201**, 153-168.

Hudson, J. A., 1980, Overall properties of a cracked solid: Math. Proc. Camb. Phil. Soc., **88**, 371-384.

Hudson, J. A., 1981, Wave speeds and attenuation of elastic waves in material containing cracks: Geophys. J. R. Astr. Soc., **64**, No. 1, 133-150.

Hudson, J. A., 1986, A higher order approximation to the wave propagation constants for a cracked solid, Geophys. J. R. Astr. Soc., **87**, 265-274.

Hudson, J. A., 1988, Seismic wave propagation through material containing partially saturated cracks: Geophys. J. R. Astr. Soc., **92**, 33-37.

Hudson, J. A., 1990, Overall elastic properties of isotropic materials with arbitrary distribution of circular cracks: Geophysical Journal International, **102**, No. 2, 465–469.

Hudson, J. A., 1991, Crack distributions which account for a given seismic anisotropy: Geophysical Journal International, **104**, No. 3, 517–521.

Hudson, J. A., and Harrison, J. P., 1997, Engineering Rock Mechanics: An Introduction to the Principles, Imperial College of Science, Technology and Medicine, University of London, United Kingdom.

Hudson, J. A., Liu, E., and Crampin S., 1996, The mechanical properties of materials with interconnected cracks and pores: Geophysical Journal International, **124**, 105-112.

Hudson, J. A., Liu, E., and Crampin, S., 1997, The mean transmission properties of a fault with imperfect facial contact: Geophysical Journal International, **129**, 720-726.

Hudson, J. A., and Liu, E., 1999, Effective elastic properties of heavily faulted structures: Geophysics, **64**, 479-485.

Hsu, K., Esmersoy, C., and Schoenberg, M., 1988, Seismic velocities and anisotropy from high resolution sonic logs: Expanded Abstract, 58th Annual International SEG Meeting, 114-116.

Jefferies, N. L., Clabburn, S., Tabb, C., Watkins, V. M. B., and Bromley, A. V., and 2000, Groundwater flow at Reskajeage Quarry, Cornwall: Acquisition of borehole data for the NAPSAC Fracture Network Program: AEA Technology Report AEAT/ERRA-0087.

Johnston, D. H., and Toksöz, M. N., 1980, Ultrasonic P and S wave attenuation in dry and saturated rocks under pressure: Journal of Geophysical Research, **85**, 925-936.

Jones, S. M., 1995, The effects of confining pressure, pore fluid salinity and saturation on the acoustic properties of sandstones: Ph.D. thesis, University of Reading.

Jones, T. D., 1986, Pore fluids and frequency-dependent wave propagation in rocks: Geophysics, **51**, 1939-1953.

Kendall, K., and Tabor, D., 1971, An ultrasonic study of the area of contact between stationary and sliding surfaces: Proc. R. Soc. Lond., A323, 321-340.

King, M. S., 1966, Wave velocities in rock as a function of changes in overburden pressure and pore fluid saturants: Geophysics, **31**, 50-73.

King, M. S., Myer, L. R., and Rezowalli, J. J., 1986, Experimental studies of elastic-wave propagation in a columnar-jointed rock mass: Geophysical Prospecting, **34**, No. 8, 1185-1199.

King, M. S., and Shams-Khanshir, M., 1998, Petrophysics studies of sedimentary rocks from a cross-hole seismic test site: International Journal of Rock Mechanics and Mining Sciences, **35**, 279-289.

Klimentos, T., and McCann, C., 1990, Relationships among compressional wave attenuation, porosity, clay content, and permeability in sandstones: Geophysics, **55**, No 8, 998-1014.

Kragh, E., Chapman, C., Emsley, S., and Dodds, K., 1996, Anisotropic Traveltime Tomography in a Hard-Rock Environment: First Break, **14**, No. 10, 391-397.

Liu, E., Crampin, S., and Queen, J. H., 1991, Fracture detection using crosshole surveys and reverse vertical seismic profiles at the Conoco borehole test facility, Oklahoma: Geophysical Journal International, **107**, 449-463.

Liu, E., Crampin, S., Queen, J. H., and Rizer, W. D., 1993, Velocity and attenuation anisotropy caused by microcracks and macrofractures in azimuthal reverse VSPs: Canadian Journal of Exploration Geophysics, **29**, 177-188.

Liu, E., Hudson, J. A., and Pointer, T., 2000, Equivalent medium representation of fractured rock: Journal of Geophysical Research, **105**, No. B2, 2981-3000.

Liu, E., and Li, X.Y., 2000, Estimation of pore or fracture fluids from seismic measurements: 62nd European Association of Geoscientists and Engineers, Expanded Abstracts, Paper No. C-6.

Liu, E., MacBeth, C. D., Pointer, T., Hudson, J. A, and Crampin, S., 1996, The effective elastic compliance of fractured rock: Paper presented at the 66th Annual SEG Conference, Denver Colorado, 1842-1845.

Lomize, G. M., 1951, Water flow through jointed rock. Moscow: Gosenergoizdat.

Lubbe, R., and Worthington, M. H., 2003, A field investigation of the compliance of fractured rock, 65th European Association of Geoscientists and Engineers, Stavanger, Norway.

MacBeth, C. D., 1995, How well can seismic anisotropy resolve natural fractures in hydrocarbon reservoirs, and is there room fore improvement?: 4th International Congress of the Brazilian Geophysical Society, 571-574.

Majer, E. L., Peterson, J. E., Daley, T., Kaelin, B., Myer, L. R., Queen, J., D'Onfro, P., and Rizer, W., 1997, Fracture detection using crosswell and single well surveys: Geophysics, **62**, 495-504.

Mandelbrot, B. B., 1982, The fractal geometry of nature, W. H. Freeman, New York.

Mavko, G. M., and Nur, A., 1975, Melt squirt in the asthenosphere: Journal of Geophysical Research, **80**, No. B11, 1444-1448.

Mavko, G. M., and Nur, A., 1979, Wave attenuation in partially saturated rocks, Geophysics, **44**, No. 2, 161-178.

Mavko, G., Mukerji, T., and Dvorkin, J., 1998, The Rock Physics Handbook: Tools for Seismic Analysis in Porous Media: Cambridge University Press.

McCann, C., and Sothcott, J., 1992, Laboratory measurements of the seismic properties of sedimentary rocks. In: Geological applications of wireline logs II (Eds. Hurst, A.,

Griffiths, C. M, and Worthington, P. F.), Special Publication of the Geological Society of London, **65**, 285-297.

Meissner, R., 1983, Attenuation of seismic waves in sediments: Proc. 11th World Petroleum Congress, 363-379.

Moos, D., and Zoback, M. D., 1983, In situ studies of velocity in fractured crystalline rocks: Journal of Geophysical Research, **88**, No. B3, 2345-2358.

Mukerji, T., and Mavko, G., 1994, Pore fluid effects on seismic velocity in anisotropic rocks: Geophysics, **59**, No. 2, 233–244.

Myer, L. R., Hopkins D., and Cook, N. G. W., 1985, Effect of contact area of an interface on acoustic wave transmission characteristics, in Proceedings of the 26th US Rock Mechanics symposium, Balkema, Boston, Massachusetts, **1**, 565-572.

Myer, L. R., Hopkins, D., Peterson, J. E., and Cook, N. G. W., 1995, Seismic wave propagation across multiple fractures. In Myer, Tsang, Cook and Goodman, editors: Fractured and Jointed Rock Masses, Balkema, 105-109.

Neep, J. P., 1995, Field studies of seismic attenuation at a borehole test site: Ph.D. thesis, Imperial College of Science Technology and Medicine, University of London.

Neep, J. P., Sams, M. S, Worthington, M. H., and O'Hara-Dhand, K. A., 1996, Measurements of seismic attenuation from high resolution crosshole data: Geophysics, **61**, 1175-1188.

O'Connell, R. J., and Budiansky, B., 1977, Viscoelastic properties of fluid–saturated cracked solids: Journal of Geophysical Research, **82**, No. 36, 5719-5736.

Pain, C. C., Herwanger, J. V., Worthington, M. H., and de Oliveira, C. R. E., 2002, Effective multidimensional resistivity inversion using finite element techniques: Geophysical Journal International, **151**, 710-719.

Papadakis, E. P., 1966, Ultrasonic diffraction loss and phase change in anisotropic materials: Journal of the Acoustical Society of America, **40**, 863-876.

Papadakis, E. P., 1972, Ultrasonic diffraction loss and phase change for broad-band pulses: Journal of the Acoustical Society of America, **52**, 847-849.

Papadakis, E. P., Fowler, K. A., and Lynworth, L. C., 1973, Ultrasonic attenuation by spectral analysis of pulses in buffer rods: method and diffraction corrections: Journal of the Acoustical Society of America, **53**, 1336-1343.

Pointer, T., Liu, E., and Hudson, J. A., 2000, Seismic wave propagation in cracked porous media: Geophysical Journal International, **142**, 199-231.

Portsmouth, I. R., Worthington, M. H., and Kerner, C. C., 1993, A field study of seismic attenuation in layered sedimentary rocks - I. VSP data: Geophysical Journal International, **113**, 124-134.

Portsmouth, I. R., Worthington, M. H., and Neep, J. P., 1993, A field study of seismic attenuation in layered sedimentary rocks - II. Crosshole data: Geophysical Journal International, **113**, 135-143.

Pratt, R. G., and Chapman, C. P., 1992, Traveltime Tomography in Anisotropic Media – II. Application: Geophysical Journal International, **109**, No. 1, 20-37.

Pratt, R. G., McGaughey, W. G., and Chapman, C. H., 1993, Anisotropic velocity tomography: A case study in near surface rock mass: Geophysics, **58**, No. 12, 1748-1763.

Pratt, R. G., and Sams, M. S., 1996, Reconciliation of cross-hole seismic velocities with well information in a layered sedimentary environment: Geophysics, **61**, 549-560.

Pride, S. R., Berryman, J. G., and Harris, J. M., 2004, Seismic attenuation due to wave-induced flow: Journal of Geophysical Research, **109**, 1-19.

Priest, S. D., 1985, Hemispherical Projection Methods in Rock Mechanics: George Allen and Unwin Ltd., London.

Pyrak-Nolte, L. J., 1988, Seismic visibility of fractures: Ph.D. thesis, University of California.

Pyrak-Nolte, L. J., 1996, The seismic response of fractures and the interrelationships among fracture properties: International Journal of Rock Mechanics Mining Science & Geomechanics Abstracts, **33**, No. 8, 785-802.

Pyrak-Nolte, L. J., and Morris, J. P., 2000, Single fractures under normal stress: The relation between fracture specific stiffness and fluid flow: International Journal of Rock Mechanics and Mining Sciences, **37**, 245-262.

Pyrak-Nolte, L. J., and Nolte, D. D., 1992, Frequency dependence of fracture stiffness: Geophysical Research Letters, **19**, No. 3, 325-328.

Pyrak-Nolte, L. J., Cook, N. G. W., and Myer, L. R., 1987, Seismic visibility of fractures: In Proceedings of Rock Mechanics: 28th US Symposium on Rock Mechanics, Tucson, 47-56.

Pyrak-Nolte, L. J., Meyer, L. R., and Cook, N. G. W., 1990a, Transmission of seismic waves across natural fractures: Journal of Geophysical Research, **95**, No. B6, 8617-8638.

—— 1990b, Anisotropy in Seismic Velocities and Amplitudes from Multiple Parallel Fractures: Journal of Geophysical Research, **95**, No. B7, 11345-11358.

Pyrak-Nolte, L. J., Meyer, L. R., Cook, N. G. W., and Witherspoon, P. A., 1987a, Hydraulic and mechanical properties of natural fractures in low permeability rock: In Proceedings of the 6th International Congress of Rock Mechanics, Montreal, Balkema, Boston, Massachusetts, **1**, 225-232.

Raikes, S. A., and White, R. E., 1984, Measurements of earth attenuation from downhole and surface seismic recordings: Geophysical Prospecting, **32**, 892-919.

Raven, K. G., and Gale, J. E., 1985, Water flow in natural factures as a function of stress and sample size: International Journal of Rock Mechanics Mining Science & Geomechanics Abstracts, **22**, 251.

Re, F., Scavia, C., and Zaninetti, A., 1997, Variation in contact areas of rock joint surfaces as a function of scale: International Journal of Rock Mechanics and Mining Sciences, **34**, Paper No. 254.

Richards, P. G., and Menke, W., 1983, The apparent attenuation of a scattering medium: Bull. Seism. Soc. Am., **73**, 1005-1021.

Sams, M. S., Neep, J. P., Worthington, M. H., and King, M. S., 1997, The measurement of velocity dispersion and frequency-dependent intrinsic attenuation in sedimentary rocks: Geophysics, **62**, No. 5, 1456-1464.

Sayers, C. M., and Kachanov, M., 1991, A simple technique for finding effective elastic constants of cracked solids for arbitrary crack orientation statistics: Int. J. Solids Struct., **27**, 671-680.

Schoenberg, M., 1980, Elastic wave behaviour across linear slip interfaces: Journal of the Acoustical Society of America, **68**, No. 5, 1516-1521.

Schoenberg, M., and Douma, J., 1988, Elastic wave propagation in media with parallel fractures and aligned cracks: Geophysical Prospecting, **36**, 571-590.

Schoenberg, M., and Sayers C. M., 1995, Seismic Anisotropy of Fractured Rock: Geophysics, **60**, No. 1, 204-211.

Schoenberg, M., 1998, Acoustic characterization of underground fractures: Expanded Abstract, 68th Annual International SEG Meeting, New Orleans, 1624-1627.

Sheriff, R. E., and Geldart, L. P., 1999, Exploration Seismology: Cambridge University Press, Cambridge, 2nd ed.

Sothcott, J., 1991, Report on performance of Jones and Shipman surface grinder for preparing parallel faces on rock cores, University of Reading.

Spencer, J. W., 1981, Stress relaxation at low frequencies in fluid saturated rocks: Attenuation and modulus dispersion: Journal of Geophysical Research, **86**, No. B3, 1803-1812.

Swan, G., 1983, Determination of stiffness and other joint properties from roughness measurements: Rock Mech. and Rock Eng., **16**, No 1, 19-38.

Telford, W. M., Geldart, L. P., and Sheriff, R. E., 1990, Applied Geophysics: Cambridge University Press, Cambridge, 2nd ed.

Thompson, T. F., 1966, San Jacinto tunnel: In Engineering Geology in Southern California, Association of Engineering Geologists, Los Angeles, California, 105-107.

Thomsen, L., 1986, Weak elastic anisotropy: Geophysics, **51,** No. 10, 1954-1966.

Tittmann, B. R., Balau, J. R., and Abdel-Gawad, M., 1984, The role of viscous fluid in the attenuation and velocity of elastic waves in porous rocks, in Physics and Chemistry of Porous Media: American Institute of Physics, 131-143, Eds. Johnson, D. L. & Sen, P. N.

Toksöz, M. N., Johnston, D. H., and Timur, A., 1979, Attenuation of seismic waves in dry and saturated rocks, I: Laboratory measurements: Geophysics, **44**, 681-690.

Vlastos, S., Liu, E., Main, I. G., and Li, X. Y., 2003, Numerical simulation of wave propagation in media with discrete distributions of fractures: effects of fracture sizes and spatial distributions: Geophysical Journal International, **152**, 649-668.

Winkler, K. W., and Murphy, W. F. III, 1995, Acoustic velocity and attenuation in porous rock: Rock physics and phase relation. A handbook of physical constants, AGU Reference shelf 3, 20-34.

Winkler, K. W., 1985, Dispersion analysis of velocity and attenuation in Berea sandstone: Journal of Geophysical Research, **90**, 6793-6800.

Winkler, K. W., and Nur, A., 1982, Seismic attenuation: Effects of pore fluids and frictional sliding: Geophysics, **45**, No. 1, 1-15.

Winkler, K. W., and Plona, T. J., 1982, Technique for measuring ultrasonic velocity and attenuation spectra in rocks under pressure: Journal of Geophysical Research, **87**, 10776-10780.

Worthington, M. H., and Hudson, J. A., 2000, Fault properties from seismic *Q*: Geophysical Journal International, **143**, 937-944.

Wu, T. T., 1966, The effect of inclusion shape on the elastic moduli of a two-phase material: Int. J. Solids Struct., **2**, 1-8.

Xie, H., 1993, Fractals in Rock Mechanics, Balkema, Rotterdam.

Xu, S., and King, M. S., 1992, Modelling the elastic and hydraulic properties of fractured rocks: Marine and Petroleum Geology, **9**, 155-166.

Yamamoto, K., Kosuga, M., and Hirasawa, T., 1981, A theoretical method of the determination of effective elastic constants of isotropic composite: Tôhoku Geophysical Journal, Science Reports of the Tohoku University, Series 5, **28**, 47-67.

Yielding, G., Walsh, J., and Watterson, J., 1992, The prediction of small-scale faulting in reservoirs: First Break, **10**, 449-460.

Yoshioka, N., and Kikuchi, M., 1993, Visco-elastic response of joints to transmission waves: Geophysical Research Letters, **20**, 1143-1146.

Zemanek, J., Glenn, E. E., Norton, L. J., and Caldwell, R. L., 1970, Formation evaluation by inspection with the borehole televiewer: Geophysics, **35**, No. 2, 254-269.

Zimmerman, R. W., Chen, D. W., Long, J. C. S., and Cook, N. G. W., 1990, Hydromechanical coupling between stress, stiffness, and hydraulic conductivity of rock joints and fractures. In: Barton, Stephansson, editors. Rock Joints, Rotterdam: Balkema, 571-577.

Zoback, K. L., and Zoback, M., 1980, State of stress in the conterminous United States: Journal of Geophysical Research, **85**, 6133-6156.